3D Nonlocal Damage Modeling for Steel Structures under Earthquake Loading

Dissertation

submitted to and approved by the

Department of Architecture, Civil Engineering and Environmental Sciences
University of Braunschweig - Institute of Technology

and the

Faculty of Engineering
University of Florence

in candidacy for the degree of a
Doktor-Ingenieur (Dr.-Ing.) /
Dottore di Ricerca in "Mitigation of Risk due to Natural Hazards on Structures and Infrastructures" *)

by
Jana Velde
born 15.10.1981
from Kassel, Germany

Submitted on	18 March 2010
Oral examination	07 May 2010
Professorial advisors	Prof. Dr.-Ing. Dieter Dinkler Prof. Dr.-Ing. Luca Facchini

2010

*) Either the German or the Italian form of the title may be used.

ISBN 978-3-926031-08-2

Herausgeber: Prof. Dr.-Ing. Dieter Dinkler

Kurzfassung

Die zunehmende Anzahl starker Erdbeben erfordert Modelle, mit denen die daraus resultierenden Risiken für die von Menschen gebaute Umwelt abgeschätzt werden können. Im Rahmen dieser Arbeit wird ein Modell zur Beschreibung des Materialverhaltens von Stahl vorgestellt um den Zustand von Stahlkonstruktionen nach Erdbeben bewerten zu können. Der Schwerpunkt der Arbeit liegt auf der Modellierung der Materialschädigung und der Schädigungsevolution unter zyklischer Beanspruchung. Der Gesamtschädigungszustand kann über einen globalen Schädigungsindex abgeschätzt werden. Ausgewählte Beispiele zeigen die Schädigungsevolution in Baustahl unter dynamischer Anregung und bekräftigen, dass das vorgestellte Modell ein wertvolles Werkzeug zur Abschätzung des durch Erdbeben hervorgerufenen Schädigungszustandes ist.

Abstract

The increasing number of strong earthquakes requires models for estimating the resulting risks on the human built environment. Within this work, a model describing the material behavior of steel is presented in order to evaluate the condition of steel structures after seismic action. The main focus is on modeling material damage and damage evolution under cyclic loading. The overall damage state can be assessed via a global damage index. Selected examples show the damage evolution in mild structural steel under dynamic excitation and confirm that the proposed model is a powerful tool in order to estimate damage states caused by earthquakes.

Contents

Notations

Mathematical symbols and numerical parameters

∂	partial derivative
∇	Nabla-operator
$\cdot$	scalar product
$:$	double scalar product
$\times$	vector product
$H(x)$	Heaviside function
$\delta(x)$	Dirac delta function
$tr[\,]$	trace of a tensor
$det[\,]$	determinant of a tensor
$\langle\,\rangle$	McAuley brackets
γ, β	parameter of Newmark integration
ξ	position of collocation

Scalars, vectors, and tensors

$\mathbf{u}$	node displacement vector
$\mathbf{p}$	volume load vector
$\bar{\mathbf{t}}$	surface load vector
$\boldsymbol{\sigma}$	stress tensor
$\boldsymbol{\sigma}^D$	deviatoric part of stress tensor
σ_{eq}	equivalent stress
σ_{ex}	over stress
$\boldsymbol{\varepsilon}$	total strain tensor
$\boldsymbol{\varepsilon}^{el}$	elastic strains
$\boldsymbol{\varepsilon}^{in}$	inelastic strains
ε_{eq}^{in}	equivalent inelastic strain
p	viscoplastic strain
p^+	active viscoplastic strain
r, K	isotropic hardening
$\alpha, \mathbf{X}$	kinematic hardening
$\bar{\mathbf{M}}$	damage effect tensor
D	damage variable

$\bar{D}$	nonlocal damage variable
$\mathbf{Y}$	energy release rate
$\mathbf{Q}, \mathbf{Q}^*$	direction tensor
$\mathbf{E}$	elasticity tensor
$\mathbf{K}$	stiffness matrix
$\mathbf{C}$	damping matrix
$\mathbf{M}$	mass matrix
M	strain memory surface
$\boldsymbol{\beta}$	displacement of the strain memory surface
q	amplitude of the strain memory surface
$\mathbf{n}_F$	normal to the yield surface
$\mathbf{n}_M$	normal to the strain memory surface

Material parameters

E	Modulus of elasticity
ν	Poisson's ratio
σ_y	yield stress
a_1, a_2	yield stress parameter
σ_P, n	viscoplasticity parameter
b, Q	isotropic hardening
a, C	kinematic hardening
c_i	ductile damage parameter
σ_K, s, t	creep damage parameter
ρ	density
c_α, c_β	Rayleigh damping parameter
h	crack closure parameter
ε_D^{in}	damage threshold strain
l_c	internal length

Other variables are defined in the context of their appearing.

1 Introduction

The increasing number of strong earthquakes over the past years has raised the awareness of consequences of seismically induced catastrophes. The primary seismic hazards like fault breaks and ground motion are followed by a destruction of the human built environment leading to injuries or casualties of human beings. Several potentially dangerous situations triggered by primary hazards may follow, like tsunamis caused by fault break, soil liquefaction, landslides caused by ground shaking, fire, or flooding produced by dam break. Without worldwide assistance, rise would be given to economical breakdown, crime, or spread of epidemics due to e.g. a reduced disposition of drinking water. The worldwide need for tools that help to deal with the unpredictable nature of this hazard has caused the development of methods that predict damage and losses caused by earthquakes and give advices how to counteract such catastrophes. A fundamental tool helping to calculate the expected number of losses due to natural catastrophes and helping to make decisions to reduce the losses is risk management.

1.1 Motivation

Risk management is a valuable tool in order to deal with strong earthquakes or other types of natural hazards. The whole process of risk management can be divided primarily into risk identification, risk assessment, and risk treatment [113]. After the risk is identified, risk assessment deals with the calculation and evaluation of risk and results into decisions how to treat the risk. Figure 1.1 gives an overview of the whole chain of the risk management process. The assessment of risk comprises risk analysis and risk evaluation. Risk analysis mainly consists of exposure analysis, hazard analysis, vulnerability analysis, and the assessment of damage, losses, and consequences. Thereby, exposure analysis deals with the identification of all items, called elements at risk, which are exposed to a certain hazard. The characterization of the hazard in terms of its intensity and frequency is accomplished by hazard analysis. While the vulnerability analysis creates the relation between hazard intensity and resulting damage, the assessment of damage and losses results in a measure for risk.
Measures for risk can be divided into measures for structural risk or total risk. Structural risk is of primary importance for engineers in order to predict the behavior and the response of a structure or structural element. It is defined as the annual probability of occurrence of a hazard multiplied by the expected damage:

$$\text{structural risk} = \text{probability x damage} \qquad [\text{damage measure / year}]$$

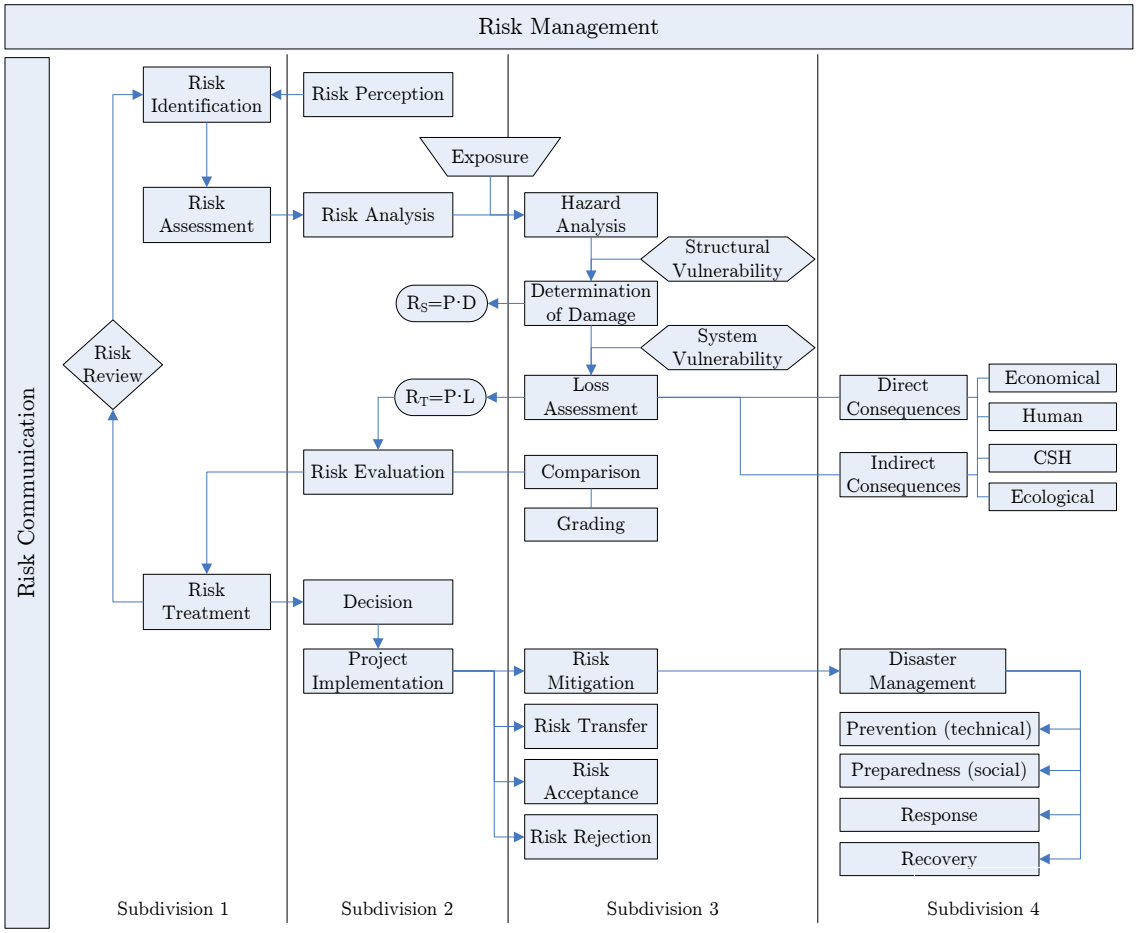

Figure 1.1: Overview of the risk management process [113]

The total risk comprises all consequences and is, if reasonable, expressed in monetary units. It can be calculated by the product of the annual probability of occurrence of a hazard and the expected losses:

$$\text{total risk} = \text{probability x loss} \qquad [\text{loss unit / year}]$$

1.2 Goal of research

This work makes a contribution concerning the estimation of damage for seismic structural risk. The objective is the development of a model that is able to describe the evolution of damage in structures subjected to seismic ground motion. The model is embedded into the framework of seismic risk analysis and can be used as a new and valuable tool for vulnerability analysis. The assessment of seismic damage is realized through a global damage index.

The proposed model is based on numerical time integration of the equation of motion and considers nonlinear material behavior. The material model is developed for the description of steel. While seismic damage is often related from measures like displacement or plastic strain, this work perceives damage as material deterioration. In order to accurately describe deteriorated material due to seismically induced vibrations, a continuum damage approach is chosen which is derived from thermodynamics. Besides viscoplasticity and hardening, the main focus is on the development of material equations for the description of damage.
The development of the damage evolution law raises two important questions which are not satisfactorily answered in literature: How does damage appear in mild construction steel which is mainly used for steel civil engineering buildings and how does damage evolute under cyclic loading? Within this work, those two questions are specifically traced in order to develop a precise model for the prediction of damage in steel structures subjected to inelastic cyclic straining as it occurs during earthquakes.
After having determined evolution laws for the description of material damage caused by seismic action, global damage indices permit the evaluation of the overall structural condition and allow the calculation of structural risk for seismic risk analysis and risk management.

1.3 Layout

Chapter 2 gives a brief introduction to earthquakes and their handling using seismic risk analysis. The parts of the seismic risk analysis chain are generally described and their relevance for this work is outlined.
Chapter 3 describes the material behavior and the characteristics of mild construction steel. Mild construction steel is mainly used for civil engineering structures and is therefore exposed to earthquakes. While the elastic structural behavior of steel buildings under seismic action is widely investigated, the inelastic response under consideration of material damage is still insufficiently assessed. In order to develop a material damage model for steel buildings subjected to seismic loading, the material behavior of mild structural steel is analyzed in detail.
A new procedure proposed for vulnerability analysis and damage assessment of steel structures under seismic action is developed in chapter 4. The model is based on numerical time integration of the equation of motion and includes nonlinear material behavior. Viscoplasticity, isotropic and kinematic hardening as well as softening and damage are included in the material model. Particularly examined is the description of damage evolution under cyclic loading. The thermodynamical consistency of the material model is shown. Since softening and damage are always accompanied by localization of the deformation field, which leads to a dependance on the fineness of finite-element discretization, the model is extended by a nonlocal implicit gradient enhanced formulation. The extension leads to an additional partial differential equation, called gradient equation. Furthermore, a procedure is proposed for assessing material damage. In order to make an overall statement about the level of damage and evaluate structural stability,

safety, and life time, a global damage index is proposed that transforms the output of the material model into one global measure of damage.
The numerical implementation of the model is described in chapter 5. Spatial discretization of the equation of motion and the gradient equation is performed using the finite-element method. The discretization in time of the equation of motion is accomplished with the Newmark method. The material equations are discretized in time using the implicit Euler approach. A solving scheme illustrated the calculation procedure.
Chapter 6 deals with parameter identification and evaluation by means of comparison with experiments. New experiments are performed on the mild construction steel S 355 in order to create an experimental basis for the adjustment of the model parameters.
The abilities of the new model are demonstrated in chapter 7. The material behavior under reversed loading is investigated by means of selected examples and the accuracy of the damage model is demonstrated by comparison with experimental data. The assessment of cantilevers serves for proving coupling of structural dynamics and advanced material behavior. Finally, three-dimensional structures subjected to seismic loading are analyzed. In order to make an overall statement about the structural stability, safety, and residual life time of those structures after the earthquake, a global damage index is calculated.

2 Seismic risk analysis

Seismic risk analysis deals with the estimation of damage and losses due to earthquakes. Earthquakes are geological occurrences linked to plate tectonics of the earth's crust. The movement of the plates, caused by thermal processes, leads to a formation of stresses. If the stresses exceed the resistance of the plate at a certain position, a crack will occur. This point of origin is called hypocenter, while the location at the surface above the hypocenter is called epicenter. Starting at the hypocenter, seismic waves lead to ground shaking or even permanent deformations of the earth's surface. Figure 2.1a shows a road damage after permanent ground deformations through an earthquake in Japan, 2004. Propagation of seismic waves is very complex due to the inhomogeneities of the earth's crust.
Seismic waves can be classified into body waves and surface waves. The body waves consist of primary or longitudinal waves and secondary, also called transversal, waves. Rayleigh waves and Love waves are surface waves, where the latter are the most destructive ones. If seismic waves encounter buildings and infrastructure, they can cause significant damage to single structures and whole areas. Figure 2.1b/c exemplarily shows seismic induced damage on steel structures.

(a) (b) (c)

Figure 2.1: (a) road damage after surface deformations due to an earthquake in Japan in 2004, (b) collapsed steel building after the Mexico City earthquake in 1985, (c) steel fracture in brace to column connection after the Kobe earthquake, 1995

Representation of earthquakes
In order to characterize the power of an earthquake for a certain region measured ground motion data can be used. Acceleration measurements, which are most suitable for the

description of earthquakes, can be obtained by accelerometers. From time to time seismic ground motion is also described by velocity and displacement measurements. As a typical record of seismic ground motion figure 2.2 presents ground acceleration, velocity, and displacement of the Loma Prieta earthquake in 1989. The signals are shown in time and frequency domain. The frequency content can be identified using a Fourier Transformation and shows that the main frequency content of the acceleration signal range from 0 to 10 Hz. The frequency spectrum of the velocities has a range from 0 to 4 Hz and the spectrum of displacement is further limited to a range between 0 and 1 Hertz. These changes in frequency content can be reconstructed using integration since velocity and displacement can be obtained from acceleration by integration which leads to a shift of frequencies in the frequency spectrum.

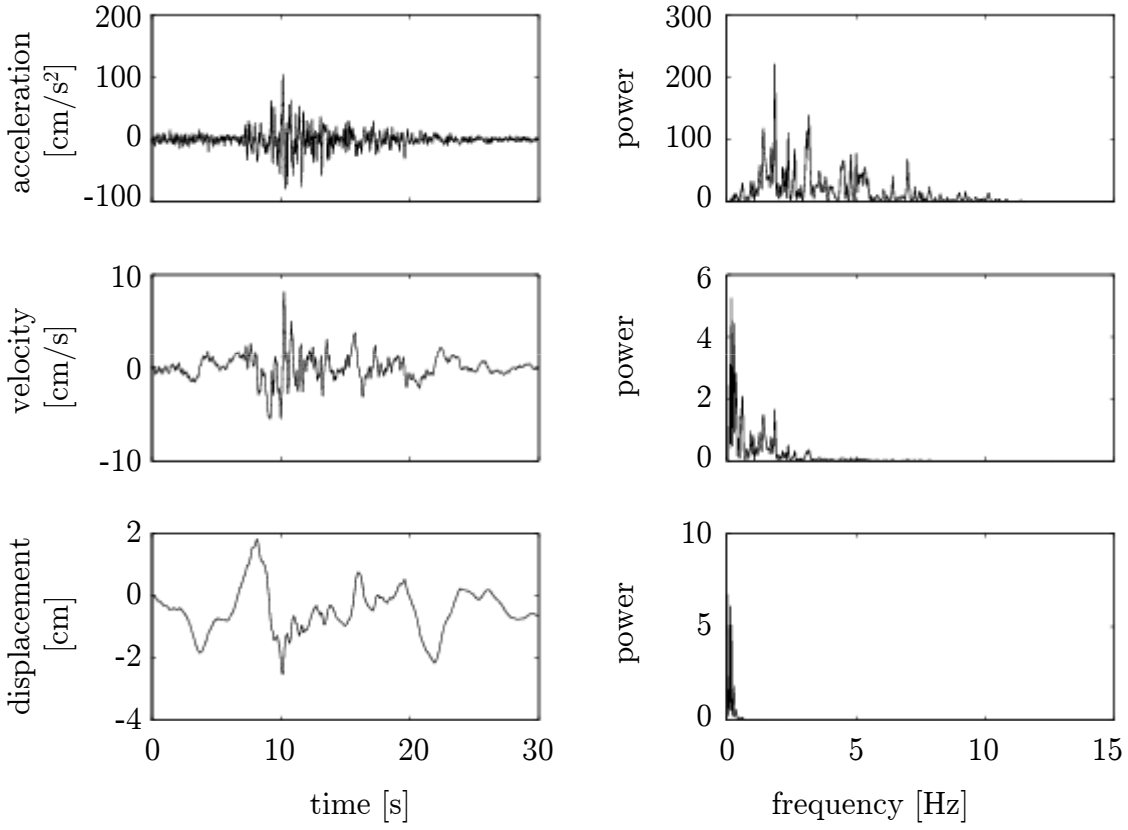

Figure 2.2: Ground acceleration, velocity and displacement in the time and frequency domain of the Loma Prieta earthquake of 1989

The representation in frequency domain leads to a second important way of characterizing earthquakes, namely by means of response spectra. A response spectrum can be obtained by solving numerically the differential equations of single-mass oscillators with fixed damping and varying eigenfrequencies due to a certain given earthquake. The maximum displacement responses S_d plotted over the corresponding periods T lead to a

curve that represents the behavior of structures with a certain damping due to a certain seismic event (see figure 2.3).

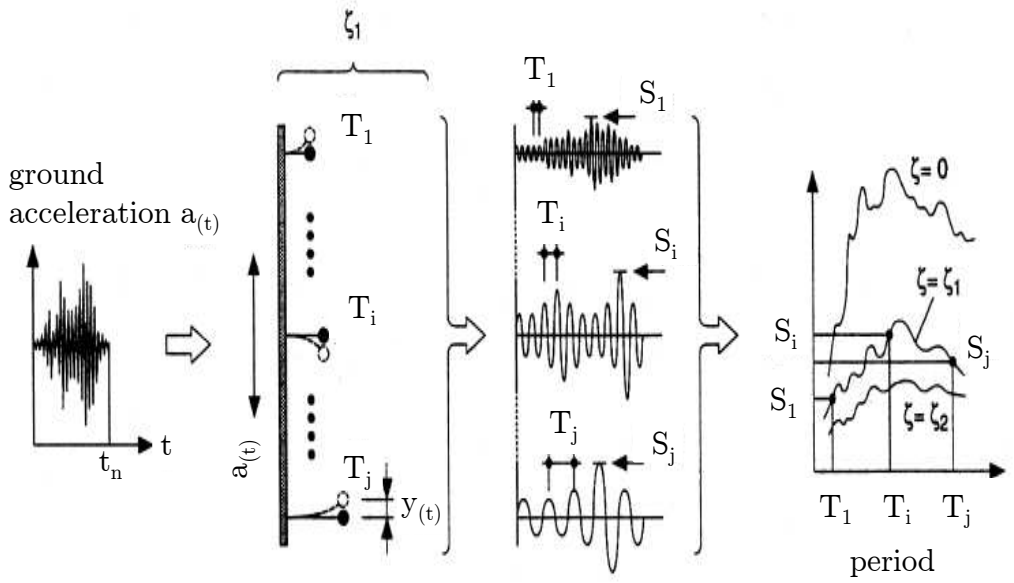

Figure 2.3: Procedure for the construction of response spectra [40]

The spectral ordinates of displacement S_d can be converted into spectral ordinates of velocity S_v and acceleration S_a:

$$S_d = \frac{1}{\omega} S_v = \frac{1}{\omega^2} S_a. \tag{2.1}$$

where ω is the eigen angular frequency of the single-mass oscillator. Using a double logarithmic representation, spectral displacement, velocity, and acceleration can be plotted into one diagram (see figure 2.4). For small periods, meaning stiff systems, a constant spectral acceleration can be read off, while big periods of flexible systems are related to constant spectral displacement.
Response spectra can be employed if detailed investigations with time integration should be avoided. Given the eigenfrequency and damping of a structure, the maximum response values can be determined. Subsequent investigations can be performed statically using the maximum response values.
Further parameters which can be used in order to represent earthquakes are given in chapter 2.2.

Seismic design of structures
Seismic design of structures is based on design spectra, which are flattened statistical evaluations of elastic response spectra of multiple registered earthquakes of almost the same intensity and similar tectonics and type of soil [7]. The calculation is performed

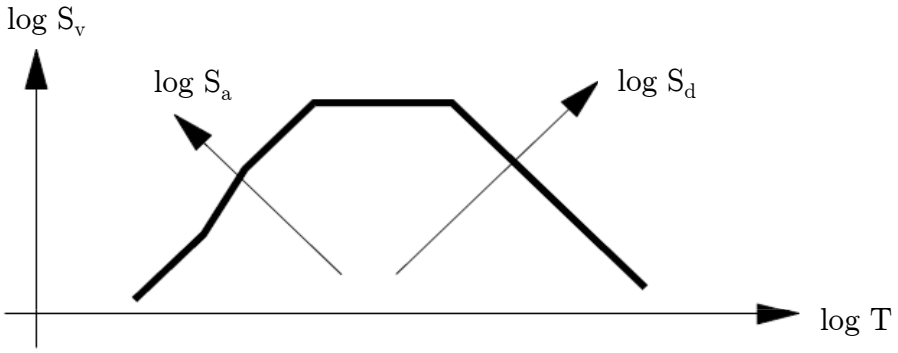

Figure 2.4: Double logarithmic response spectrum

with equivalent static forces and nonlinearities can be considered by a ductility factor q. In Germany, seismic design of structures is performed in accordance with DIN 4149. Structures, which are designed in accordance with design codes, are not necessarily safe regarding earthquakes. Strong earthquakes will still cause damage to buildings and infrastructure and can end in disasters. In order to handle the consequences of earthquakes to the human environment, risk management can be used. In the following a short overview of seismic risk analysis will be given which is an essential part of seismic risk management. The four parts of seismic risk analysis, namely exposure analysis, hazard analysis, vulnerability analysis, and the assessment of damage, seismic losses, and consequences, will be briefly explained and their relevance within this work will be outlined.

2.1 Exposure analysis

In order to characterize and analyse the exposure it is necessary to define a classification for all exposed items, denoted as elements at risk, and to determine the number of elements in each category. The classification system is different depending on the goal for which it is established. On the one hand, it is possible to group together structures, which behave similarly during a seismic event, sorted for example by the structural system, the material, or the height. On the other hand, a differentiation between the building occupation and the social function can be necessary, taking into account if the building belongs to the general building stock (e.g. residential, commercial, industrial use) or is an essential facility like buildings for government, civil defense, health and medical care, emergency response or for the purpose of education.
Within this work attention is concentrated on steel structures. Thus, the elements at risk should be classified according to the material. Seismic risk analysis can then be continued for all exposed items belonging to the group “steel“.

2.2 Seismic hazard analysis

The goal of seismic hazard analysis is the description of earthquake ground shaking motion by appropriate parameters and its presentation in terms of maps. Besides direct measurement of ground movement, three parameters - the earthquake magnitude, the earthquake intensity, and the peak ground acceleration - are mainly used to describe an earthquake [27]. While an earthquake has only one global magnitude, it has several local intensities and peak ground accelerations depending on the observation site.
The earthquake magnitude M is a global parameter for the strength of an earthquake. It is determined via seismometers which measure ground movement. Different magnitude definitions are available, for example the Richter Local Magnitude M_L, the Surface Wave Magnitude M_S, or the Body Wave Magnitude M_B. The one commonly used is the Richter magnitude M_L. It is defined as

$$M_L = log\ A - log\ A^0 \tag{2.2}$$

where A is the maximum amplitude recorded and $log\ A^0$ is a calibration factor. Large earthquakes have Richter magnitudes around 7, the largest one since 1990 had a magnitude of 9. Within an average year, about $10,000$ earthquakes occur with a magnitude of ≥ 4, 10-15 having disastrous consequences.
The earthquake intensity describes qualitatively the local strength of an earthquake at the surface and is directly linked to the consequences for human beings and structures. Although different intensity scale definitions exist, the intensities mainly vary between 1 and 12 and are related by observed damage on the natural and built environment and by human and animal reaction at the location. Widespread is the Mercalli intensity scale, see for example [27].
The peak ground acceleration PGA is a physical-mechanical parameter and is simply given by the largest absolute value of horizontal acceleration measured by an accelerometer during a certain earthquake.
Another important point of seismic hazard analysis is the determination of the probability of occurrence of a certain seismic event at a certain site. In order to predict this probability of occurrence, empirical ground motion prediction equations can be used. Those equations are obtained from statistical regression of ground motion databases or statistical regression of macroseismic observation and lead to a prediction of intensity or PGA, which may occur at a certain site within a specified time period.
Another possibility to describe seismic ground motion is the direct measurement of ground movement and its representation in terms of time records. Most commonly performed are ground acceleration measurements using accelerometers. The most important difference is that the exact time records of future earthquakes cannot be predicted. However, if measured, they can be used to evaluate the structural response by hindsight at a high precision. In order to design structures for future earthquakes using time records, synthetic ground motion data can be generated. After selecting an earthquake with a certain intensity which is likely to occur in a certain region within a certain time period, a possible time record can be modeled as a stationary process using stationary noise multiplied by a specific function of time, called envelope (see [28] for example for more

information). Within this work both measured and generated time acceleration records will be used in order to determine the response of structures subjected to seismic action.

2.3 Vulnerability analysis

The aim of seismic vulnerability methods is to establish a measure for damage of structures when hit by an earthquake. Three types of vulnerability approaches exist: observed vulnerability methods, methods based on expert judgement, and analytical methods [50]. While the first two methods deal with empirical approaches, statistical observations, or experience, analytical methods are based on the mathematical calculation of structural response. The structural response can consist of different measures, like displacement, curvature, or rotation to name a few examples. All outcomes need to be related to critical values in order to qualify the response. This leads to the introduction of a damage measure, in the following referred to as damage index (see chapter 2.4 or 4.5, respectively, for detailed information). Below, some of the most important analytical methods are presented. They differ in the consideration of material behavior (linear/nonlinear) and in the calculation procedure (static/dynamic).

Approach with statical equivalent forces
A simple approach to calculate the response of regular structures under seismic action uses statical equivalent forces in order to replace the real seismic loading. The procedure consists of three steps. First, a total equivalent force has to be determined. It can be obtained by multiplication of the structure's mass with a ground acceleration and a correction factor. The ground acceleration can be found using response spectra and the first eigenfrequency of the structure. The correction factor considers the fact that the effective modal mass of the first mode is on average 15% smaller than the total mass of the structure. The second step involves the distribution of the total equivalent force on the structure. For example, the force can be distributed linearly or according to the first eigenmode of the structure. In a third step, the structural response due to the static load is calculated using either linear or nonlinear material behavior.
The German code DIN 4149 for seismic design of regular structures is based on the approach with statical equivalent forces. Nonlinear material behavior is considered by a factor q which reduces the statical equivalent forces.

Modal response spectrum approach
If the structure is irregular, the modal response spectrum approach can be used. This method is based on decoupling a multi-mass oscillator into several single-mass oscillators, each presenting a natural mode of the original vibration. For every modal differential equation the maximum response, namely maximum acceleration, velocity, or displacement, can be obtained using response spectra. The total maximum response can be obtained by superposition of the single responses. In order to calculate the resulting internal forces, equivalent forces can be determined and distributed on the structure as described above in the former paragraph. Since it is important, how many vibration

modes are taken into account, effective modal masses are introduced. All vibration modes, that essentially contribute to the global vibration behavior, are considered if the sum of all effective modal masses which are included into the calculation is at least 90% of the total mass and if all modal modes with effective modal masses higher than 5% of the total mass are taken into account.
The modal response spectrum approach is used in DIN 4149 for irregular structures. While the calculation can be performed in 2D if the ground plan is regular, irregular structures with irregular ground plans have to be investigated in 3D.

Capacity spectrum method
The capacity spectrum method, developed by Freeman et al. in 1975, uses a response spectrum curve as well as a capacity or push-over curve. Both curves are plotted in one diagram so that the intersection point of the two curves, called performance point, indicates the maximum spectral displacement. The capacity curve is a load-displacement curve due to inelastic material behavior obtained from ultimate load analysis. Both curves have to be transformed into spectral displacement and spectral acceleration coordinates, respectively, in order to be combined in one diagram, before the estimated maximum displacement can be determined.

Numerical integration
Numerical time integration of total or single modal differential equations leads to results with the highest precision. Earthquakes are mainly characterized by ground acceleration records $\ddot{u}_g$. Seismic loading is embedded into the equation of motion by

$$m \cdot \ddot{u}_a + c \cdot \dot{u}_r + k \cdot u_r = 0 \tag{2.3}$$

with mass m, damping c, stiffness k, absolute acceleration $\ddot{u}_a = \ddot{u}_r + \ddot{u}_g$, and relative values for acceleration $\ddot{u}_r$, velocity $\dot{u}_r$, and displacement u_r, respectively. The equation of motion for structures under seismic excitation can then be written as

$$m \cdot \ddot{u}_r + c \cdot \dot{u}_r + k \cdot u_r = -m \cdot \ddot{u}_g. \tag{2.4}$$

Different numerical time integration schemes are available in order to solve the equation of motion, for example the method of central differences or the Newmark method. The structural systems can be simplified as single- or multi-mass oscillators or modelled continuously. If nonlinear behavior due to strong earthquakes is expected, inelastic material behavior can be considered. The material models may be extended if necessary, taking into account e.g. rate-independent or -dependent plasticity, viscosity, hardening, and damage.
Seismic analysis of structures including damage is mainly performed for concrete structures. The continuum damage mechanics theory is for example successfully applied to concrete dams. Calayir & Charaton [19] develop a 2D-continuum damage model which assumes that damage evolutes only under tensile stress states, whereas Lee & Fenves [79]

and Cervera et al. [21] propose models with two damage variables, one for tension and one for compression. In order to obtain unique and mesh objective numerical solutions a rate-dependent regularization is applied.
The investigation of reinforced concrete frames or buildings is mainly based on beam models. Faleiro et al. [46] present a beam model using a lumped plasticity approach in order to adapt damage models to the analysis of framed structures with damage concentrated in plastic hinges. Mata et al. [87] investigate two different damage models in order to describe deteriorated material behavior at the two-dimensional, cross-sectional scale. The combination of concrete and steel of reinforced concrete is considered by the mixing theory. At the global structural scale they use a three-dimensional beam model. Scotta et al. [122] propose a beam fibre approach which includes damage models for concrete and steel reinforcement and additionally comprises buckling of the reinforcement bars.
Seismic damage analysis of steel structures can hardly be found in literature. Dynamic analyses of a two-story steel frame subjected to different synthetic acceleration records of the El Centro earthquake are conducted by Shen & Wu [124]. They develop a finite-element model with a beam element and a structural solid element, respectively, which considers damage by a fatigue based damage law. Bleck et al. [15], Seal et al. [123], and Kanvinde & Deierlein [67] aim at the prediction of damage in steel structures under seismic loading but have investigated until now only the behavior of steel subjected to cyclic loading neglecting dynamic effects and mass inertia. Bleck et al. take into account fracture and damage mechanics. The damage model for cyclic loading is termed as an Ultra Low Cycle Fatigue Model which is a combination of a fracture process and a fatigue mechanism. Within their work, Bleck et al. propose the use of a void volume fraction model based on [78] which is extended to cyclic conditions by kinematic hardening. Hence, damage evolution does not differ for tensile and compressive stress states. Additionally to this model, the effective damage concept [98] according to Ohata and Toyoda with the advanced two-parameter criterion is applied for damage analyses. Seal et al. [123] propose a low cycle fatigue damage model. According to the authors, however, the model is until now only verified for fully reversed strain histories and the extension to irregular cyclic loading is still to be investigated. Kanvinde & Deierlein suggest the use of ultra low cycle fatigue in order to simulate the initiation of ductile fracture which is often the governing limit state in steel structures subjected to earthquakes. Ultra low cycle fatigue is characterized by a few reverse loading cycles to large inelastic strain amplitudes. While their work is concentrated on the development of a cyclic void growth model in order to accurately describe material deterioration in case of cyclic loading, investigations of steel structures under seismic action are not made.
Within this work a three-dimensional continuum damage model for steel will be developed that can describe the nonlinear structural response considering viscoplastic material behavior, isotropic and kinematic hardening, and ductile and creep damage under irregular cyclic loading as it may occur during earthquakes.

2.4 Assessment of seismic damage, losses, and consequences

The last step of the seismic risk analysis chain is the assessment of seismic damage, losses, and consequences. In a first step, structural damage can be obtained by evaluating the outcomes of the structural response of a system. Thereupon, structural risk can be calculated by multiplying structural damage and the probability of occurrence of an earthquake. Subsequently, total damage can be determined which includes all losses and consequences that occur due to an earthquake. The consequences for human beings, animals, and nature can be classified into economic, human, cultural, social, historical, and ecological consequences and are for example the number of casualties, economic losses like breakdowns of commercial, industrial, or agricultural business, or downtime (time out of service) resulting from damage. After all consequences are taken into account and the loss has been determined, the total risk can be calculated by the product of total damage and the probability of occurrence of an earthquake.
This work does not focus on total risk, so that total damage including all losses and consequences is not estimated, but takes into account structural damage in order to permit the estimation of structural risk of chosen earthquakes. Structural damage can be expressed best by means of damage indices, which normally have a range of zero to one. While zero corresponds to the undamaged state, a value of one is connected with structural collapse. In literature there exist many different proposals for damage indices which relate variables of structural response to critical or original values of structural response in order to obtain scaled damage measures. They differ according to the material, to the structure, or to the calculation procedure. In the following, an overview of the most important damage indices will be given.

Non-cumulative damage indices

The earliest and simplest measures of damage are non-cumulative indices. They do not account for effects of cumulative damage due to repeated inelastic deformation and effects of the duration and frequency content of ground motion. However, they are widely used due to their simplicity. The best known indices are the ductility ratio and the interstorey drift.

The ductility ratio μ is defined as the ratio of maximum deformation u_{max} to yield deformation u_{yield}:

$$\mu = \frac{u_{max}}{u_{yield}} = 1 + \frac{u_{max} - u_{yield}}{u_{yield}}. \tag{2.5}$$

It is commonly assumed that failure occurs when the ductility ratio (response) exceeds the structural ductility (capacity) that is equal to the ratio of the ultimate deformation under monotonic static load and the yield deformation.

The interstorey drift ID is the maximum relative displacement between two storeys Δu normalized to the storey height h:

$$ID = \frac{\Delta u}{h}. \tag{2.6}$$

If the maximum relative displacement is substituted by permanent displacement the index is called maximum permanent drift. According to Sozen [128] the percentage of damage of the structure D can be derived from the maximum interstorey drift in percentage:

$$D = ID \cdot 50 - 25. \tag{2.7}$$

As it can be easily seen this definition is only expedient for a certain range of small values of interstorey drift. From analysis of test data on components and small-scale structures it was found that an interstorey drift value smaller than 1 % corresponds to damage of non-structural components while values larger than 4 % may result in irreparable structural damage or collapse. Collapse is considered to occur when the interstorey drift exceeds 6 % [117].

Another non-cumulative damage index is the slope ratio. The slope ratio is a measure of damage due to stiffness degradation during seismic loading. It is defined as the ratio of the slope of the loading branch of the force-displacement diagram and the slope of the unloading branch. Roufaiel & Meyer [117] suggest that the ratio of initial stiffness and reduced secant stiffness at maximum displacement, called flexural damage ratio, can also be used as a measure of damage.

Cumulative damage indices

Although cumulative damage indices may not predict damage caused by a single, very large deformation, they consider the duration and intensity of an earthquake and describe the evolution of damage over time. The modeling of damage is usually performed either by using a low-cycle fatigue formulation, in which damage is taken as a function of the accumulated plastic deformation, or by incorporating a term related to the hysteretic energy absorbed during the loading.

Stephens & Yao [130] develop a cumulative index based on displacement ductility D. With Δu^+ as the displacement increment from negative to positive displacement and Δu^- as the displacement increment from positive to negative displacement within one cycle, the index is defined as

$$D = \sum \left(\frac{\Delta u^+}{\Delta u_f} \right)^{1-br} \tag{2.8}$$

with $r = \Delta u^+ / \Delta u^-$, Δu_f as the value of Δu^+ in a single-cycle test to failure and b as a constant. They recommend to assume Δu_f as 10 % of the storey height and b as 0.77.

The theory of low-cycle-fatigue has also been applied to the seismic analysis of structures to estimate the state of damage. Jeong & Iwan [62] propose an approach which is calibrated against observed failures of reinforced concrete columns. The number of cycles to failure n_f at a given ductility μ is found from a relationship similar to the well-known Coffin-Manson law:

$$n_f \mu^s = c \tag{2.9}$$

in which the constants s and c are taken as 6 and 416 respectively. The damage index is then found using Miner's rule for combining the effects of cycles at varying amplitude:

$$D = \sum_i \frac{n_i}{n_{f,i}} = \frac{n_i \mu_i^s}{c}. \tag{2.10}$$

An energy-based cumulative index is developed by Krätzig et al. [71]. The method is based on the definition of primary and follower half-cycles. A primary half cycle is defined as the first half-cycle of loading at a given amplitude, with subsequent half-cycles termed followers unless they exceed the previous maximum amplitude. For the positive deformation parts of the response the cumulative damage parameter is defined as

$$D^+ = \frac{\sum E_{p,i}^+ + \sum E_i^+}{E_f^+ + \sum E_i^+} \tag{2.11}$$

where $E_{p,i}$ is the dissipated energy in a primary half-cycle, E_i is the energy in a follower half-cycle, and E_f is the energy absorbed in a monotonic test to failure (see figure 2.5). After computing a similar parameter for the negative deformations, the overall damage index is found from

$$D = D^+ + D^- - D^+ D^-. \tag{2.12}$$

The model can account for both deformation and fatigue-type damage, since a high value of the index can be generated either by a single high-amplitude cycle or by repeated cycling at a lower amplitude.

Combined damage indices

An efficient way to characterize the damage state of structures is the combination of damage indices which take into account non-cumulative as well as cumulative damage. Like the index of Krätzig et al. [71], combined damage indices are able to compute high damage either by a single high-amplitude cycle or by repeated cycling at a lower amplitude.

The best-known and most widely used combined index is the index of Park & Ang

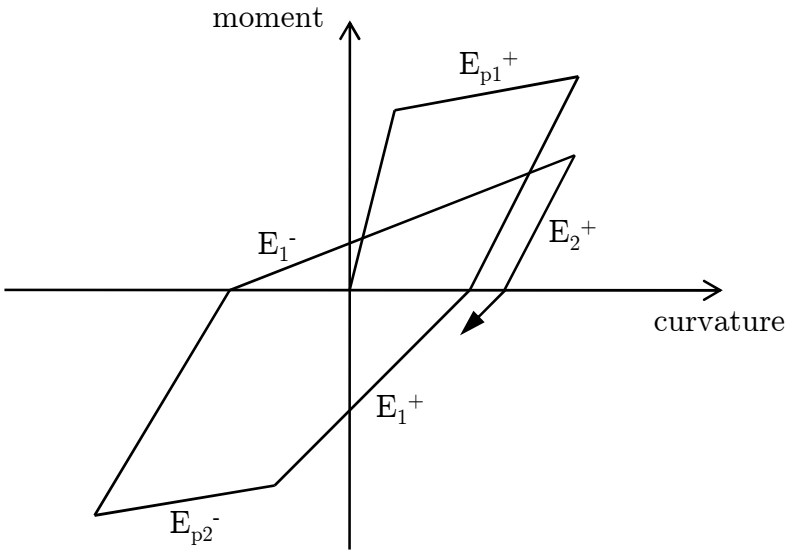

Figure 2.5: Dissipated energy in primary and follower half-cycles [71]

[103]. It consists of a simple linear combination of normalized deformation and energy absorption:

$$D = \frac{u_{max}}{u_{ult}} + \beta \frac{\int dE}{F_{yield}\ u_{ult}} \tag{2.13}$$

with the maximum displacement u_{max}, the ultimate displacement u_{ult}, the dissipated energy E, the yielding force F_{yield} and a parameter β for strength deterioration. The first term is a simple, pseudo-static displacement measure. It takes no account of cumulative damage, which is accounted for solely by the second energy term. The authors suggest the following classification for reinforced concrete structures:

	D	≤ 0.1	No damage or localized minor cracking
$0.1 \leq$	D	≤ 0.25	Minor damage - light cracking
$0.25 \leq$	D	≤ 0.4	Moderate damage - severe cracking, localized spalling
$0.4 \leq$	D	≤ 1.0	Severe damage - crushing of concrete, reinforcement exposed
	D	≥ 1.0	Collapse

Global damage indices

Global damage indices can be obtained either by weighting of local damage or by investigating the change of modal parameters before and after the earthquake. A generalized definition of a weighted global index is

$$D = \frac{\sum w_i D_i^{b+1}}{\sum w_i D_i^b}. \tag{2.14}$$

A high value of the exponent b will result in a greater emphasis on the most severely damaged elements, while the introduction of weights w_i enables the consideration of additional parameters. In its simplest form this formulation reduces to

$$D = \frac{\sum D_i^2}{\sum D_i}. \tag{2.15}$$

While many researchers agree on the use of local energy absorption as a weight, e.g. [104], [75], or [31], Bracci et al. [17] define the weights w_i as the gravity load supported by element i divided by the total weight of the structure. Using this definition, damage at the base of a structure is given a far higher weighting than damage of upper storeys, since it stands a greater chance of causing complete structural collapse. However, Ghobarah et al. [49] point out that the use of weighted average procedures to calculate global damage indices does not properly account for the local concentration of damage, does not distinguish between a column and a beam, and may lead to misleading results. It is possible that a few structural members of the building have suffered severe damage without being reflected in the global index.

For this reason, global damage can be deduced more reliably from modal parameters. Assessment of damage from changes in modal parameters may be based on natural periods and frequencies or involve the use of mode shapes to locate damage. It is well-known that damage causes a change in the dynamic characteristics of a structure. Usually there is an increase in the natural period (decrease in frequency) caused principally by stiffness degradation and also an increase in damping (energy dissipation). Damping has been found to be a too variable parameter and one with too many different causes to serve as a damage indicator. Therefore, attention has been focused on changes in period (frequency) mainly taking into account the first vibration mode. In case of localized or relatively minor damage it is likely that damage will have a significant effect only on the higher modes of vibration. Under these circumstances, examination of the higher mode shapes can be used as a method of identifying both magnitude and location of structural damage.
Krätzig & Petryna [72] propose a global damage measure based on the evolution of the eigenvalues λ of the tangential stiffness matrix $\mathbf{K_T}$. The damage indicator is defined as

$$D = 1 - \frac{\lambda^{damaged}}{\lambda^{undamaged}}. \tag{2.16}$$

Structural failure will occur if at least one eigenvalue of $\mathbf{K_T}$ diminishes. Thus, the indicator reaches a value of one if a plastic hinge occurs, although the appearance of a plastic hinge is not connected with failure for statically undetermined systems. For dynamic problems the authors recommend using the eigenfrequencies of the structure

$$D = 1 - \frac{\omega^{damaged}}{\omega^{undamaged}} \tag{2.17}$$

since the tangential stiffness matrix does not continuously provide physically reasonable results under reversed loading. The investigation of damage measures obtained from the

first, second, and third eigenvalue for cooling towers under wind action [72] shows that the most crucial one is the first eigenvalue. They also try to relate damage to structural life time. From their experience, the following limits apply to reinforced concrete structures:

D	$= 0.0$	undamaged state
D	$< 0.15 - 0.2$	no quality loss in case of recent RC structures
D	$< 0.05 - 0.08$	no quality loss in case of elderly RC structures
D	≥ 0.6	total insurance loss
D	$= 1.0$	theoretical failure

Indices based on mode shapes are developed by Allemang & Brown [4] and Lieven & Ewins [85]. The MAC index by Allemang and Brown indicates the correlation between two sets of mode shapes, i.e. the mode shapes of the intact and the damaged structure. This index is a matrix with values between 0 and 1. The value 0 represents the complete orthogonality between the two sets of modes and the value 1 indicates that there is a complete concordance between both. Lieven and Ewins propose the COMAC index which indicates a correlation between the mode shapes of the intact and damaged structures at a selected point and thus can be used to identify the points where the damage is located.

Indices specifically for steel

While all the aforementioned indices are mainly applied to concrete structures, the following paragraphs give a literature review for indices which are specifically proposed for steel structures. Khashaee [68] proposes an index which is based on ductility

$$D = \frac{1 - \mu^{-1}}{1 - \mu_u^{-1}}. \tag{2.18}$$

The structure has the potential to collapse when the ductility μ reaches its ultimate ductility μ_u. The overall damage index for a building is then computed following equation 2.15.
Benavent-Climent [14] suggests an index as the ratio of total dissipated energy to the ultimate energy dissipation capacity of a steel component. This model explicitly accounts for the fact that the ultimate energy dissipation capacity is path-dependent and changes over the entire response duration.
A general damage index independent of the material is defined by Colombo & Negro [33]. It is based on the ratio of the initial and the reduced resistance capacity of a structure, which is evaluated by using an evolution equation for the yield strength in which the structural damageability is included. The evolution equation consists of a first part which considers maximum deformation, a second part which takes into account the energy dissipation in ductile elements, and a third part which is related to the energy

dissipation in brittle elements.
Ghobarah et al. [49] propose an approach for the global damage assessment of structures based on stiffness matrices obtained from push-over analysis. The damage measure relates the final K_{final} to the initial stiffness matrix $K_{initial}$:

$$D = 1 - \frac{K_{final}}{K_{initial}}. \tag{2.19}$$

The index is valid for both concrete and steel structures. Stiffness degradation, pinching, and strength deterioration are considered in the element model. Earthquakes of different intensities are used to evaluate the ability of the index and it is found that damage indices based on stiffness are consistent, rational, and accurate while simple to implement. Depending on the amount of damage, the values of the damage indices range from zero to one. However, in practical terms, collapse may be defined at a lower damage index corresponding to a certain percentage loss of stiffness.
Shen & Wu [124] concentrate on damage variables which deteriorate the material properties in order to describe seismic damage in detail. The damage variable is defined as

$$D = (1 - \beta)\frac{\epsilon_m^p}{\epsilon_u^p} + \sum_{i=1}^{N} \beta \frac{\epsilon_i^p}{\epsilon_u^p} \tag{2.20}$$

where β is a constant, ϵ_i^p is the plastic strain of a half cycle i, ϵ_m^p is the maximum plastic strain occurring during cyclic loading, ϵ_u^p is the ultimate plastic strain of the material obtained from standard tensile test, and N is the number of half cycles. The Young's modulus and the yield strength are directly influenced by the damage variables in a multiplicative manner. Instead of a global damage index, sectional equivalent damage variables are defined as

$$\tilde{D} = \frac{\int D_i \; dA_i}{A} \tag{2.21}$$

where D_i is the damage variable of a subarea i, A_i is the area of the subarea i, and A is the area of the cross-section.

Within this work, a continuum damage approach is used in order to describe deteriorated material behavior. Since damage is not related from other measures like displacement or plastic strain but is determined via damage evolution equations, global damage indices are most suitable. Global damage indices directly transfer the information about material deterioration into global measures for structural integrity. The definition and evaluation of the global damage indices for steel structures used within this work is given in chapter 4.5.

3 Material behavior of mild construction steel

In order to determine the condition of steel buildings after earthquakes, the structural response and therewith the material behavior of mild structural steel needs to be investigated in detail. This chapter gives an overview of the specific behavior of mild steel under different loading conditions, see figure 3.1. The main focus is on the question how material damage appears in mild construction steel. In order to identify the material behavior, the macroscopic behavior will be illustrated based on the description of the micromechanical processes. Since the material considered within this work is the mild construction steel S 355, a relationship will be established between every material mechanism and the experimentally observed behavior of steel S 355.

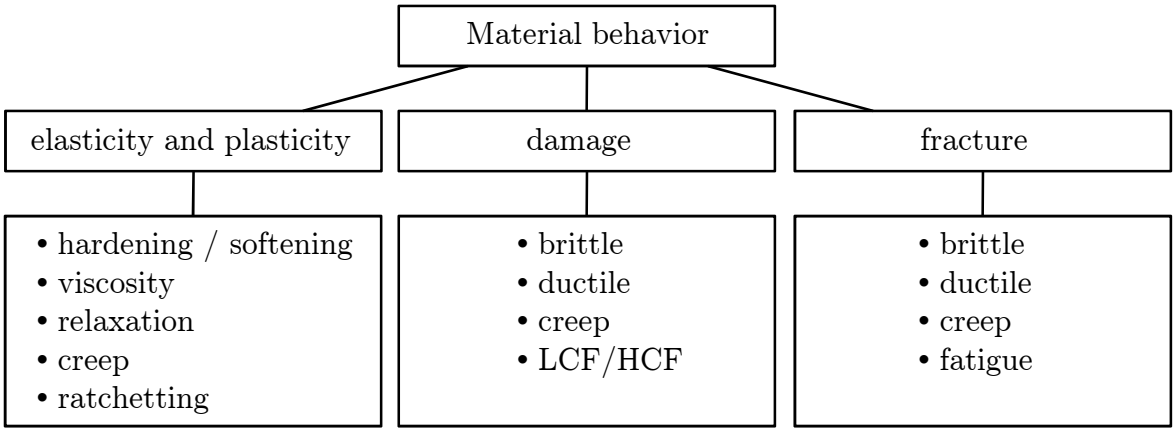

Figure 3.1: Overview of material phenomena for mild construction steel

3.1 Elasticity and Plasticity

If a material is subjected to a load, it is first deformed elastically. Elasticity is characterized by reversible deformations which only cause stresses below the yield stress. In this range, the relationship between stress and strain is linear. At microstructural level elastic deformations correspond to a widening of the interatomic distance. Depending on the material, the maximum strains in the elastic range lie between $0.2 - 0.5\%$ [81]. For the steel S 355, the transition from the elastic into the plastic range occurs around 0.2% [18]. Figure 3.2 depicts a typical stress-strain curve for a steel S 355 under monotonic loading. Within the elastic range the stress increases linearly between zero and the upper yield point.

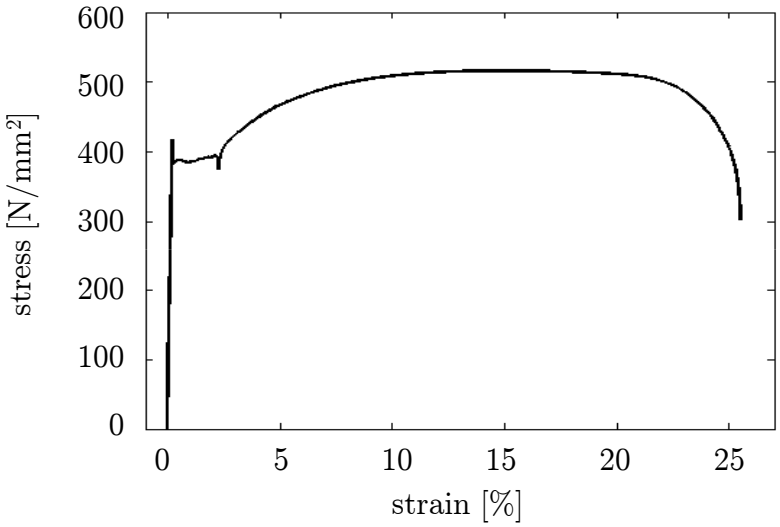

Figure 3.2: Stress-strain curve of a tensile test on a round bar of steel S 355 with a loading velocity of $\dot{\varepsilon} = 10^{-2}$ [18]

At the end of the elastic range, metallic materials show a more or less sharp transition into the plastic range which is characterized by irreversible plastic deformations. Plastic deformations result from a movement of dislocations. Dislocations are linear lattice defects in crystal lattices of atoms. Figure 3.3 depicts a lattice with an edge dislocation. Stresses which are high enough to cause a movement of dislocations lead to plastic deformations.

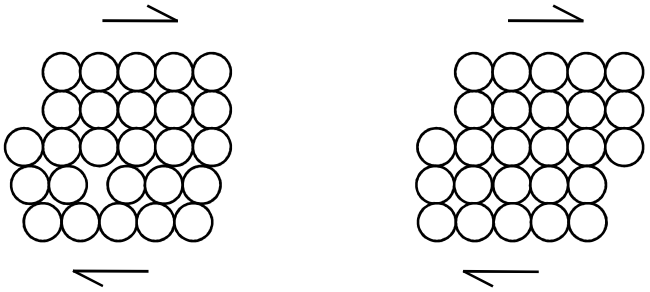

Figure 3.3: Crystal lattice of atoms with an edge dislocation. Plastic deformations are caused by a movement of dislocations

The stress which marks the transition between the elastic and the plastic range is called yield stress or yield point. Figure 3.2 shows an upper yield point and a lower yield point which is typical for the structural steel S 355 at first loading. Since plastic deformations result from the shift of dislocations, the blocking of the movement of the dislocations leads to a difference between the upper and lower yield point [38, 18]. The stronger the

blocking, the more difficult is the formation, multiplication, and unsnapping of dislocations which causes yielding. Thus, the stress is incipiently higher before the unhindered multiplication of dislocations is initiated and yielding occurs at the level of the lower yield point.
In the three-dimensional stress space, the yield stress is replaced by a yield function. Yield functions and their change during plastic deformation can be measured. A comprehensive overview can for example be found in [108, 39].
Real structures exhibiting plastic deformations do not show a uniform distribution of plastic strain. Material instabilities cause a local concentration of plastic strain, which is called strain localization. Under increasing loading the localization spreads in the form of a shear band (see figure (3.4)).

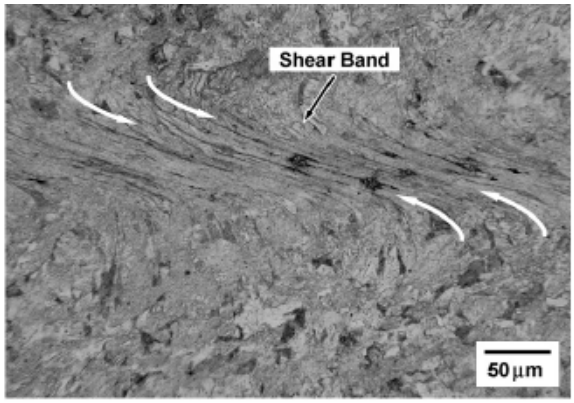

Figure 3.4: Formation of a shear band due to strain localization [61]

3.2 Hardening and softening

Hardening and softening are phenomena that occur in connection with inelastic deformations and influence the size, position, and shape of the yield surface. In stress-strain diagrams, hardening appears as an increase of stress while softening leads to a decrease of stress (see for example figure 3.2 where the stress increases between $2\% < \varepsilon < 15\%$ and decreases for $\varepsilon > 15\%$).
It is to be distinguished between isotropic, kinematic, and formative hardening/softening. In the following, the three types of hardening and softening are described in detail and a special characteristic of mild steel is shown, namely cyclic hardening and softening.

Isotropic hardening/softening
While isotropic hardening describes an expansion of the yield surface in the principle stress space, isotropic softening is related to a reduction of the yield surface. The expansion or reduction occurs equally in all directions. It has been found that there exists

a minimum yield surface size which limits the reduction of the yield surface [39]. Microscopically, isotropic hardening is connected with a hindered movement of dislocations due to the increase in dislocation density or the interpenetration of gliding planes (see figure 3.5). The microstructural changes that cause isotropic softening correspond to the changes that induce damage (see section 3.4).

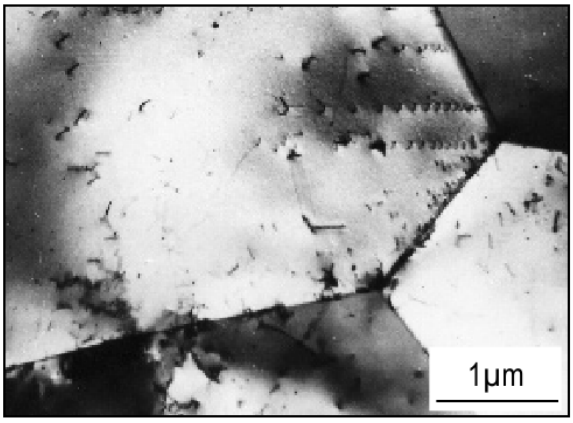

Figure 3.5: Piled up dislocations leading to an increase of dislocation density and hardening [58]

Kinematic hardening
Under cyclic loading it can be observed that the motion of dislocations is anisotropic. Obstacles can interfere with the movement of dislocations so that dislocations pile up between the obstacle and the source of dislocations until a maximum density of dislocations is reached. With load reversal a motion of dislocations is already possible at lower stresses. This phenomenon of a greater yield stress in the current loading direction as in the opposite direction is called Bauschinger effect. Kinematic hardening considers the Bauschinger effect and results in a translation of the yield surface in loading direction. As it can be seen in figure 3.6 yielding occurs first at a stress of about 380 N/mm^2. Under reversed loading, plastic deformations occur already at a stress of approximately -100 N/mm^2.

Formative hardening/softening
Formative hardening/softening deals with the deformation of the yield surface. The incorporation of formative hardening is complex and exceeds the required accuracy of practical civil engineering applications. Details can be found in [131, 39].

Cyclic hardening and softening for S 355
Under cyclic loading, a special characteristic of mild steel appears, which is investigated, for example, by Scheibe [120] and Böttcher [18] for the steel S 355. Provided a mean strain $\varepsilon_m = 0$ and cycling with constant strain amplitude ε_a, cyclic softening with a

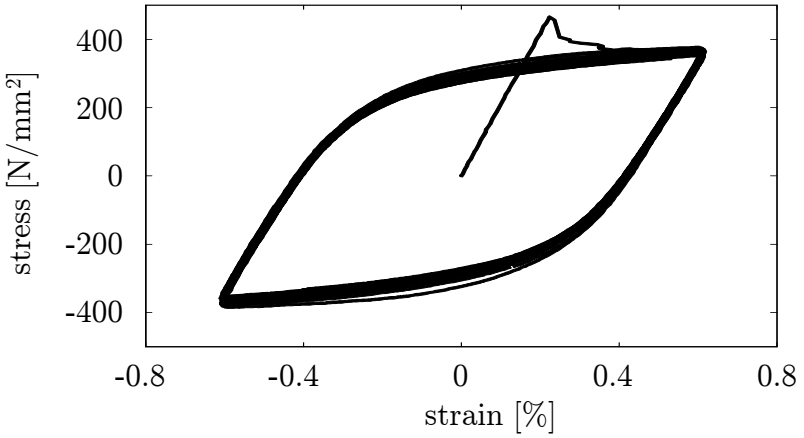

Figure 3.6: The Bauschinger effect for a round bar of steel S 355 under cyclic loading with an amplitude of $\varepsilon_a = 0.6\%$ and a loading velocity of $\dot{\varepsilon} = 10^{-2}$ [18]

decrease of stress amplitude occurs for strain amplitudes $\varepsilon_a < 0.6$ %, while cyclic hardening with an increase of stress amplitude evolves for strain amplitudes $\varepsilon_a > 0.6$ % (see figure 3.7). Cycles with a strain amplitude of $\varepsilon_a = 0.6$ % are cyclically neutral.

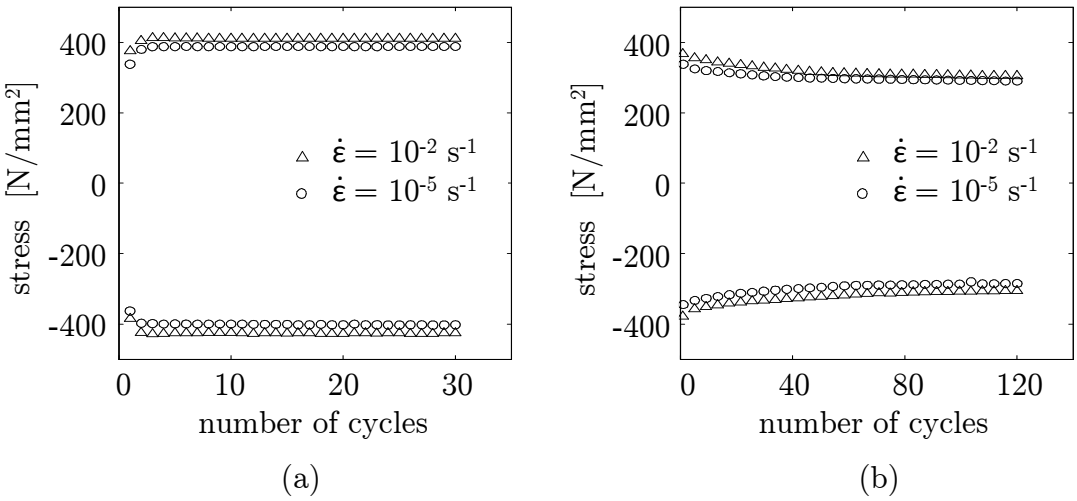

Figure 3.7: Evolution of stress at the reversal points for cyclic tests with different loading velocities $\dot{\varepsilon} = 10^{-2}$ and $\dot{\varepsilon} = 10^{-5}$ and strain amplitudes of (a) $\varepsilon_a = 1.2\%$, (b) $\varepsilon_a = 0.3\%$ [18]

Peil et al. [108] and Böttcher [18] investigate cyclic hardening and softening of mild steel under complex cyclic loading. They find that the saturated stress amplitude under cyclic loading only depends on the strain amplitude ε_a and not on the mean strain ε_m. Further experimental investigations of mild steel regarding cyclic hardening and soften-

ing deal with yield surface deformations under biaxial cyclic loading. Due to the limited practical aspects, the reader is referred to the literature for further information [108, 39].

3.3 Time-variant effects

Metals are known to show a viscous, time-dependent behavior. In the following, important time-dependent characteristics are described, namely the dependance on the loading velocity, relaxation, creep, and ratchetting.

Dependance on the loading velocity
A time-dependent behavior of metals appears for example at loading with different velocities. Figure 3.8a depicts the influence of different loading velocities on the stress-strain curve of the steel S 355. With increasing loading velocity $\dot{\varepsilon}$ a higher level of stress can be reached. A comprehensive overview of the velocity sensitivity of the behavior of the steel S 355 is given in [18].

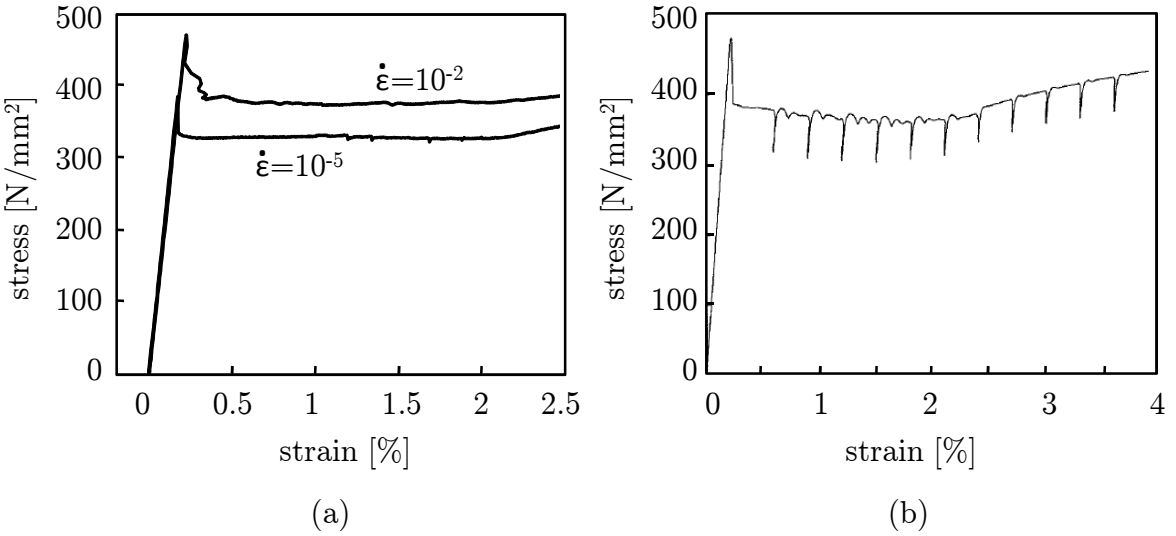

Figure 3.8: (a) The influence of different loading velocities on the stress-strain curve of the steel S 355 under monotonic loading [18], (b) Relaxation of steel S 355 occurring during a monotonic test with relaxation phases of 1800 s [18]

Relaxation
Relaxation considers the reduction of stress under constant strain. Figure 3.8b exemplarily shows the effect of relaxation for the steel S 355. A monotonic test with a loading velocity of $\dot{\varepsilon} = 10^{-2}s^{-1}$ is interrupted by relaxation phases with constant strain starting at $\varepsilon = 0.6$ % and proceeding with relaxation phases every $\Delta\varepsilon = 0.3$ %. During the relaxation phases with a length of $t = 1800$ s the stress decreases rapidly and approaches

a saturation value which depends on the associated constant strain value ε. Details concerning the relaxation behavior of mild steel S 355 in consideration of different loading velocities can be found in [18].

Creep

Creep is characterized by an increase of strain under constant loading and stress. It is based on the viscosity of steel and mainly occurs at elevated temperatures. However, creep can also occur at room temperature if the stress level is high enough. The progress of creep can be divided into three phases (see figure 3.9a). At the beginning, the material shows instant, time-independent strains. During the phase of primary creep (I), the creep rate decreases due to hardening which results from an increase of the number of dislocations with plastic deformations. Since the number of dislocations can also decrease due to material recovery with dislocations annihilating by climb, an equilibrium between both processes can be found. This equilibrium leads to a constant creep rate and secondary creep (II). In the phase of tertiary creep (III) the creep rate increases again due to material damage leading to the rupture of the material.

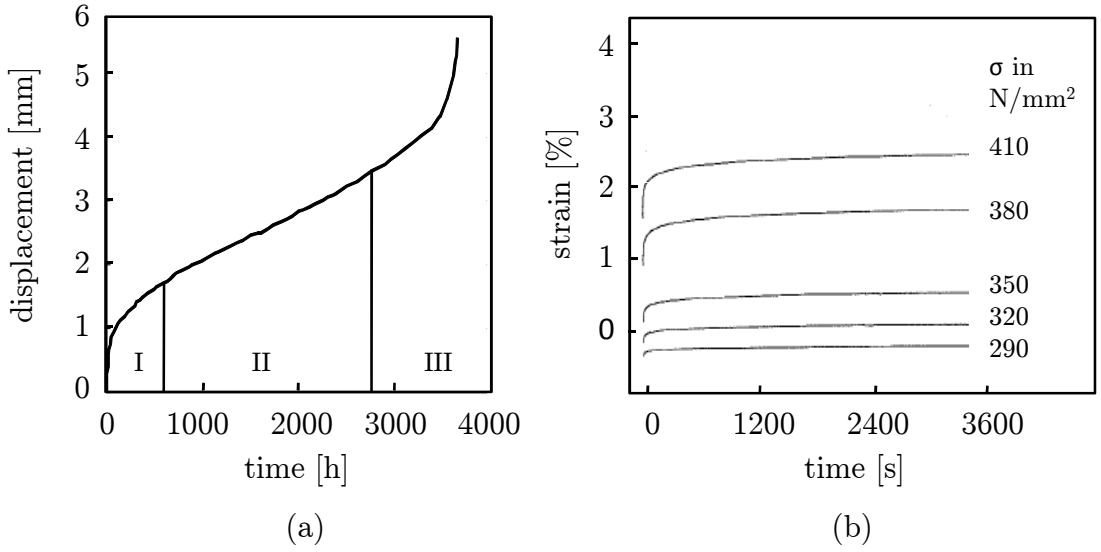

Figure 3.9: (a) Creep curve of a 12% chromium steel at 550°C [91] showing the three phases of creep, (b) Creep tests on round steel bars for the steel S 355 [18]

The evolution of creep depends on the state of stress. A higher level of stress causes a higher creep rate during the phase of secondary creep as well as earlier failure of the material. Figure 3.9b depicts creep tests for the construction steel S 355 at different stress levels after cyclic preloading for the phases of primary and secondary creep. It can be seen that higher stress levels lead to pronounced creep.

Ratchetting
Ratchetting can be understood as cyclic creep. If the material is subjected to a constant load with an additional superimposed cyclic load, the strain increases with time. Figure 3.10 represents this phenomenon for the steel S 355 which is subjected to a constant load of 120 kN superimposed with 40 cycles of a load with an amplitude of 120 kN. The increase of strain under this cyclic loading is clearly visible. Peil et al. [108] observe a distinct mean stress, where no ratchetting is found. The amount of ratchetting depends on the difference between the actual mean stress and the mean stress, which leads to zero ratchetting. In addition, ratchetting increases with increasing stress amplitude. A comprehensive overview of ratchetting for mild steel S 355 can be found in [74].

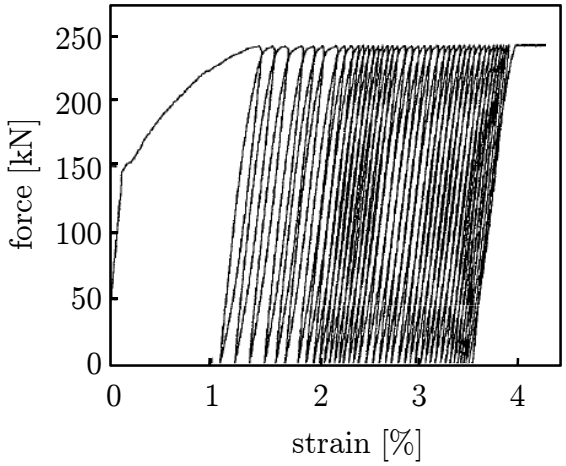

Figure 3.10: Ratchetting of structural steel S 355 under combined constant and cyclic loading [18]

3.4 Damage

In general, material damage can be understood as the decrease of the number of bonds at the level of atoms which leads to material deterioration with a decrease of the elementary area of resistance. Damage occurs in connection with inelastic deformations due to microscopic defects and is, in general, strongly anisotropic.
At the microscale, metals consist of a regular array of atoms except for many lines of dislocations where atoms are missing. If stress is applied, the dislocations may move by the displacement of bonds, thus creating a plastic strain by slip without any debonding. However, if a dislocation is stopped by an obstacle like a microdefect or a microstress concentration, the movement of other dislocations in that area is also stopped leading to an accumulation of dislocations. This process cannot occur without a debonding damage, which is the beginning of a damage process and leads to the nucleation of microvoids. Since the accumulation of dislocations and the nucleation of microvoids occur

at obstacles, damage leads to decohesions of these obstacles. The nucleation is followed by growth and coalescence of microvoids which results in macroscopic cracks.

While damage in mechanical engineering steel is widely investigated, the different damage characteristics in civil engineering steel are still a disregarded field of research. Since the stability of steel structures is mainly characterized by buckling, necking or fatigue, the detailed evolution of material damage in mild construction steel was often neglected. Nevertheless, there exist cases where it is worth considering the material state before instabilities occur. Firstly, damage mechanics characterizes the material condition and predicts if the material is on the brink of failure [98]. Tests have shown that the condition of cyclically loaded specimens made of mild steel cannot be specified by means of mechanical, macroscopic measures. While damage mechanics can continuously describe the deteriorated material behavior, macroscopic measures detect the upcoming failure only shortly before the collapse. Secondly, damage mechanics comprises every location where the material is weakened. Niessner et al. [97] investigate the failure mechanism under monotonic tension of sharp notched steel specimens made of the structural steel S 275. They find that specimens first show damage at the notch base before damage followed by necking and fracture occurs in the middle of the specimen. Due to that fact, the investigation of damage in mild steel is the only possibility to detect the location and the amount of deteriorated material behavior at positions where no macrocrack has occurred yet. This is especially important for complex structures with complex loading histories where failure locations are not known a priori. Moreover, damage assessment allows the site evaluation of entire steel building constructions for example in view of life time estimations before the damage is big and obvious and endangers the human environment.

The appearance of damage can be divided according to the circumstance under which damage manifests. This leads to a differentiation between brittle, ductile, creep, and fatigue damage. After the subsequent section which will give information about possibilities to measure damage, brittle, ductile, creep and fatigue damage will be investigated in detail.

3.4.1 Measurement of damage

Since damage cannot be measured directly a large variety of possible indirect damage measurement methods has been developed. In general, damage measurement methods can be grouped into measures from the microstructure and measures from physical parameters. Different results obtained from different damage measurement procedures demonstrate that the appropriate procedure has to be carefully selected and conducted. Damage measurements which are related to changes in the microstructure base on geometrical parameters like density, surface area fraction, or volume fraction. Although these parameters are directly related to damage, it is questionable whether their measurement may reach the required accuracy due to intrinsic experimentation errors [133].

Volume measurements, for example, show significant scatter even when high precision equipment is used [57]. Surface area fraction measurements from scanning electron microscopy, on the other hand, suffer from errors introduced by the specimen preparation [132]. Direct volume fraction measurements (e.g. using X-ray microtomography) avoid these effects as specimen preparation is not required, however, limitations in spatial resolution affect the accuracy, especially when voids are smaller than a few micrometers [86].
Other methods derive damage from physical parameters. A relatively easy to conduct and widely-used method is the measurement of the mechanical parameters hardness or modulus of elasticity. Both can be obtained from microindentation tests [82]. Having determined the hardness H_0 of the original, undamaged material, damage can be defined as

$$D = 1 - \frac{H_d}{H_0} \tag{3.1}$$

where H_d is the measured damaged hardness. The same can be carried out for the modulus of elasticity, leading to the definition

$$D = 1 - \frac{E_d}{E_0} \tag{3.2}$$

where E_d is the damaged, reduced modulus of elasticity and E_0 is the undamaged, original modulus of elasticity. Besides from indentation tests, the change of the modulus of elasticity can also be measured with strain gauges at several phases of unloading during a tensile test. However, it has been observed that the change in hardness and elastic modulus does not always reveal damage [54, 99, 37, 90]. Alves reports that good damage estimates can be obtained for an aluminum alloy but not for mild steel [5]. Tasan et al. find that damage derived from hardness or modulus of elasticity obtained from indentation tests during tensile loading is intrinsically flawed and should not be used [133]. The reason for that is that hardness and the elastic modulus change not only due to damage but also due to a number of additional microstructural mechanisms, such as strain hardening, grain shape change, texture development, residual stresses, and indentation pile up. Other authors observe the same phenomenon for cyclic tests on mild construction steel [73]. Since the measurement of the reduction of the Young's modulus or of stress amplitudes under cyclic loading does not necessarily reveal damage although it exists, another criterion is proposed for damage under cyclic loading:

$$D = 1 - \frac{N}{N_f} \tag{3.3}$$

where N is the number of current cycles and N_f is the number of cycles to failure. This criterion bases on the linear Miner's rule and assures a continuous grow of damage with every cycle. However, it only can be applied if the number of cycles up to failure is known. On account of that, Krümmling [73] proposes an acoustic emission analysis for fatigue in structural steel. This nondestructive method is found to detect well the

transition from microscopic cracks to macroscopic cracks but not the microcrack propagation itself. Thus, it is concluded that acoustic emission analysis for mild construction steel cannot accurately capture the complex processes in the microstructure in order to derive a significant damage variable. Other methods based on physical parameters consider ultrasonic wave propagation or the measurement of the electrical resistance. While ultrasonic wave propagation is a destructive method based on the determination of wave speed in undamaged and damaged material, the measurement of the electrical resistance takes into account the drop of potential and requires the estimation of the material resistivity [80].
The various methods for damage measurements described in this paragraph illustrate the complexity and inconsistency of damage quantification methods. While damage irrevocably exists, not every method is suitable in order to detect damage, so that appropriate methods have to be carefully chosen in accordance with the specific steel and specimen geometry. Especially for mild construction steel, no adequate method is provided so far in order to observe damage. Thus, the investigation of damage measurement methods is still an open field of research.

3.4.2 Brittle damage

Brittle damage occurs if a crack initiates without a large amount of plastic strains. Following [80], brittle damage occurs if the plastic strain ε^{in} does not exceed the elastic strain ε^{el}. This means that the cleavage forces are below the forces that could produce slips but are higher than the debonding forces. The degree of localization during brittle fracture processes is high.

3.4.3 Fatigue damage

Fatigue damage occurs when a material is subjected to cyclic loading. It is the kind of damage which is mainly considered in connection with structural steel. For the sake of simplicity, the process of fatigue is often not observed at a microstructural level, but is related from the number of cycles a specimen already has undergone and the number of cycles a specimen can withstand before it fails. Since the number of cycles up to failure is not known a priori for real constructions, the identification of the progress of fatigue damage with regard to life time estimation is still an important area of research.
In order to assess the progress of fatigue damage precisely, the microstructural processes need to be identified. Fatigue failure can be divided into three phases, namely crack initiation, crack propagation, and final fracture. During the phase of crack initiation, dislocation movement at slip planes occurs. The dislocations accumulate at the material surface leading to a roughen of the surface by forming extrusions and intrusions. Figure 3.11 depicts extrusions at the surface of a ferritic steel caused by fatigue damage which are the basis for subsequent crack propagation. Therefore, the process of crack initiation can be slowed down by surface treatment like polishing or hardening. The notches

induced by the extrusions and intrusions are the starting point for crack initiation. While cracks initiate at many positions, their speed of growth depends on the microstructural conditions like the orientation of the grains. Cracks which exceed a length of $0.05 - 2$mm [121] enter the phase of crack propagation, which is characterized by stable crack growth with every cycle and a stoppage of crack propagation as soon as the material is loaded statically. Final fracture occurs if the crack length exceeds a critical crack length and the reduced cross section cannot withstand the loading.

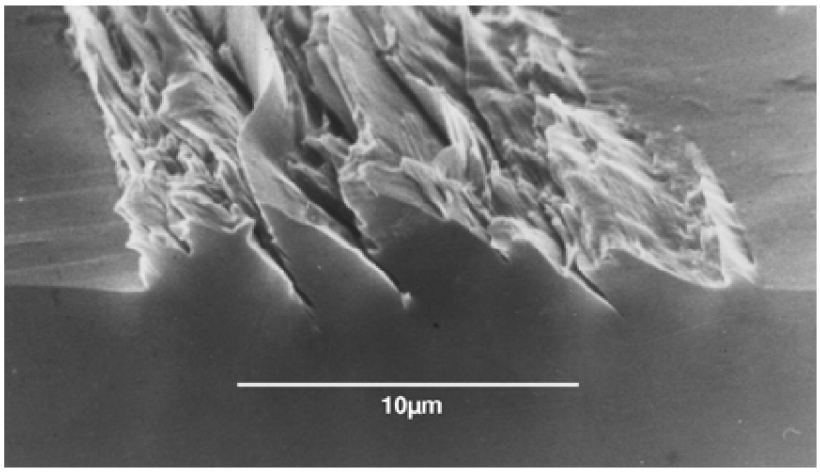

Figure 3.11: Scanning electron micrograph of extrusions in steel [60]

Figure 3.12 depicts the phases of crack initiation and propagation of fatigue failure by means of the change of the hysteresis shape with proceeding number of cycles N for the mild construction steel S 355 [73]. It is noticeable, that the shape of the hystereses does not change during the phase of crack initiation. Thus, a damage measure based on the reduction of the elastic modulus would yield erroneous results. During the phase of crack propagation a macrocrack evolves. The existence of a macrocrack changes the shape of the hysteresis. Firstly, the stresses in the reversal points decrease since the material is weakened. Secondly, the hysteresis shape in compression changes due to the closure of the macrocracks. After the macrocracks are closed the material is able to absorb higher forces which leads to increased stiffness and an ear in the hysteresis shape. In the end, the material fails completely by final fracture.
Fatigue damage can be divided into low cycle fatigue damage and high cycle fatigue damage. Low cycle fatigue damage is related to high values for stress and strain and a number of cycles $N < 10.000$. High cycle fatigue damage occurs for a number of cycles $N > 100.000$ and develops due to local stress concentrations while globally the plastic strain is negligible. The underlying micromechanical processes for low and high cycle fatigue damage remain the same, though.

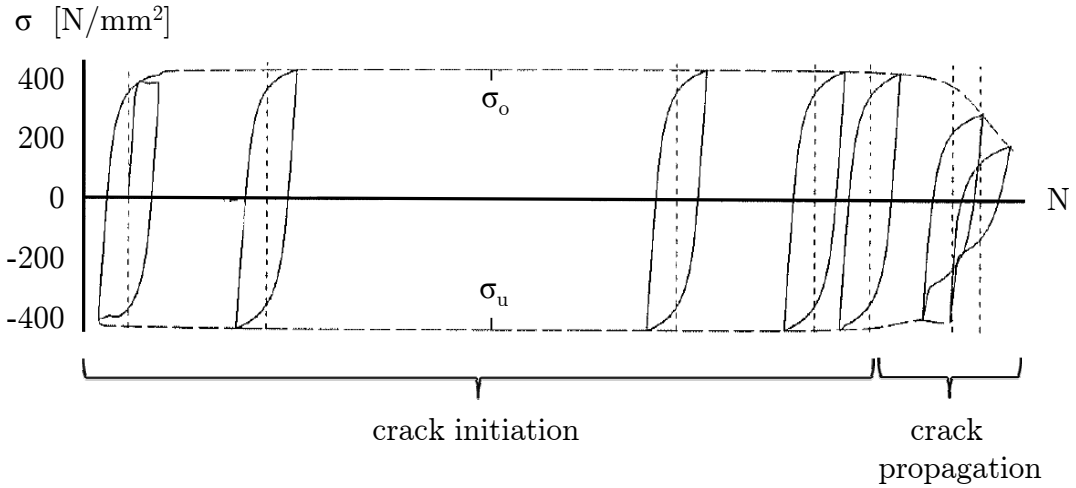

Figure 3.12: Change of hysteresis shape for the steel S 355 under cyclic loading with a strain amplitude of 0.8% [73]

3.4.4 Ductile damage

Ductile damage occurs simultaneously with inelastic strains. In literature, little can be found about ductile damage in connection with the steel S 355, since the eventual failure mechanism for this construction steel is induced by structural instabilities (buckling, necking) or fatigue. However, in order to describe the deteriorated condition prior to failure, the determination of detailed material processes is important.
Ductile damage results from the nucleation of cavities due to decohesions between inclusions in the matrix followed by their growth and coalescence. Figure 3.13 represents the three phases of ductile damage evolution. First, voids arise since the accumulation of dislocations at inclusions leads to decohesion, then the voids grow, before finally the voids coalesce and a macrocrack initiates. The rate of ductile damage evolution depends on the triaxiality of the state of stress. The bigger the triaxiality, the higher is the damage rate. The characteristic transgranular crack of ductile damage [80] is shown in figure 3.14.
Figure 3.2 depicts the relation of stress and strain of a round specimen of steel S 355 under monotonic tensile loading until fracture. After the tensile strength is reached at a strain of about 15%, the stress decreases until failure occurs at a strain of approximately 25%. The range between 15% and 25% is characterized by ductile damage evolution superimposed with necking. While necking initiates when the stress-strain curve begins to decrease, the starting point of ductile damage evolution is hard to estimate. Niessner et al. [97] state that ductile damage in mild construction steel starts to occur at strains > 5 %. From the micromechanical point of view damage can develop as soon as dislocations accumulate and pile up [80], since the accumulation of dislocations leads to debonding damage. While it is known that hardening occurs simultaneously with an increase of dislocation density, it is not proven if this process leads to ductile damage

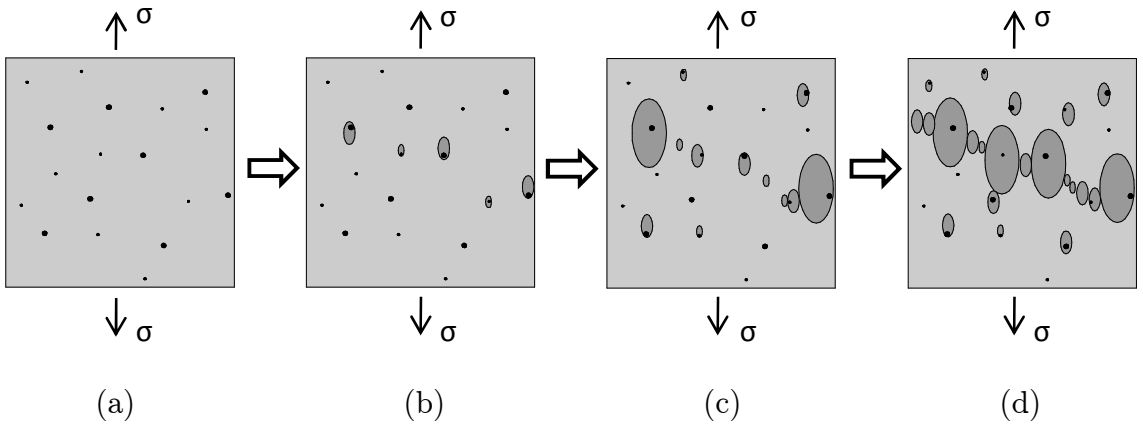

Figure 3.13: Evolution of ductile damage: (a) undamaged matrix with inclusions, (b) nucleation of voids, (c) growth of voids, (d) coalescence of voids and initiation of a macrocrack

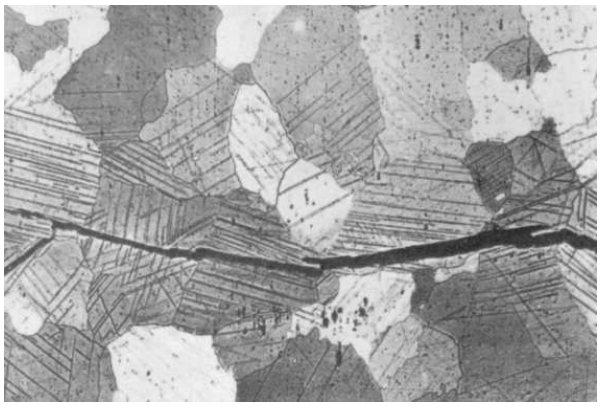

Figure 3.14: Ductile damage leads to a transgranular crack

right from the beginning. There may be a critical dislocation density, below which only hardening occurs while above both hardening and damage develop. Due to the lack of information on critical dislocation densities, it can only be reasoned that the initiation of damage may coincide with or follow after the occurrence of hardening.
Bonora et al. [16] investigate the evolution of damage in the low alloy steel A 533 class 1, grade B, which is commonly used in nuclear industry. A monotonic tensile test interrupted by several phases of unloading and reloading is used to assess the change in the modulus of elasticity and thus to get an idea about the appearance and evolution of damage. The modulus of elasticity is measured during the unloading ramp [81]. Figure 3.15 presents the tensile test with the phases of unloading and reloading and the evolutions of the modulus of elasticity and of damage. It can be seen that the modulus of elasticity decreases during the loading process while damage, defined as $D = 1 - \frac{E_{dam}}{E_0}$, increases. The evolution of damage seems to start right with the development of plastic

deformations. However, as already mentioned in section 3.4.1, the measurement of the decrease of the elastic modulus is not an universally valid method in order to detect damage.

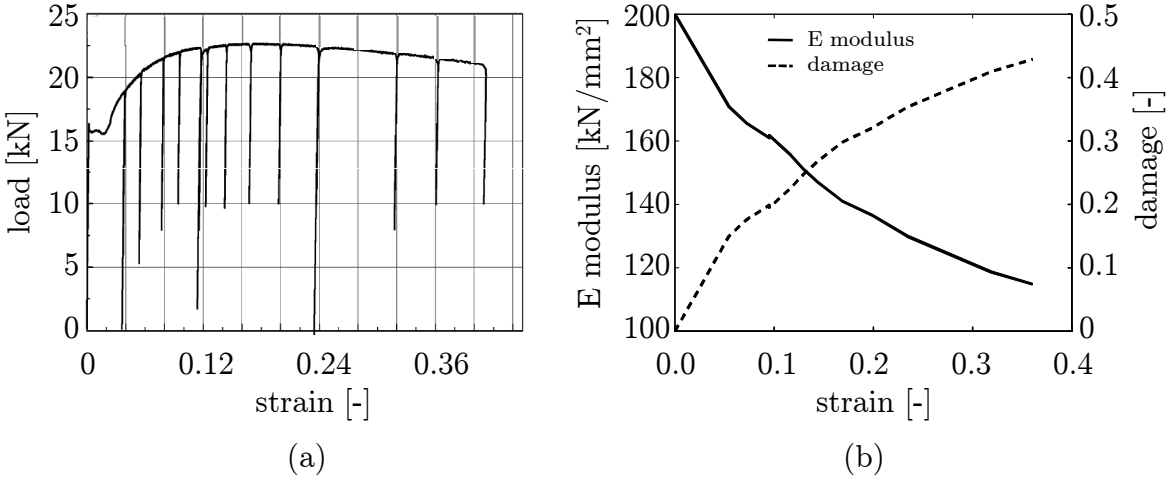

Figure 3.15: Monotonic tensile test on low alloy steel with several phases of unloading (a) in order to determine the decrease of the modulus of elasticity and the evolution of damage (b) [16]

Ductile damage under cyclic loading

Ductile damage normally characterizes damage in materials under monotonic loading with large strains. If the material is subjected to cyclic loading with alternating tension and compression, it has to be investigated how ductile damage evolves under compressive states of stress. In literature, the discussion about occurrence of damage under compressive states of stress and the related mechanisms is still open. However, there is an agreement that the evolution of damage under compression does not comply with the damage evolution under tension or shear. While damage evolutes mainly under tensile loading [65, 29], compressive loading may lead to reduced or no damage evolution at all, or even may lead to recovery of damage. Kanvinde and Deierlein [67] find that compressive loads lead to the collapse of voids into oblate or penny-shaped flat voids (see figure 3.16). Void closure may lead to stiffness recovery so that the material shows different stiffnesses under tension and compression [112]. However, while the percentage of voids decreases under compression, the collapsed voids show sharper stress/strain concentrations than the spherical or prolate voids leading to a pronounced damage evolution if the loading direction is reversed again.

In order to clarify if the change of the modulus of elasticity is appropriate for the identification of damage in the steel S 355 under cyclic loading, experimental data has been analyzed. The incidence of damage is supposed to lead to a reduced modulus of elasticity which can be estimated during the elastic unloading after tension or compression.

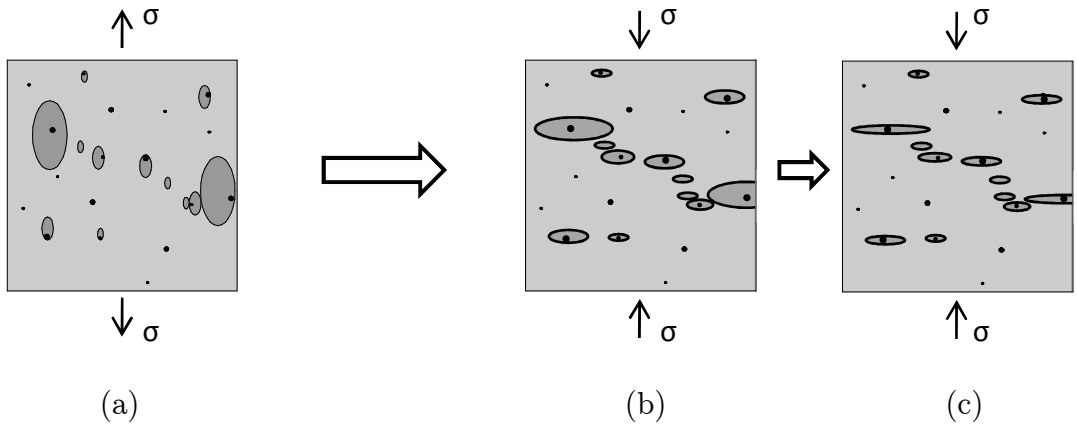

Figure 3.16: Evolution of ductile damage under compression: (a) voids in a predamaged matrix, (b) alteration of shape of voids, (c) oblate and flat voids

Böttcher [18] investigates the evolution of the moduli of elasticity under different cyclic loading conditions. Single-step and multi-step tests are performed with strain amplitudes between 0.3% and 1.2%. It is found that the modulus of elasticity decreases rapidly during the first cycles and then remains constant for the next 30 cycles for the single-step test with an amplitude of 1.2%. For the single-step test with an amplitude of 0.3% the modulus of elasticity decreases slowly and continuously until a constant value is reached after approximately 80 cycles. The same result is found for the multi-step test with increasing sequence of amplitudes, while the multi-step test with decreasing sequence of amplitudes shows again a rapid decrease of the modulus of elasticity with a subsequent constant trend.

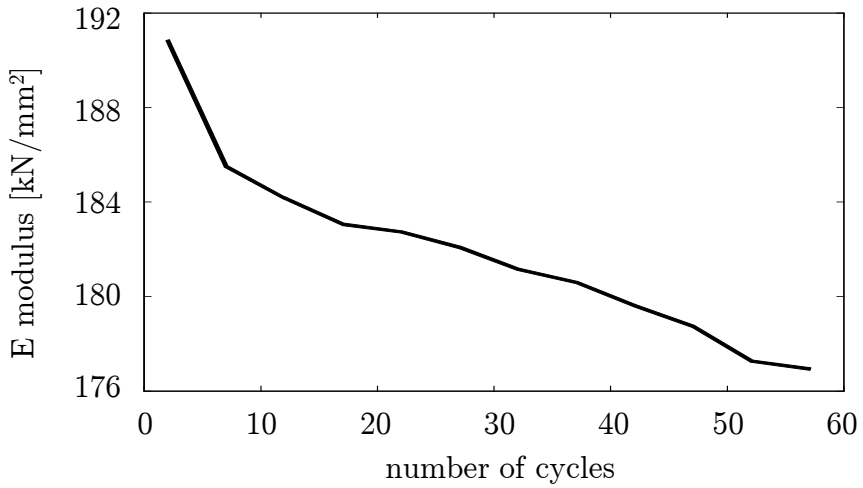

Figure 3.17: The decrease of the modulus of elasticity during cyclic loading due to ductile damage for a test on steel S 355 with a strain amplitude of $\varepsilon_a = 0.3\%$

Figure 3.17 shows the appearance of damage for the single-step test with an amplitude of 0.3%. The modulus of elasticity is estimated by linear regression of the measurement points during the elastic unloading after tension. It can be seen that the modulus of elasticity decreases and thus damage increases with proceeding number of cycles. However, the trend is not continuous but approaches a certain value. The plastic deformations, on the other hand, accumulate continuously with every cycle. This together with the results obtained from cyclic tests with strain amplitudes of 1.2% indicates that the method to evaluate damage based on the reduction of the elastic modulus is not appropriate for mild steel S 355, since the microstructure is continuously damaged with every cycle.

3.4.5 Creep damage

Creep damage is connected with a viscous behavior of steel and emerges as an accelerated increase of strain at constant stress during tertiary creep (see figure 3.9a). The rate of creep damage evolution depends on the level of constant stress. The increase of the strain rate during the evolution of creep damage follows from nucleation, growth, and coalescence of voids at the grain boundaries and leads to an intergranular debonding [92], which is generally anisotropic. Figure 3.18 shows an intergranular crack as it occurs for creep damage.

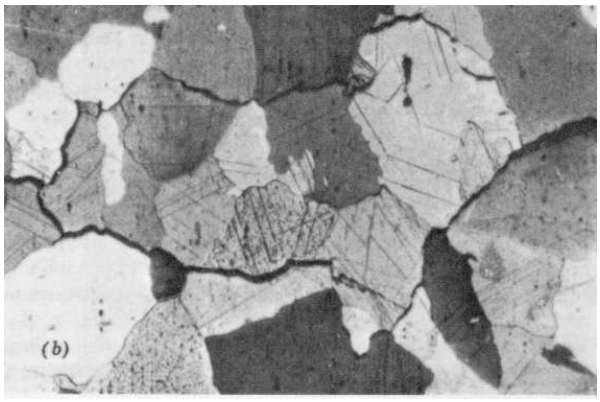

Figure 3.18: Creep damage leads to an intergranular crack

3.5 Fracture

Damage characterizes material deterioration up to crack lengths of approximately 1 mm [23]. Subsequently, the cracks are referred to as macrocracks which evolute until complete fracture. Fracture occurs after a material has already suffered from inelastic deformations, hardening, and damage. In accordance with damage, fracture can be divided into brittle, ductile, fatigue, or creep fracture.

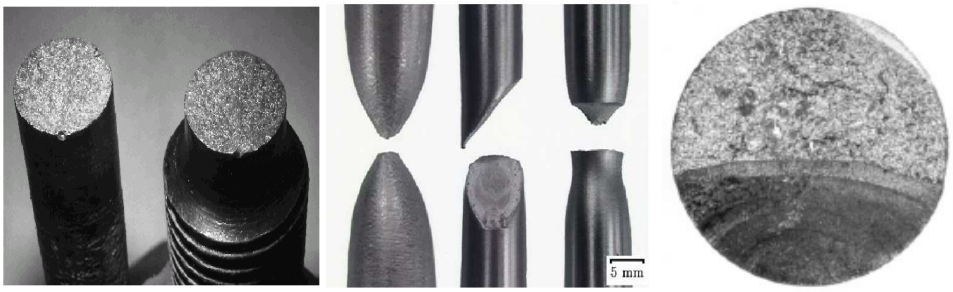

(a) (b) (c)

Figure 3.19: (a) brittle fracture, (b) ductile fracture [76], (c) fatigue fracture [118]

Figure 3.19 shows fracture appearances for brittle, ductile and fatigue fracture. In contrast to brittle fracture, ductile fracture is related to large plastic deformations. The fracture pattern can be characterized by necking, shear fracture, or cup-and-cone fracture. Figure 3.19c illustrates a typical fatigue fracture which shows a dark area of material damaged by fatigue (crack initiation and propagation with lines of rests) and a bright area of subsequent, ductile, final fracture.
In addition to the investigation of the fracture appearance, technical measures like the ultimate strain can be used in order to define the ductility of a steel. Following a normalized procedure, the ultimate strain, which corresponds to the permanent strain after rupture, can be measured and compared to other steels.
In comparison to damage, fracture or the existence of macrocracks is easily detectable. A number of non-destructive inspection methods like penetrant flaw detection or magnetic particle inspection already exist in order to identify macrocracks in the material and there is a lot of research going on concerning the development of new methods in order to improve their monitoring [107, 45, 51, 53, 102, 101, 88]. Damage, on the other hand, is very hard to determine with non-destructive inspection methods which requires accurate simulation techniques in order to predict the influence of damage on structural life time estimations.

4 Vulnerability analysis and damage assessment

In this chapter a model is introduced in order to calculate damage of steel structures caused by earthquakes for vulnerability evaluation of seismic risk analysis. The model is developed within the framework of continuum mechanics and uses numerical time integration of the equation of motion. The basic equations of continuum mechanics are given in section 4.1. The central point of this work is the development of a material model (see section 4.2), which needs to correctly represent the specific behavior of mild structural steel under seismic loading. Seismic loading is characterized by cyclic load reversals with different amplitudes and frequencies, which cause alternating high tensile and compressive stresses in the material. Within this work, the material model is adjusted to the behavior of the construction steel S 355, which is used for civil engineering structures. This type of steel is characterized by pronounced yielding and shows phenomena like a dependance on the loading velocity, creep, relaxation, hardening, softening, and damage (see chapter 3).
The material model is established within the framework of thermodynamics. For the description of the evolution of deteriorated material behavior either damage mechanics or fracture mechanics can be used. While damage mechanics describes the material from the undamaged state up to the initiation of macrocracks, fracture mechanics applies to material with macrocracks up to complete failure. The transition from damage to fracture mechanics takes place for crack lengths of approximately 1 mm [23]. In order to describe deteriorated material behavior from the beginning on, this work takes into account a continuum damage approach, which characterizes the damage state of the material with damage variables.
Damage is always accompanied by material softening leading to the phenomenon of strain localization in small process zones. Due to the undefined width of those process zones, the solutions needs to be regularized. This can be done by means of a model extension (see section 4.3) which includes an additional parameter called internal length in order to determine the width of the damage process zone. Mainly integral or gradient extensions are used. This work investigates an implicit gradient enhanced model.
Finally, the damage variables, which provide the distribution of damage in a structure at the material point, need to be transformed into a global damage index. By means of this global damage index a statement about structural stability and safety can be made enabling to predict if a structure can further be used. The definition and evaluation of the global damage index may be found in section 4.5.

4.1 Basic equations of continuum mechanics

The equations of continuum mechanics can be divided into material dependent and material independent equations. This section deals with material independent equations, namely the mechanical balance equations, the balance equations of thermodynamics, and the equation of kinematics. The material dependent equations are given in section 4.2.

4.1.1 Mechanical balance equations

The mechanical balance equations of continuum mechanics are the balance of mass, the balance of linear momentum, and the balance of angular momentum, which are presented in the following under consideration of small strains.

Balance of mass
The mass of a body m can be obtained by

$$m = \int_{\Omega} \rho d\Omega \tag{4.1}$$

where ρ is the density and Ω specifies the considered volume. Assuming constant density, the mass of a body does not change in time ($\dot{m} = 0$) and the law of conservation of mass is fulfilled.

Balance of linear momentum
Forces acting on a body defined by a volume Ω may consist of inertia forces, body forces, and traction forces. The balance of linear momentum equals the sum of all forces acting on the continuum

$$\int_{\Omega} \rho \ddot{\mathbf{u}} d\Omega = \int_{\Omega} \rho \mathbf{b} d\Omega + \int_{\partial\Omega} \bar{\mathbf{t}} d\partial\Omega \tag{4.2}$$

with the acceleration vector $\ddot{\mathbf{u}}$, volume based mass force $\rho\mathbf{b}$, and the vector of surface traction $\bar{\mathbf{t}}$ acting normally to the surface. Transferring the boundary integral of equation (4.2) with $\bar{\mathbf{t}} = \boldsymbol{\sigma} \cdot \mathbf{n}$ and the theorem of Gauss into a volume integral, one obtains

$$\int_{\partial\Omega} \boldsymbol{\sigma} \cdot \mathbf{n} d\partial\Omega = \int_{\Omega} \nabla \cdot \boldsymbol{\sigma} d\Omega \tag{4.3}$$

with Cauchy stresses $\boldsymbol{\sigma}$, normal vector $\mathbf{n}$, and the nabla operator ∇. Inserting this into equation (4.2), the local form of the equation of linear momentum is defined as

$$\rho\ddot{\mathbf{u}} - \nabla\boldsymbol{\sigma} = \rho\mathbf{b}. \tag{4.4}$$

Since the balance of linear momentum considers mass inertia and describes a moving continuum, it is in the following referred to as equation of motion.

Balance of angular momentum
The balance of angular momentum results from the sum of moments of all forces acting on the continuum about any arbitrary point:

$$\int_\Omega \mathbf{x} \times \rho \ddot{\mathbf{u}} d\Omega = \int_\Omega \mathbf{x} \times \rho \mathbf{b} d\Omega + \int_{\partial\Omega} \mathbf{x} \times \bar{\mathbf{t}} d\Omega. \tag{4.5}$$

After transformation the local formulation of angular momentum leads to the symmetry condition of the stress tensor:

$$\sigma_{ij} = \sigma_{ji}. \tag{4.6}$$

4.1.2 Balance equations of thermodynamics

The balance equations of thermodynamics allow the plausibility check of physical processes by means of energetic observations. Thermodynamic potentials, which characterize the energetic condition of a body, and the laws of thermodynamics lead to restrictions for the material equations.

First law of thermodynamics
The first law of thermodynamics deals with the balance of energy. The total energy of a closed system consists of the internal energy U and the kinetic energy K. While the total energy of a closed system is constant, it increases for open systems under supply of mechanical power P and heat Q:

$$\dot{U} + \dot{K} = P + Q \tag{4.7}$$

with

$$\begin{aligned} U &= \int_\Omega \rho e d\Omega \\ K &= \frac{1}{2} \int_\Omega \rho \dot{\mathbf{u}}^2 d\Omega \\ P &= \int_\Omega \rho \mathbf{b} \cdot \dot{\mathbf{u}} d\Omega + \int_{\partial\Omega} \bar{\mathbf{t}} \cdot \dot{\mathbf{u}} d\partial\Omega \\ Q &= \int_\Omega \rho r d\Omega - \int_{\partial\Omega} \mathbf{q} \cdot \mathbf{n} d\partial\Omega \end{aligned}$$

where e is the internal energy density per mass unit, r is a heat source inside a volume and $\mathbf{q}$ is a heat flux through the surface.
For the description of the thermodynamic condition of a system only the internal energy is of interest. For states of equilibrium the kinetic energy does not exist. The balance equation for the internal energy equals the first law of thermodynamics, here given in the local form:

$$\rho \dot{e} = \boldsymbol{\sigma} : \dot{\boldsymbol{\varepsilon}} + \rho r - \nabla \cdot \mathbf{q}. \tag{4.8}$$

A constant total energy only allows a transformation of one energy form into another. Information about the direction of such energy transformation is not provided by the first law of thermodynamics. Therefore, the second law of thermodynamics has to be introduced.

Second law of thermodynamics
The material equations have to correspond to the second law of thermodynamics in order to be physically reasonable. The second law of thermodynamics is an inequality which considers the balance of entropy. The entropy S measures the irreversibility of a process. Every irreversible change of state produces entropy. The rate of change in time of the entropy equals at least the flux of entropy Q_T which is described by the second law of thermodynamics:

$$\dot{S} - Q_T \geq 0 \tag{4.9}$$

with

$$S = \int_\Omega \rho s d\Omega$$
$$Q_T = \int_\Omega \frac{\rho r}{T} d\Omega - \int_{\partial\Omega} \frac{\mathbf{q} \cdot \mathbf{n}}{T} d\partial\Omega$$

where s is the entropy density per mass unit and T is the absolute temperature.
The entropy-inequality or Clausius-Duhem inequality here presented in the local form

$$\boldsymbol{\sigma} : \dot{\boldsymbol{\varepsilon}} + \rho T \dot{s} - \rho \dot{e} - \mathbf{q} \cdot \frac{\nabla T}{T} \geq 0 \tag{4.10}$$

follows after elimination of r in equation (4.9) with the first law of thermodynamics (equation (4.8)).

Thermodynamics of irreversible processes
Based on the preceding considerations, the concept of thermodynamics of irreversible processes can be derived, which allows the formulation of thermodynamically consistent material models. Thermodynamically consistent material models postulate that the released energy during irreversible processes, denoted as dissipation Φ, is equal to or greater than zero:

$$\rho\Phi = \mathbf{k} \cdot \mathbf{j} \geq 0 \tag{4.11}$$

where $\mathbf{j} = \rho\{\dot{\boldsymbol{\varepsilon}}^{in}, \dot{V}_i, \mathbf{q}\}$ is the vector of mechanical flux with internal variables V_i, which characterize the material condition in the framework of continuum damage mechanics, and $\mathbf{k} = \{\boldsymbol{\sigma}, A_i, \mathbf{g}/T\}$ is its thermodynamically conjugated force vector. The total dissipation is composed of mechanical and thermal dissipation.
The thermodynamically conjugated forces $\boldsymbol{\sigma}$, A_i, and $\mathbf{g}$ and the evolution equations of the material $\dot{\boldsymbol{\varepsilon}}^{in}$, $\dot{V}_i$, and $\mathbf{q}$ can be derived from thermodynamical potentials. The

thermodynamically conjugated forces may be obtained by partial derivatives of the free Helmholtz energy Ψ. The free Helmholtz energy depends on the state variables $\{\boldsymbol{\varepsilon}, T, \mathbf{V_i}\}$ and follows from Legendre transformation

$$\Psi = e - \frac{\partial e}{\partial s} s = e - Ts. \tag{4.12}$$

After substituting the rate of the internal energy density $\dot{e}$ in the Clausius-Duhem inequality (4.10) by the rate of the free Helmholtz energy $\dot{\Psi}$ one obtains

$$\int_\Omega \frac{1}{T} \left[\left(\boldsymbol{\sigma} - \rho \frac{\partial \Psi}{\partial \boldsymbol{\varepsilon}} \right) : \dot{\boldsymbol{\varepsilon}} + \rho \left(-s - \frac{\partial \Psi}{\partial T} \right) \dot{T} - \sum_i \rho \frac{\partial \Psi}{\partial V_i} \dot{V}_i - \mathbf{q} \cdot \frac{\nabla T}{T} \right] d\Omega \geq 0 \tag{4.13}$$

which leads to

$$\boldsymbol{\sigma} = \rho \frac{\partial \Psi}{\partial \boldsymbol{\varepsilon}} \ , \quad s = -\frac{\partial \Psi}{\partial T} \ , \quad A_i = \rho \frac{\partial \Psi}{\partial V_i} \ , \quad \mathbf{g} = \nabla T \ . \tag{4.14}$$

The evolution equations of the material may be derived from a dissipation potential ϕ. Assuming the dissipation potential depending on the conjugated variables, the partial derivatives of the dissipation potential lead to

$$\dot{\boldsymbol{\varepsilon}}^{in} = \frac{\partial \phi}{\partial \boldsymbol{\sigma}} \ , \quad \dot{V}_i = -\frac{\partial \phi}{\partial A_i} \ , \quad \mathbf{q} = -\frac{\partial \phi}{\partial \mathbf{g}/T} \ . \tag{4.15}$$

4.1.3 Equation of kinematics

The deformation of a body from a reference configuration into a momentary configuration is determined via the deformation gradient

$$\mathbf{F} = \nabla_x \mathbf{u} + \mathbf{I}. \tag{4.16}$$

The symmetric Green-Lagrange strain tensor is chosen

$$\mathbf{G} = \frac{1}{2}(\mathbf{F}^T \cdot \mathbf{F} - \mathbf{I}) \tag{4.17}$$

which remains zero for the reference configuration or rigid body displacements.
In the following small strains are considered. Because of this, the kinematic equations can be linearized geometrically. The strain tensor

$$\mathbf{G} = \frac{1}{2}(\nabla_x^T \mathbf{u} + \nabla_x \mathbf{u} + \nabla_x^T \mathbf{u} \cdot \nabla_x \mathbf{u}), \tag{4.18}$$

neglecting the product $\nabla_x^T \mathbf{u} \cdot \nabla_x \mathbf{u}$ that is small due to higher order, reduces to

$$\boldsymbol{\varepsilon} = \frac{1}{2}(\nabla_x^T \mathbf{u} + \nabla_x \mathbf{u}) = \nabla^{sym} \mathbf{u} \tag{4.19}$$

which means that the linearized strain tensor equals the symmetric part of the displacement gradient.

4.2 Material equations

In the following, the material-dependent equations of continuum mechanics are developed. The proposed material model is part of the unified models, which assume that yielding and creep can be modelled with only one single part of inelastic deformations, since both phenomena base on the same micromechanical mechanisms. Unified models can be divided into microscopic and macroscopic models. While microscopic models describe e.g. the density of dislocations, macroscopic models deal with e.g. isotropic and kinematic hardening. Within this work, a macroscopic unified model is developed, which bases on micromechanical observations in a sufficient large volume, called representative volume element, in which all constituents are distributed representatively in a statistic sense. The macroscopic description of the material condition is obtained by means of external variables (stress, strain) and a set of internal variables V based on the concept of continuum mechanics. The internal variables reflect the evolution of the material.
The constitutive equations which describe the evolution of the material need to accurately describe the material behavior of civil engineering steel structures under seismic action. Strong earthquakes cause structures to behave inelastically. In addition, earthquakes occur with different intensities and velocities inducing material loading with different strain rates in the range of $10^{-4} < \dot{\varepsilon} < 10^{0}$ [18], so that the material equations have to be formulated in dependance on the strain rate. In order to account for those effects, viscoplasticity is chosen. Inelastic deformations are accompanied by the phenomenon of hardening which results in an increase of stress. Here, isotropic and kinematic hardening will be considered in order to correctly reproduce the true material behavior of steel under monotonic and cyclic loading. One critical point in seismic engineering is the determination of damage due to earthquakes. Here, damage is described by continuum damage mechanics with evolution equations for ductile and creep damage, which provide the distribution and development of damage in structures in terms of damage variables. Since the evolution of damage is in general strongly anisotropic, anisotropy is included.
A consistent description of the constitutive and evolution equations for elastic-viscoplastic and damaged material is possible using thermodynamics of irreversible processes (see section 4.1.2). Partial derivatives of the free Helmholtz energy Ψ lead to equations of state of variables which are conjugated to state variables. The state variables can be obtained from partial derivatives of the dissipation potential ϕ.
In the following, a material model is developed which is capable of reproducing the important characteristics of the material behavior of mild steel S 355. For embedding the constitutive equations into the framework of thermodynamics, the free Helmholtz energy and the dissipation potential are extended along with every enhancement of the material model. The thermodynamical consistency of the model is proven and the model parameters are presented and explained.

4.2.1 Elasticity

The structural steel S 355 and other mild steels behave elastically up to a maximum strain of about 0.2%. Elastic deformations are reversible and occur spontaneously.
In order to describe linear-elastic behavior, the free Helmholtz energy for elasticity is given by

$$\Psi(\boldsymbol{\varepsilon}^{el}) = \frac{1}{2}\boldsymbol{\varepsilon}^{el} : \mathbf{E} : \boldsymbol{\varepsilon}^{el} \tag{4.20}$$

where $\boldsymbol{\varepsilon}^{el}$ represents the elastic strains and the elasticity tensor $\mathbf{E}$ contains the modulus of elasticity E which describes the connection between stress and strain of the material. The partial derivative

$$\frac{\partial \Psi}{\partial \boldsymbol{\varepsilon}^{el}} = \mathbf{E} : \boldsymbol{\varepsilon}^{el} = \boldsymbol{\sigma} \tag{4.21}$$

leads to the equation of state for the stresses $\boldsymbol{\sigma}$. Since the material model is based on evolution equations, the elastic strain rate is given after rearrangement by

$$\dot{\boldsymbol{\varepsilon}}^{el} = \frac{d}{dt}[\mathbf{E}^{-1} : \boldsymbol{\sigma}]. \tag{4.22}$$

4.2.2 Viscoplasticity

In order to correctly capture the inelastic, time-variant behavior of structural steel, viscoplasticity is incorporated into the model. The rheological model consists of a series connection of a Hooke-body in order to take into account elastic deformations and a Bingham-body, which comprises a parallel connection of a Newton- and a St.Venant-body in order to consider viscoplasticity (see figure 4.1).

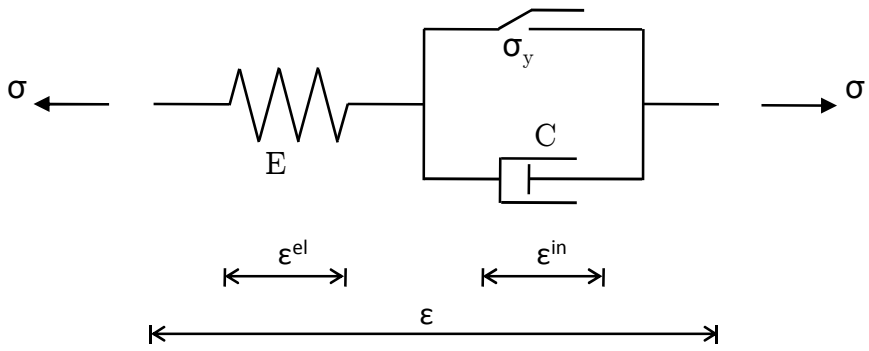

Figure 4.1: Rheological model of viscoplasticity

The transition from the elastic domain into the inelastic domain is marked by the yield stress in the one dimensional case or a yield condition in the multiaxial case. While

the classical theory of plasticity does not allow stress-states above the yield stress, the theory of viscoplasticity is based on the concept of over-stress. The over-stress is the difference between the actual stress and the yield stress and determines the onset of viscoplastic deformations. Under constant strain-controlled loading, which generates a stress state σ above the yield stress σ_y, the over-stress σ_{ex} is degraded with time which reveals that viscoplasticity may describe relaxation (see figure 4.2).

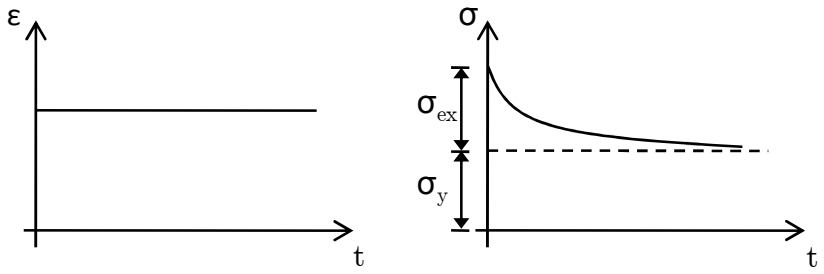

Figure 4.2: Stress relaxation: under constant strain controlled loading within the inelastic range (left) the over-stress σ_{ex} is degraded with time (right)

The creep behavior is also modelled by means of viscoplasticity. Figure 4.3 shows the evolution of strain obtained by a viscoplastic material model if a material is subjected to a constant stress above the yield stress. The first phase, called primary creep, is characterized by a rapid increase of strain. The reason is the exponential approach of the isotropic hardening variable against its saturation value (see chapter 4.2.3). Once the hardening has reached its saturation value, the second phase, called secondary creep, is initiated, which is characterized by a constant strain rate. Primary and secondary creep can both be modelled using a viscoplastic material model.

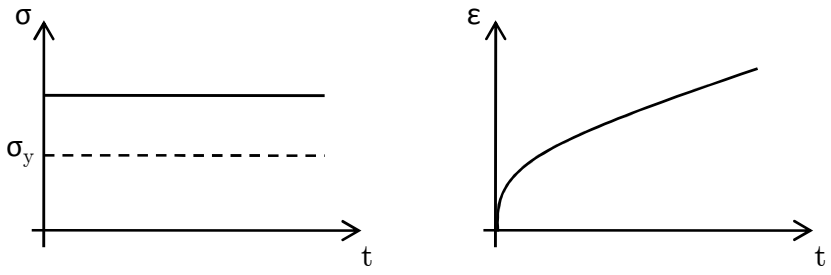

Figure 4.3: Primary and secondary creep: under constant stress controlled loading above the yield stress σ_y (left) the strain increases with time (right)

Viscoplasticity also considers the influence of different loading velocities (see figure 3.8), which is important since earthquakes are mainly characterized by irregular loading with different loading velocities. Additionally, viscoplasticity includes the effect of stress on the evolution of strain under creep conditions, as it was already shown in figure 3.9. For this reason, it is used for further investigations in order to accurately describe the

behavior of steel under seismic action.

The modeling of viscoplastic material behavior is based on the well-known approach by Chaboche & Rousselier [25], [26]. Under assumption of small strains, the total strain rate is split up into an elastic part and an inelastic part:

$$\dot{\boldsymbol{\varepsilon}} = \dot{\boldsymbol{\varepsilon}}^{el} + \dot{\boldsymbol{\varepsilon}}^{in}. \tag{4.23}$$

The dissipation potential for viscoplasticity is given by

$$\phi(\boldsymbol{\sigma}) = \frac{\sigma_p}{n+1}\dot{\varepsilon}_0 \left\langle \frac{\sigma_{eq} - \sigma_y}{\sigma_p} \right\rangle^{n+1} = \frac{\sigma_p}{n+1}\dot{\varepsilon}_0 \left\langle \frac{\sigma_{ex}}{\sigma_p} \right\rangle^{n+1} \tag{4.24}$$

with the equivalent stress σ_{eq}, the over-stress σ_{ex}, the viscosity parameter $\dot{\varepsilon}_0$ for assuring unit conformity, and the material parameters σ_y, σ_p, and n. The parameter σ_y corresponds to the yield stress. The parameter n is called stress exponent and leads to a disproportionate relation between the inelastic strains and the overstress σ_{ex}. The partial derivative of the dissipation potential ϕ with respect to $\boldsymbol{\sigma}$ leads to the equation for the inelastic strain rate $\dot{\boldsymbol{\varepsilon}}^{in}$

$$\dot{\boldsymbol{\varepsilon}}^{in} = \frac{\partial \phi}{\partial \boldsymbol{\sigma}} = \frac{\partial \sigma_{ex}}{\partial \boldsymbol{\sigma}}\dot{\varepsilon}_0 \left\langle \frac{\sigma_{ex}}{\sigma_p} \right\rangle^{n} = \frac{\partial \sigma_{ex}}{\partial \boldsymbol{\sigma}}\dot{p} \tag{4.25}$$

with the over-stress σ_{ex} following equation 4.27. The partial derivative of the over-stress characterizes the evolution direction of inelastic strains. The viscoplastic strain rate

$$\dot{p} = \dot{\varepsilon}_0 \left\langle \frac{\sigma_{ex}}{\sigma_p} \right\rangle^{n} \tag{4.26}$$

describes the rate of accumulated plastic strains using the McAuley bracket which only yields results different from zero if the over-stress is positive. The over-stress σ_{ex} is based on the second invariant of the deviatoric stress tensor $J_2(\boldsymbol{\sigma}^D) = \frac{1}{2}tr(\boldsymbol{\sigma}^D \cdot \boldsymbol{\sigma}^D)$

$$\sigma_{ex} = \sigma_{eq} - \sigma_y = \sqrt{3J_2(\boldsymbol{\sigma}^D)} - \sigma_y = \sqrt{\frac{3}{2}tr(\boldsymbol{\sigma}^D \cdot \boldsymbol{\sigma}^D)} - \sigma_y. \tag{4.27}$$

The dependance of the over-stress on the second invariant indicates that inelastic deformations are connected with volume constancy.
The appearance of an upper and lower yield point in the stress-strain curve of structural steels cannot be modelled using the given equations for viscoplasticity, as they only consider one yield point. The consequences of this simplification, however, are negligibly small.

4.2.3 Hardening

Hardening occurs due to dislocations, which pile up at obstacles, and results in an increase of stress. Here, two evolution equations for isotropic and kinematic hardening are considered in order to describe different specifications. Figure 4.4 depicts the influence of isotropic and kinematic hardening in the two-dimensional principle stress space. While isotropic hardening leads to an expansion of the yield surface by the isotropic hardening variable K, kinematic hardening results in a translation of the yield surface by the kinematic hardening tensor $\mathbf{X}$.

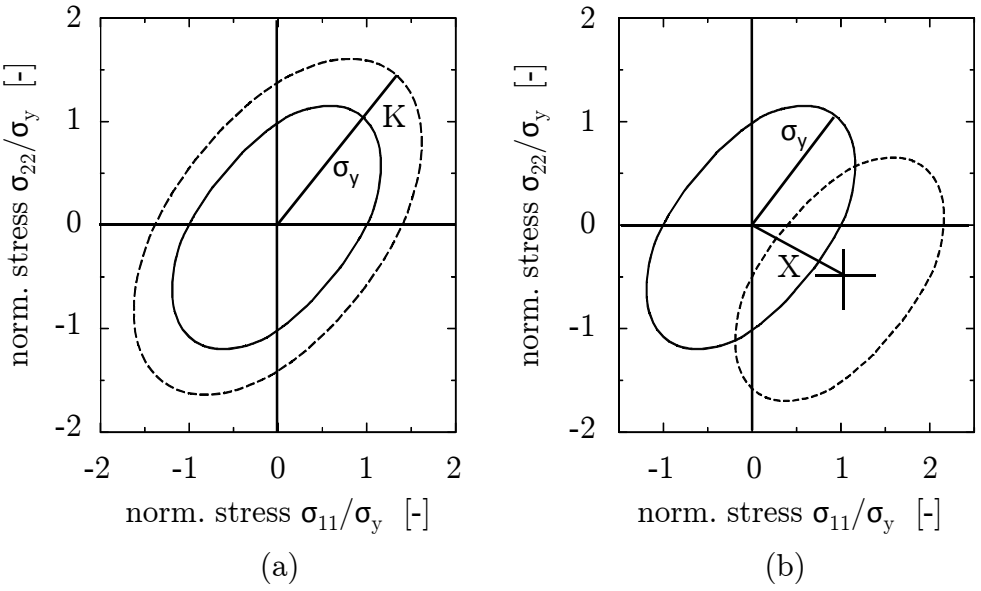

Figure 4.4: The influence of (a) isotropic and (b) kinematic hardening on the yield surface

In the framework of thermodynamics, the evolution equations for isotropic and kinematic hardening are derived from the free Helmholtz energy Ψ and the dissipation potential ϕ. Partial derivatives of the extended free Helmholtz energy assumed as

$$\Psi(\boldsymbol{\varepsilon}^{el}, r, \boldsymbol{\alpha}) = \frac{1}{2}\boldsymbol{\varepsilon}^{el} : \mathbf{E} : \boldsymbol{\varepsilon}^{el} + \frac{1}{2}bQr^2 + \frac{1}{3}aC\boldsymbol{\alpha} : \boldsymbol{\alpha} \tag{4.28}$$

lead to the equations of state for isotropic hardening K and kinematic hardening $\mathbf{X}$

$$K = \frac{\partial \Psi}{\partial r} = bQr \tag{4.29}$$

$$\mathbf{X} = \frac{\partial \Psi}{\partial \boldsymbol{\alpha}} = \frac{2}{3}aC\boldsymbol{\alpha} \tag{4.30}$$

with parameters b, Q, a, and C and the internal variables $V_i = \{r, \boldsymbol{\alpha}\}$. The variables K and $\mathbf{X}$ are the energetic conjugated forces for the internal variables r and $\boldsymbol{\alpha}$.

The dissipation potential for hardening is given by

$$\phi(\boldsymbol{\sigma}, K, \mathbf{X}) = \frac{\sigma_p}{n+1}\dot{\varepsilon}_0 \left\langle \frac{\sigma_{ex}}{\sigma_p} \right\rangle^{n+1} \tag{4.31}$$

with the extended over-stress

$$\begin{aligned}\sigma_{ex} = &\sqrt{\frac{3}{2}(\boldsymbol{\sigma} - \mathbf{X})^D : (\boldsymbol{\sigma} - \mathbf{X})^D} - \sigma_y - K \\ &+ \left[\frac{K^2}{2Q} - \frac{b^2 Q}{2} r^2\right] + \left[\frac{3}{4C}\mathbf{X} : \mathbf{X} - \frac{a^2 C}{3}\boldsymbol{\alpha} : \boldsymbol{\alpha}\right] \qquad (4.32) \\ = &\sigma_{eq} - \sigma_y - K + \left[\frac{K^2}{2Q} - \frac{b^2 Q}{2} r^2\right] + \left[\frac{3}{4C}\mathbf{X} : \mathbf{X} - \frac{a^2 C}{3}\boldsymbol{\alpha} : \boldsymbol{\alpha}\right]. \qquad (4.33)\end{aligned}$$

The extension is based on [109]. The expressions in square brackets are formulated in conjugated force and state variables and equal zero. Saturation terms limit the growth of hardening and describe dislocation movement. Partial derivatives lead to the evolution equations of the internal variables

$$\dot{r} = -\frac{\partial \phi}{\partial K} = \left(1 - \frac{K}{Q}\right)\dot{p}, \tag{4.34}$$

$$\dot{\boldsymbol{\alpha}} = -\frac{\partial \phi}{\partial \mathbf{X}} = \left(\frac{\partial \sigma_{eq}}{\partial \boldsymbol{\sigma}} - \frac{3}{2C}\mathbf{X}\right)\dot{p}. \tag{4.35}$$

Inserting equation (4.34) in equation (4.29) and equation (4.35) in equation (4.30), respectively, results in the evolution equations for isotropic hardening $\dot{K}$ and kinematic hardening $\dot{\mathbf{X}}$

$$\dot{K} = b(Q - K)\dot{p}, \tag{4.36}$$

$$\dot{\mathbf{X}} = a\left(\frac{2}{3}C\frac{\partial \sigma_{eq}}{\partial \boldsymbol{\sigma}} - \mathbf{X}\right)\dot{p}. \tag{4.37}$$

While the parameters b and a describe the velocity of the development of hardening, Q and C specify the saturation values.

In figure 4.5 the influence of hardening on the stress-strain curve of a cyclic test is shown. The influence of isotropic and kinematic hardening is investigated separately. It can be seen that isotropic hardening leads to an increase of stress due to the expansion of the yield surface. The stress increases until the saturation value Q is reached. Once the saturation value is reached, the shape of the hysteresis loops is similar to the shape of hysteresis curves with perfect elastic-plastic material behavior. Kinematic hardening considers the Bauschinger effect and leads to a shift of the yield surface. Thus, the initiation of plastic deformations after load reversals occurs earlier than under consideration of isotropic hardening. The shift of the yield surface, and therewith the developing of the values of the kinematic hardening variable, coincides with the developing of inelastic strains and therefore is cyclic.

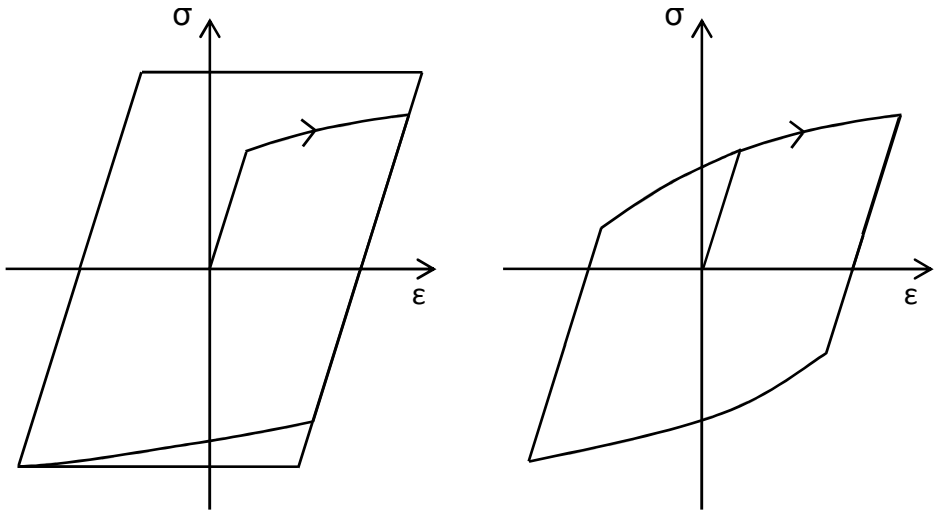

(a) isotropic hardening (b) kinematic hardening

Figure 4.5: The influence of isotropic and kinematic hardening on the stress-strain behavior

Figure 4.6 shows the evolution of the variables of isotropic and kinematic hardening for a material under uniaxial, alternating tension and compression. The developing of strain represents the loading history. The equivalent stress exceeds the yield stress σ_y under both tension and compression. The isotropic hardening variable K increases continuously when the equivalent stress is exceeding the yield stress. Thus, it increases both under tension and compression. The variable approaches the saturation value Q with the velocity b. The approach of the saturation value Q occurs exponentially, which is visible not only in the plot of the isotropic hardening variable K but also in the plot of the equivalent stress. With decreasing change in the hardening variable K, the equivalent stress also approaches a maximum value. The plot of the developing of the values of the kinematic hardening variable $\mathbf{X}$ shows the cyclic behavior. The cyclicity is induced by considering not only the amount of plastic deformations but also the direction. Kinematic hardening depends on two parameters, where the parameter C specifies the saturation value of kinematic hardening evolution and the parameter a describes the evolution velocity. If the equivalent stress falls below the yield stress σ_y, the kinematic hardening variable stays constant. Otherwise it in- or decreases in accordance with tension and compression, respectively.

Using equation 4.36 and 4.37 for the description of hardening, the characteristic yield plateau of mild structural steel cannot be represented. The evolution of the hardening variables depends on the accumulated plastic strains p and thus hardening will start to increase as soon as the material behaves inelastically. For the description of cyclic material behavior, however, the consequences are negligible, since deviations caused by neglecting the yield plateau are compensated after a few cycles already.

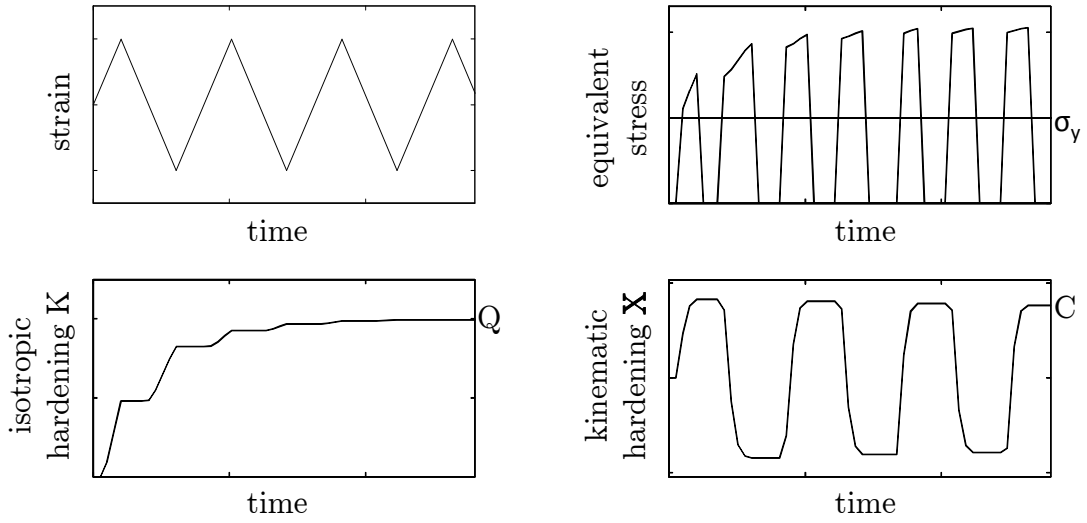

Figure 4.6: Evolution of isotropic and kinematic hardening variables under cyclic loading

The special characteristic of mild construction steel showing cyclic softening for strain amplitudes $\varepsilon_a < 0.6$ % can be neglected when dealing with seismic loading, since seismic loading being relevant for reducing structural stability requires strain amplitudes that exceed the neutral strain amplitude $\varepsilon_a = 0.6$ % by far.
Softening, meaning isotropic and formative softening with a reduction or a deformation of the yield surface, is not considered within this work. Deteriorated material behavior is taken into account using damage described in chapter 4.2.5.

4.2.4 Strain memory surface

Experiments have shown that the cyclic deformation behavior of steel is closely related to the inelastic strain amplitude history [24, 120]. The evolution laws of internal variables, which in the model depend on the accumulated plastic strain, do not accurately describe the observed material behavior under cyclic loading, since the accumulated plastic strain does not include a memory of the strain loading path. The isotropic hardening variable K, for example, would increase under small cyclic straining with a constant strain amplitude until its saturation value Q is reached after a sufficient number of cycles which is contradictory to experimental observations.
A remedy can be found in using strain memory surfaces. Analogous to the yield surface in the stress space, a condition in the plastic strain space can be established which is invariant to coordinate transformations and results in a closed convex hypersurface (strain memory surface). The strain memory surface M

$$M = \frac{2}{3}(\varepsilon^{in} - \beta)(\varepsilon^{in} - \beta) - q^2 \leq 0 \tag{4.38}$$

depends on two new variables β and q where β describes the displacement of the surface and q specifies its amplitude. In order to consider the influence of the strain memory

surface on isotropic hardening, the saturation value of isotropic hardening Q is now a function of the amplitude of the strain memory surface q:

$$Q = f(q). \tag{4.39}$$

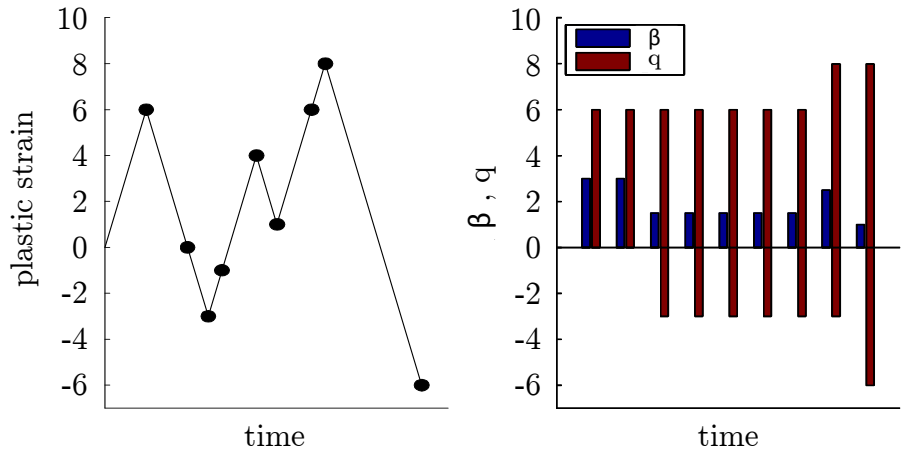

Figure 4.7: Evolution of the monotonic strain memory variables β and q

In literature, different formulations of strain memory surfaces can be found. Many formulations base on the approach by Chaboche et al. from 1979 [24]. Chaboche and his co-workers propose a memory model for the maximum equivalent inelastic strain amplitude. A plastic strain state outside the current strain memory surface leads to the growth and adjustment of the variables $\boldsymbol{\beta}$ and q, while $\boldsymbol{\beta}$ and q remain constant for plastic strain states inside the memory surface. Thus, the inelastic strain amplitude q will not decrease and always remembers the maximum strain reached so far during loading. Extensions are made by Yang [143, 144] and others [66]. They include a fading memory rate function in order to account for the cyclic order of amplitudes. Therewith, the inelastic strain amplitude q can decrease and will approach the current real inelastic strain amplitude regardless of previous history with larger amplitudes. Scheibe [120] distinguishes between three strain memory surfaces which are called monotonic strain memory, current strain memory, and saturation strain memory. The monotonic strain memory corresponds with the concept of maximum inelastic strain amplitude of Chaboche and the current strain memory is related to the extension of the before mentioned model to a fading memory rate function. The saturation strain memory considers the saturation process due to cycling with constant amplitude. The saturation strain memory is always situated within the monotonic strain memory and characterizes the current saturated plastic strain range.
The evolution rule of the saturation value of isotropic hardening Q widely spreads in its complexity. While linear evolution functions do without introducing a multitude of new material constants [6], quadratic [144] or exponential functions [66] require additional parameters.

Within this work, a maximum strain amplitude memory or monotonic strain memory surface is defined in the three-dimensional space as

$$M = \frac{2}{3}(\boldsymbol{\varepsilon}^{in} - \boldsymbol{\beta})(\boldsymbol{\varepsilon}^{in} - \boldsymbol{\beta}) - q^2 \leq 0 \tag{4.40}$$

with

$$\dot{\boldsymbol{\beta}} = 0.5H(M)\dot{\boldsymbol{\varepsilon}}^{in}, \tag{4.41}$$
$$\dot{q} = 0.5H(M)\mathbf{n}_F\mathbf{n}_M\dot{p}, \tag{4.42}$$

where $H(M)$ is the Heaviside function with $H(M) = 1$ if $M \geq 0$ and $H(M) = 0$ if $M < 0$, $\mathbf{n}_F$ is the normal to the yield surface, and $\mathbf{n}_M$ is the normal to the strain memory surface. The evolution rule of the saturation value of isotropic hardening Q is assumed to be linear in order to reduce the number of material constants:

$$\dot{Q} = \dot{q} \cdot Q. \tag{4.43}$$

Figure 4.7 exemplarily shows the evolution of the monotonic strain memory variables $\boldsymbol{\beta}$ and q for a predefined plastic strain history.

4.2.5 Damage

Continuum damage mechanics describes damage as the decrease of the elementary area of resistance which results from a decrease of the number of bonds at the level of atoms. This debonding leads to the nucleation, growth, and coalescence of microvoids up to the initiation of macrocracks. Damage mechanics tries to understand the micromechanical processes during damage evolution and describes them macroscopically with damage evolution equations. The evolution equations for damage can be divided according to the circumstance under which damage manifests. This leads to a differentiation between brittle, ductile, creep, and fatigue damage. The following paragraphs identify the most suitable damage evolution laws in order to accurately describe damage evolution under seismic loading.
Since steel structures under seismic action are designed to show ductile material behavior, brittle damage can be neglected.
As a first approximation, ductile and fatigue damage can both be used in order to describe the material behavior under cyclic loading. However, they show different advantages and disadvantages. Fatigue damage can be divided into low cycle fatigue damage and high cycle fatigue damage. Low cycle fatigue is better suited in order to describe structures under seismic loading, since seismic loading is characterized by a small number of cycles. In both cases however, the quantification of damage is linked to the number of cycles and thus, fatigue damage is only suitable for loading histories where the number of cycles can be specified. The random nature of earthquakes makes it difficult to apply fatigue damage to structures under seismic loading. Another drawback of fatigue damage is the dependance on the number of cycles up to failure. While single structural

members can easily be evaluated in respect of fatigue, since their reproducibility makes it possible to define the number of cycles up to failure, fatigue and life time estimations of real constructions are not directly feasible. Therefore, fatigue damage is mainly applied to structural components, while the assessment of real constructions requires other formulations of damage mechanics.
Ductile damage evolution laws describe deteriorated material behavior due to large inelastic strains which are characteristic of structures under seismic loading. In order to adapt ductile damage laws to cyclic loading, the evolution equation needs to be extended.
The advantages of ductile damage laws with an extension to cyclic loading in order to cope with the irregular, dynamic loading situation of earthquakes prevail the advantages of fatigue damage laws. Thus, this work considers the use of ductile damage evolution equations for the description of damage under seismic loading. A main focus is on the extension of ductile damage evolution laws in order to account for damage evolution under cyclic straining.
Additionally, creep damage is incorporated. Although creep damage does not play an important role during earthquakes, it is worth being considered for long term damage evolution after an earthquake, if predamaged structures are again subjected to service loads.

The evolution of damage is in general strongly anisotropic. Therefore, the following considerations include anisotropic damage based on the comprehensive work of Zümendorf [146].

For the description of the condition of the elastically-viscoplastically deformed and damaged material via internal variables V_i, a symmetric damage tensor $\mathbf{D}$ is chosen besides the isotropic hardening variable r and the tensor of second order $\boldsymbol{\alpha}$ for kinematic hardening:

$$V_i = \{r, \boldsymbol{\alpha}, \mathbf{D}\}.$$

The energy release rate $\mathbf{Y}$ is the energetic conjugated quantity for the damage tensor $\mathbf{D}$.

In the following, the basic assumptions of the damage model are given in order to derive the evolution equations for the damage variables and determine the incorporation of damage into the existing model.

Damage variables

The evolution of material damage can be described by means of damage variables which are part of the internal variables. In the framework of continuum damage mechanics the true distribution of material defects is homogenized by means of the damage variables. The damage variables can be scalars, vectors, or tensors. For anisotropic damage a

tensor of second or higher order is necessary. The damage variables can be embedded differently in the relation between stress and strain, namely using the concept of effective stress [125, 126], the principle of strain equivalence [22], or the principle of energy equivalence [34]. Assuming isotropic damage with a scalar damage variable, damage can be understood as the ratio of damaged area $A_{damaged}$ to total area A_{total}

$$D = \frac{A_{damaged}}{A_{total}}. \tag{4.44}$$

If only the undamaged area A_{netto} is able to carry loads, the stress must increase. This is taken into account by means of the concept of effective stress

$$\tilde{\sigma} = \frac{A_{total}}{A_{netto}}\sigma = \frac{1}{1-D}\sigma \ . \tag{4.45}$$

For macroscopic models, however, damage variables cannot be directly derived from the microscopic area reduction, since also stress concentrations influence the material properties [92].
Chaboche extends the concept of effective stress and proposes the principle of strain equivalence [22], which assumes that the elastic strain of the undamaged material due to the effective stress equals the strain of the damaged material due to the macroscopic stress. According to that, only the stress is affected by damage while the strain remains unaffected:

$$\tilde{\sigma} = \frac{1}{1-D} \cdot \sigma \quad , \quad \tilde{\varepsilon} = \varepsilon. \tag{4.46}$$

For a multiaxial approach we obtain

$$\tilde{\boldsymbol{\sigma}} = \bar{\mathbf{M}}(\mathbf{D}) : \boldsymbol{\sigma} \quad , \quad \tilde{\boldsymbol{\varepsilon}} = \boldsymbol{\varepsilon} \tag{4.47}$$

where $\bar{\mathbf{M}}$ is the damage effect tensor defined in the next section. However, this approach is not in agreement with the potential theory [127] and for the case of anisotropic damage the integrability conditions are in general not fulfilled:

$$\tilde{\mathbf{E}} = \bar{\mathbf{M}}^{-1} : \mathbf{E} \quad \rightarrow \quad \tilde{E}_{ijkl} \neq \tilde{E}_{klij}. \tag{4.48}$$

The principle of energy equivalence [34] considers both stress and strain as affected by damage:

$$\tilde{\sigma} = \frac{1}{1-D} \cdot \sigma \quad , \quad \tilde{\varepsilon} = (1-D) \cdot \varepsilon \tag{4.49}$$

or in the three-dimensional case

$$\tilde{\boldsymbol{\sigma}} = \bar{\mathbf{M}}(\mathbf{D}) : \boldsymbol{\sigma} \quad , \quad \tilde{\boldsymbol{\varepsilon}} = \bar{\mathbf{M}}(\mathbf{D})^{-1} : \boldsymbol{\varepsilon}. \tag{4.50}$$

Since the application of the energy equivalence principle fullfills the condition of integrability,

$$\tilde{\mathbf{E}} = \bar{\mathbf{M}}^{-1} : \mathbf{E} : \bar{\mathbf{M}}^{-1} \quad \rightarrow \quad \tilde{E}_{ijkl} = \tilde{E}_{klij} \tag{4.51}$$

this work takes into account the principle of energy equivalence.

Damage effect tensor

The damage effect tensor $\bar{\mathbf{M}}$ is composed of damage variables and transforms the undamaged material tensor into the damaged one. In the simplest case of isotropic damage, the damage effect tensor is given by

$$\bar{\mathbf{M}} = \frac{1}{1-D} \ . \tag{4.52}$$

For anisotropic damage, the damage effect tensor of 4^{th} order by Murakami & Ohno [93] can be used:

$$\bar{M}_{ijkl} = \frac{1}{2}(\bar{M}_{ik} I_{jl} + \bar{M}_{jl} I_{ik}) \tag{4.53}$$

with

$$\bar{M}_{ij} = (I_{ij} - D_{ij})^{-1}. \tag{4.54}$$

In the following, the same damage effect tensor and the same damage variables are used for the transformation of all material properties, although the reduction of the yield stress due to damage is in general not proportional to the reduction of the elasticity tensor.

Coupling of viscoplasticity and damage

The change in material behavior due to increasing material damage has to be considered in the yield function. So far it is assumed that permanent deformations are connected with volume constancy which leads to a dependance of the yield function on the second invariant of the stress tensor. Micromechanical investigations by Gurson [55] and Tvergaard & Needleman [137] prove that damaged material also shows an increase of volume. Thus, the yield function has to be extended in order to correctly represent this behavior.
The over-stress σ_{ex} used within this work, which corresponds to the yield function, is given as

$$\begin{aligned}
\sigma_{ex} = \Bigg(& \frac{3}{2} a_1 (\bar{\mathbf{M}} : \boldsymbol{\sigma}^D - \mathbf{X}^D)^T : (\bar{\mathbf{M}} : \boldsymbol{\sigma}^D - \mathbf{X}^D) \\
& + \frac{a_2}{6} tr[\mathbf{D}/3] (\bar{\mathbf{M}} : \boldsymbol{\sigma}^H - \mathbf{X}^H)^T : (\bar{\mathbf{M}} : \boldsymbol{\sigma}^H - \mathbf{X}^H) \Bigg)^{\frac{1}{2}} \\
& - \sigma_y - K + [K - bQr] + \left[bQr - K + \frac{K^2}{2Q} - \frac{b^2 Q}{2} r^2 \right] \frac{1}{1 - tr[\mathbf{D}/3]} \\
& + \left[\frac{3}{4C} X : X - \frac{a^2 C}{3} \alpha : \alpha \right].
\end{aligned} \tag{4.55}$$

Firstly, damage affects the equivalent stress σ_{eq}, which now consists of two terms within the root. The first term contains the v.Mises yield condition where the deviatoric stress $\boldsymbol{\sigma}^D$ is substituted by the effective deviatoric stress $\tilde{\boldsymbol{\sigma}}^D = \bar{\mathbf{M}} : \boldsymbol{\sigma}^D$. The additional second term allows volumetric deformations in case of damage and is therefore based on the hydrostatic part of the stress tensor $\boldsymbol{\sigma}^H$. Secondly, the formulation of isotropic hardening within the over-stress σ_{ex} is extended by a term depending on the damage variables. This extension is aimed at balancing the reduction of the viscoplastic equivalent strain rate $\dot{\varepsilon}_v^{in}$ with increasing damage and creating a dependence of hardening on the inelastic strains. Kinematic hardening is not influenced by damage [1]. The extended yield function of equation (4.55) is used in the over-stress model of viscoplasticity and allows a descriptive coupling of viscoplasticity and damage.
Figure 4.8 shows half of the yield function in three-dimensional principle stress space for the undamaged and for the damaged case. In case of undamaged material, the yield function corresponds to the v.Mises yield cylinder. The consideration of damage leads to a contraction and a formation of caps at the end of the yield cylinder.

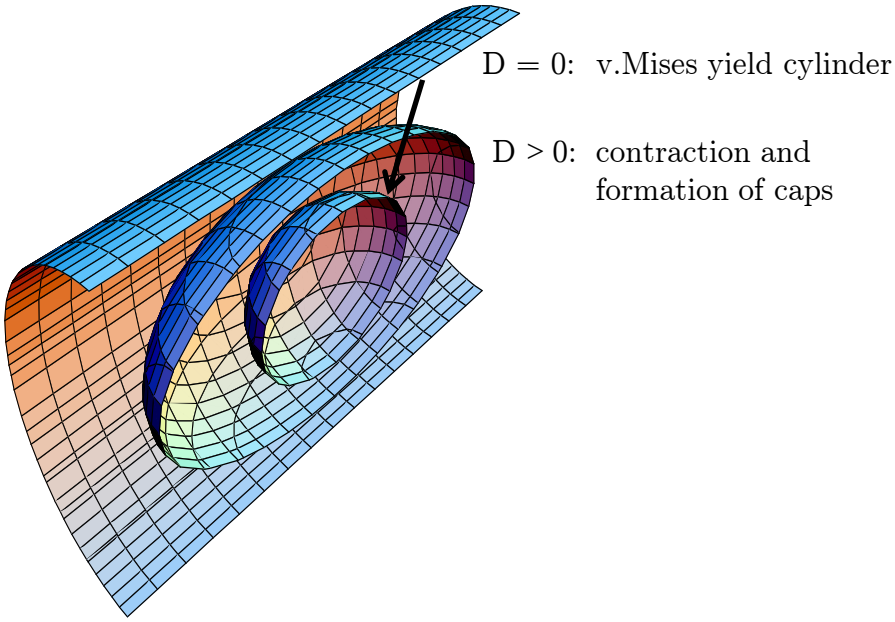

Figure 4.8: Half of the yield surface in the undamaged and damaged case in the three-dimensional principle stress space

Damage evolution

According to Chaboche [22], the equation of damage evolution can be separated into a direction tensor $\mathbf{Q}$ and a scalar evolution equation for the damage variable $\dot{D}$:

$$\dot{\mathbf{D}} = \mathbf{Q}\dot{D}. \tag{4.56}$$

The direction tensor is a linear combination of an isotropic part $\mathbf{I}$ and an anisotropic part $\mathbf{S}^+$:

$$\mathbf{Q} = \gamma \mathbf{S}^+ + (1-\gamma)\mathbf{I}. \tag{4.57}$$

The parameter γ controls the contribution of the isotropic and the anisotropic part. The scalar evolution equation for the damage variable $\dot{D}$ is additively composed of the single evolution equations for the different damage manifestations. Within this work, creep damage D_c and ductile damage D_d are considered:

$$\dot{D} = \dot{D}_c + \dot{D}_d. \tag{4.58}$$

Evolution of creep damage

Creep is based on the viscosity of steel and mainly occurs at elevated temperatures. At room temperature, creep can also occur but its development is less pronounced. Creep damage is characterized by intergranular decohesions which produce an increase of the strain rate during the period of tertiary creep. The rate of creep damage evolution depends on the level of the constant stress.
Based on Kachanov [64] and Rabotnov [115], Zümendorf [146] develops an anisotropic and multiaxial evolution law for creep damage

$$\dot{D}_c = \left\langle \frac{\chi(\tilde{\boldsymbol{\sigma}})}{\sigma_K} \right\rangle^s \left(\frac{\chi(\boldsymbol{\sigma})}{\sigma_K} \right)^{t-s} \tag{4.59}$$

with the material-dependent model parameters σ_K, s, and t and the equivalent stress of Hayhurst $\chi(\boldsymbol{\sigma})$ [56]

$$\chi(\boldsymbol{\sigma}) = \alpha J_0(\boldsymbol{\sigma}) + \beta J_1(\boldsymbol{\sigma}) + \gamma J_2(\boldsymbol{\sigma}) \tag{4.60}$$

where α, β, and γ are material-dependent model parameters, J_1 and J_2 are the first and second invariant of the stress tensor, and J_0 is the maximum principal normal stress.

Thermodynamical consistency is achieved by the following extension of the free Helmholtz energy Ψ and the split of the dissipation potential ϕ in an inelastic (ϕ^{in}) and a time-dependent term (ϕ^t):

$$\Psi(\boldsymbol{\varepsilon}^{el}, r, \boldsymbol{\alpha}, \mathbf{D}) = \frac{1}{2}\boldsymbol{\varepsilon}^{el} : \bar{\mathbf{M}}^{-1} : \mathbf{E} : \bar{\mathbf{M}}^{-1} : \boldsymbol{\varepsilon}^{el} + \frac{1}{2} bQr^2 + \frac{1}{3} aC\boldsymbol{\alpha} : \boldsymbol{\alpha}, \tag{4.61}$$

$$\begin{aligned}\phi &= \phi^{in}(\boldsymbol{\sigma}, K, \mathbf{X}; \boldsymbol{\varepsilon}^{el}, r, \boldsymbol{\alpha}, \mathbf{D}) + \phi^t(\mathbf{Y}; \boldsymbol{\varepsilon}^{el}, \mathbf{D}) \\ &= \frac{\sigma_p}{n+1}\dot{\varepsilon}_0 \left\langle \frac{\sigma_{ex}}{\sigma_p} \right\rangle^{n+1} + [\mathbf{Q}^* : \mathbf{Y}] \left\langle \frac{\chi(\tilde{\mathbf{E}} : \boldsymbol{\varepsilon}^{\boldsymbol{el}}, \mathbf{D})}{\sigma_K} \right\rangle^s \left\langle \frac{\chi(\tilde{\mathbf{E}} : \boldsymbol{\varepsilon}^{\boldsymbol{el}})}{\sigma_K} \right\rangle^{t-s},\end{aligned} \tag{4.62}$$

with the over-stress σ_{ex} given in equation 4.55, the energy release rate $\mathbf{Y}$, $\tilde{\mathbf{E}}$ following equation 4.51, and the extended direction tensor $\mathbf{Q}^*$

$$\mathbf{Q}^* = (1-\gamma)\mathbf{S}^+ + \gamma\frac{(\mathbf{I}-\mathbf{D})\cdot(\mathbf{I}-\mathbf{D})}{det[\mathbf{I}-\mathbf{D}]} \tag{4.63}$$

which leads to accelerated damage evolution in the less damaged direction. The isotropic effect of the direction tensor $\mathbf{Q}^*$ allows the simulation of crack growth, since complete material separation can only be described by isotropic damage [146].

Evolution of ductile damage

Ductile damage results from the nucleation of cavities due to decohesions of inclusions from the matrix followed by their growth and coalescence. The rate of ductile damage evolution depends on the triaxiality of the state of stress. The bigger the triaxiality, defined as the ratio of hydrostatic stress to v.Mises equivalent stress, the higher is the damage rate.
In literature many different formulations of ductile damage exist, which differentiate between phenomenological, micromechanical, and thermodynamical approaches. In addition, the formulations can be distinguished according to the quantity which determines the evolution of damage. However, it is found that damage bases best on the cumulative equivalent plastic strain [67]. Besides the choice of the quantity that determines damage evolution, the shape of the damage evolution function plays an important role. Thakkar and Pandey [134] give an overview of different damage evolution laws with linear, exponential, or parabolic damage growth. Another crucial factor of the development of damage evolution laws is the estimation when damage initiates. In order to account for the fact that damage may not develop with the first appearance of plastic strain, some authors include a threshold for the plastic strain into their ductile damage evolution laws [16, 70]. Only if a predefined plastic strain measure exceeds this threshold, damage starts to evolute. The need for an accurate starting point of damage evolution is more critical for linear damage evolution laws than it is for example for exponential damage evolution laws.
Gurson [55] develops a microphysically based model in order to describe the growth of pores in metals. He uses a yield function which reduces to the v.Mises yield condition if the newly defined variable f, which describes the volume part of the voids in the material, is zero. In case of material damage, f increases and leads to a compressible material which is considered in the yield function by the hydrostatic stress. Tvergaard and Needleman [136, 137] propose an extension of the Gurson model. Two additional constants are introduced in order to more accurately fit experimental results. In addition, the volume part of voids f is substituted by an effective volume part of voids $f^*_{(f)}$ which takes into account accelerated damage due to coalescence of voids and a limit value for f^*_u from which on no stress can be absorbed. Chu and Needleman [30] consider the growth of existing voids as well as the nucleation of new voids in the evolution

equation for f

$$\dot{f} = \dot{f}_{growth} + \dot{f}_{nucleation} = (1-f)tr(\dot{\boldsymbol{\varepsilon}}^{in}) + \frac{f_n}{\sqrt{(}2\pi s_n^2)} e^{-\frac{(\dot{\varepsilon}_{eq}^{in} - \varepsilon_n)^2}{2s_n^2}} \dot{\varepsilon}_{eq}^{in} \tag{4.64}$$

where f_n is the total volume part of void creating particles, $\dot{\varepsilon}_{eq}^{in} = \sqrt{2/3\ \dot{\boldsymbol{\varepsilon}}^{in} \cdot \dot{\boldsymbol{\varepsilon}}^{in}}$ is the plastic equivalent strain, and ε_n is the mean of the plastic equivalent strain caused by void creating particles with the standard deviation s_n.
All of the aforementioned approaches do not consider the change in stiffness due to increasing porosity. On the contrary, this is taken into account in the thermodynamically based evolution equation for isotropic ductile damage by Lemaitre [80]. Based on his proposals and including extensions towards anisotropic material behavior [146], the free Helmholtz energy Ψ used within this work is given by

$$\Psi(\boldsymbol{\varepsilon}^{el}, r, \boldsymbol{\alpha}, \mathbf{D}) = \frac{1}{2}\boldsymbol{\varepsilon}^{el} : \bar{\mathbf{M}}^{-1} : \mathbf{E} : \bar{\mathbf{M}}^{-1} : \boldsymbol{\varepsilon}^{el} + \frac{1}{2}bQr^2 + \frac{1}{3}aC\boldsymbol{\alpha} : \boldsymbol{\alpha} \tag{4.65}$$

which leads to the equation of state for the energy release rate $\mathbf{Y}$

$$\mathbf{Y} = \frac{\partial \Psi}{\partial \mathbf{D}} = \left(\boldsymbol{\varepsilon}^{el} : \frac{\partial \bar{\mathbf{M}}^{-1}}{\partial \mathbf{D}} : \mathbf{E} : \bar{\mathbf{M}}^{-1} : \boldsymbol{\varepsilon}^{el} \right)^{sym} . \tag{4.66}$$

The dissipation potential ϕ is given by

$$\begin{aligned} \phi &= \phi^{in}(\boldsymbol{\sigma}, K, \mathbf{X}, \mathbf{Y}; \boldsymbol{\varepsilon}^{el}, r, \boldsymbol{\alpha}, \mathbf{D}) + \phi^{t}(\mathbf{Y}; \boldsymbol{\varepsilon}^{el}, \mathbf{D}) \\ &= \frac{\sigma_p}{n+1}\dot{\varepsilon}_0 \left\langle \frac{\sigma_{ex}}{\sigma_p} \right\rangle^{n+1} + [\mathbf{Q}^* : \mathbf{Y}] \left\langle \frac{\chi(\tilde{\mathbf{E}} : \boldsymbol{\varepsilon}^{\boldsymbol{el}} \cdot \mathbf{D})}{\sigma_K} \right\rangle^{s} \left\langle \frac{\chi(\tilde{\mathbf{E}} : \boldsymbol{\varepsilon}^{\boldsymbol{el}})}{\sigma_K} \right\rangle^{t-s} \end{aligned} \tag{4.67}$$

with the extended over-stress

$$\begin{aligned} \sigma_{ex} = \Bigg(& \frac{3}{2}a_1(\bar{\mathbf{M}} : \boldsymbol{\sigma}^D - \mathbf{X}^D)^T : (\bar{\mathbf{M}} : \boldsymbol{\sigma}^D - \mathbf{X}^D) \\ & + \frac{a_2}{6}tr[\mathbf{D}/3](\bar{\mathbf{M}} : \boldsymbol{\sigma}^H - \mathbf{X}^H)^T : (\bar{\mathbf{M}} : \boldsymbol{\sigma}^H - \mathbf{X}^H) \Bigg)^{\frac{1}{2}} \\ & - \sigma_y - K + [K - bQr] + \left[bQr - K + \frac{K^2}{2Q} - \frac{b^2 Q}{2} r^2 \right] \frac{1}{1 - tr[\mathbf{D}/3]} \\ & + \left[\frac{3}{4C}\mathbf{X} : \mathbf{X} - \frac{a^2 C}{3}\boldsymbol{\alpha} : \boldsymbol{\alpha} \right] + [\mathbf{Q}^* : (\mathbf{Y} - \mathbf{Z})] f(\boldsymbol{\varepsilon}^{el}, \mathbf{D}) \end{aligned} \tag{4.68}$$

where $\mathbf{Z}$ equals the absolute value of the energy release rate $\mathbf{Y}$

$$\mathbf{Z} = \frac{1}{2}\left(\boldsymbol{\varepsilon}^{el} : \frac{\partial \bar{\mathbf{M}}^{-1}}{\partial \mathbf{D}} : \mathbf{E} : \bar{\mathbf{M}}^{-1} : \boldsymbol{\varepsilon}^{el} + \boldsymbol{\varepsilon}^{el} : \bar{\mathbf{M}}^{-1} : \mathbf{E} : \frac{\partial \bar{\mathbf{M}}^{-1}}{\partial \mathbf{D}} : \boldsymbol{\varepsilon}^{el} \right). \tag{4.69}$$

The evolution equation for ductile damage follows from partial derivative of the dissipation potential ϕ

$$\begin{aligned}\dot{D}_d &= \frac{\partial \phi}{\partial \mathbf{Y}} = f(\boldsymbol{\varepsilon}^{el}, \mathbf{D})\dot{p} \\ &= \Bigg((c_1 + c_2 c_3 e^{-c_3 \frac{1}{1-tr[\mathbf{D}/3]} p}) \frac{1}{1 - tr[\mathbf{D}/3]} \\ &\quad + c_4 c_5 \frac{a_1 tr[\mathbf{D}/3] \left\langle tr\left[\bar{\mathbf{M}} : \bar{\mathbf{M}} : \mathbf{S} : \tilde{\mathbf{E}} : \boldsymbol{\varepsilon}^{el}\right]\right\rangle}{6(\tilde{\mathbf{E}} : \boldsymbol{\varepsilon}^{el})_{eq}} (1 - tr[\mathbf{D}/3]) \Bigg) \dot{p}\end{aligned} \tag{4.70}$$

where the transformation tensor $\mathbf{S}$ serves for generating hydrostatic conditions. It can be seen that the evolution of ductile damage depends on the evolution of the accumulated plastic strains $\dot{p}$. According to Chu and Needleman [30], the first part within the brackets provides the description of transient and saturation behavior in damage nucleation and the second part considers damage evolution by means of void growth in dependance on hydrostatic states of stress.

Damage evolution under cyclic loading

Main focus of this work is on the development of a damage model for the description of damage evolution under seismic action. As already discussed at the beginning of chapter 4.2.5, a ductile damage law with an extension towards cyclic loading is required. Ductile damage evolution laws are originally intended for the description of damage evolution under monotonically increasing plastic strains. In order to establish a ductile damage evolution equation for the description of damage under cyclic loading, the corresponding equations have to be modified.
So far, the evolution of ductile damage is activated if inelastic strains occur. The loading direction, meaning tension, compression, or shear, is not considered, though. Since the derivation of ductile damage laws is based on the characterization of the microstructural material mechanisms, the microstructural occurrences under tension and compression have to be investigated in order to establish an appropriate cyclic ductile damage evolution equation.
In literature, however, the discussion about occurrence of damage under compressive as opposed to tensile states of stress and the related microstructural mechanisms is still open. There is an agreement, though, that the evolution of damage under compression does not comply with the damage evolution under tension or shear. Most commonly used are models which allow damage evolution under tensile or shear loading [65, 29], but impede the increase of damage under compressive loading. Pirondi and Bonora [112] propose that damage accumulates if the stress triaxiality is positive. In addition, damage effects are inactive when the material is subjected to compressive loading, which means that there is no reduction of the modulus of elasticity. Kreiser at al. [70] propose a fatigue based model which assumes that damage accumulates only for tensile (positive)

elastic energy. Mediavilla et al. [89] extend their evolution law for damage by a threshold so that damage will grow in tension and under small compressive triaxiality states, while for large compressive hydrostatic stresses damage will not grow and the material will thus only continue to harden. Ohata and Toyoda [98] propose a criterion which does not avoid the growth of damage under compressive loading in general but assumes that after stress reversal piled-up mobile dislocations move in the opposite direction and form the same dislocation density after a certain straining. All plastic straining up to the same dislocation density as reached previously do presumably not aggravate material damage. Thus, damage only evolutes if the current total plastic strain is bigger than any of the plastic strains reached before.
While all of the aforementioned models do not consider the recovery of existing damage because of void closure, Kanvinde and Deierlein [67] find that compressive loads lead to the collapse of voids into oblate or penny-shaped flat voids. However, while the percentage of voids decreases, the collapsed voids show sharper stress/strain concentrations than the spherical or prolate voids. In order to account for that, they develop a model that takes into account that negative triaxiality states lead to void shrinkage. In addition though, compressive states of stress are thought to diminish the maximum critical void capacity which triggers earlier rupture of the material.

Within this work, a modification is proposed, which assumes that the damage evolution is interrupted under compressive stress states. Compressive stress states are defined by a negative first invariant $J_1 = \frac{1}{3}tr(\boldsymbol{\sigma}_{eff})$ of the effective stress tensor $\boldsymbol{\sigma}_{eff} = \boldsymbol{\sigma} - \mathbf{X}$. In addition, a reduction of stiffness due to damage is attenuated, since damaged material can carry compressive loads more easily than tensile loads. Hardening is assumed to be independent of the stress state and develops during tension and compression.
If damage only accumulates if the first invariant is positive, it cannot depend on the accumulated equivalent plastic strain p, since the equivalent plastic strain increases both in tension and compression. In order to avoid a sudden jump and a discontinuous damage evolution law that has no physical sound, a new internal variable p^+, called active accumulated plastic strain, is introduced [112]. This newly defined variable corresponds to the equivalent plastic strain accumulated if the first invariant is greater than zero. Rewriting of equation (4.26) and (4.70) leads to the active equivalent plastic strain

$$\dot{p}^+ = \dot{p} \left\langle \frac{J_1}{|J_1|} \right\rangle = \dot{\varepsilon}_0 \left\langle \frac{\sigma_{ex}}{\sigma_p} \right\rangle^n \left\langle \frac{J_1}{|J_1|} \right\rangle \tag{4.71}$$

and the active ductile damage law

$$\begin{aligned} \dot{D}_d = \Bigg(& (c_1 + c_2 c_3 e^{-c_3 \frac{1}{1-tr[\mathbf{D}/3]} p^+}) \frac{1}{1 - tr[\mathbf{D}/3]} \\ & + c_4 c_5 \frac{a_1 tr[\mathbf{D}/3] \left\langle tr\left[\bar{\mathbf{M}} : \bar{\mathbf{M}} : \mathbf{S} : \tilde{\mathbf{E}} : \boldsymbol{\varepsilon}^{el}\right] \right\rangle}{6(\tilde{\mathbf{E}} : \boldsymbol{\varepsilon}^{el})_{eq}} (1 - tr[\mathbf{D}/3]) \Bigg) \dot{p}^+. \end{aligned} \tag{4.72}$$

Recovery of existing damage because of void closure is not modelled here.
Figure 4.9 reveals the influence of the proposed criterion on the evolution of damage under cyclic loading. A simple bar is subjected to alternating high tension and compression with negligible elastic strains in comparison with plastic strains. The evolution of plastic strains is shown at the top of figure 4.9. The next row represents the first invariant $J_1/|J_1|$ whereby it is only distinguished between positive values and negative values. The third row shows the equivalent plastic strain p which increases continuously whereas the fourth row depicts the active equivalent plastic strain p^+ which only increases if the first invariant is positive. Finally, the last row demonstrates that damage D grows in accordance with the active equivalent plastic strain.

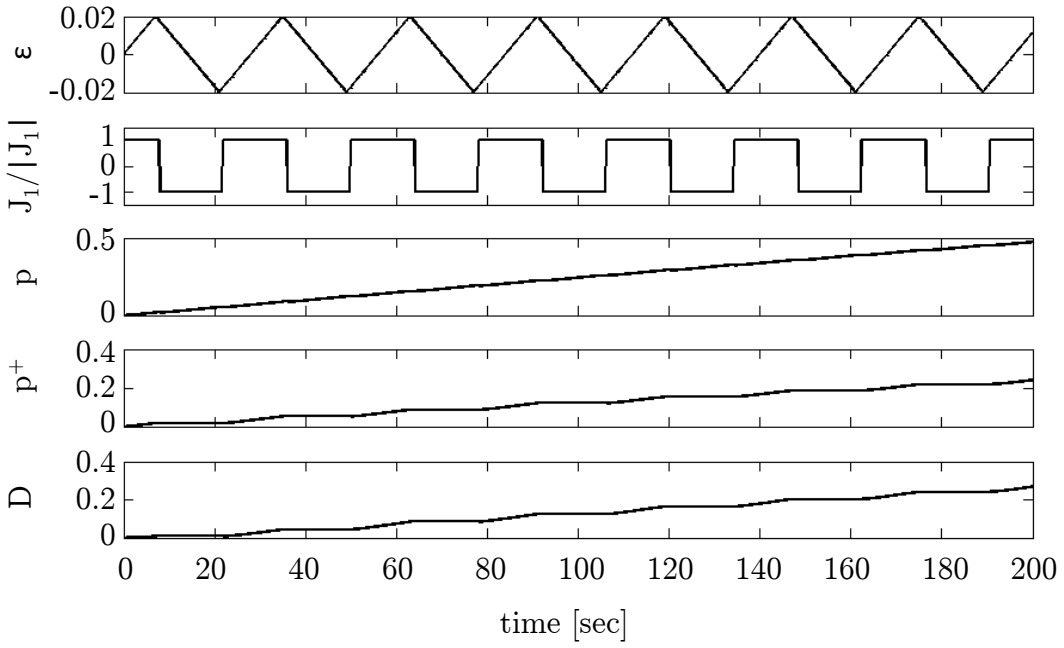

Figure 4.9: Evolution of plastic strain ε, the first invariant $J_1/|J_1|$, the equivalent plastic strain p, the equivalent plastic active strain p^+, and damage D under cyclic loading

Stiffness under tension and compression

The influence of damage on stiffness under alternating tension and compression is considered in the principle of energy equivalence. According to Lemaitre [80], it is assumed that some but not every crack closes under compression so that the stiffness of the material under compression lies between the undamaged and the damaged stiffness. In order to define the compressive stiffness of damaged material a crack closure parameter h is introduced. Thus, effective stress and strain are defined differently for tension (+) and

compression (-):

$$\tilde{\sigma}^+ = \frac{1}{1-D} \cdot \sigma^+ \qquad \tilde{\varepsilon}^+ = (1-D) \cdot \varepsilon^+ \tag{4.73}$$

$$\tilde{\sigma}^- = \frac{1}{1-Dh} \cdot \sigma^- \qquad \tilde{\varepsilon}^- = (1-Dh) \cdot \varepsilon^- \tag{4.74}$$

and in the three-dimensional case

$$\tilde{\boldsymbol{\sigma}}^+ = \bar{\mathbf{M}}(\mathbf{D}) : \boldsymbol{\sigma}^+ \qquad \tilde{\boldsymbol{\varepsilon}}^+ = \bar{\mathbf{M}}(\mathbf{D})^{-1} : \boldsymbol{\varepsilon}^+ \tag{4.75}$$

$$\tilde{\boldsymbol{\sigma}}^- = \bar{\mathbf{M}}(\mathbf{D}, h) : \boldsymbol{\sigma}^- \qquad \tilde{\boldsymbol{\varepsilon}}^- = \bar{\mathbf{M}}(\mathbf{D}, h)^{-1} : \boldsymbol{\varepsilon}^-. \tag{4.76}$$

For $h = 0$ the initial stiffness of the material is recovered and a value of $h = 1$ assumes that the stiffness under tension is on par with the stiffness under compression . Lemaitre proposes to use a value of $h = 0.2$. The material tensor is now defined as

$$\tilde{\mathbf{E}}^+ = \bar{\mathbf{M}}(\mathbf{D})^{-1} : \mathbf{E} : \bar{\mathbf{M}}(\mathbf{D})^{-1} \qquad \tilde{\mathbf{E}}^- = \bar{\mathbf{M}}(\mathbf{D}, h)^{-1} : \mathbf{E} : \bar{\mathbf{M}}(\mathbf{D}, h)^{-1}. \tag{4.77}$$

Figure 4.10 qualitatively depicts the change of stiffness under tension and compression. The elasticity tensor $\mathbf{E}$ is used at first loading. Inelastic deformations lead to the growth of damage so that unloading takes place with the diminished material tensor $\tilde{\mathbf{E}}^+$. For reloading in compression the effect of damage on stiffness is reduced so that reloading in compression is performed with the material tensor $\tilde{\mathbf{E}}^-$. If $h = 0$ the material tensor $\tilde{\mathbf{E}}^-$ equals the elasticity tensor $\mathbf{E}$. Unloading in compression using $\tilde{\mathbf{E}}^-$ is followed by reloading in tension with $\tilde{\mathbf{E}}^+$.

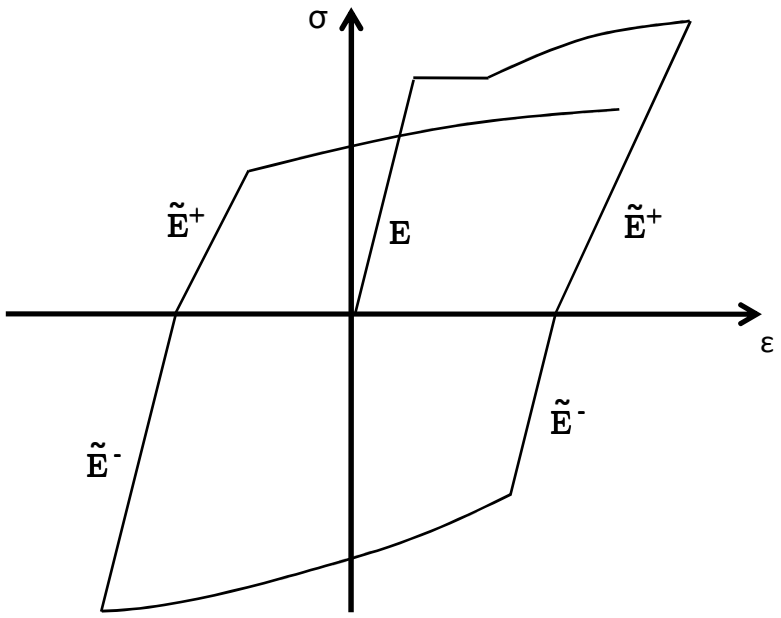

Figure 4.10: Stiffness under tension and compression

Differences between the influence of damage on the description of the yield surface under tensile and compressive stress states are assumed to be negligible. The yield surface depends on the amount of hardening and damage but does not account for the influence of damage due to different loading directions. Thus, in case of compression, hardening develops for stress states exceeding the yield surface while the evolution of damage is disabled.

Damage threshold surface

The inconsistency of evolution laws of internal variables, which depend on the accumulated plastic strain, also applies to the damage evolution law. The accumulated plastic strain does not include a memory of the strain loading path. Thus, after a sufficient number of cycles, cyclic loading with small amplitudes leads to the same amount of accumulated plastic strain as cyclic loading with big amplitudes after a few cycles only. While the model assigns the same amount of damage in both cases due to the dependance of damage on the accumulated plastic strains, experiments have shown that small numbers of cycles with big amplitudes are related to earlier failure than big numbers of cycles with small amplitudes. The absence of a strain memory for damage can only be partially compensated by the dependance of the damage evolution equation on the active accumulated plastic strain. Therefore, a damage threshold surface is additionally included within this work. Since large cyclic straining is crucial for the evolution of damage under earthquakes, the extension is aimed at a differentiation between small and large strain amplitudes.
Damage thresholds are a common method in order to prevent damage evolution at small strains. They are meaningful not only for cyclic loading but also for monotonic loading since experiments have shown that nucleation of cavities does not occur below a certain amount of plastic strain. However, the available formulations for damage thresholds differ widely.
According to Lemaitre [80] and Lemaitre and Chaboche [81] damage thresholds and damage initiation criteria can depend on plastic strain, accumulated plastic strain, or stress and may slightly change due to the underlying damage mechanism. For example, a damage threshold p_D can be defined in terms of stress

$$p_D = \varepsilon_D^{in} \, \frac{\sigma_u - \sigma_f}{\sigma_{eq} - \sigma_f} \tag{4.78}$$

with the tensile strength σ_u, the fatigue limit σ_f, and the damage threshold strain parameter ε_D^{in}, leading to the damage initiation criterion

$$p > p_D. \tag{4.79}$$

While this criterion permits damage as soon as the accumulated plastic strain exceeds the plastic strain threshold, which assures damage evolution under small cyclic straining after a sufficient number of cycles, other criteria, which depend on plastic strain or stress,

entirely neglect the incidence of damage for small cyclic strains.
Within this work, the damage threshold surface is defined via the equivalent plastic strain

$$\varepsilon_{eq}^{in} = \sqrt{\frac{2}{3}\left(\langle\varepsilon_{11}^{in}\rangle^2 + \langle\varepsilon_{22}^{in}\rangle^2 + \langle\varepsilon_{33}^{in}\rangle^2 + 2\langle\varepsilon_{12}^{in}\rangle^2 + 2\langle\varepsilon_{13}^{in}\rangle^2 + 2\langle\varepsilon_{23}^{in}\rangle^2\right)} \tag{4.80}$$

where the McAuley brackets only allow positive strains and thus prohibit damage evolution not only under small strains but also under compression. The damage initiation criterion is then given by

$$\begin{aligned} \varepsilon_{eq}^{in} - \varepsilon_{D}^{in} \leq 0 &\longrightarrow \dot{D} = 0 \\ > 0 &\longrightarrow \dot{D} \end{aligned} \tag{4.81}$$

where the scalar ε_D^{in} is the damage threshold strain parameter. While Pirondi and Bonora [112] propose that the damage threshold strain decreases under compression due to the presence of broken inclusions, the damage threshold strain is here assumed to be constant.
The criterion presented in equation (4.80),(4.81) was chosen in order to firstly capture the characteristics of mild construction steel and secondly establish an accurate tool for the description of the material behavior under seismic action. Since mild construction steel S 355 does not show pronounced damage in the form of a continuous reduction of the modulus of elasticity for cyclic loading with small strain amplitudes [73], the model prohibits damage evolution below a certain amount of plastic strain. Thus, fatigue which occurs in connection with many cycles at small strains cannot be captured by the model. However, since fatigue is not the main failure mechanism for structures subjected to earthquakes, it is more important to simulate ductile damage due to irregular large cyclic straining. The chosen criterion enables ductile damage evolution under large strains and thus provides a precise method in order to describe damage evolution under seismic loading.

4.2.6 Thermodynamical consistency

A consistent description of the constitutive and evolution equations for elastic-viscoplastic and damaged material is possible using thermodynamics of irreversible processes (see section 4.1.2). In the following the thermodynamical consistency of the constitutive equations of the material model is proven. Note that the strain memory surface cannot be included in the thermodynamic framework [138].
From the free Helmholtz energy Ψ

$$\Psi(\boldsymbol{\varepsilon}^{el}, r, \boldsymbol{\alpha}, \mathbf{D}) = \frac{1}{2}\boldsymbol{\varepsilon}^{el} : \bar{\mathbf{M}}^{-1} : \mathbf{E} : \bar{\mathbf{M}}^{-1} : \boldsymbol{\varepsilon}^{el} + \frac{1}{2}bQr^2 + \frac{1}{3}aC\boldsymbol{\alpha} : \boldsymbol{\alpha} \tag{4.82}$$

with the internal variables r of isotropic hardening, $\boldsymbol{\alpha}$ of kinematic hardening, and the damage effect tensor $\bar{\mathbf{M}}$ including the internal variables for damage $\mathbf{D}$, follow the

equations of state for $\boldsymbol{\sigma}$, K, $\mathbf{X}$, and $\mathbf{Y}$

$$\boldsymbol{\sigma} = \frac{\partial \Psi}{\partial \boldsymbol{\varepsilon}^{el}} = \bar{\mathbf{M}}^{-1} : \mathbf{E} : \bar{\mathbf{M}}^{-1} : \boldsymbol{\varepsilon}^{el}, \tag{4.83}$$

$$K = \frac{\partial \Psi}{\partial r} = bQr, \tag{4.84}$$

$$\mathbf{X} = \frac{\partial \Psi}{\partial \boldsymbol{\alpha}} = \frac{2}{3} aC\boldsymbol{\alpha}, \tag{4.85}$$

$$\mathbf{Y} = \frac{\partial \Psi}{\partial \mathbf{D}} = \left(\boldsymbol{\varepsilon}^{el} : \frac{\partial \bar{\mathbf{M}}^{-1}}{\partial \mathbf{D}} : \mathbf{E} : \bar{\mathbf{M}}^{-1} : \boldsymbol{\varepsilon}^{el} \right)^{sym}, \tag{4.86}$$

where K is the energetic conjugated force for r, $\mathbf{X}$ is the energetic conjugated force for $\boldsymbol{\alpha}$, and the energy release rate $\mathbf{Y}$ is the energetic conjugated quantity for $\mathbf{D}$. The dissipation potential for viscoplastic material behavior, isotropic and kinematic hardening, and anisotropic ductile and creep damage is given by

$$\phi = \phi^{in}(\boldsymbol{\sigma}, K, \mathbf{X}, \mathbf{Y}; \boldsymbol{\varepsilon}^{el}, r, \boldsymbol{\alpha}, \mathbf{D}) + \phi^{t}(\mathbf{Y}; \boldsymbol{\varepsilon}^{el}, \mathbf{D})$$

with

$$\phi^{in} = \frac{\sigma_p}{n+1} \dot{\varepsilon}_0 \left\langle \frac{\sigma_{ex}}{\sigma_p} \right\rangle^{n+1}, \tag{4.87}$$

$$\phi^{t} = [\mathbf{Q}^* : \mathbf{Y}] \left\langle \frac{\chi(\tilde{\mathbf{E}} : \boldsymbol{\varepsilon}^{\boldsymbol{el}}, \mathbf{D})}{\sigma_K} \right\rangle^{s} \left\langle \frac{\chi(\tilde{\mathbf{E}} : \boldsymbol{\varepsilon}^{\boldsymbol{el}})}{\sigma_K} \right\rangle^{t-s}, \tag{4.88}$$

and the overstress σ_{ex}

$$\begin{aligned}
\sigma_{ex} = \Bigg(& \frac{3}{2} a_1 (\bar{\mathbf{M}} : \boldsymbol{\sigma}^D - \mathbf{X}^D)^T : (\bar{\mathbf{M}} : \boldsymbol{\sigma}^D - \mathbf{X}^D) \\
& + \frac{a_2}{6} tr[\mathbf{D}/3] (\bar{\mathbf{M}} : \boldsymbol{\sigma}^H - \mathbf{X}^H)^T : (\bar{\mathbf{M}} : \boldsymbol{\sigma}^H - \mathbf{X}^H) \Bigg)^{\frac{1}{2}} \\
& - \sigma_y - K + [K - bQr] + \left[bQr - K + \frac{K^2}{2Q} - \frac{b^2 Q}{2} r^2 \right] \frac{1}{1 - tr[\mathbf{D}/3]} \\
& + \left[\frac{3}{4C} \mathbf{X} : \mathbf{X} - \frac{a^2 C}{3} \boldsymbol{\alpha} : \boldsymbol{\alpha} \right] \\
& + [\mathbf{Q}^* : (\mathbf{Y} - \mathbf{Z})] \Bigg((c_1 + c_2 c_3 e^{-c_3 \frac{1}{1 - tr[\mathbf{D}/3]} p^+}) \frac{1}{1 - tr[\mathbf{D}/3]} \\
& + c_4 c_5 \frac{a_1 tr[\mathbf{D}/3] \left\langle tr \left[\bar{\mathbf{M}} : \bar{\mathbf{M}} : \mathbf{S} : \tilde{\mathbf{E}} : \boldsymbol{\varepsilon}^{el} \right] \right\rangle}{6 (\tilde{\mathbf{E}} : \boldsymbol{\varepsilon}^{el})_{eq}} (1 - tr[\mathbf{D}/3]) \Bigg) \frac{\dot{p}^+}{\dot{p}}.
\end{aligned} \tag{4.89}$$

The evolution equations of the state variables $\dot{\boldsymbol{\varepsilon}}^{in}$, $\dot{r}$, $\dot{\boldsymbol{\alpha}}$, and $\dot{\mathbf{D}}$ are obtained by partial derivatives of the dissipation potential ϕ:

$$\dot{\boldsymbol{\varepsilon}}^{in} = \frac{\partial \phi}{\partial \boldsymbol{\sigma}} = \frac{\partial \sigma_{ex}}{\partial \boldsymbol{\sigma}} \dot{\varepsilon}_0 \left\langle \frac{\sigma_{ex}}{\sigma_p} \right\rangle^n , \tag{4.90}$$

$$\dot{r} = -\frac{\partial \phi}{\partial K} = \frac{1 - K/Q}{1 - tr[\mathbf{D}/3]} \dot{p}, \tag{4.91}$$

$$\dot{\boldsymbol{\alpha}} = -\frac{\partial \phi}{\partial \mathbf{X}} = \left(\frac{\partial \sigma_{eq}}{\partial \boldsymbol{\sigma}} - \frac{3}{2C} \mathbf{X} \right) \dot{p}, \tag{4.92}$$

$$\begin{aligned} \dot{\mathbf{D}} = \frac{\partial \phi}{\partial \mathbf{Y}} = \mathbf{Q}^* \Bigg[\Bigg(& (c_1 + c_2 c_3 e^{-c_3 \frac{1}{1 - tr[\mathbf{D}/3]} p^+}) \frac{1}{1 - tr[\mathbf{D}/3]} \\ & + c_4 c_5 \frac{a_1 tr[\mathbf{D}/3] \left\langle tr\left[\bar{\mathbf{M}} : \bar{\mathbf{M}} : \mathbf{S} : \tilde{\mathbf{E}} : \boldsymbol{\varepsilon}^{el} \right] \right\rangle}{6 (\tilde{\mathbf{E}} : \boldsymbol{\varepsilon}^{el})_{eq}} (1 - tr[\mathbf{D}/3]) \Bigg) \dot{p}^+ \\ & + \left\langle \frac{\chi(\boldsymbol{\sigma}, \mathbf{D})}{\sigma_K} \right\rangle^s \left\langle \frac{\chi(\boldsymbol{\sigma})}{\sigma_K} \right\rangle^{t-s} \Bigg] . \end{aligned} \tag{4.93}$$

The model is in agreement with the thermodynamic principles if dissipation is positive. Following equation (4.11), the total dissipation of the material model is given by

$$\rho \Phi = \boldsymbol{\sigma} : \dot{\boldsymbol{\varepsilon}}^{in} - K \dot{r} - \mathbf{X} : \dot{\boldsymbol{\alpha}} - \mathbf{Y} : \dot{\mathbf{D}} - \mathbf{q} \cdot \frac{\nabla T}{T} \geq 0. \tag{4.94}$$

For decoupling of mechanical and thermal dissipation and assuming isothermal and adiabatic processes ($\dot{T} = 0,\ \mathbf{q} = 0$) and an independance of inelastic yielding and damage processes, equation (4.94) can be splitted into

$$\boldsymbol{\sigma} : \dot{\boldsymbol{\varepsilon}}^{in} - K \dot{r} - \mathbf{X} : \dot{\boldsymbol{\alpha}} \geq 0 \qquad \text{and} \qquad - \mathbf{Y} : \dot{\mathbf{D}} \geq 0. \tag{4.95}$$

Dissipation due to damage evolution is always positive since damage is an irreversible process. After inserting the evolution equations of the state variables (equation (4.90)-(4.93)) into the first part of the dissipation inequality (4.95), one obtains

$$\begin{aligned} \Bigg(\boldsymbol{\sigma} : & \frac{\mathbf{R} : \bar{\mathbf{M}} : \mathbf{I} : \bar{\mathbf{M}} : \mathbf{R} : \boldsymbol{\sigma} - \mathbf{R} : \bar{\mathbf{M}} : \mathbf{R} : \mathbf{X}}{\sigma_{eq}} - K \\ & - \mathbf{X} : \left(\frac{\mathbf{R} : \bar{\mathbf{M}} : \mathbf{R} : \boldsymbol{\sigma} - \mathbf{R} : \mathbf{X}}{\sigma_{eq}} - \frac{3}{2C} \mathbf{X} \right) \Bigg) \dot{p} \ \geq 0 \end{aligned} \tag{4.96}$$

$$\Rightarrow \quad \left(\sigma_{eq} - K + \frac{3}{2C} \mathbf{X} : \mathbf{X} \right) \dot{p} \ \geq 0. \tag{4.97}$$

This inequality is fulfilled if the parameter C is positive, since inelastic processes ($\dot{p} > 0$) only occur for

$$\sigma_{eq} - K > 0 \tag{4.98}$$

and $\mathbf{X} : \mathbf{X}$ is always positive.

4.2.7 Summary of material equations

In the following, the equations of state and evolution equations for viscoplastic material behavior with isotropic and kinematic hardening and anisotropic ductile and creep damage are again summarized:

$$\begin{aligned}
\dot{\boldsymbol{\varepsilon}} &= \dot{\boldsymbol{\varepsilon}}^{el} + \dot{\boldsymbol{\varepsilon}}^{in}, \\
\dot{\boldsymbol{\varepsilon}}^{el} &= \frac{\partial}{\partial t}(\bar{\mathbf{M}} : \mathbf{E}^{-1} : \bar{\mathbf{M}} : \boldsymbol{\sigma}), \\
\dot{\boldsymbol{\varepsilon}}^{in} &= \frac{\partial \sigma_{ex}}{\partial \boldsymbol{\sigma}} \dot{\varepsilon}_0 \left\langle \frac{\sigma_{ex}}{\sigma_p} \right\rangle^n, \\
\dot{K} &= \frac{b(Q-K)}{1 - tr[\mathbf{D}/3]} \dot{p}, \\
\dot{\mathbf{X}} &= a \left(\frac{2}{3} C \frac{\partial \sigma_{eq}}{\partial \boldsymbol{\sigma}} - \mathbf{X} \right) \dot{p}, \\
\dot{\mathbf{D}} &= \mathbf{Q}^* \left[\left((c_1 + c_2 c_3 e^{-c_3 \frac{1}{1-tr[\mathbf{D}/3]} p^+}) \frac{1}{1 - tr[\mathbf{D}/3]} \right.\right. \\
&\quad \left.\left. + c_4 c_5 \frac{a_1 tr[\mathbf{D}/3] \left\langle tr\left[\bar{\mathbf{M}} : \bar{\mathbf{M}} : \mathbf{S} : \tilde{\mathbf{E}} : \boldsymbol{\varepsilon}^{el} \right] \right\rangle}{6 (\tilde{\mathbf{E}} : \boldsymbol{\varepsilon}^{el})_{eq}} (1 - tr[\mathbf{D}/3]) \right) \dot{p}^+ \right. \\
&\quad \left. + \left\langle \frac{\chi(\boldsymbol{\sigma}, \mathbf{D})}{\sigma_K} \right\rangle^s \left\langle \frac{\chi(\boldsymbol{\sigma})}{\sigma_K} \right\rangle^{t-s} \right],
\end{aligned}$$

with the inelastic strain rate

$$\dot{p} = \dot{\varepsilon}_0 \left\langle \frac{\sigma_{ex}}{\sigma_p} \right\rangle^n, \quad \dot{p}^+ = \dot{p} \left\langle \frac{J_1}{|J_1|} \right\rangle,$$

the strain memory surface

$$M = \frac{2}{3} (\boldsymbol{\varepsilon}^{in} - \boldsymbol{\beta})(\boldsymbol{\varepsilon}^{in} - \boldsymbol{\beta}) - q^2 = 0,$$

and the damage threshold surface

$$\sqrt{\frac{2}{3} \left(\langle \varepsilon_{11}^{in} \rangle^2 + \langle \varepsilon_{22}^{in} \rangle^2 + \langle \varepsilon_{33}^{in} \rangle^2 + 2\langle \varepsilon_{12}^{in} \rangle^2 + 2\langle \varepsilon_{13}^{in} \rangle^2 + 2\langle \varepsilon_{23}^{in} \rangle^2 \right)} - \varepsilon_D^{in} = 0.$$

The damage evolution equation considers both ductile and creep damage. In the following, the range of application for ductile and creep damage is investigated. The influence of separately and coupled applied laws for creep and ductile damage on the material behavior is studied in [146]. Creep and tensile tests are evaluated in order to investigate the operating conditions for creep and ductile damage. The results are shown in figure 4.11. For creep tests it is found that for stress states below the yield stress of the material creep damage is crucial while above the yield stress the description of the material behavior can be approximated by means of ductile damage. For tensile tests it is concluded that creep damage appropriately describes the behavior at strain rates smaller than $\dot{\varepsilon} = 10^{-4}s^{-1}$, while ductile damage should be used for strain rates bigger than $\dot{\varepsilon} = 10^{-1}s^{-1}$. In the transition zone coupled creep and ductile damage can be applied.

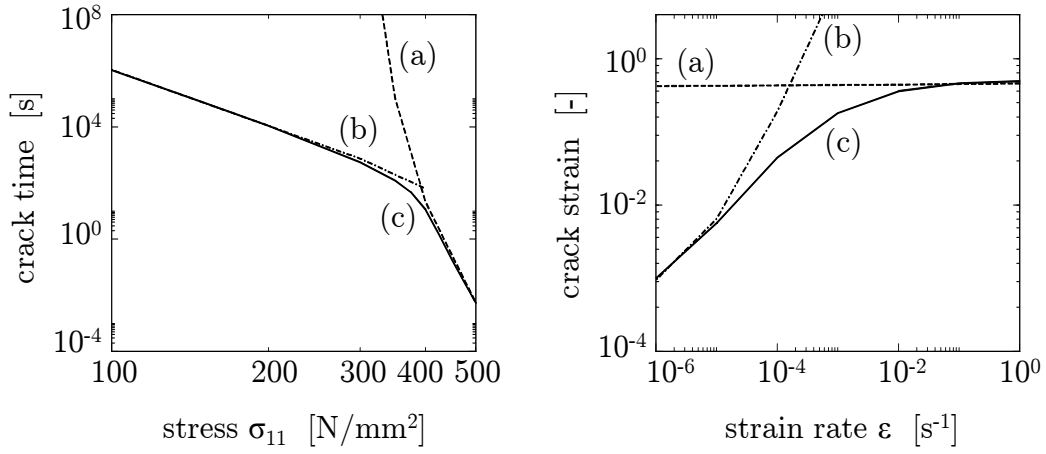

Figure 4.11: Influence of separately and coupled applied laws for creep and ductile damage for a creep and a tensile test (a) ductile, (b) creep, (c) coupled

Due to the consideration of viscoplasticity, it is possible to describe creep damage with strain dependent ductile damage [80]. The following investigations therefore use the combination of viscoplasticity and ductile damage in order to model creep damage.

4.3 Nonlocal extension

Since softening and damage are always accompanied by energy dissipation, inelastic effects, and high strain gradients which accumulate in small areas of undefined width, called process zones, local damage models suffer from a dependency on the fineness of finite-element discretization, because the element size serves as a length that determines the dimension of the process zones. Increasing fineness of discretization would lead to a damage process taking place in an evanescent volume without dissipation, which is physically impossible. Mathematically, the problem becomes ill-posed since the differential equations loose their elliptic form in the static case and their hyperbolic form in the dynamic case, respectively, and the acoustic tensor of the tangential stiffness tensor becomes singular [80, 95]. A material-dependent internal length scale needs to be defined in order to determine the size of the process zone, regularize the solution, and create an independence of the finite-element discretization.
The problem of localization is already mentioned in e.g. [9, 10]. Since then, a large variety of different non-local extensions is proposed, e.g. [77, 94, 41], in order to prevent the boundary value problem from becoming ill-posed. Thereby, the models can be applied to concrete [106] as well as to steel [116]. An extension by random fluctuations of material behavior is among others studied by Kowalsky et al. [69] and Colliat et al. [32]. An overview of the current state of the art for different non-local extensions may be found in [11, 63]. Cosserat [36], for example, proposes the theory of polar continua which includes additional parameters to define the width of the process zone. Leppin [83] and Wells et al. [141] apply a discontinuous finite-element method in order to take into account localization. Non-local integral models are based on weighting and averaging of local variables in an area defined by an internal length in order to build non-local variables. Bazant et al. [12], for example, apply the non-local integral approach to the equivalent strain. Due to the high complexity in implementing non-local integral models into finite-element code, gradient formulations are proposed.
In contrast to strain gradient models, which include the gradient of the strain field into the material equations [47], the kinematics and the equilibrium equation remain unchanged when using models with gradients of internal variables. Liebe and Steinmann, for example, incorporate the gradient of the internal variable for isotropic hardening into a thermodynamically consistent formulation at small strains [84]. Peerlings et al. [105] and Engelen et al. [44] show the derivation of models with gradients of internal variables from non-local integral models and differentiate between explicit and implicit gradient models.
This work examines the use of a non-local implicit gradient model in order to define the width of the damage process zone. By means of an additional gradient equation which contains the parameter of the internal length, non-local substitutes of the local variables can be obtained. Adapted from integral models, an arbitrary non-local variable $\bar{k}(\mathbf{x})$ in a material point $\mathbf{x}$ is defined as the weighted mean value of the local variables $k(\mathbf{y})$ of all material points in an area Ω

$$\bar{k}(\mathbf{x}) = \frac{1}{\Phi(\mathbf{x})} \int_{\Omega} \phi(\mathbf{y}; \mathbf{x}, l) k(\mathbf{y}) d\Omega \tag{4.99}$$

where $\mathbf{y}$ is the position vector of the volume Ω, $\phi(\mathbf{y};\mathbf{x},l)$ is the weight function, and $\Phi(\mathbf{x})$ is the scale function [44]. Possible weight functions are for example the Gaussian distribution, the Green's function, or polynomial functions. The length l determines the size of the volume which builds the non-local variable and is a parameter dependent on the microstructure of the material. The non-local integral formulation is consistent, because it contains the local continuum for $l \to 0$. Since the implementation of non-local integral models leads to complex changes of the finite-element code, gradient formulations may be applied. Gradient formulations can be developed from a Taylor series of $k(\mathbf{y})$ from equation (4.99)

$$k(\mathbf{y}) = k(\mathbf{x}) + \frac{\partial k}{\partial x_i}(y_i - x_i) + \frac{1}{2!}\frac{\partial^2 k}{\partial x_i \partial y_i}(y_i - x_i)(y_j - x_j) + \frac{1}{3!}\frac{\partial^3 k}{\partial x_i \partial x_j \partial x_k}(y_i - x_i)(y_j - x_j)(y_k - x_k) + ... \tag{4.100}$$

where Einstein's summation convention applies to the indices i, j, and k. Substituting this series in equation (4.99) and solving the integral leads to

$$\bar{k}(\mathbf{x}) = k(\mathbf{x}) + c(l)\nabla^2 k(\mathbf{x}) + d(l)\nabla^4 k(\mathbf{x}) + ... \tag{4.101}$$

with $\nabla^2 = \sum_i \frac{\partial^2}{\partial x_i^2}$ and $\nabla^{2n} = (\nabla^2)^n$. The odd derivatives vanish due to the symmetry of the weight functions. Neglecting terms of fourth and higher order leads to

$$\bar{k}(\mathbf{x}) = k(\mathbf{x}) + c(l)\nabla^2 k(\mathbf{x}) \tag{4.102}$$

which is called explicit gradient formulation [44], since the non-local field $\bar{k}$ is directly obtained from the local field k. An enhancement can be achieved by an implicit gradient approach. Applying the Laplace operator to equation (4.101) leads to

$$\nabla^2 \bar{k}(\mathbf{x}) = \nabla^2 k(\mathbf{x}) + c(l)\nabla^4 k(\mathbf{x}) + ... \ . \tag{4.103}$$

If the derivatives of higher order of the local variable are multiplied by $c(l)$ and then subtracted from the right side of equation (4.101) one obtains

$$\bar{k}(\mathbf{x}) - c(l)\nabla^2 \bar{k}(\mathbf{x}) = k(\mathbf{x}) + [d(l) - c(l)^2]\nabla^4 k(\mathbf{x}) + ... \ . \tag{4.104}$$

Neglecting the terms of high order, starting with $[d(l) - c(l)^2]\nabla^4 k(\mathbf{x}) = 0$, results in the implicit gradient approach

$$\bar{k}(\mathbf{x}) - c(l)\nabla^2 \bar{k}(\mathbf{x}) = k(\mathbf{x}) \tag{4.105}$$

with $c(l) = l_c^2$. This implicit formulation of equation (4.99) is a partial differential equation of the Helmholtz type with respect to the non-local variable $\bar{k}$. Engelen et al. [44] show that equation (4.105) can be obtained even without neglecting the terms of high order if the Green's function is used as weight function. Using the Green's function as weight function leads to $d(l) - c(l)^2 = 0$, so that all terms with differences of coefficient

pairs will vanish.
Here, gradients of the damage variable are used [146, 119]. The non-local damage variable $\bar{D}$ is obtained by the gradient equation

$$\bar{D} - l_c^2 \nabla^2 \bar{D} = D \tag{4.106}$$

with the local damage variable D and the material-specific internal length l_c. Equation (4.106) can be assumed to be time-independent since the spatial propagation of the nonlocal damage variable $\bar{D}$ is very fast compared to the evolution of the other variables.

In the following, two examples are investigated in order to visualize the phenomenon of localization and the regularization due to the non-local extension. Figure 4.12 presents the distribution of total strain ε, plastic strain ε^{in}, and non-local damage $\bar{D}$ in a bar under constant tension for different timesteps. With an imposed imperfection by means of a reduction of the yield stress in the middle of the bar, localization of deformation can be observed. Neglecting the regularization by a non-local extension would lead to mesh-dependent results and a discontinuity in the centre of the bar for finer discretizations.

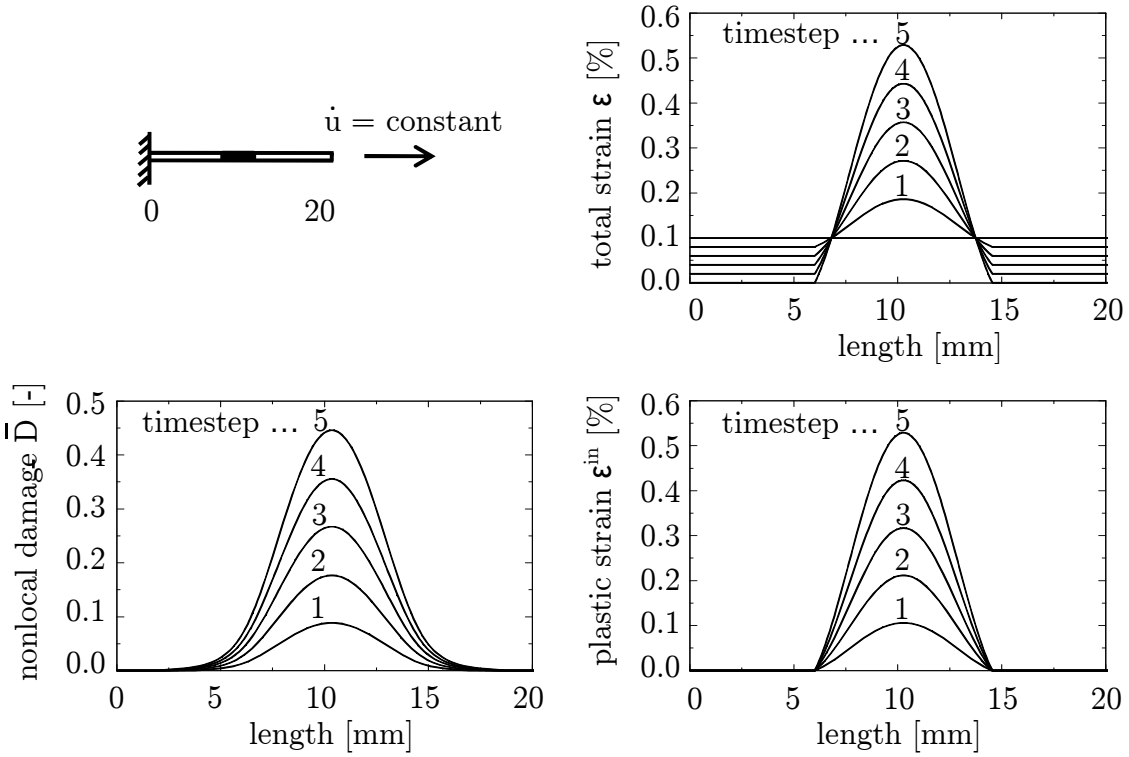

Figure 4.12: Distribution of total strain, plastic strain, and non-local damage in a bar under constant tension velocity for different timesteps

Figure 4.13 demonstrates the influence of different internal length scales and different discretizations. Therefore, a rectangular plate with constant thickness of $t = 1$ mm

under increasing tension is investigated considering different FE-discretizations of 224, 1456, and 5824 9-node plate elements. The internal length scales are set to 0.25, 0.5, and 1 mm, whereby the finest mesh size is still larger than the biggest internal length. As imperfection a small central part of the plate has a slightly lower yield stress than the rest of the plate. An elastic end-restraint is obtained by an increase of the yield stress at the boundary elements. The resulting stresses may exceed the yield stress due to the concept of overstresses. The stress-displacement curve shows that firstly, the results depend strongly on the choice of the internal length and secondly, the results are almost independent of the discretization. However, it can be observed that there is a connection between the choice of the internal length and the choice of discretization. The smaller the internal length, the bigger is the influence of discretization. This is due to the fact that the largest deviation between internal length and discretization emerges in the case of $l_c = 0.25$ mm. Therefore, the discretization needs to be chosen in consideration of the internal length. Based on [20], it is proposed that the internal length should exceed the element length in order to eliminate any error induced by an inappropriate ratio between internal length and discretization.

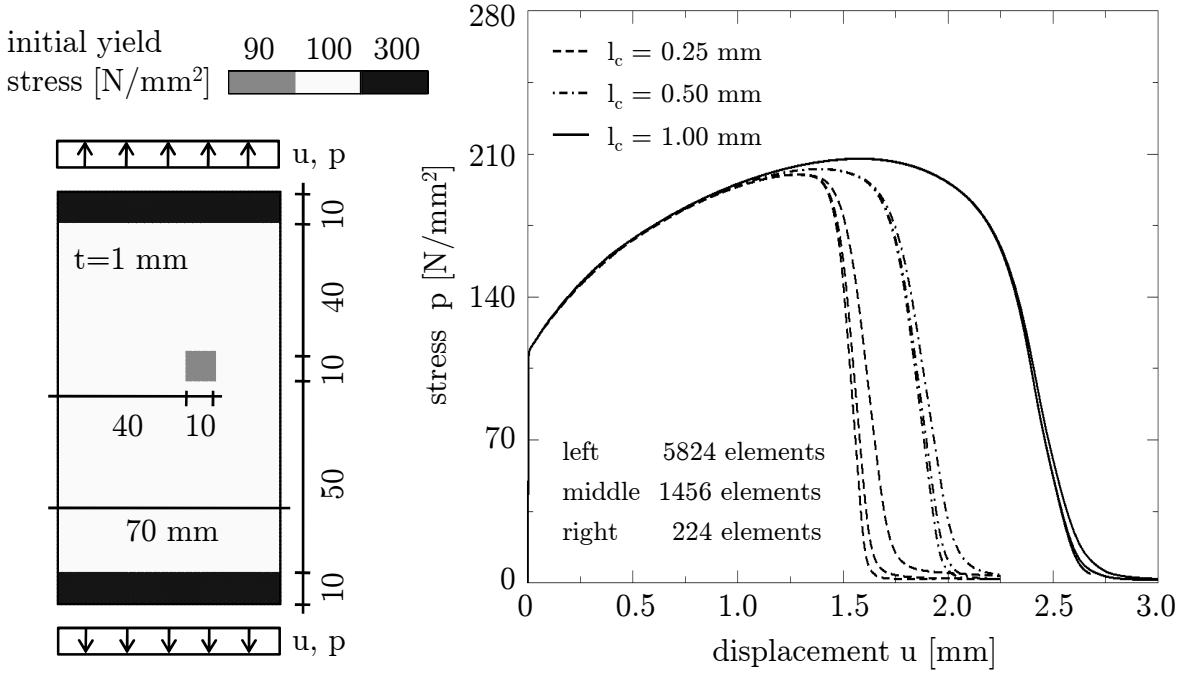

Figure 4.13: Stress-displacement diagrams for different internal length scales and FE-discretizations of a plate under tension [139]

The formation of shear bands for the different internal length scales and a discretization with 1456 elements is presented in figure 4.14. The upper row shows the deformation while the lower row depicts the distribution of damage. The link between the width of the localization zone and the internal length is clearly visible.

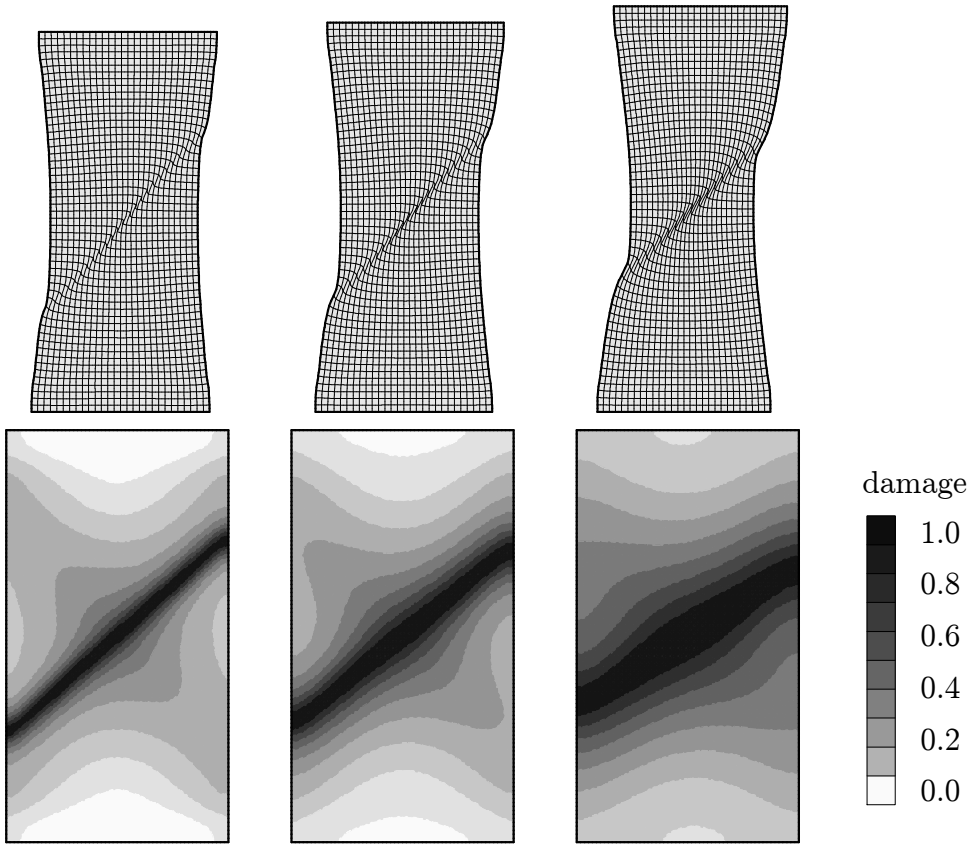

(a) lc=0.25 (b) lc=0.50 (c) lc=1.00

Figure 4.14: Distribution of damage for different internal length scales and FE-discretizations of a plate under tension [146]

A difficulty arises from the determination of the additional parameter of the internal length. This length scale cannot be directly measured but can be indirectly inferred by inverse analysis of test results. In order to reliably identify the internal length, the underlying experiments have to be sensitive to the non-local aspects of the material behavior. Carmeliet [20] proposes an inverse method based on the Markov estimation procedure which yields the most accurate parameter estimations if applied to local displacement analysis close to the crack. In concrete, the internal length can be derived from crack spacing in reinforced members [100]. An overview of other methods, like the size effect method, can be found in [11], but they all base on extensive experimental investigations.

Current research deals with evolving internal length scales. Voyiadjis et al. [140] propose that internal length scales may evolve under monotonic loading due to the change in contact surface between particles, damage of the particles or/and change in the local void ratio within the domain that will change the shearband thickness. Kanvinde &

Deierlein [67] pose the question if the internal length for cyclic loading is the same as the internal length for monotonic loading. Without further investigations concerning the necessity of evolving internal length scales, however, they propose the use of a constant internal length.

4.4 Summary of equations

In the following, all equations of continuum mechanics are summarized which are embedded into the model for further investigations. The compacted model considers elastic-viscoplastic material behavior, isotropic and kinematic hardening with a strain memory surface, isotropic ductile damage, and the nonlocal implicit gradient extension. The modeling of ductile damage includes extensions concerning the description of damage under cyclic loading, different stiffnesses under tension and compression, and a damage threshold surface. Creep damage is neglected since it is possible to describe creep damage with strain dependend ductile damage [80] due to the consideration of viscoplasticity. It is assumed that damage occurs locally but acts nonlocally. The effective damage $\bar{D}$ is obtained via the gradient equation which averages the local damage. The integrated amount of nonlocal, effective damage equals the integrated amount of local damage.

Balance of linear momentum

$$\rho\ddot{\mathbf{u}} + c\dot{\mathbf{u}} - \nabla\boldsymbol{\sigma} - \mathbf{p} = 0$$

Gradient equation

$$\bar{D} - l_c^2\nabla^2\bar{D} - D = 0$$

Elasticity

$$\dot{\boldsymbol{\varepsilon}}^{el} = \frac{1}{(1-\bar{D})^2}\mathbf{E}^{-1} : \dot{\boldsymbol{\sigma}}$$

Viscoplasticity

$$\begin{aligned}
\dot{\boldsymbol{\varepsilon}} &= \dot{\boldsymbol{\varepsilon}}^{el} + \dot{\boldsymbol{\varepsilon}}^{in} \\
\dot{\boldsymbol{\varepsilon}}^{in} &= \frac{\partial\sigma_{ex}}{\partial\boldsymbol{\sigma}}\dot{p} \\
\dot{p} &= \dot{\varepsilon}_0 \left\langle \frac{\sigma_{ex}}{\sigma_p} \right\rangle^n, \quad \dot{p}^+ = \dot{p}\left\langle \frac{J_1}{|J_1|} \right\rangle
\end{aligned}$$

with

$$\sigma_{ex} = \frac{1}{1-\bar{D}}\sqrt{a_1 \cdot \frac{3}{2} tr((\boldsymbol{\sigma}-\mathbf{X})^D \cdot (\boldsymbol{\sigma}-\mathbf{X})^D) + a_2\bar{D} \cdot tr(\boldsymbol{\sigma}-\mathbf{X}) \cdot tr(\boldsymbol{\sigma}-\mathbf{X})} - \sigma_y - K$$

Isotropic hardening

$$\dot{K} = b(Q - K)\frac{1}{1-\bar{D}}\dot{p}$$

Kinematic hardening

$$\dot{\mathbf{X}} = a\left(\frac{2}{3}C\frac{\partial\sigma_{eq}}{\partial\boldsymbol{\sigma}} - \mathbf{X}\right)\dot{p}$$

Ductile damage

$$\dot{D} = (c_1 + c_2 e^{-c_3\frac{1}{(1-\bar{D})}p^+})\frac{1}{(1-\bar{D})}\dot{p}^+ + c_5(c_4 - \bar{D})\left\langle tr\left(\frac{\partial\sigma_{ex}}{\partial\boldsymbol{\sigma}}\dot{p}^+\right)\right\rangle$$

Strain memory surface

$$M = \frac{2}{3}(\boldsymbol{\varepsilon}^{in} - \boldsymbol{\beta})(\boldsymbol{\varepsilon}^{in} - \boldsymbol{\beta}) - q^2 = 0$$

Damage threshold surface

$$\sqrt{\frac{2}{3}\left(\langle\varepsilon_{11}^{in}\rangle^2 + \langle\varepsilon_{22}^{in}\rangle^2 + \langle\varepsilon_{33}^{in}\rangle^2 + 2\langle\varepsilon_{12}^{in}\rangle^2 + 2\langle\varepsilon_{13}^{in}\rangle^2 + 2\langle\varepsilon_{23}^{in}\rangle^2\right)} - \varepsilon_D^{in} = 0.$$

4.5 Global damage assessment

The constitutive equations given in the last chapters describe the evolution of damage at every single material point. The damage variables D lie within a range of 0 and 1 and can be visualized as the ratio of damaged area to total area. The damage distribution allows the identification of weak structural parts and crack initiation. However, a global statement about the overall structural condition cannot be derived yet. Due to that reason, a global damage index is developed, which is based on damage variables, summarizes their influence, and leads to only one single statement about the global structural stability. This global damage index, here abbreviated with GDI, ideally has a range of 0 to 1 where 0 corresponds to the undamaged state before the incidence of a hazard and a value of 1 relates to the collapse of a structure.
Chapter 2.4 already gives an overview of different index definitions. In the following, three global damage indices are presented and evaluated using a cantilever with a length of 5 meters and a rectangular cross-section with an edge length of 100 x 300 mm. For the sake of simplicity, deteriorated material is prescribed using three different values of damage D and four different damage locations with different volume portions under assumption of a constant damage distribution over the cross-section. The advantages and disadvantages of the three indices for the description of global structural integrity are demonstrated.

Global damage indicator GDI_I

The first damage indicator GDI_I considers the amount and portion of damaged material:

$$GDI_I = \frac{\sum V_i \cdot D_i}{\sum V_i} \tag{4.107}$$

where V_i is a volume and D_i is the amount of damage assigned to that volume. An overview of this damage index for different damage scenarios of the cantilever is given in table 4.1. This index only makes a statement about the amount and severity of damaged material but does not provide information about the position of damage. For the case of completely damaged material (D=1.0) in a small zone close to the base (1 vol-%), which would cause the structure to collapse entirely, the index only reaches a value of 0.01. Thus, the index does not represent global failure but quantifies the amount of material which has to be repaired.

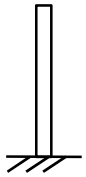	D=0.1	D=0.5	D=1.0
1 vol-% at the base	0.001	0.005	0.01
10 vol-% at the base	0.01	0.05	0.1
10 vol-% in the middle	0.01	0.05	0.1
100 vol-%	0.1	0.5	1.0

Table 4.1: Overview of results for the global damage index GDI_I

Global damage indicator GDI_{II}

The second group of indices to be evaluated is based on the change of modal parameters. Krätzig and Petryna [72], DiPasquale et al. [43], and others propose different formulations for global damage indices based on eigenvalue decompositions of the stiffness matrix or the stiffness and the mass matrix. The stiffness matrix is a suitable assemblage of structural damage information since it preserves the influence of damage. Two different eigenvalue problems may be considered:

$$\left[\mathbf{K} - \lambda^2 \mathbf{I}\right] \mathbf{v} = \mathbf{0} \tag{4.108}$$

$$\left[\mathbf{K} - \omega^2 \mathbf{M}\right] \mathbf{v} = \mathbf{0} \tag{4.109}$$

where $\mathbf{I}$ is the identity matrix, $\mathbf{M}$ is the mass matrix, $\mathbf{K}$ is either the initial secant stiffness matrix $\mathbf{K}_0$ or the secant stiffness matrix $\mathbf{K}_t$ at time t following figure 4.15, λ and ω are the eigenvalues, and $\mathbf{v}$ the corresponding eigenvectors. Under consideration of the i'th eigenvalue the eigenvalue problems

$$\left[\mathbf{K}_0 - \lambda_{0,i}^2 \mathbf{I}\right] \mathbf{v}_{0,i} = \mathbf{0} \quad , \quad \left[\mathbf{K}_t - \lambda_{t,i}^2 \mathbf{I}\right] \mathbf{v}_{t,i} = \mathbf{0} \tag{4.110}$$

and

$$\left[\mathbf{K}_0 - \omega_{0,i}^2 \mathbf{M}\right] \mathbf{v}_{0,i} = \mathbf{0} \quad , \quad \left[\mathbf{K}_t - \omega_{t,i}^2 \mathbf{M}\right] \mathbf{v}_{t,i} = \mathbf{0} \tag{4.111}$$

lead to global damage indices GDI_{II} defined as

$$GDI_{II,\lambda,i} = 1 - \frac{\lambda_{t,i}^2}{\lambda_{0,i}^2} \tag{4.112}$$

$$GDI_{II,\omega,i} = 1 - \frac{\omega_{t,i}^2}{\omega_{0,i}^2} \tag{4.113}$$

which lie in the range of zero to one.

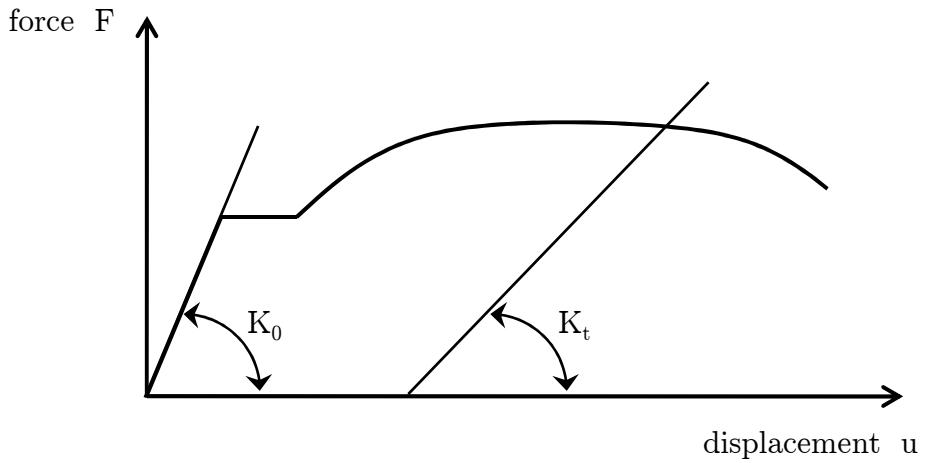

Figure 4.15: The initial stiffness matrix K_0 and the current stiffness matrix K_t for the definition of the global damage index

The computation of both global damage indices for the cantilever for different damage scenarios using either equation (4.112) or (4.113) yields equal results, since the damage information is contained in the stiffness matrix which is present in both formulations. The use of either mass matrix or identity matrix leads to different eigenvalues but equal ratios of damaged to undamaged eigenvalue. Therefore, the results presented in table 4.2 only show the outcomes using equation (4.113). In order to evaluate indices depending on higher eigenfrequencies, the first three eigenfrequencies are considered.

First of all, it can be seen that the index GDI_{II} reaches a value of one as soon as one single part is completely damaged. The position of the completely damaged part is of no consequence. With increasing amount of damage, the index represents the growth of the global damage level. Inducing a higher volume percentage of damaged material at the base leads to an increase of the global damage index. If damage occurs at the base, the first eigenvalue is most crucial for the description of the global damage state.
Remarkable results are achieved by prescribing damaged material in the middle of the

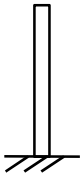	eigenvalue	D=0.1	D=0.5	D=1.0
1 vol-% at the base	1	0.009	0.106	1.0
	2	0.009	0.096	1.0
	3	0.009	0.088	1.0
10 vol-% at the base	1	0.076	0.513	1.0
	2	0.051	0.271	1.0
	3	0.036	0.201	1.0
10 vol-% in the middle	1	0.008	0.090	1.0
	2	0.046	0.362	1.0
	3	0.007	0.297	1.0
100 vol-%	1	0.190	0.750	1.0
	2	0.190	0.750	1.0
	3	0.190	0.750	1.0

Table 4.2: Overview of results for the global damage index GDI_{II}

cantilever. The global damage index based on the first eigenvalue is reduced as expected. The crucial index is now based on the second eigenvalue. This is due to the fact that the second eigenmode is of higher frequency. Critical positions of damaged material, which strongly influence the global behavior of this mode, do not only occur at the base, but also at other locations. Those locations can be identified by means of the eigenmode's curvature. Figure 4.16 depicts the second eigenvector of the cantilever with its slope and curvature normalized to one. Additionally, the global damage index based on the second eigenvalue $\mathrm{GDI}_{II,2}$ is presented. The calculation of the index assumes 10 vol-% of damage $D = 0.5$. The vertical axis specifies the location of the damaged section while the horizontal axis presents the corresponding value of the GDI_{II}. In figure 4.16 it can be seen that the index depends on the curvature, since high values of the index occur if the curvature is strong which is represented by high absolute curvature values. From this observation it follows, that the selection of the number of eigenvalues for the accurate description of global damage has to consider the location of damage. Eigenmodes, which show strong curvature at this location, should be included in the global damage calculation. However, in civil engineering practice, not every eigenmode with high curvature at this location has to be included, since only the first few modes are crucial for the global behavior. High-frequency modes are strongly damped, contain little energy, and thus do not need to be considered. Krätzig and Petryna [72] investigate damage measures obtained from the first, second, and third eigenvalue. They find that this limited number of modes can deliver sufficiently good damage estimates [111] and that in most cases the most crucial one is the first eigenvalue.

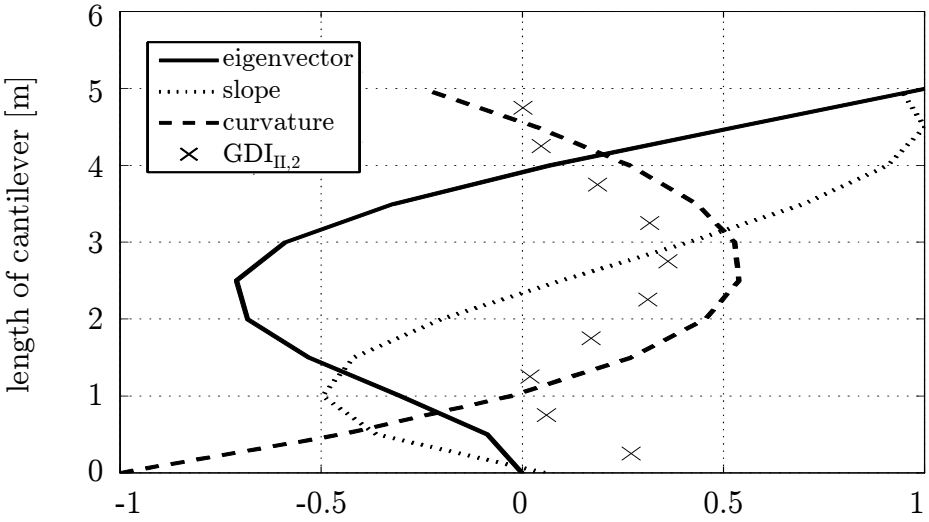

Figure 4.16: Second eigenvector of the cantilever with its slope and curvature (normalized to one) in comparison with the global damage index $\mathrm{GDI}_{II,2}$ based on the second eigenvector for a damaged segment with the size of 10 vol-% and an amount of damage $D = 0.5$ which is shifted from the base to the top

Global damage indicator GDI_{III}

The global damage index GDI_{II} investigated in the last preceding paragraphs is not capable of considering correctly the location of damage with only one eigenmode. Additionally, the index yields one as soon as one random part is completely damaged ($D = 1.0$). This drawback will be overcome by a newly defined global damage index GDI_{III}, which takes into account information contained in the eigenvalue as well as in the eigenvector.

The index GDI_{III} is based on the eigenvalue decomposition

$$\left[\mathbf{K}_t - \lambda_{t,i}^2 \mathbf{K}_0\right] \mathbf{v}_{t,i} = \mathbf{0}. \tag{4.114}$$

This eigenvalue problem results in eigenvalues λ_t which exactly specify the amounts of damage occurred in single parts of the structure. The first eigenvalue represents the maximum amount of damage. The eigenvectors $\mathbf{v}_t$ represent a movement of those structural parts which are damaged or which are moved due to damage of other parts. Thereby, only the first eigenvector is crucial for the description of the global behavior. For further investigations, the eigenvectors are normalized to one. Figure 4.17 shows first eigenvectors of a cantilever for different damage scenarios. Damage at the top of the cantilever, for example, leads to no movement of the bottom part which is reflected in figure 4.17c. Damage at the bottom of the cantilever will cause all parts of the structure to move (see figure 4.17a). The global damage index GDI_{III}, which only bases on the

first eigenmode, consists of two parts

$$GDI_{III} = (1 - \lambda_t) \cdot \frac{||\mathbf{M}\mathbf{v}_t||}{||\mathbf{M}\mathbf{v}_{ref}||} \tag{4.115}$$

where the first part considers the maximum amount of damage by $1 - \lambda_t$ and the second part takes into account the position of damage. The position of damage is determined by the norm of the product of mass matrix and eigenvector in order to represent the amount of displaced mass. In order to compare the amount of displaced mass due to a certain damage $||\mathbf{M}\mathbf{v}_t||$, it is divided by the amount of displaced mass due to a fully damaged structure $||\mathbf{M}\mathbf{v}_{ref}||$ (see figure 4.17e for $\mathbf{v}_{ref}$).

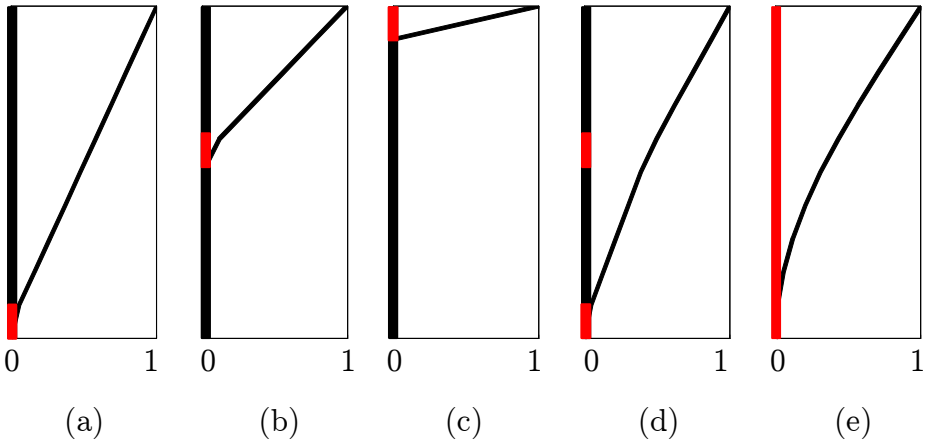

Figure 4.17: First eigenvectors of the eigenvalue problem given in equation 4.114 for different damage scenarios (the location and spread of damage is marked in red)

The combination of both amount of damage and location of damage leads to the results of the global damage index presented in table 4.3. First of all, it can be seen that the amount of damage D is reflected well in the index. If D increases, also the index GDI_{III} increases. Secondly, the consideration of a bigger damage volume at the base leads to a reduced value of the index. This is contradictory to the previously defined index GDI_{II} but is justifiable. Damage in a small area is more hazardous than distributed damage since subsequent loads and deformations lead to a concentration of damage evolution in this predamaged area. A small predamaged section leads to damage localization which is connected with imminent failure. The newly defined index GDI_{III} considers this fact. Thirdly, the index accurately takes into account reduced global damage if the position of damage is shifted to less critical locations, namely from the bottom towards the top for the cantilever. While the crucial damage index $\text{GDI}_{II} = 0.362$ was based on the second eigenvalue for 10 % volume damage with $D = 0.5$ in the middle of the cantilever, the newly defined global damage index yields a value of $\text{GDI}_{III} = 0.3876$ being based on the first eigenvalue. For 100 % volume damage the index reflects precisely the amount of

damage D. Another characteristic of this index is that the index can exceed the value of 1 for high amounts of damage at critical locations. This results from the second part of index $\frac{||\mathbf{M}\mathbf{v}_t||}{||\mathbf{M}\mathbf{v}_{ref}||}$, which increases the maximum amount of damage $1 - \lambda_t$ if damage occurs at critical locations. The index can then be rounded down to one, since the expressiveness of the global damage index for practical problems is thereby not detracted. Additionally, the index is capable of reaching values smaller than 1 even if the material is completely damaged ($D = 1.0$) at a single location which is not critical for the overall collapse.

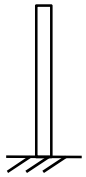	D=0.1	D=0.5	D=1.0
1 vol-% at the base	0.1205	0.6027	1.0000
10 vol-% at the base	0.1176	0.5882	1.0000
10 vol-% in the middle	0.0775	0.3874	0.7749
100 vol-%	0.1000	0.5000	1.0000

Table 4.3: Overview of results for the global damage index GDI_{III}

Practical significance of the global damage indicators

The global damage indices defined and evaluated within the last preceding paragraphs enable to assess the condition of structures subjected to seismic events. In the following, the practical significance of the indices is evaluated.

First of all, the global damage indices can be related to damage states. Different proposals are made in [72, 142, 49, 35]. While the limits between the damage states differ slightly, they agree in the general segmentation. The first segment comprises no or minor damage and goes up to index values between $0.11 - 0.33$. Apparent damage which is still repairable occurs up to values between $0.3 - 0.66$ followed by irreparable damage and structural collapse. The inconsistency of the limits is due to the calibration to different testing schemes and materials. It is remarkable that the upper limit of the global damage index with a value of 1.0 was found to be only of theoretical nature.

In the following, the previously defined indices GDI_{II} and GDI_{III} are related to damage states. Since the index GDI_I only represents the amount and volume of damage but does not provide a sufficient measure for global structural stability, it is not addressed any further. Due to the fact that the indices are not calibrated using experimental data, the proposals are based on theoretical observations. For the index GDI_{II} the following proposal is made, which is also based on a segmentation into three parts:

$$\begin{array}{rlll} & \mathrm{GDI}_{II} & < 0.1 & \text{light damage, serviceable} \\ 0.1 \leq & \mathrm{GDI}_{II} & < 0.25 & \text{severe damage, repairable} \\ 0.25 \leq & \mathrm{GDI}_{II} & < 1.0 & \text{irreparable or collapsed} \end{array}$$

The transitions from light to severe damage and from severe damage to collapse result from global damage index calculations. The basis for the calculations is a certain amount of damage D of 5 volume-% at the base, since this location is the most critical location for cantilevers. The amount of damage D which specifies these transitions is derived from values in literature. While rupture theoretically occurs for $D = 1.0$, experiments show that material failure already appears for values $D < 1.0$ [52]. Following [80], rupture starts to occur for $D = 0.2 - 0.5$ depending on the material. Under consideration of ductile fracture, the transition from damage to collapse is here set to $D = 0.4$. The transition from light to severe damage is assumed to be at $D = 0.2$.
Applying the same preconditions for the third index GDI_{III} leads to

$$\begin{array}{rlll} & \mathrm{GDI}_{III} & < 0.24 & \text{light damage, serviceable} \\ 0.24 \leq & \mathrm{GDI}_{III} & < 0.48 & \text{severe damage, repairable} \\ 0.48 \leq & \mathrm{GDI}_{III} & < 1.0 & \text{irreparable or collapsed} \end{array}$$

Compared to the index GDI_{III}, it can be seen that small values of the global damage index GDI_{II} are already related to high damage states. This means that the eigenfrequency of a structure does not significantly change before the structure collapses. Additionally, the index GDI_{II} is very sensitive to the portion of damaged volume. The transition values of the index GDI_{III} are not sensitive to the portion of damaged volume and correspond well to the transitions proposed by Ghobarah for steel structures [49].

Moreover, the global damage indices can be used to calculate structural risk of a certain earthquake by multiplying the index with the probability of occurrence of the seismic event. The definition of the probability of occurrence is not objective of this thesis and thus should be included in the information accompanying the employed acceleration records. Structural risk is measured in damage per time and can be implicated in structural life time estimations. In general, the life time (LT) of a structures bases on a critical value of global damage D_{cr} divided by structural risk as the amount of damage (GDI) that occurs within a specified time

$$\mathrm{LT} = \frac{D_{cr}}{\mathrm{GDI/time}}. \tag{4.116}$$

Using equation 4.116, the life time of a structure can be calculated no matter what event has caused damage. Therefore, it is also possible to combine different damaging effects. Table 4.4 exemplarily shows residual life time estimates for different fictitious impacts with $D_{cr} = 1.0$. It can be seen that earthquakes, which do not strongly affect a structure on its own, become an important issue in combination with other deteriorating effects.

In the following, structural risk and life time estimations are derived for the Great Hanshin earthquake. The Great Hanshin earthquake occurred in Japan in 1995 with a

Parameter	LT $= D_{cr}/\sum$(GDI/time)
Damage due to normal loads GDI/time $= 0.03$/year	LT $= 33.3$ years
Damage due to earthquake GDI/time $= 0.1/10$years	LT $= 100$ years
Damage due to normal loads and earthquake $\sum$(GDI/time) $= 0.01$/year $+ 0.03$/year	LT $= 25$ years

Table 4.4: Life time estimates for different fictitious impacts

magnitude of 6.9 and had an intensity of XI-XII on the Modified Mercalli scale in the area of the city Kobe. In Japan, earthquakes with magnitudes equal or larger than 6.9 take place in average every $15 - 20$ years. According to researchers on active faults, the fault that caused the Kobe earthquake would become active every 1000 to 2000 years. Here it is assumed that the probability of recurrence for such an earthquake in the area of Kobe is 1/1000 years. Referring to the index GDI_{III}, the critical amount of damage for an irreparable or collapsed state is $D_{cr} = 0.48$. Thus, structural risk and life time estimates for steel structures in Kobe can be calculated with the model proposed within this work. With the calculated global damage index GDI_{III} and the occurrence probability the structural risk is

$$\text{structural risk} = \mathrm{GDI}_{III} \cdot 0.001 \quad [1/\text{year}] \; . \tag{4.117}$$

The life time if only damage due to that kind of earthquakes is assumed is

$$\mathrm{LT} = \frac{0.48}{\mathrm{GDI}_{III} \cdot 0.001} \quad [\text{year}] \tag{4.118}$$

and the reduction of life time with damage D summarizing damage due to other effects is

$$\Delta\mathrm{LT} = \frac{0.48}{\mathrm{D} \cdot 0.001} - \frac{0.48}{\mathrm{D} \cdot 0.001 + \mathrm{GDI}_{III} \cdot 0.001} \quad [\text{year}] \; . \tag{4.119}$$

Calculations of the GDI_{III} for structures subjected to the Kobe earthquake can be found in chapter 7.

5 Numerical implementation

The stress-displacement analysis represents an initial-boundary-value-problem. It contains coupled partial differential equations in space and time, which describe the equation of motion, the gradient equation, the kinematics, and the material equations. The analytical solution of the differential equations with application to engineering problems is often not possible. Therefore, numerical methods need to be implemented. After transformation of the differential equations into equivalent weak integral formulations, the finite-element method is used in order to accomplish spatial discretization of the equation of motion and the gradient equation. Discretization in time of the equation of motion is obtained by the Newmark method. The time dependent evolution equations of the material are discretized using the implicit Euler approach. In the following the applied integration methods are briefly described.

Finite-element method
The finite-element method is one of the most popular methods in order to accomplish spatial discretization. Detailed information can be found in literature [3, 2, 8, 145]. Within the framework of the finite-element-method, the total area is decomposed into several subareas. In every subarea, denoted as element, the distribution of the unknown values is approximated by ansatz functions in dependance on node values. The ansatz functions have to correspond to the continuity requirements.

The distribution of the unknown displacements $\mathbf{u}_{(\xi)}$ of the equation of motion and of the unknown nonlocal damage $\bar{\mathbf{D}}_{(\xi)}$ of the gradient equation follows from

$$\mathbf{u}_{(\boldsymbol{\xi})} = \sum \mathbf{N}_{(\boldsymbol{\xi})} \mathbf{u} \tag{5.1}$$

$$\bar{\mathbf{D}}_{(\boldsymbol{\xi})} = \sum \mathbf{N}_{(\boldsymbol{\xi})} \bar{\mathbf{D}} \tag{5.2}$$

where $\mathbf{N}$ are the ansatz functions, $\mathbf{u}$ or $\bar{\mathbf{D}}$ respectively are the unknown node values of displacement and nonlocal damage, and $\boldsymbol{\xi}$ is the local coordinate within the element. Within this work, 27-node elements with quadratic shape functions are used for 3D-structural analysis.
The field of strains $\boldsymbol{\varepsilon}$ follows from the gradient of the displacement field as the product of the node values $\mathbf{u}$ and the spatial gradient of the ansatz functions $\nabla\mathbf{N}$

$$\boldsymbol{\varepsilon} = \sum \nabla\mathbf{N}\mathbf{u} = \sum \mathbf{B}\mathbf{u} \tag{5.3}$$

while the gradient of the nonlocal damage field $\nabla\bar{\mathbf{D}}$ is given by the product of the node values $\bar{\mathbf{D}}$ and the ansatz functions $\nabla\mathbf{N}$

$$\nabla\bar{\mathbf{D}} = \sum \nabla\mathbf{N}\bar{\mathbf{D}} = \sum \mathbf{B}\bar{\mathbf{D}}. \tag{5.4}$$

Newmark method

The equation of motion and the gradient equation do not only have to be discretized in space but also in time. Since time developments of the gradient equation are assumed to occur very fast in comparison with the equation of motion, only the latter has to be discretized in time. A variety of different integration schemes exists. Zienkiewicz and Taylor [145], for instance, give an overview. Widely used for the solution of structural dynamic problems for seismic loading is the Newmark method [96]. Strictly speaking, the Newmark method is a family of methods due to integration parameters which can be diversified in order to adapt the method to certain requirements. Within this work, the Newmark method is used in order to solve the equation of motion, which is here given as

$$\mathbf{m}\ddot{\mathbf{u}}_{i+1} + \mathbf{c}\dot{\mathbf{u}}_{i+1} + \mathbf{k}\mathbf{u}_{i+1} = \mathbf{f}_{i+1} \tag{5.5}$$

with mass matrix $\mathbf{m}$, acceleration $\ddot{\mathbf{u}}$, damping matrix $\mathbf{c}$, velocity $\dot{\mathbf{u}}$, stiffness matrix $\mathbf{k}$, displacement $\mathbf{u}$, and loads $\mathbf{f}$ at time $i+1$. An extended Taylor approximation is made for the displacement

$$\mathbf{u}_{i+1} = \mathbf{u}_i + \Delta t \cdot \dot{\mathbf{u}}_i + \Delta t^2 \cdot \left[\beta \cdot \ddot{\mathbf{u}}_{i+1} + \left(\frac{1}{2} - \beta\right) \cdot \ddot{\mathbf{u}}_i\right] \tag{5.6}$$

where the approximation is stopped after the second derivative of the displacement, and for the velocity

$$\dot{\mathbf{u}}_{i+1} = \dot{\mathbf{u}}_i + \Delta t \cdot (\gamma \cdot \ddot{\mathbf{u}}_{i+1} + (1-\gamma) \cdot \ddot{\mathbf{u}}_i) \tag{5.7}$$

where the approximation is stopped after the first derivative of the velocity. The subscript i denotes known variables at time i while $i+1$ denotes unknown variables at time $i+1$. The integration parameters β and γ define the approximation functions of the variables and serve for controlling numerical stability. For $\beta = 0$ or $\gamma = 0$ respectively, one obtains the normal Taylor approximation.
After inserting equation (5.6) in equation (5.7), solving for $\ddot{\mathbf{u}}_{i+1}$ and $\dot{\mathbf{u}}_{i+1}$

$$\ddot{\mathbf{u}}_{i+1} = \frac{1}{\beta\Delta t^2} \cdot (\mathbf{u}_{i+1} - \mathbf{u}_i) - \frac{1}{\beta\Delta t} \cdot \dot{\mathbf{u}}_i - \left(\frac{1}{2\beta} - 1\right) \cdot \ddot{\mathbf{u}}_i \tag{5.8}$$

$$\dot{\mathbf{u}}_{i+1} = \frac{\gamma}{\beta\Delta t}(\mathbf{u}_{i+1} - \mathbf{u}_i) + \left(1 - \frac{\gamma}{\beta}\right) \dot{\mathbf{u}}_i + \Delta t \left(1 - \frac{\gamma}{2\beta}\right) \ddot{\mathbf{u}}_i \tag{5.9}$$

and inserting equation (5.8) and (5.9) into equation (5.5), one obtains after rearranging

$$\begin{aligned}\left(\frac{1}{\beta\Delta t^2}\mathbf{m} + \frac{\gamma}{\beta\Delta t}\mathbf{c} + \mathbf{k}\right)\mathbf{u}_{i+1} = \mathbf{f}_{i+1} &+ \mathbf{m}\left(\frac{1}{\beta\Delta t^2}\mathbf{u}_i + \frac{1}{\beta\Delta t}\dot{\mathbf{u}}_i + (1 - \frac{1}{2\beta})\ddot{\mathbf{u}}_i\right) \\ &+ \mathbf{c}\left(\frac{\gamma}{\beta\Delta t}\mathbf{u}_i - (1 - \frac{\gamma}{\beta})\dot{\mathbf{u}}_i - \Delta t(1 - \frac{\gamma}{2\beta})\ddot{\mathbf{u}}_i\right)\end{aligned} \tag{5.10}$$

which can be used to calculate the unknown displacement vector $\mathbf{u}_{i+1}$ of the new time step. Subsequently, the acceleration and velocity vector of the new time step can be obtained using equation (5.8) and (5.9).

The factors γ and β of the Newmark method control the numerical stability and the order of the approximation functions for the unknowns of the equation of motion. For

$$\gamma \geq \frac{1}{2}, \beta \geq \frac{\gamma}{2} \tag{5.11}$$

the approach is unconditionally stable [13]. Within this work, the parameters are set to $\gamma = \frac{1}{2}, \beta = \frac{\gamma}{2}$ which leads to an order of consistency of one [59] and the approach of constant mean acceleration. The order of convergence of the Newmark method is two.

Besides the integration parameters, the time-step width Δt influences the accuracy of the solution. Thereby, the time-step width always has to be seen in connection with the vibration period T of the smallest vibration mode which contributes to a correct description of the structural response. In Bathe [8] it can be found that the Newmark method is characterized by a conservation of amplitude but an elongation of vibration period in dependance on the ratio $\frac{T}{\Delta t}$ provided that the integration parameters are set to $\gamma = \frac{1}{2}, \beta = \frac{\gamma}{2}$. For a percental period elongation smaller than 3% the ratio between the period and the time-step width has to be $\frac{T}{\Delta t} > 10$.
While a ratio of $\frac{T}{\Delta t} = 5$ may be sufficient for structural systems with linear material behavior, Bathe [8] recommends to use ratios up to $\frac{T}{\Delta t} = 200$ for complex systems with nonlinear material behavior.

Implicit Euler approach
The material equations are time-dependent ordinary differential equations of first order which are solved within this work with the collocation approach which yields the implicit Euler approach for $\xi = 1$. The numerical solution of the initial value problem

$$\dot{x} = f(t, x) \ , \quad x(t_0) = x_0 \tag{5.12}$$

is obtained by

$$x_{i+1} = x_i + \xi \Delta t f(t_{i+\xi}, x_{i+\xi}) \tag{5.13}$$

where ξ is the collocation position, Δt is the time-step width of discretization, and i is the control variable running over the time steps Δt. The order of convergence of the implicit Euler approach is one.

In the course of this work, the evolution equations of the material need to be solved in time. The discretization in time transforms the differential equations of the material into an incremental formulation. In the following, the material residuals $\Delta \mathbf{r}_M = \{\Delta \mathbf{r}_{\boldsymbol{\varepsilon}}, \Delta r_p, \Delta r_p^+, \Delta r_K, \Delta \mathbf{r}_{\mathbf{X}}, \Delta r_D, \Delta r_q, \Delta \mathbf{r}_\beta\}$ are assorted in their incremental formulation in dependance on the collocation variable ξ. For the sake of simplicity, the residuals

Δr_K, $\Delta \mathbf{r}_{\mathbf{X}}$, Δr_D ,Δr_q, and $\Delta \mathbf{r}_\beta$ are summarized to residuals of internal variables $\Delta \mathbf{r}_{\mathbf{V}_i}$:

$$\Delta \mathbf{r}_{\boldsymbol{\varepsilon}} = \Delta\boldsymbol{\varepsilon} - \mathbf{E}(\mathbf{V}_{i+\xi}) : \boldsymbol{\sigma}_{i+\xi} + \mathbf{E}(\mathbf{V}_i) : \boldsymbol{\sigma}_i - \frac{\partial \sigma_{eq}}{\partial \boldsymbol{\sigma}}_{i+\xi} \Delta p = \mathbf{0}, \tag{5.14}$$

$$\Delta r_p = \Delta p - \dot{p}(\boldsymbol{\sigma}_{i+\xi}, \mathbf{V}_{i+\xi})\Delta t = 0, \tag{5.15}$$

$$\Delta r_p^+ = \Delta p^+ - \dot{p}^+(\boldsymbol{\sigma}_{i+\xi}, \mathbf{V}_{i+\xi})\Delta t = 0, \tag{5.16}$$

$$\Delta r_{\mathbf{V}_i} = \Delta \mathbf{V}_i - \dot{\mathbf{V}}(\boldsymbol{\sigma}_{i+\xi}, \mathbf{V}_{i+\xi})\Delta t = \mathbf{0}. \tag{5.17}$$

Here, the implicit Euler approach is applied, which means that ξ is set to 1.
In order to solve the material residuals $\Delta \mathbf{r}_M$ for the unknown increments of the material variables $\Delta \mathbf{z} = \{\Delta\boldsymbol{\sigma}, \Delta p, \Delta p^+, \Delta K, \Delta \mathbf{X}, \Delta D, \Delta q, \Delta\boldsymbol{\beta}\}$ an elastic predictor is applied which calculates a test stress

$$\boldsymbol{\sigma}^{test} = \boldsymbol{\sigma}_i + \mathbf{E}(\mathbf{V}_i)\Delta\boldsymbol{\varepsilon} \tag{5.18}$$

based on the predetermined strain increment $\Delta\boldsymbol{\varepsilon}$. If the over-stress including the test stress is zero or negative, the material behaves elastically and only $\Delta\boldsymbol{\sigma}$ is different from zero. If the test stress is followed by a positive over-stress, the material behaves inelastically and all material variables are affected. The material equations represent a nonlinear system of equations which is solved with the Newton-Raphson-method. During the integration of the material equations the total strains remain constant. The linearized equation system

$$\mathbf{J}\Delta\Delta\mathbf{z} = -\Delta\mathbf{r}_M \tag{5.19}$$

$$\Rightarrow \begin{bmatrix} \frac{\partial \Delta \mathbf{r}_{\boldsymbol{\varepsilon}}}{\partial \Delta \boldsymbol{\sigma}} & \frac{\partial \Delta \mathbf{r}_{\boldsymbol{\varepsilon}}}{\partial \Delta p} & \frac{\partial \Delta \mathbf{r}_{\boldsymbol{\varepsilon}}}{\partial \Delta p^+} & \frac{\partial \Delta \mathbf{r}_{\boldsymbol{\varepsilon}}}{\partial \Delta K} & \frac{\partial \Delta \mathbf{r}_{\boldsymbol{\varepsilon}}}{\partial \Delta \mathbf{X}} & \frac{\partial \Delta \mathbf{r}_{\boldsymbol{\varepsilon}}}{\partial \Delta D} & \frac{\partial \Delta \mathbf{r}_{\boldsymbol{\varepsilon}}}{\partial \Delta q} & \frac{\partial \Delta \mathbf{r}_{\boldsymbol{\varepsilon}}}{\partial \Delta \boldsymbol{\beta}} \\ \frac{\partial \Delta r_p}{\partial \Delta \boldsymbol{\sigma}} & \frac{\partial \Delta r_p}{\partial \Delta p} & \frac{\partial \Delta r_p}{\partial \Delta p^+} & \frac{\partial \Delta r_p}{\partial \Delta K} & \frac{\partial \Delta r_p}{\partial \Delta \mathbf{X}} & \frac{\partial \Delta r_p}{\partial \Delta D} & \frac{\partial \Delta r_p}{\partial \Delta q} & \frac{\partial \Delta r_p}{\partial \Delta \boldsymbol{\beta}} \\ \frac{\partial \Delta r_p^+}{\partial \Delta \boldsymbol{\sigma}} & \frac{\partial \Delta r_p^+}{\partial \Delta p} & \frac{\partial \Delta r_p^+}{\partial \Delta p^+} & \frac{\partial \Delta r_p^+}{\partial \Delta K} & \frac{\partial \Delta r_p^+}{\partial \Delta \mathbf{X}} & \frac{\partial \Delta r_p^+}{\partial \Delta D} & \frac{\partial \Delta r_p^+}{\partial \Delta q} & \frac{\partial \Delta r_p^+}{\partial \Delta \boldsymbol{\beta}} \\ \frac{\partial \Delta r_K}{\partial \Delta \boldsymbol{\sigma}} & \frac{\partial \Delta r_K}{\partial \Delta p} & \frac{\partial \Delta r_K}{\partial \Delta p^+} & \frac{\partial \Delta r_K}{\partial \Delta K} & \frac{\partial \Delta r_K}{\partial \Delta \mathbf{X}} & \frac{\partial \Delta r_K}{\partial \Delta D} & \frac{\partial \Delta r_K}{\partial \Delta q} & \frac{\partial \Delta r_K}{\partial \Delta \boldsymbol{\beta}} \\ \frac{\partial \Delta \mathbf{r}_{\mathbf{X}}}{\partial \Delta \boldsymbol{\sigma}} & \frac{\partial \Delta \mathbf{r}_{\mathbf{X}}}{\partial \Delta p} & \frac{\partial \Delta \mathbf{r}_{\mathbf{X}}}{\partial \Delta p^+} & \frac{\partial \Delta \mathbf{r}_{\mathbf{X}}}{\partial \Delta K} & \frac{\partial \Delta \mathbf{r}_{\mathbf{X}}}{\partial \Delta \mathbf{X}} & \frac{\partial \Delta \mathbf{r}_{\mathbf{X}}}{\partial \Delta D} & \frac{\partial \Delta \mathbf{r}_{\mathbf{X}}}{\partial \Delta q} & \frac{\partial \Delta \mathbf{r}_{\mathbf{X}}}{\partial \Delta \boldsymbol{\beta}} \\ \frac{\partial \Delta r_D}{\partial \Delta \boldsymbol{\sigma}} & \frac{\partial \Delta r_D}{\partial \Delta p} & \frac{\partial \Delta r_D}{\partial \Delta p^+} & \frac{\partial \Delta r_D}{\partial \Delta K} & \frac{\partial \Delta r_D}{\partial \Delta \mathbf{X}} & \frac{\partial \Delta r_D}{\partial \Delta D} & \frac{\partial \Delta r_D}{\partial \Delta q} & \frac{\partial \Delta r_D}{\partial \Delta \boldsymbol{\beta}} \\ \frac{\partial \Delta r_q}{\partial \Delta \boldsymbol{\sigma}} & \frac{\partial \Delta r_q}{\partial \Delta p} & \frac{\partial \Delta r_q}{\partial \Delta p^+} & \frac{\partial \Delta r_q}{\partial \Delta K} & \frac{\partial \Delta r_q}{\partial \Delta \mathbf{X}} & \frac{\partial \Delta r_q}{\partial \Delta D} & \frac{\partial \Delta r_q}{\partial \Delta q} & \frac{\partial \Delta r_q}{\partial \Delta \boldsymbol{\beta}} \\ \frac{\partial \Delta \mathbf{r}_\beta}{\partial \Delta \boldsymbol{\sigma}} & \frac{\partial \Delta \mathbf{r}_\beta}{\partial \Delta p} & \frac{\partial \Delta \mathbf{r}_\beta}{\partial \Delta p^+} & \frac{\partial \Delta \mathbf{r}_\beta}{\partial \Delta K} & \frac{\partial \Delta \mathbf{r}_\beta}{\partial \Delta \mathbf{X}} & \frac{\partial \Delta \mathbf{r}_\beta}{\partial \Delta D} & \frac{\partial \Delta \mathbf{r}_\beta}{\partial \Delta q} & \frac{\partial \Delta \mathbf{r}_\beta}{\partial \Delta \boldsymbol{\beta}} \end{bmatrix} \begin{bmatrix} \Delta\Delta\boldsymbol{\sigma} \\ \Delta\Delta p \\ \Delta\Delta p^+ \\ \Delta\Delta K \\ \Delta\Delta \mathbf{X} \\ \Delta\Delta D \\ \Delta\Delta q \\ \Delta\Delta\boldsymbol{\beta} \end{bmatrix} = - \begin{bmatrix} \Delta \mathbf{r}_{\boldsymbol{\varepsilon}} \\ \Delta r_p \\ \Delta r_p^+ \\ \Delta r_K \\ \Delta \mathbf{r}_{\mathbf{X}} \\ \Delta r_D \\ \Delta r_q \\ \Delta \mathbf{r}_{\boldsymbol{\beta}} \end{bmatrix} \tag{5.20}$$

with Jacobian matrix $\mathbf{J}$ leads to increments of the material variables $\Delta\Delta\boldsymbol{\sigma}$, $\Delta\Delta p$, $\Delta\Delta p^+$, $\Delta\Delta K$, $\Delta\Delta \mathbf{X}$, $\Delta\Delta D$, $\Delta\Delta q$, and $\Delta\Delta\boldsymbol{\beta}$ where the first Δ stands for the time step increment and the second Δ for the iteration increment.

In the following the numerical implementation of the model is shown using the integration methods described in the previous paragraphs.

5.1 Weak formulation

The balance equations of continuum mechanics allow the analysis of moving continuous bodies. In order to solve the differential equations, they have to be transformed into equivalent integral equations leading to a weak formulation. The transition from the differential equation to the equivalent weak formulation is achieved by the principle of virtual work.
The first equation which has to be transformed is the equation of motion (see equation (4.4)) in the region Ω

$$\rho\ddot{\mathbf{u}} + c\dot{\mathbf{u}} - \nabla\boldsymbol{\sigma} - \mathbf{p} = 0 \tag{5.21}$$

with either Dirichlet boundary condition $\bar{\mathbf{u}}$ or Neumann boundary condition $\bar{\mathbf{t}}$ on the boundary $\partial\Omega$

$$\bar{\mathbf{u}} - \mathbf{u} = \mathbf{0} \qquad \text{and} \qquad \bar{\mathbf{t}} - \boldsymbol{\sigma}\cdot\mathbf{n} = \mathbf{0}. \tag{5.22}$$

Its weak form is obtained by the principle of virtual work

$$\int_\Omega \delta\mathbf{u}(\rho\ddot{\mathbf{u}} + c\dot{\mathbf{u}} - \nabla\boldsymbol{\sigma} - \mathbf{p})d\Omega = 0. \tag{5.23}$$

Assuming linear kinematics $\boldsymbol{\varepsilon} = \nabla\mathbf{u}$ and including the boundary conditions

$$\int_\Omega \delta\mathbf{u}\rho\ddot{\mathbf{u}}d\Omega + \int_\Omega \delta\mathbf{u}c\dot{\mathbf{u}}d\Omega + \int_\Omega \delta\boldsymbol{\varepsilon} : \boldsymbol{\sigma}d\Omega = \int_\Omega \delta\mathbf{u}\cdot\mathbf{p}d\Omega + \int_{\partial\Omega} \delta\mathbf{u}\cdot\bar{\mathbf{t}}d\partial\Omega \tag{5.24}$$

equation (5.24) allows a simple physical interpretation. The integrals on the left side represent inner work of the real forces on the virtual displacements while the integrals on the right side describe outer work of the external loading on the virtual displacements.

The second equation which has to be transformed is the gradient equation (see equation (4.106))

$$\bar{D} - l_c^2\nabla^2\bar{D} - D = 0 \tag{5.25}$$

with Neumann boundary condition

$$\nabla\bar{D} = \bar{t}_{\bar{D}}. \tag{5.26}$$

The weak form

$$\int_\Omega \delta\bar{Y}(\bar{D} - l_c^2\nabla^2\bar{D} - D)d\Omega = 0 \tag{5.27}$$

is obtained using the virtual nonlocal energy release rate $\delta\bar{Y}$, which is the conjugated quantity to the nonlocal damage variable. Including the boundary condition, the weak form is given by

$$\int_\Omega \delta\bar{Y}\bar{D}d\Omega - \int_\Omega \delta\bar{Y}Dd\Omega - \int_\Omega \delta\bar{Y}l_c^2\nabla^2\bar{D}d\Omega = \int_\Omega \delta\bar{Y}l_c^2\bar{t}_{\bar{D}}d\Omega. \tag{5.28}$$

During analysis the natural boundary condition $\bar{t}_{\bar{D}} = 0$ is used.

5.2 Spatial discretization

For spatially solving the equation of motion and the gradient equation the finite-element method is applied. For the real and virtual variables the same ansatz functions are used (see equation (5.1)-(5.4)). After inserting the ansatz functions into the weak form of the equation of motion (5.24) and the weak form of the gradient equation (5.28) one obtains the element virtual works

$$\begin{aligned}\delta A_{e,\mathbf{u}} = \delta\mathbf{u} \Bigg(&\int_{\Omega_e} \mathbf{N}^T \rho \mathbf{N} d\Omega_e \; \ddot{\mathbf{u}} + \int_{\Omega_e} \mathbf{C} d\Omega_e \; \dot{\mathbf{u}} + \int_{\Omega_e} \mathbf{B}^T : \boldsymbol{\sigma} d\Omega_e \\ &- \int_{\Omega_e} \mathbf{N}^T \cdot \mathbf{p} d\Omega_e - \int_{\partial\Omega_e} \mathbf{N}^T \cdot \bar{\mathbf{t}} d\partial\Omega_e \Bigg), \end{aligned} \tag{5.29}$$

$$\delta A_{e,\bar{D}} = \delta\bar{Y} \left(\int_{\Omega_e} \mathbf{N}^T \mathbf{N} \bar{D} - \mathbf{N}^T D + l_c^2 \mathbf{B}^T \mathbf{B} \bar{D} \; d\Omega_e - l_c^2 \int_{\partial\Omega_e} \mathbf{N}^T t_{\bar{D}} \; d\partial\Omega_e \right). \tag{5.30}$$

The system virtual work as the sum over all element virtual works is zero for arbitrary virtual variables $\delta\mathbf{u}$ and $\delta\bar{Y}$ which leads to the residual of the equation of motion $\mathbf{r}_\mathbf{u}$ and the residual of the gradient equation $\mathbf{r}_{\bar{D}}$

$$\begin{aligned}\mathbf{r}_\mathbf{u} = \sum \Bigg(&\int_{\Omega_e} \mathbf{N}^T \rho \mathbf{N} d\Omega_e \; \ddot{\mathbf{u}} + \int_{\Omega_e} \mathbf{C} d\Omega_e \; \dot{\mathbf{u}} + \int_{\Omega_e} \mathbf{B}^T : \boldsymbol{\sigma} d\Omega_e \\ &- \int_{\Omega_e} \mathbf{N}^T \cdot \mathbf{p} d\Omega_e - \int_{\partial\Omega_e} \mathbf{N}^T \cdot \bar{\mathbf{t}} d\partial\Omega_e \Bigg) = \mathbf{0} \end{aligned} \tag{5.31}$$

$$\mathbf{r}_{\bar{D}} = \sum \left(\int_{\Omega_e} \mathbf{N}^T \mathbf{N} \bar{D} - \mathbf{N}^T D + l_c^2 \mathbf{B}^T \mathbf{B} \bar{D} \; d\Omega_e - l_c^2 \int_{\partial\Omega_e} \mathbf{N}^T t_{\bar{D}} \; d\partial\Omega_e \right) = 0. \tag{5.32}$$

The damping given in equation (5.31) is proportional to the velocity. Velocity proportional damping is referred to as viscous damping, which depends on damping parameters. For finite-element calculations it is very hard if not impossible to determine single element damping parameters so that the damping matrix is composed of mass and stiffness matrix in connection with a limited number of experimentally obtained damping values. The derivation of this approach is based on the description of a dynamic system in the modal form and assigns a certain damping to every vibration mode. Considering two damping parameters, one obtains Rayleigh-damping, which is used within this work. The damping matrix is then defined as

$$\sum \left(\int_{\Omega_e} \mathbf{C} d\Omega_e \right) = c_\alpha \mathbf{M} + c_\beta \mathbf{K} \tag{5.33}$$

where $\mathbf{M}$ is the mass matrix, $\mathbf{K}$ is the stiffness matrix

$$\mathbf{M} = \sum \left(\int_{\Omega_e} \mathbf{N}^T \rho \mathbf{N} d\Omega_e \right),$$

$$\mathbf{K} = \sum \left(\int_{\Omega_e} \mathbf{B}^T : \boldsymbol{\sigma} d\Omega_e \right),$$

and c_α and c_β are parameters which control the influence of the mass matrix and the stiffness matrix, respectively, on damping. For $c_\alpha = 0$ one obtains stiffness proportional damping while $c_\beta = 0$ refers to mass proportional damping. For continuous systems the parameters c_α and c_β can be obtained by two known eigenfrequencies ω_i and their damping ratios ϑ_i [110]. For the first two eigenfrequencies one obtains

$$c_\alpha = 2\frac{\omega_2\vartheta_1 - \omega_1\vartheta_2}{\omega_2^2 - \omega_1^2}\omega_1\omega_2, \tag{5.34}$$

$$c_\beta = 2\frac{\omega_2\vartheta_2 - \omega_1\vartheta_1}{\omega_2^2 - \omega_1^2}, \tag{5.35}$$

for the determination of the parameters c_α and c_β of Rayleigh damping.

5.3 Discretization in time

Equations (5.31) and (5.32) now need to be solved in time. As already stated, the gradient equation is assumed to develop very fast compared to the equation of motion. Thus, a time integration scheme only needs to be considered for equation (5.31). Here, the Newmark method is used [8]. After inserting equation (5.8) and (5.9) into the residual of the equation of motion (5.31) and rearrangement, one obtains

$$\begin{aligned}\mathbf{r_u} = \sum \Bigg(&\frac{1}{\beta\Delta t^2}\int_{\Omega_e} \mathbf{N}^T\rho\mathbf{N}d\Omega_e\ \mathbf{u}_{i+1} + \frac{\gamma}{\beta\Delta t}\int_{\Omega_e}\mathbf{C}d\Omega_e\ \mathbf{u}_{i+1} + \int_{\Omega_e}\mathbf{B}^T : \boldsymbol{\sigma}_{i+1}d\Omega_e \\ &- \int_{\Omega_e}\mathbf{N}^T\cdot\mathbf{p}_{i+1}d\Omega_e - \int_{\Omega_e}\mathbf{N}^T\rho\mathbf{N}d\Omega_e\left(\frac{1}{\beta\Delta t^2}\mathbf{u}_i + \frac{1}{\beta\Delta t}\dot{\mathbf{u}}_i + (\frac{1}{2\beta}-1)\ddot{\mathbf{u}}_i\right) \\ &- \int_{\Omega_e}\mathbf{C}d\Omega_e\left(\frac{\gamma}{\beta\Delta t}\mathbf{u}_i + (\frac{\gamma}{\beta}-1)\dot{\mathbf{u}}_i + \Delta t(\frac{\gamma}{2\beta}-1)\ddot{\mathbf{u}}_i\right) - \int_{\partial\Omega_e}\mathbf{N}^T\cdot\bar{\mathbf{t}}_{i+1}d\partial\Omega_e\Bigg) = \mathbf{0}.\end{aligned} \tag{5.36}$$

The incremental formulation of both residuals $\Delta\mathbf{r_u}$ and $\Delta\mathbf{r}_{\bar{D}}$ results in

$$\begin{aligned}\Delta\mathbf{r_u} = \sum \Bigg(&\frac{1}{\beta\Delta t^2}\int_{\Omega_e}\mathbf{N}^T\rho\mathbf{N}d\Omega_e\ \Delta\mathbf{u} + \frac{\gamma}{\beta\Delta t}\int_{\Omega_e}\mathbf{C}d\Omega_e\ \Delta\mathbf{u} \\ &+ \int_{\Omega_e}\mathbf{B}^T : (\boldsymbol{\sigma}_i + \Delta\boldsymbol{\sigma})d\Omega_e - \int_{\Omega_e}\mathbf{N}^T\rho\mathbf{N}d\Omega_e\left(\frac{1}{\beta\Delta t}\dot{\mathbf{u}}_i + (\frac{1}{2\beta}-1)\ddot{\mathbf{u}}_i\right) \\ &- \int_{\Omega_e}\mathbf{C}d\Omega_e\left((\frac{\gamma}{\beta}-1)\dot{\mathbf{u}}_i + \Delta t(\frac{\gamma}{2\beta}-1)\ddot{\mathbf{u}}_i\right) \\ &- \int_{\Omega_e}\mathbf{N}^T\cdot(\mathbf{p}_i + \Delta\mathbf{p})d\Omega_e - \int_{\partial\Omega_e}\mathbf{N}^T\cdot(\bar{\mathbf{t}}_i + \Delta\bar{\mathbf{t}})d\partial\Omega_e\Bigg) = \mathbf{0},\end{aligned} \tag{5.37}$$

$$\begin{aligned}\Delta\mathbf{r}_{\bar{D}} = \sum \Bigg(&\int_{\Omega_e}\mathbf{N}^T\mathbf{N}\Delta\bar{D} - \mathbf{N}^T\Delta D + l_c^2\mathbf{B}^T\mathbf{B}\Delta\bar{D}\ d\Omega_e \\ &- l_c^2\int_{\partial\Omega_e}\mathbf{N}^T\Delta t_{\bar{D}}\ d\partial\Omega_e\Bigg) = 0.\end{aligned} \tag{5.38}$$

In order to solve the nonlinear residuals $\Delta\mathbf{r} = \{\Delta\mathbf{r}_\mathbf{u}, \Delta\mathbf{r}_{\bar{D}}\}$ for the unknowns $\Delta\mathbf{d} = \{\Delta\mathbf{u}, \Delta\bar{D}\}$ the Newton-Raphson-method is used. The linearization requires the derivatives of the residuals with respect to the unknown increments. The iterative increments $\Delta\Delta\mathbf{u}$ and $\Delta\Delta\bar{D}$ can be obtained by the linearized system of equations

$$\begin{aligned} \mathbf{K}_{tan} \cdot \Delta\Delta\mathbf{d} &= -\Delta\mathbf{r} \\ \Rightarrow \begin{bmatrix} \frac{\partial\Delta\mathbf{r}_\mathbf{u}}{\partial\Delta\mathbf{u}} & \frac{\partial\Delta\mathbf{r}_\mathbf{u}}{\partial\Delta\bar{D}} \\ \frac{\partial\Delta\mathbf{r}_{\bar{D}}}{\partial\Delta\mathbf{u}} & \frac{\partial\Delta\mathbf{r}_{\bar{D}}}{\partial\Delta\bar{D}} \end{bmatrix} \begin{bmatrix} \Delta\Delta\mathbf{u} \\ \Delta\Delta\bar{D} \end{bmatrix} &= - \begin{bmatrix} \Delta\mathbf{r}_\mathbf{u} \\ \Delta\mathbf{r}_{\bar{D}} \end{bmatrix} \end{aligned} \tag{5.39}$$

where $\mathbf{K}_{tan}$ is the consistent stiffness matrix

$$\mathbf{K}_{tan} = \begin{bmatrix} \mathbf{K}_{uu} & \mathbf{K}_{u\bar{D}} \\ \mathbf{K}_{\bar{D}u} & \mathbf{K}_{\bar{D}\bar{D}} \end{bmatrix} = \begin{bmatrix} \frac{\partial\Delta\mathbf{r}_\mathbf{u}}{\partial\Delta\mathbf{u}} & \frac{\partial\Delta\mathbf{r}_\mathbf{u}}{\partial\Delta\bar{D}} \\ \frac{\partial\Delta\mathbf{r}_{\bar{D}}}{\partial\Delta\mathbf{u}} & \frac{\partial\Delta\mathbf{r}_{\bar{D}}}{\partial\Delta\bar{D}} \end{bmatrix} \tag{5.40}$$

with

$$\mathbf{K}_{uu} = \sum \left(\int_{\Omega_e} \mathbf{B}^T \mathbf{E}_{uu} \mathbf{B} d\Omega_e + \frac{1}{\beta\Delta t^2} \int_{\Omega_e} \mathbf{N}^T \rho \mathbf{N} d\Omega_e + \frac{\gamma}{\beta\Delta t} \int_{\Omega_e} \mathbf{C} d\Omega_e \right), \tag{5.41}$$

$$\mathbf{K}_{u\bar{D}} = \sum \left(\int_{\Omega_e} \mathbf{B}^T \mathbf{E}_{u\bar{D}} \mathbf{N} d\Omega_e \right), \tag{5.42}$$

$$\mathbf{K}_{\bar{D}u} = \sum \left(- \int_{\Omega_e} \mathbf{N}^T \mathbf{E}_{\bar{D}u} \mathbf{B} d\Omega_e \right), \tag{5.43}$$

$$\mathbf{K}_{\bar{D}\bar{D}} = \sum \left(\int_{\Omega_e} \mathbf{N}^T (1 - \mathbf{E}_{\bar{D}\bar{D}}) \mathbf{N} + l_c^2 \mathbf{B}^T \mathbf{B} d\Omega_e \right). \tag{5.44}$$

The unknown material tangents $\mathbf{E}_{uu}$, $\mathbf{E}_{u\bar{D}}$, $\mathbf{E}_{\bar{D}u}$, and $\mathbf{E}_{\bar{D}\bar{D}}$ are defined by

$$\mathbf{E}_{uu} = \frac{\partial\Delta\boldsymbol{\sigma}}{\partial\Delta\boldsymbol{\varepsilon}}, \quad \mathbf{E}_{u\bar{D}} = \frac{\partial\Delta\boldsymbol{\sigma}}{\partial\Delta\bar{D}}, \quad \mathbf{E}_{\bar{D}u} = \frac{\partial\Delta D}{\partial\Delta\boldsymbol{\varepsilon}}, \quad \mathbf{E}_{\bar{D}\bar{D}} = \frac{\partial\Delta D}{\partial\Delta\bar{D}} \tag{5.45}$$

and can be obtained by the the total differential of the residuals of the material equations

$$d\Delta\mathbf{r}_M = \frac{\partial\Delta\mathbf{r}_M}{\partial\Delta\mathbf{z}} d\Delta\mathbf{z} + \frac{\partial\Delta\mathbf{r}_M}{\partial\Delta\mathbf{g}} d\Delta\mathbf{g} = \mathbf{0} \tag{5.46}$$

with the material residuals $\Delta\mathbf{r}_M = \{\Delta\mathbf{r}_{\boldsymbol{\varepsilon}}, \Delta r_p, \Delta r_p^+, \Delta r_K, \Delta\mathbf{r}_\mathbf{X}, \Delta r_D, \Delta r_q, \Delta\mathbf{r}_{\boldsymbol{\beta}}\}$, the unknowns of the material equations $\Delta\mathbf{z} = \{\Delta\boldsymbol{\sigma}, \Delta p, \Delta p^+, \Delta K, \Delta\mathbf{X}, \Delta D, \Delta q, \Delta\boldsymbol{\beta}\}$, and the unknown field variables $\Delta\mathbf{g} = \{\Delta\boldsymbol{\varepsilon}, \Delta\bar{D}\}$. As previously described, the material residuals $\Delta\mathbf{r}_M$ are obtained by time integration with the implicit Euler approach. After transformation, the unknown material tangents can be calculated from the linear equation system

$$\frac{\partial\Delta\mathbf{r}_M}{\partial\Delta\mathbf{z}} \frac{\partial\Delta\mathbf{z}}{\partial\Delta\mathbf{g}} = - \frac{\partial\Delta\mathbf{r}_M}{\partial\Delta\mathbf{g}} \tag{5.47}$$

with

$$\mathbf{J} = \frac{\partial \Delta \mathbf{r}_M}{\partial \Delta \mathbf{z}} = \begin{bmatrix} \frac{\partial \Delta \mathbf{r}_{\boldsymbol{\varepsilon}}}{\partial \Delta \boldsymbol{\sigma}} & \frac{\partial \Delta \mathbf{r}_{\boldsymbol{\varepsilon}}}{\partial \Delta p} & \frac{\partial \Delta \mathbf{r}_{\boldsymbol{\varepsilon}}}{\partial \Delta p^+} & \frac{\partial \Delta \mathbf{r}_{\boldsymbol{\varepsilon}}}{\partial \Delta K} & \frac{\partial \Delta \mathbf{r}_{\boldsymbol{\varepsilon}}}{\partial \Delta \mathbf{X}} & \frac{\partial \Delta \mathbf{r}_{\boldsymbol{\varepsilon}}}{\partial \Delta D} & \frac{\partial \Delta \mathbf{r}_{\boldsymbol{\varepsilon}}}{\partial \Delta q} & \frac{\partial \Delta \mathbf{r}_{\boldsymbol{\varepsilon}}}{\partial \Delta \beta} \\ \frac{\partial \Delta r_p}{\partial \Delta \boldsymbol{\sigma}} & \frac{\partial \Delta r_p}{\partial \Delta p} & \frac{\partial \Delta r_p}{\partial \Delta p^+} & \frac{\partial \Delta r_p}{\partial \Delta K} & \frac{\partial \Delta r_p}{\partial \Delta \mathbf{X}} & \frac{\partial \Delta r_p}{\partial \Delta D} & \frac{\partial \Delta r_p}{\partial \Delta q} & \frac{\partial \Delta r_p}{\partial \Delta \beta} \\ \frac{\partial \Delta r_p^+}{\partial \Delta \boldsymbol{\sigma}} & \frac{\partial \Delta r_p^+}{\partial \Delta p} & \frac{\partial \Delta r_p^+}{\partial \Delta p^+} & \frac{\partial \Delta r_p^+}{\partial \Delta K} & \frac{\partial \Delta r_p^+}{\partial \Delta \mathbf{X}} & \frac{\partial \Delta r_p^+}{\partial \Delta D} & \frac{\partial \Delta r_p^+}{\partial \Delta q} & \frac{\partial \Delta r_p^+}{\partial \Delta \beta} \\ \frac{\partial \Delta r_K}{\partial \Delta \boldsymbol{\sigma}} & \frac{\partial \Delta r_K}{\partial \Delta p} & \frac{\partial \Delta r_K}{\partial \Delta p^+} & \frac{\partial \Delta r_K}{\partial \Delta K} & \frac{\partial \Delta r_K}{\partial \Delta \mathbf{X}} & \frac{\partial \Delta r_K}{\partial \Delta D} & \frac{\partial \Delta r_K}{\partial \Delta q} & \frac{\partial \Delta r_K}{\partial \Delta \beta} \\ \frac{\partial \Delta \mathbf{r}_{\mathbf{X}}}{\partial \Delta \boldsymbol{\sigma}} & \frac{\partial \Delta \mathbf{r}_{\mathbf{X}}}{\partial \Delta p} & \frac{\partial \Delta \mathbf{r}_{\mathbf{X}}}{\partial \Delta p^+} & \frac{\partial \Delta \mathbf{r}_{\mathbf{X}}}{\partial \Delta K} & \frac{\partial \Delta \mathbf{r}_{\mathbf{X}}}{\partial \Delta \mathbf{X}} & \frac{\partial \Delta \mathbf{r}_{\mathbf{X}}}{\partial \Delta D} & \frac{\partial \Delta \mathbf{r}_{\mathbf{X}}}{\partial \Delta q} & \frac{\partial \Delta \mathbf{r}_{\mathbf{X}}}{\partial \Delta \beta} \\ \frac{\partial \Delta r_D}{\partial \Delta \boldsymbol{\sigma}} & \frac{\partial \Delta r_D}{\partial \Delta p} & \frac{\partial \Delta r_D}{\partial \Delta p^+} & \frac{\partial \Delta r_D}{\partial \Delta K} & \frac{\partial \Delta r_D}{\partial \Delta \mathbf{X}} & \frac{\partial \Delta r_D}{\partial \Delta D} & \frac{\partial \Delta r_D}{\partial \Delta q} & \frac{\partial \Delta r_D}{\partial \Delta \beta} \\ \frac{\partial \Delta r_q}{\partial \Delta \boldsymbol{\sigma}} & \frac{\partial \Delta r_q}{\partial \Delta p} & \frac{\partial \Delta r_q}{\partial \Delta p^+} & \frac{\partial \Delta r_q}{\partial \Delta K} & \frac{\partial \Delta r_q}{\partial \Delta \mathbf{X}} & \frac{\partial \Delta r_q}{\partial \Delta D} & \frac{\partial \Delta r_q}{\partial \Delta q} & \frac{\partial \Delta r_q}{\partial \Delta \beta} \\ \frac{\partial \Delta \mathbf{r}_\beta}{\partial \Delta \boldsymbol{\sigma}} & \frac{\partial \Delta \mathbf{r}_\beta}{\partial \Delta p} & \frac{\partial \Delta \mathbf{r}_\beta}{\partial \Delta p^+} & \frac{\partial \Delta \mathbf{r}_\beta}{\partial \Delta K} & \frac{\partial \Delta \mathbf{r}_\beta}{\partial \Delta \mathbf{X}} & \frac{\partial \Delta \mathbf{r}_\beta}{\partial \Delta D} & \frac{\partial \Delta \mathbf{r}_\beta}{\partial \Delta q} & \frac{\partial \Delta \mathbf{r}_\beta}{\partial \Delta \beta} \end{bmatrix},$$

$$\frac{\partial \Delta \mathbf{z}}{\partial \Delta \mathbf{g}} = \begin{bmatrix} \frac{\partial \Delta \boldsymbol{\sigma}}{\partial \Delta \boldsymbol{\varepsilon}} & \frac{\partial \Delta \boldsymbol{\sigma}}{\partial \Delta \bar{D}} \\ \frac{\partial \Delta p}{\partial \Delta \boldsymbol{\varepsilon}} & \frac{\partial \Delta p}{\partial \Delta \bar{D}} \\ \frac{\partial \Delta p^+}{\partial \Delta \boldsymbol{\varepsilon}} & \frac{\partial \Delta p^+}{\partial \Delta \bar{D}} \\ \frac{\partial \Delta K}{\partial \Delta \boldsymbol{\varepsilon}} & \frac{\partial \Delta K}{\partial \Delta \bar{D}} \\ \frac{\partial \Delta \mathbf{X}}{\partial \Delta \boldsymbol{\varepsilon}} & \frac{\partial \Delta \mathbf{X}}{\partial \Delta \bar{D}} \\ \frac{\partial \Delta D}{\partial \Delta \boldsymbol{\varepsilon}} & \frac{\partial \Delta D}{\partial \Delta \bar{D}} \\ \frac{\partial \Delta q}{\partial \Delta \boldsymbol{\varepsilon}} & \frac{\partial \Delta q}{\partial \Delta \bar{D}} \\ \frac{\partial \Delta \beta}{\partial \Delta \boldsymbol{\varepsilon}} & \frac{\partial \Delta \beta}{\partial \Delta \bar{D}} \end{bmatrix}, \quad -\frac{\partial \Delta \mathbf{r}_M}{\partial \Delta \mathbf{g}} = - \begin{bmatrix} \frac{\partial \Delta \mathbf{r}_{\boldsymbol{\varepsilon}}}{\partial \Delta \boldsymbol{\varepsilon}} & \frac{\partial \Delta \mathbf{r}_{\boldsymbol{\varepsilon}}}{\partial \Delta \bar{D}} \\ \frac{\partial \Delta r_p}{\partial \Delta \boldsymbol{\varepsilon}} & \frac{\partial \Delta r_p}{\partial \Delta \bar{D}} \\ \frac{\partial \Delta r_p^+}{\partial \Delta \boldsymbol{\varepsilon}} & \frac{\partial \Delta r_p^+}{\partial \Delta \bar{D}} \\ \frac{\partial \Delta r_K}{\partial \Delta \boldsymbol{\varepsilon}} & \frac{\partial \Delta r_K}{\partial \Delta \bar{D}} \\ \frac{\partial \Delta \mathbf{r}_{\mathbf{X}}}{\partial \Delta \boldsymbol{\varepsilon}} & \frac{\partial \Delta \mathbf{r}_{\mathbf{X}}}{\partial \Delta \bar{D}} \\ \frac{\partial \Delta r_D}{\partial \Delta \boldsymbol{\varepsilon}} & \frac{\partial \Delta r_D}{\partial \Delta \bar{D}} \\ \frac{\partial \Delta r_q}{\partial \Delta \boldsymbol{\varepsilon}} & \frac{\partial \Delta r_q}{\partial \Delta \bar{D}} \\ \frac{\partial \Delta \mathbf{r}_\beta}{\partial \Delta \boldsymbol{\varepsilon}} & \frac{\partial \Delta \mathbf{r}_\beta}{\partial \Delta \bar{D}} \end{bmatrix}.$$

5.4 Scheme of solving algorithm

An overview of the solving algorithm for the nonlinear problem is given in table 5.1. Under consideration of boundary and initial conditions, the unknown state variables of the next time step are iteratively calculated. Within one time step, the procedure is divided into a global and a local iteration.

The global iteration implies the solution of the equation of motion and of the gradient equation which are obtained by spatial discretization with the finite-element method and discretization in time with the Newmark method. The unknown increments of the field variables $\mathbf{d}$, namely the displacement $\mathbf{u}$ and the nonlocal damage $\bar{D}$, can be obtained from a linearized system of equations using the Newton-Raphson approach. The linearized system of equations consists of the consistent stiffness matrix $\mathbf{K}_{tan}$ and the residuals $\mathbf{r}$. The consistent stiffness matrix includes the material tangents, the mass matrix, and the damping matrix. After having updated the displacement $\mathbf{u}$, velocity $\dot{\mathbf{u}}$ and acceleration $\ddot{\mathbf{u}}$ can be determined.

With the current solutions of the field variables, the associated internal state variables of the material $\mathbf{z} = \{\boldsymbol{\sigma}, p, p^+, K, \mathbf{X}, D, q, \boldsymbol{\beta}\}$ can be computed within a local iteration. The evolution equations of the material are solved using the implicit Euler approach and the Newton-Raphson method in order to consider nonlinearities.
The consistent stiffness matrix for the subsequent global iteration includes the updated material variables. The iterations of a time-step end as soon as the norms of both residuals $\mathbf{r}$ and $\mathbf{r}_M$ fall below the stop criteria $\varepsilon_{tol}^{global}$ and $\varepsilon_{tol}^{local}$ respectively.

loop over all time steps $t_{i+1} = t_i + \Delta t$

global iteration

- material tangents $\mathbf{E}_{uu}, \mathbf{E}_{u\bar{D}}, \mathbf{E}_{\bar{D}u}, \mathbf{E}_{\bar{D}\bar{D}}$
- mass matrix $\mathbf{M}$
- damping matrix $\mathbf{C}$
- consistent stiffness matrix $\mathbf{K}_{tan}$
- residuals $\Delta\mathbf{r}$
- solving the equation system $\mathbf{K}_{tan} \cdot \Delta\Delta\mathbf{d} = -\Delta\mathbf{r}$
- update velocity $\dot{\mathbf{u}}$ and acceleration $\ddot{\mathbf{u}}$

local iteration

- elastic predictor $\boldsymbol{\sigma}^{test} = \boldsymbol{\sigma}_i + \mathbf{E}(\mathbf{V}_i) : \Delta\boldsymbol{\varepsilon}$
- inelastic corrector:
  - material residuum $\Delta\mathbf{r}_M$
  - Jacobian matrix $\mathbf{J}$
  - update internal variables $\mathbf{J} \cdot \Delta\Delta\mathbf{z} = -\Delta\mathbf{r}_M$
  - convergence $|\Delta\mathbf{r}_M| \leq \epsilon_{tol}^{local}$

- convergence $|\Delta\mathbf{r}| \leq \epsilon_{tol}^{global}$

Table 5.1: Scheme of solving algorithm

6 Parameter identification

The development of material models includes the identification of physically relevant processes and their description with mathematical constitutive equations. The constitutive equations depend on material parameters which have to be determined by means of experiments. An accurate choice of the model parameters leads to an optimal description of the experimentally observed material behavior by means of the model. In order to find the appropriate parameters, attention has to be payed to the parameter identification procedure. This procedure comprises the choice of a parameter adjustment algorithm and the selection of experimental data.
Parameter adjustment algorithms are based on optimization strategies. The goal of parameter adjustment is the minimization of differences between the numerically simulated and the experimental curves. The existing approaches are distinguished into stochastic and deterministic algorithms. Stochastic methods include the Monte Carlo simulation and genetic algorithms, which both use the information of foregoing steps in order to find a better parameter set. Deterministic algorithms, for instance Gradient-, Newton-, BFGS-, CG-, or Simplex-methods, search the minimum of the objective function around a predefined starting point and therefore they often find a local minimum only. Hybrid strategies combine stochastic and deterministic methods in order to ensure that the global minimum is detected. Thereby, the stochastic method is used to find a good starting point for the deterministic search. Streilein [131] provides a comprehensive overview of the aforementioned approaches. For further investigations, a genetic algorithm is chosen (see section 6.1).
In order to calculate seismically induced damage in civil engineering steel structures, experimental data of mild construction steel is needed for the identification of the model parameters. In literature, the main focus of experimental investigations of construction steel is on hardening/softening behavior which excludes investigations of damage. Therefore, new experiments have been conducted in collaboration with the Institute of Steel Structures of the University of Braunschweig. Section 6.2 describes the experiments which are used as a basis for parameter identification of mild steel. The identification and evaluation of the model parameters are given in section 6.3.

6.1 Genetic algorithms

Genetic algorithms, also called evolutionary strategies, are chosen in order to identify the model parameters because they are between the most accurate and most efficient numerical tools for global parameter identification. They mimic the metaphor of natural biological evolution in order to generate optimized sets of model parameters. Figure 6.1 presents the scheme of a genetic algorithm which is described in detail in [114].

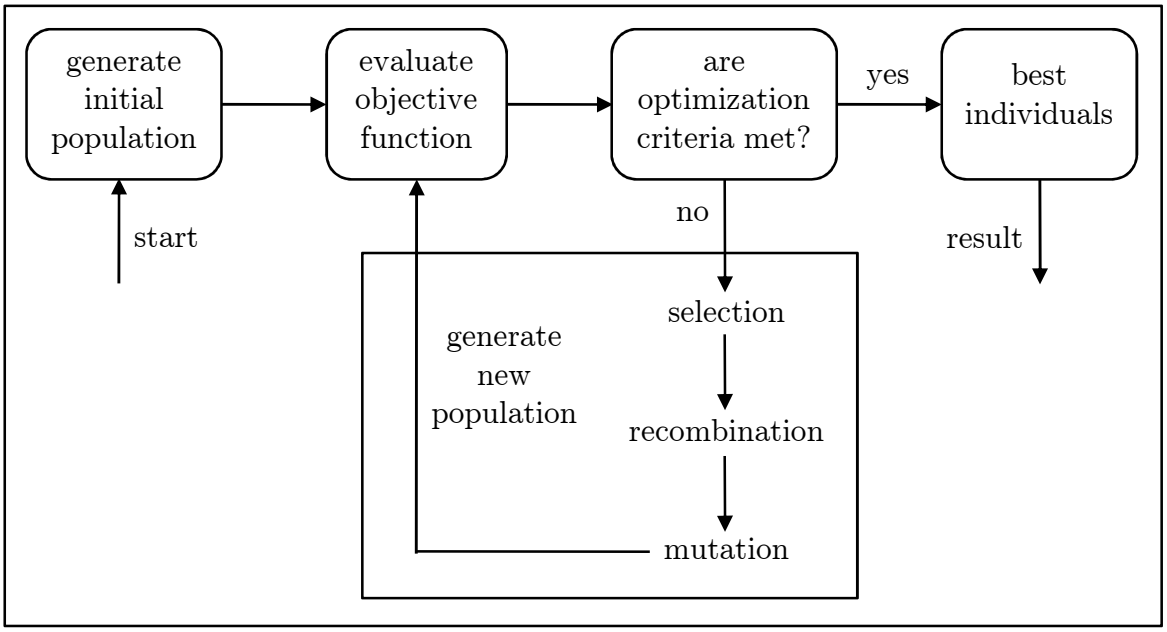

Figure 6.1: Scheme of genetic algorithms

First, an initial population of individual parameter sets is created randomly on a basis of predefined starting and limiting values. Then, the best individual sets are determined. If the optimization criteria is not met, the selected sets are recombined and mutated in order to generate new individual sets. The new individuals replace the worst individuals of the old population in order to create a new population. This evolutionary procedure is repeated until the optimization criteria is met and the best set of parameters is found.

6.2 Selection of experimental data

In order to accurately identify the model parameters required within this work, extensive experimental data is needed, which can be grouped into experiments for the estimation of the parameters of the local material model and experiments in order to define the internal length or the crack closure parameter.
The parameter of the internal length is not identified during parameter estimation using the genetic algorithm. Since parameter adjustment is carried out at the material point, the internal length as a parameter that regularizes the spatial distribution of damage remains undefined. For the identification of the internal length, additional data with special experimental equipment is needed (see for example [129, 48]). Similarly, the determination of the crack-closure parameter h requires additional experimental data, which consider microstructural observations.
The parameters, which are determined via the genetic algorithm, are the parameters of the local model, which can be obtained at the material point. They are grouped into

parameters of elasticity, viscoplasticity, isotropic and kinematic hardening and ductile damage. The determination of the model parameters for the assessment of structures subjected to earthquakes ideally requires a multitude of experiments which marks the load range of earthquakes. In order to identify the parameters of elasticity and viscoplasticity, tensile tests with different loading velocities in the range of $10^{-4}s^{-1} < \dot{\varepsilon} < 10^{0}s^{-1}$ or creep tests with different stress level are needed. The parameters of isotropic and kinematic hardening can be related from tensile and cyclic experiments within the inelastic range with corresponding loading velocities and an amplitude spectrum which covers the amplitude spectrum of earthquakes. For the identification of damage parameters, monotonic and cyclic tests are required which represent the material behavior until failure.

Appropriate experimental data for the structural steel S 355, which include damage and the load range of earthquakes, are rare. Especially experimental data for damage assessment of the steel S 355 could not be found. From the available data remain only a limited number of experiments which are suitable for this work. In a first step, a cyclic experiment with a loading velocity of $\dot{\varepsilon} = 10^{-2}s^{-1}$ and a strain amplitude of $\varepsilon_a = 1.2\%$ is selected in order to adjust the parameters to cyclic behavior. The loading velocity falls into the range of velocities that occur under seismic loading. Details concerning the experiment, the testing equipment, the steel, and the specimen can be found in [18].
Tensile and creep test data for the steel S 355 within the range of damage due to seismic loading as well as experiments for the identification of the internal length or the crack closure parameter are not available to the best of the author's knowledge. Due to feasibility reasons, only additional uniaxial tensile tests within the damage range have been conducted in order to extend the experimental basis for parameter adjustment. Following [146], the parameter of the internal length is not derived experimentally but obtained at a later date by comparison with structural experiments. The crack closure parameter is related from values in literature.

The new tensile experiments have been conducted in collaboration with the Institute of Steel Structures of the University of Braunschweig. In order to guarantee a reproducibility of the experimental data of the cyclic and the tensile tests, steel of the same batch has been used for both types of experiments.
The tensile tests are performed on unalloyed construction steel S 355 J2G3 according to DIN EN 10025 [42]. The specimen is a round specimen according to DIN 50 125. The dimensions are given in figure 6.2.

The testing machine consists of a two column test frame with uniaxial loading direction. The measurement base for measuring the strain is 60 mm. The loading velocity is set to $\dot{\varepsilon} = 10^{-2}s^{-1}$ since this velocity falls within the range of material strain rates $10^{-4}s^{-1} < \dot{\varepsilon} < 10^{0}s^{-1}$ which are induced by earthquakes [18].

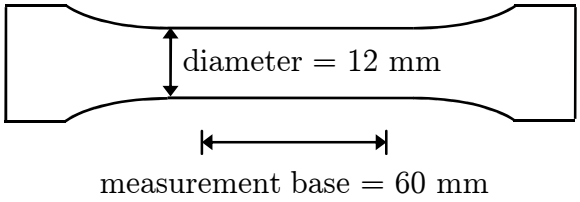

Figure 6.2: Dimensions of the round specimen

6.3 Adjustment to tensile and cyclic tests

In the following the model parameters of the local material model are determined via the genetic algorithm. While good estimations of initial values for the modulus of elasticity and the yield stress can be obtained by investigation of the stress-strain curve, initial values of the viscosity-, hardening-, and damage parameters have to be estimated on engineering judgement and improved using the above mentioned optimization strategy. Poisson's ratio and density are chosen in accordance with values in literature.

A first set of model parameters is given in table 6.1. Here, the yield stress is fixed to $\sigma_y = 320$ N/mm^2 which is geared to the minimum value of the yield stress of the steel S 355 obtained under quasi-static conditions [18].
The approach to identify the unknown model parameters is divided into two parts. First, the parameters of elasticity, viscoplasticity, and hardening are adjusted. Figure 6.3a shows plots of the experiment and its simulation neglecting damage. The deviation between the simulation and the experiment occurs due to the yield plateau. Structural steel shows a pronounced yield plateau, which the model is not able to reproduce. Since the exact shape of the measured stress-strain curve cannot be reached using the applied model, the simulation resembles the shape of the experiment after the yield plateau. This leads to an overestimation of the measured stresses at small strains but to a match between the experiment and the simulation at large strains.
The second step of the identification procedure considers the damage parameters. The parameters of elasticity, viscoplasticity, and hardening, which have already been determined in the last step, remain unchanged. Since the incorporation of damage will alter the shape of the simulation curve, the parameter optimization is targeted on a match of the integral of experimental and simulated curve. This leads to a balance of the amount of dissipated energy. The result is shown in figure 6.3b and bases on the assumption that hardening develops simultaneously with inelastic deformation while damage only increases if the equivalent plastic strain exceeds the damage threshold strain. The damage threshold strain corresponds to the strain at the end of the yield plateau since the unhindered movement of dislocations ends with the yield plateau and a pile-up of dislocations leads to damage.

Parameter	Value	
Elastic material behavior		
Young's modulus E	200000	[N/mm^2]
Poisson's ratio ν	0.3	[-]
density ρ	7.85e-6	[kg/mm^3]
Viscoplasticity		
initial yield stress σ_y	320.0	[N/mm^2]
viscosity parameter $\dot{\varepsilon}_0$	1.0	[1/s]
viscosity stress σ_p	10.0	[N/mm^2]
viscosity exponent n	9.0	[-]
$a1$	1.0	[-]
$a2$	1.0	[-]
Isotropic hardening		
saturation stress Q	15.0	[N/mm^2]
multiplier b	100.0	[-]
Kinematic hardening		
saturation stress C	120.0	[N/mm^2]
multiplier a	40.0	[-]
Ductile damage		
$c1$	0.15	[-]
$c2$	-0.01	[-]
$c3$	1.0	[-]
$c4$	6.0	[-]
$c5$	0.1	[-]
damage threshold strain ε_D^{in}	0.015	[-]

Table 6.1: Model parameters, Set 1

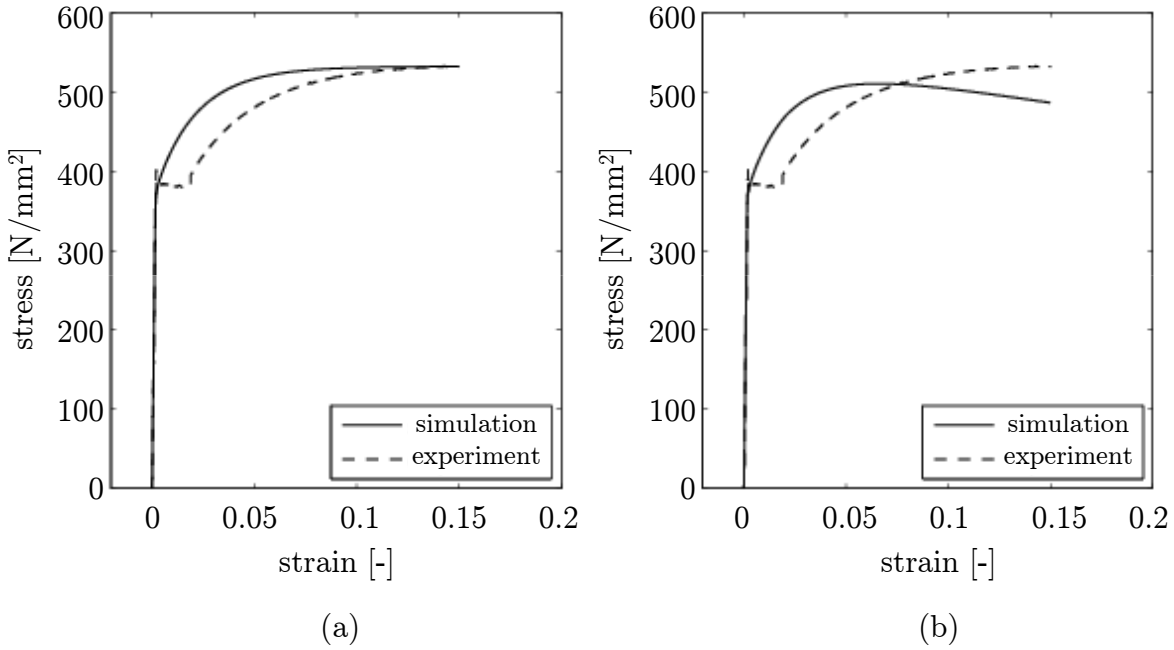

Figure 6.3: Experiment and simulation of a tensile test on the steel S 355 with a loading velocity of $\dot{\varepsilon} = 10^{-2}s^{-1}$ using the model parameters defined in table 6.1: (a) simulation without damage, (b) simulation including damage

The set of model parameters obtained from the adjustment to the monotonic tensile test is now used to simulate the material behavior under cyclic loading. Figure 6.4a shows the measured and calculated stress-strain curves obtained with the model parameter set given in table 6.1. It can be seen that the simulation matches the experiment to a high extend. The occurring differences are to be divided into stress deviation in the first cycle, displaced turnover stresses, and shape deviation.
The stress difference between the first cycle of the experiment and the first cycle of the simulation arises from the fact that the model cannot describe the yield plateau, as it was already observed for the tensile test. In the simulation, hardening develops as soon as the material behaves inelastically so that the final hardening state is reached within the first cycle. In contrast to the simulation, the steel S 355 reaches its final hardening state after the second cycle. Thus, for cyclic as opposed to monotonic tests, any deviations caused by this are compensated after the second cycle already.
A second difference between the simulated and the experimental curve is to be found in the turnover stresses. The simulated turnover stresses slightly overestimate the measured turnover stresses. This indicates that the values of the hardening parameters for the simulation of cyclic experiments are marginally too high. Since the accurate simulation of monotonic tests requires high parameter values, the small differences in the turnover-stresses are inevitable.
The third deviation is to be determined by the shape of the hysteresis curves. The model is not capable of reproducing the corner arc which marks the transition from

elastic range into inelastic range in the experiment. This deviation is undesired since it substantially influences the area of every hysteresis curve and therewith the amount of dissipated energy. In order to overcome this weakness, a second set of parameters is determined.

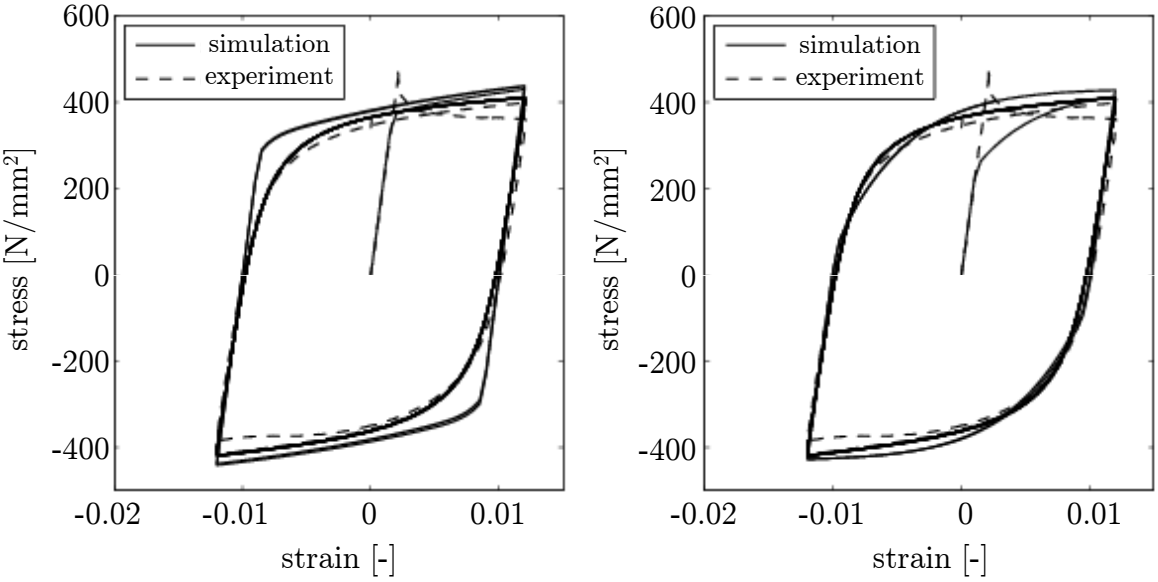

Figure 6.4: Experiment and simulation of a cyclic test on the steel S 355 with a loading velocity of $\dot{\varepsilon} = 10^{-2}s^{-1}$ and a strain amplitude of $\varepsilon_a = 1.2\%$ using the model parameters defined in (a) table 6.1 and (b) table 6.2

While the first set of model parameters bases on a realistic value of the yield stress σ_y, a second set of parameters is determined (see table 6.2), where the yield stress is assumed to be significantly lower than the previous one. Although a reproduction of initial yielding is not possible now, this assumption shows certain advantages. Figure 6.5a shows the curves of the experiment and the simulation neglecting damage. Again, the simulated curve is supposed to reproduce the shape of the experimental curve after the yield plateau.
The incorporation of damage leads to the balance of the integrals of both curves, see figure 6.5b.
The discrepancy between the hysteresis shapes of the experimental results and the numerical simulation using the model parameter set of table 6.1 can be overcome with the second set of model parameters given in table 6.2 that bases on a reduction of the yield stress. The measured and calculated stress-strain curves using the second set of parameters are shown in figure 6.4b. It can be seen that the simulation matches the experiment much better. Deviations only occur during the first cycle due to the yield

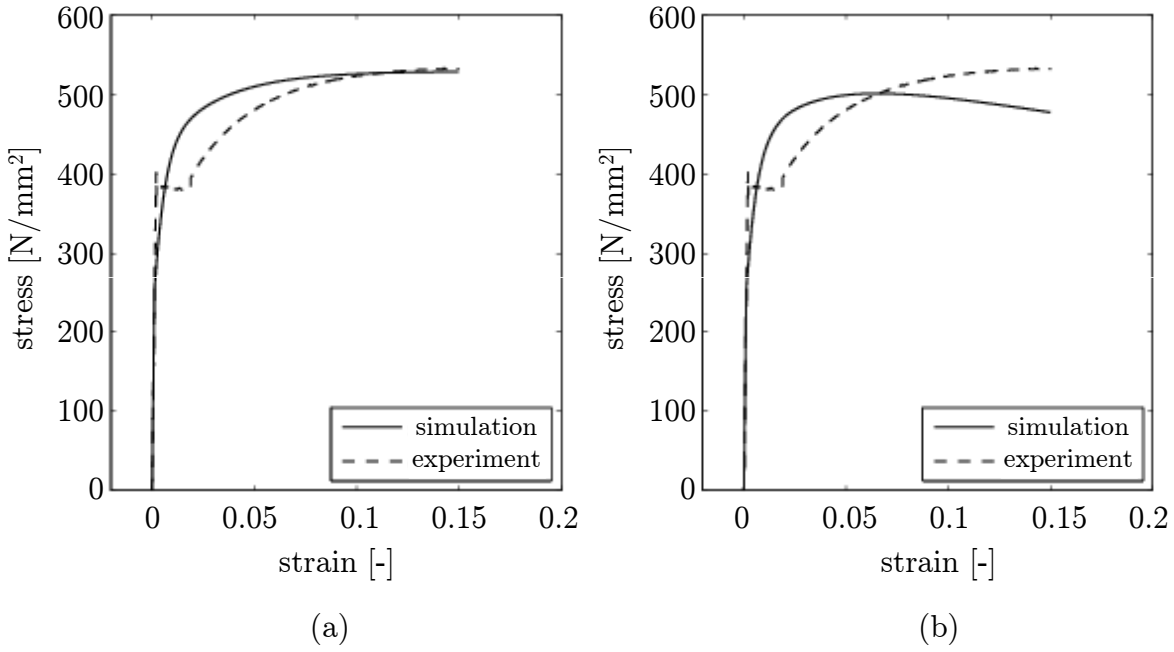

Figure 6.5: Experiment and simulation of a tensile test on the steel S 355 with a loading velocity of $\dot{\varepsilon} = 10^{-2}s^{-1}$ using the model parameters defined in table 6.2: (a) simulation without damage, (b) simulation including damage

plateau in the experiment and due to the underestimation of the yield stress in the simulation, respectively. From the second cycle on, the areas of the hysteresis curves correspond well. Therefore, the set of model parameters given in table 6.2 is used for further investigations.

It is important to mention that the time of failure for the monotonically loaded specimens cannot be appropriately predicted with the model using the parameter set given in table 6.2. While the specimens fail for strains $\varepsilon > 15\%$ which leads to a sudden drop of the experimental curves shown in figure 6.3 and 6.5 for $\varepsilon > 15\%$, the simulation does not predict failure at this point. The reason for that is, that the optimization is targeted on a match of the integral of experimental and simulated curve and not on a match of the time of failure.

Parameter	Value	
Elastic material behavior		
Young's modulus E	200000	[N/mm^2]
Poisson's ratio ν	0.3	[-]
density ρ	7.85e-6	[kg/mm^3]
Viscoplasticity		
initial yield stress σ_y	220.0	[N/mm^2]
viscosity parameter $\dot{\varepsilon}_0$	1.0	[1/s]
viscosity stress σ_p	4.0	[N/mm^2]
viscosity exponent n	8.0	[-]
$a1$	1.0	[-]
$a2$	1.0	[-]
Isotropic hardening		
saturation stress Q	87.0	[N/mm^2]
multiplier b	30.0	[-]
Kinematic hardening		
saturation stress C	150.0	[N/mm^2]
multiplier a	210.0	[-]
Ductile damage		
$c1$	0.15	[-]
$c2$	-0.01	[-]
$c3$	1.0	[-]
$c4$	6.0	[-]
$c5$	0.1	[-]
damage threshold strain ε_D^{in}	0.015	[-]

Table 6.2: Model parameters, Set 2

In the following, some simulations based on the parameter set given in table 6.2 are performed and compared to experimental data. The experimental data is taken from [18]. Figure 6.6 shows experimental and simulated curves for specimens subjected to (a) an ascending order of amplitudes and (b) a descending order of amplitudes for a strain rate of $\dot{\varepsilon} = 10^{-2}s^{-1}$. Five different amplitudes are considered, namely 5 cycles with an amplitude of $\varepsilon_a = 0.015$, 10 cycles with an amplitude of $\varepsilon_a = 0.012$, 15 cycles with an amplitude of $\varepsilon_a = 0.009$, 25 cycles with an amplitude of $\varepsilon_a = 0.006$, and 40 cycles with an amplitude of $\varepsilon_a = 0.003$. The comparisons of the experiments with the simulations show a good match. Deviations occur within the first cycle due to the underestimation of the yield stress in the simulation for both cases with ascending and descending order of amplitudes. Additionally, it can be seen that the model is not capable of modeling cyclic softening, which especially emerges in the experiment with ascending amplitude order for a strain amplitude of $\varepsilon_a = 0.003$. Due to the underestimation of the yield stress, however, the simulated hysteresis shapes correspond with the saturated experimental hysteresis shapes.

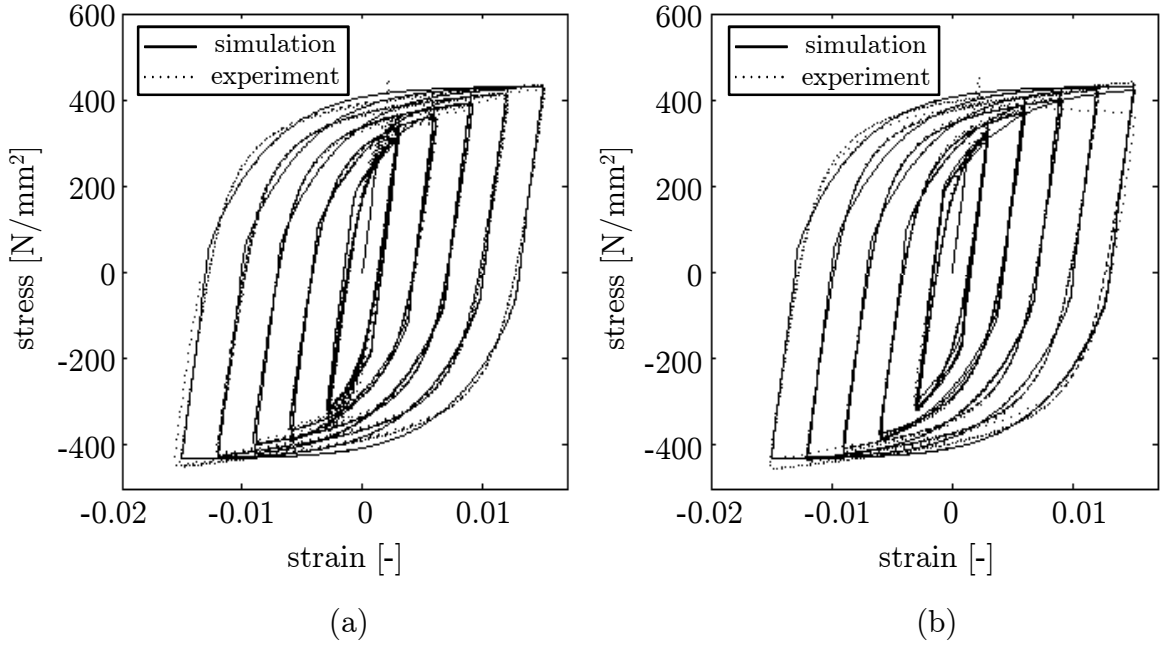

Figure 6.6: Experiment and simulation of cyclic tests on the steel S 355 with a loading velocity of $\dot{\varepsilon} = 10^{-2}s^{-1}$ using the model parameters defined in table 6.2 for (a) an ascending order of amplitudes, (b) a descending order of amplitudes

The recalculation of an experiment, where a specimen is subjected to uniaxial seismic loading, is given in the next chapter (7.4) and represents the ability to cope with different loading velocities.

7 Structural analyses

In the following, the model developed within this work is evaluated by means of different experiments. The implemented equations underlying the model are summarized in chapter 4.4. If not further specified, the model parameters base on the parameter set given in table 6.2. Since the internal length l_c and the crack-closure parameter h were not identified, they are either obtained from structural experimental investigations or related from values in literature.
The following structural analyses are performed in 3D. On the one hand, 3D-structural analyses are capable of representing correctly localized damage states in the material, since localization zones are characterized by triaxial stress states. On the other hand, three-dimensional structural investigations are required for a realistic modeling of steel structures. The spatial discretization using the finite-element method is based on 27-node brick elements with quadratic shape functions.
In a first step, structural analyses of a bar and of a CT-specimen are performed in order to show the accuracy of the damage model. Subsequently, examples with respect to earthquakes are investigated. The assessment of a frame corner shows the ability of the material model if structures are subjected to regularly alternating tension and compression. A bar under uniaxial seismic loading reveals the model's ability to cope with irregular cyclic loading. After the material behavior under reversed loading is assessed, the vibration behavior including effects resulting from mass inertia is taken into account. A simple cantilever with elastic material behavior is investigated in order to determine appropriate conditions for structural dynamic investigations. Furthermore, the combination of damage mechanics and structural dynamics is studied. Finally, three-dimensional columns under seismic excitation are assessed and the global damage index is calculated in order to evaluate structural stability and safety.

7.1 Bar under reversed loading

In order to evaluate the stress-strain behavior of structures subjected to regular, increasing cyclic straining, a bar under displacement controlled loading conditions is investigated. The bar has a length of $L = 20$ mm and is discretized in longitudinal direction by 20 elements. The model parameters used for this example are taken from table 6.2. In the middle of the bar, the yield stress is reduced in order to specify the location of damage initiation. The crack closure parameter is set to $h = 0.2$ following [80]. Since the internal length l_c should exceed the element length of 1 mm (see section 4.3), it is set to $l_c = 1.5$ mm. The geometry and the loading conditions of the bar are specified in figure 7.1. The loading and unloading velocity is set to $\dot{\varepsilon} = 1.0e^{-3}s^{-1}$, which represents the lower range of strain rates induced by earthquakes.

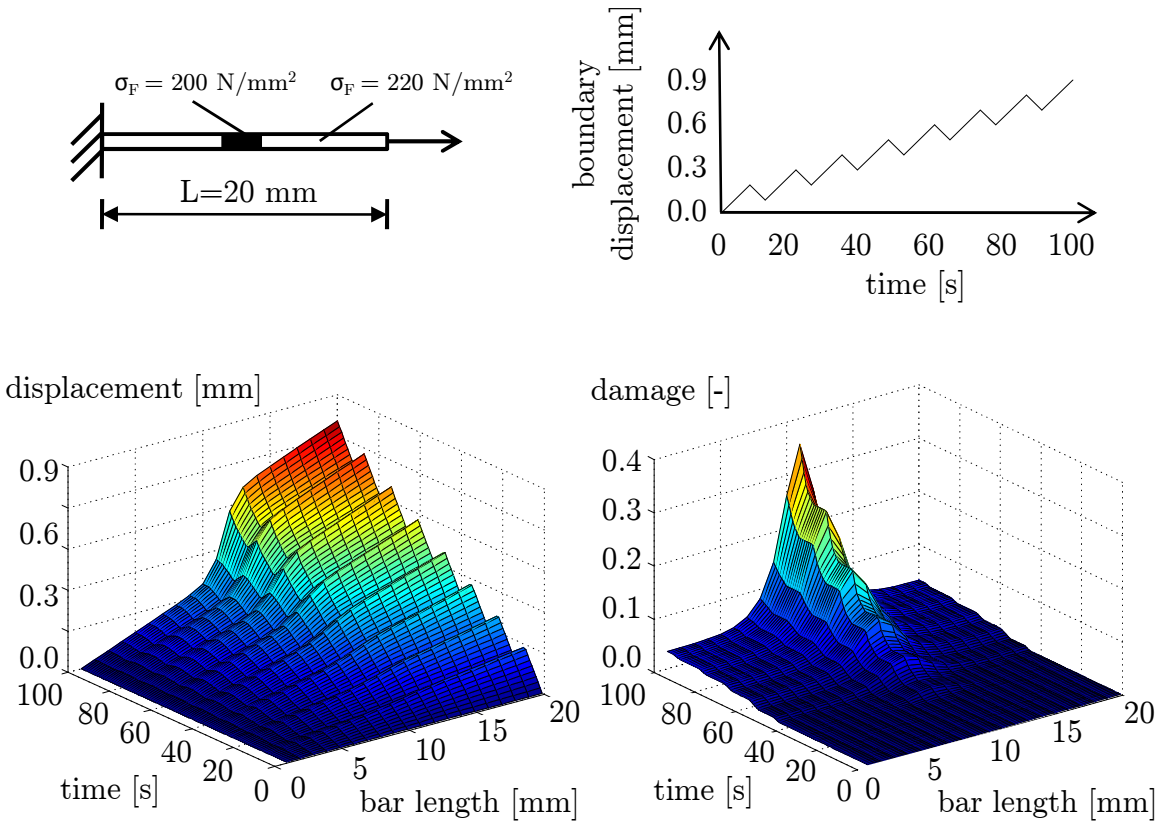

Figure 7.1: Geometry of the bar, loading conditions, and development of displacement and damage due to alternating tension and compression

The development of damage firstly reveals the distribution of damage along the length of the bar and secondly the evolution of damage under reversed loading. The evolution of damage is hindered as long as the plastic strains fall below the damage threshold strain. For plastic strains exceeding this threshold, it can be seen that the damage variables increase only under positive stress increments (tension) due to the dependance of the damage evolution law on the active accumulated plastic strains. While the damage variables remain constant under negative stress increments (compression), the plot of displacement illustrates the reduction of displacement under reversed loading. Increasing damage leads to increasing deformations combined with necking and eventual failure in the middle of the bar.

7.2 CT-specimen under creep conditions

The accuracy of the material model is evaluated by means of recalculations of experiments on compact tension specimens (CT-specimens) under permanent loading. The experiments on the CT-specimens and corresponding tensile tests for parameter adjustment are performed on a 12% Chromium steel (X 20 CrMoV 12.1) at 550 °C at the TU Darmstadt and the FIW Freiburg [91]. This kind of steel is used in plant engineering and construction.
The model parameters are determined from uniaxial creep tests, since no other experiments were available for the author for this kind of material. For the identification of the model parameters it is assumed that the loading is applied within a time period of 250 seconds and that all subsequent strains are plastic. The result is shown in figure 7.2. Since parameter adjustment is carried out at the material point, the internal length l_c cannot be defined and needs to be determined from structural experimental investigation. The obtained model parameters are given in table 7.1.

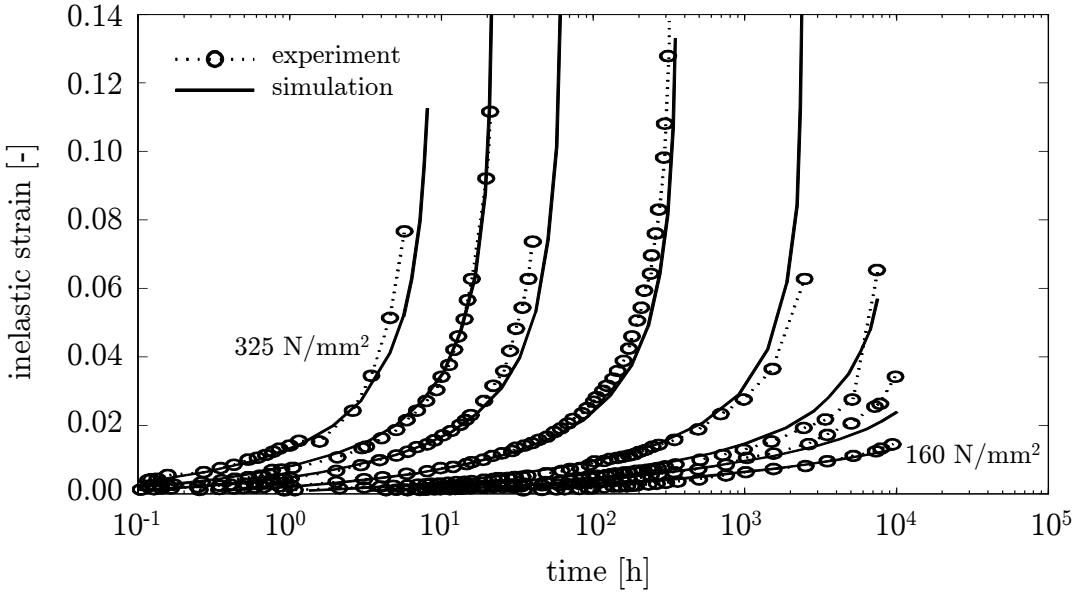

Figure 7.2: Parameter adjustment to uniaxial creep tests

After having identified the model parameters, the recalculation of experiments on CT-specimens can be performed. The specimen (see figure 7.3) has a thickness of 20 mm, a bore diameters of $d = 2$ mm, and is stressed permanently by a tangential force of $F = 8$ kN.
The time-dependent development of the displacements can only be represented correctly by 3D-structural analysis due to multiaxial stress states in the CT-specimens. Furthermore, 3D-structural analysis captures correctly the stress state in the localization zone.

Parameter	Value	
Elastic material behavior		
Young's modulus E	165000	[N/mm^2]
Poisson's ratio ν	0.3	[-]
density ρ	7.85e-6	[kg/mm^3]
Viscoplasticity		
initial yield stress σ_y	15.0	[N/mm^2]
viscosity stress σ_p	1100.0	[N/mm^2]
viscosity exponent n	8.67	[-]
a_1	1.3	[-]
a_2	1.0	[-]
Isotropic hardening		
saturation stress Q	75.0	[N/mm^2]
multiplier b	175.0	[-]
Ductile damage		
c_1	1.2	[-]
c_2	-0.02	[-]
c_3	60	[-]
c_4	40	[-]
c_5	0.1	[-]
damage threshold strain ε_D^{in}	0.0	[-]
Internal length l_c	1.2, 1.3, 1.4	[mm]

Table 7.1: Model parameters of steel X 20 CrMoV 12.1

Figure 7.3 depicts the developing of the opening displacements Δu of the CT-specimen over time. A good match between measured and calculated results is found. The results depend on the internal length l_c which is here set to 1.2 mm, 1.3 mm, and 1.4 mm. The higher the value of the internal length, the longer it takes till the specimen fails. The best fitting result is obtained for an internal length of $l_c = 1.3$ mm.
The distribution of damage for the CT-specimen is shown in figure 7.4 for the moment the opening displacement Δu at the left boundary reaches 5 mm. Three quarters of the specimen are depicted. It can be seen that damage starts inside the specimen due to the multiaxial stress state in the middle while at the boundaries a rearrangement of stress occurs.

The results indicate that the developed damage model is able to correctly reproduce the experimental investigations. In the following the approach is used to simulated structures subjected to seismic loading conditions.

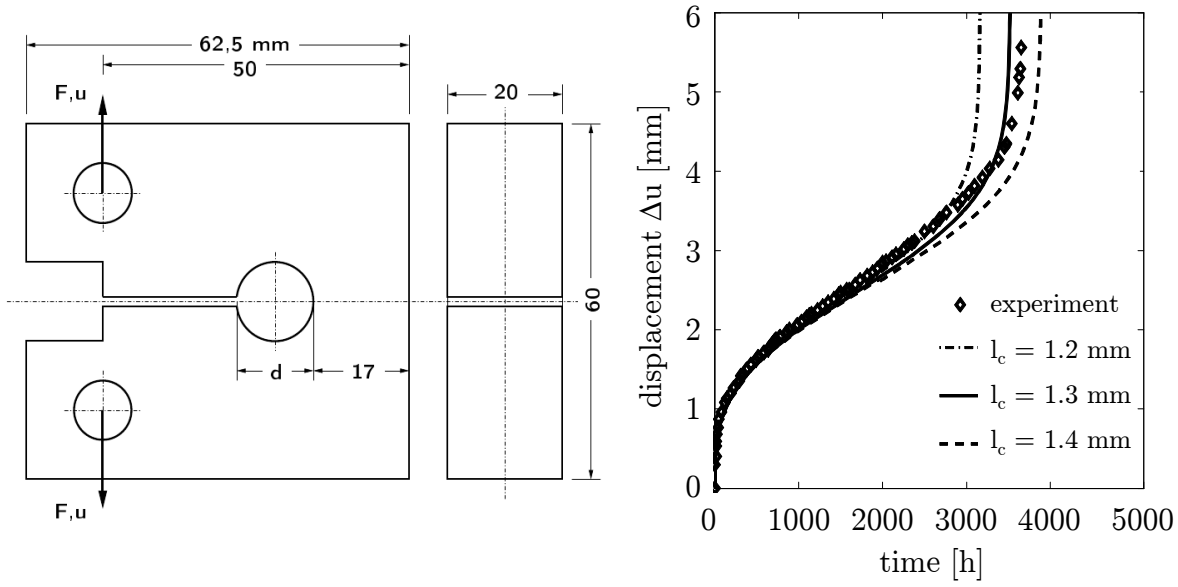

Figure 7.3: CT-specimen, left: geometry, right: evolution of deformation under constant loading ($F = 8$ kN)

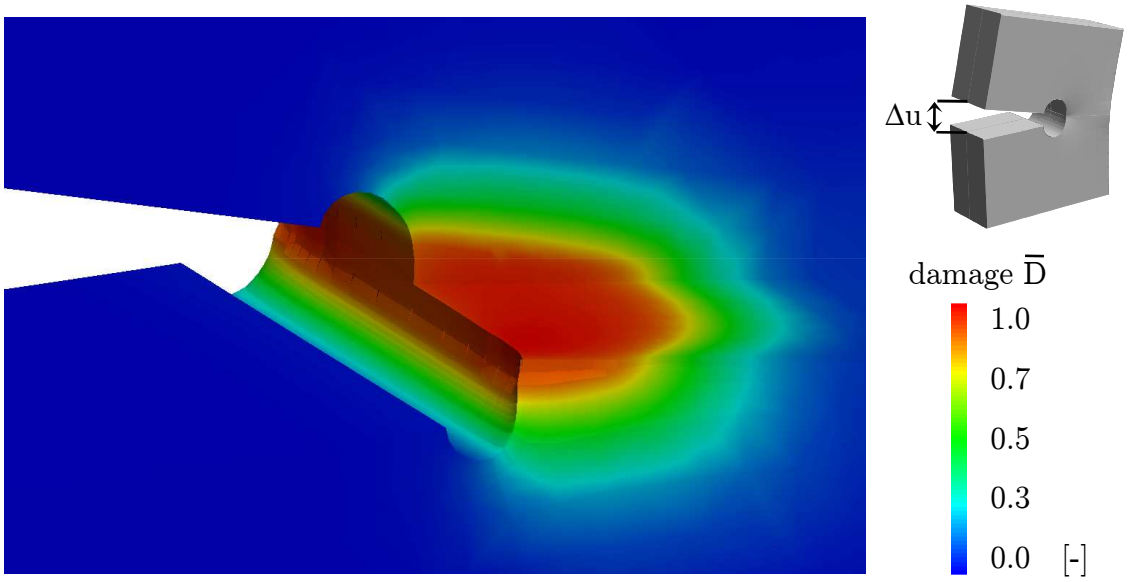

Figure 7.4: Distribution of damage for a CT-specimen under constant loading ($F = 8$ kN) for the moment the opening displacement Δu reaches 5 mm

7.3 Frame corner under alternating deformation

Earthquakes, which act on buildings in frame construction, mainly induce damage in the area of connections like the frame corners or the base. In the following, a frame corner under cyclic loading is assessed. For the sake of simplicity, the frame corner is modelled in 2D. Spatial discretization is obtained by 9-node elements with quadratic shape functions.
While the beam is assumed not to be moving due to inertia, the column is subjected to horizontal cyclic movement causing alternating tension and compression in the structure. The frame corner, its dimensions, and the loading history and direction (+/-) are shown in figure 7.5. The displacement-controlled loading takes place with a loading velocity of 0.1 mm/s. The model parameters are given in table 6.2. The internal length is set to 6 mm in order to exceed the element size of 5 mm and the crack closure parameter is assumed to be $h = 0.5$, which bisects the influence of damage under compression.

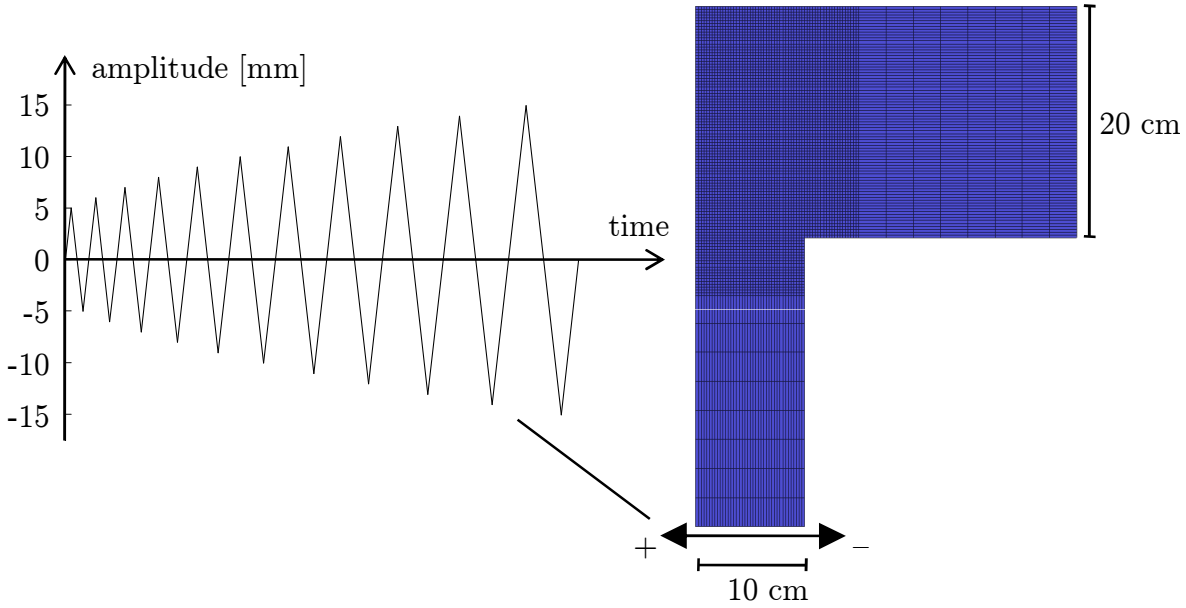

Figure 7.5: Geometry, loading history, and loading direction (+/-) of the frame corner

Figure 7.6a represents the distribution of damage after 9 cycles. Damage occurs at the transition zone between the column and the beam. The highest stresses and therewith the biggest damage emerge in the area of the nook when the displacement acts in positive direction (see figure 7.5 for the loading direction), since damage only evolutes under tension. At the opposite side, damage develops for displacements in negative direction. For larger positive amplitudes damage spreads linearly starting from the nook (see figure 7.6b). With increasing damage the stiffness of the material is reduced which leads to increasing deformations in the area of damaged material and a formation of a crack.

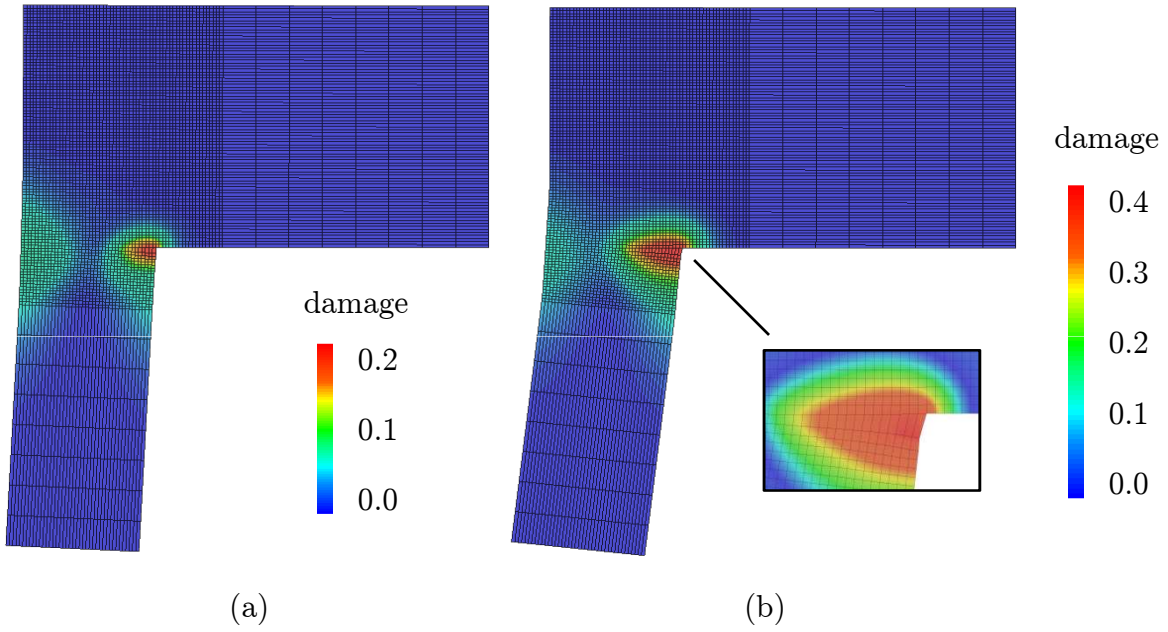

(a) (b)

Figure 7.6: Distribution of damage after cyclic loading for an amplitude of (a) 13 mm and (b) 30 mm

7.4 Bar under uniaxial seismic loading

After having evaluated the structural behavior under regular cyclic loading, a bar is now subjected to seismic loading in order to assess the behavior under irregular cyclic loading. Following [18], the bar is loaded in uniaxial direction with a predefined strain record. The strain record is deduced from the north-south component of the measured ground displacement record of the Kobe earthquake from 1995. Thereby, a displacement of 10 mm is equated with a strain of $\varepsilon = 0.1\%$. The strain velocities can be derived from the measured ground velocity record and lie in a range of $0 < \dot{\varepsilon} < 0.0813 s^{-1}$.
The model parameters are given in table 6.2. They correspond to the steel used within the experiments. Figure 7.7 represents the stress-strain curves obtained experimentally [18] and numerically with the model. It can be seen that the simulation matches the experiment to a high extend. Observable deviations occur only during the first cycle since the model is not able to reproduce the yield plateau.
The experimental and simulated developments of stress also match well. The explosive excitations at the beginning of the earthquake, which are represented by the developments of stress, are characteristic for the short-distance quake of Kobe.

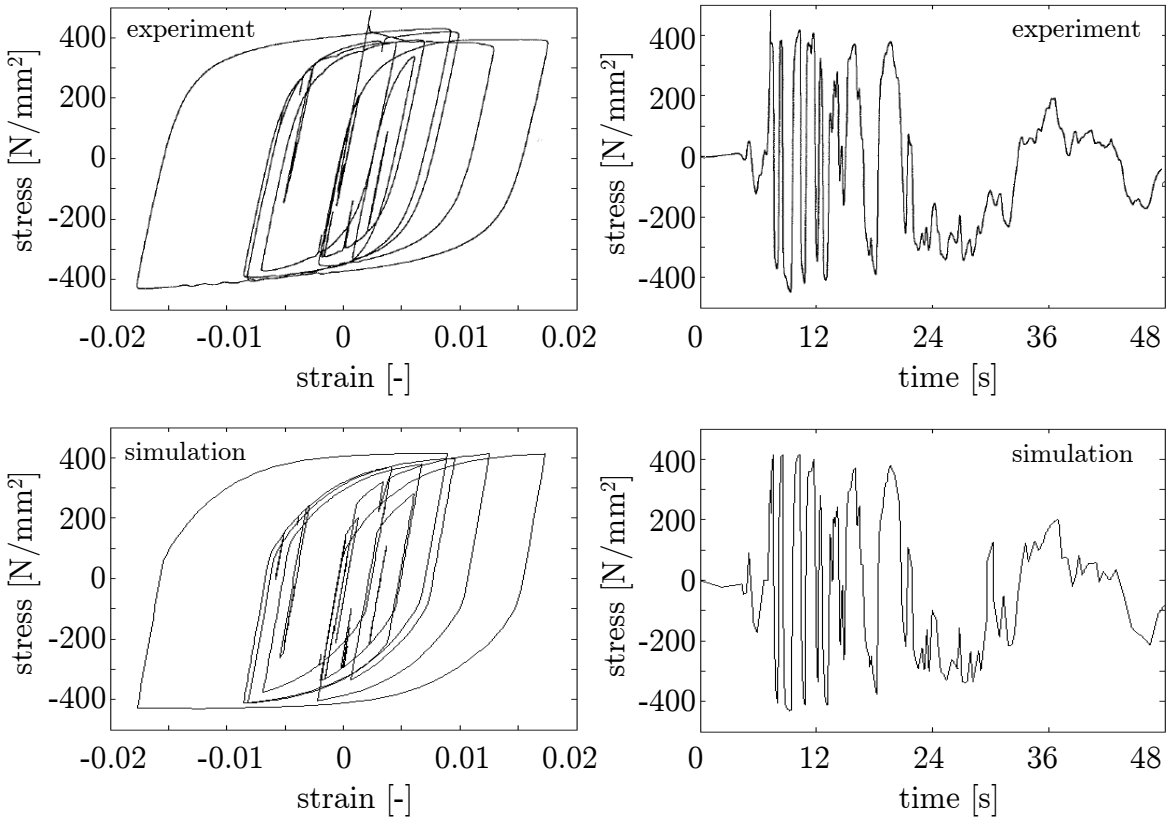

Figure 7.7: Hysteresis curves and development of stress of the Kobe earthquake obtained experimentally [18] and numerically with the model

7.5 3D-cantilever under dynamic excitation

After the material behavior has been evaluated under monotonic and different cyclic loading conditions, the vibration behavior including effects resulting from mass inertia is investigated. The structure under investigation is a cantilever with a length of 5 meters and rectangular cross-section (see figure 7.8). The cantilever is spatially discretized with ten elements in z-direction. The material parameters underlying the following calculations are given in table 6.2.
The eigenfrequencies of the cantilever are given in table 7.2. The knowledge of the eigenfrequencies is important in order to select a suitable time-step width, since the accuracy of time integration approaches depends on the ratio of vibration period T and time-step width Δt. The time integration scheme considered within this work is the Newmark method with the Newmark integration parameters $\gamma = \frac{1}{2}$ and $\beta = \frac{1}{4}$.
Before investigations concerning the choice of an appropriate time-step width are made, the vibration behavior with elastic and inelastic material is tested and the influence of damage on further loading situations is described.

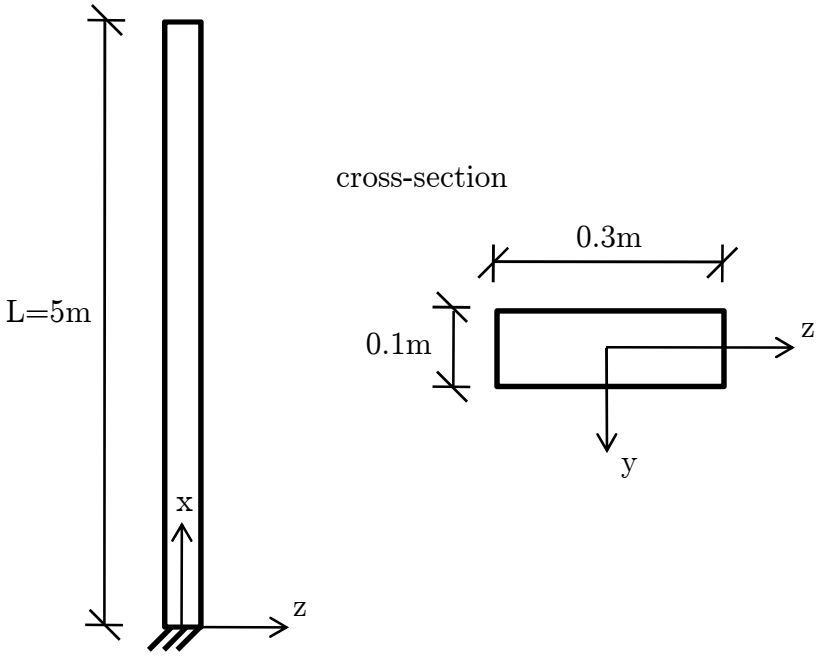

Figure 7.8: Geometry of the cantilever

vibration mode	eigenfrequency [Hz]
1. bending eigenfrequency in y-direction	3.2615
1. bending eigenfrequency in z-direction	9.7845
2. bending eigenfrequency in y-direction	20.7787
3. bending eigenfrequency in y-direction	57.2341
2. bending eigenfrequency in z-direction	62.3360
4. bending eigenfrequency in y-direction	112.2419
3. bending eigenfrequency in z-direction	171.7023
5. bending eigenfrequency in y-direction	185.5238
1. longitudinal eigenfrequency	252.3772

Table 7.2: Eigenfrequencies of the cantilever described in figure 7.8

The influence of inelastic material behavior

In order to investigate the dynamic structural response considering inelastic material behavior the cantilever is subjected to a sinusoidal load shown in figure 7.9a in longitudinal direction. Damping is not considered. The time-step width is taken to $\Delta t = 0.00001$ seconds which corresponds to a ratio $\frac{T}{\Delta t} \approx 400$, which is sufficiently small for not producing erroneous results [8]. Figure 7.9b confirms the agreement between the numerical and analytical elastic response by means of comparison of the top displacement. The numerical solution shows slightly smaller amplitudes than the analytical solution, since the fundamental oscillation with the smallest eigenfrequency of the approximate solution is superimposed with higher eigenmodes so that the first eigenmode of the numerical solution contains less energy than the first eigenmode of the analytical solution.

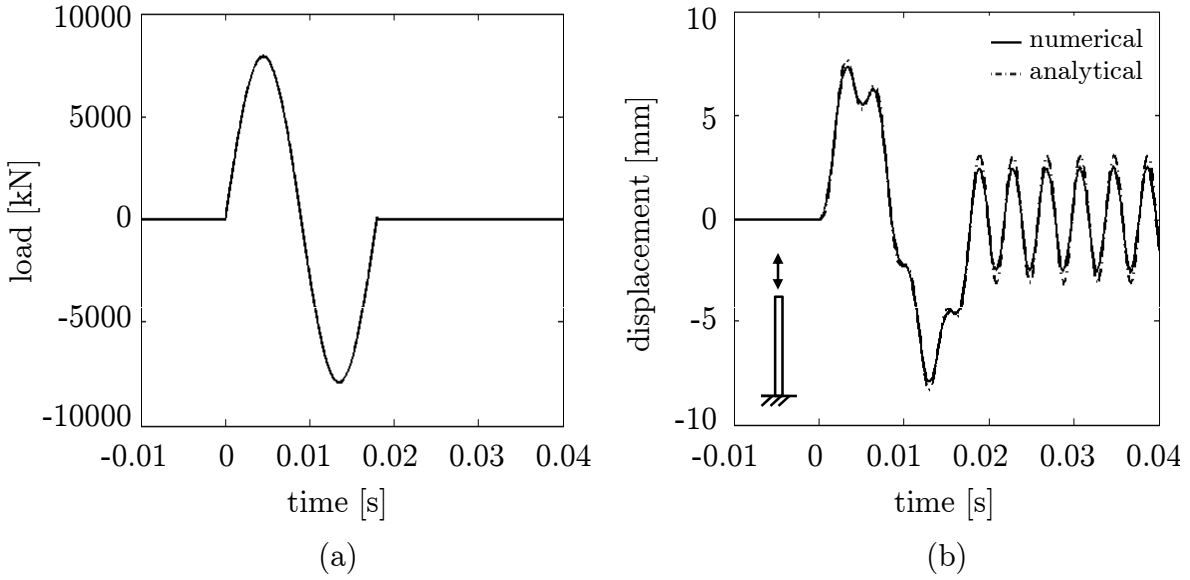

Figure 7.9: (a) loading function and (b) elastic response obtained numerically and analytically

Now, the structural response of the cantilever due to inelastic material behavior is investigated. The results given in figure 7.10a are obtained using a simple model with equal damage evolution under tension and compression and a reduction of stiffness due to damage under compression ($h = 1.0$, see equations (4.73)-(4.77)). It can be seen that the inelastic response yields higher values of top displacement than the elastic response. The steady increase of damage under both tension and compression and reduced stiffness under compression due to damage attenuating the modulus of elasticity leads to a minimum displacement during the second half of the sinusoidal loading which exceeds the minimum value of the elastic response. The vibration period of the free vibration is increased by 7% due to damage.

Figure 7.10b represents the structural behavior using the extended model where damage evolutes only under tension and where a reduction of stiffness due to damage under compression is not considered ($h = 0.0$). The enhanced results indicate that the same maximum displacement as previously is reached under tension. Under compression, on the contrary, damage does not evolute and the original stiffness is reobtained leading to reduced plastic deformations. Thus, the zero position of the free vibration is different from the zero position of the free vibration shown in figure 7.10a.

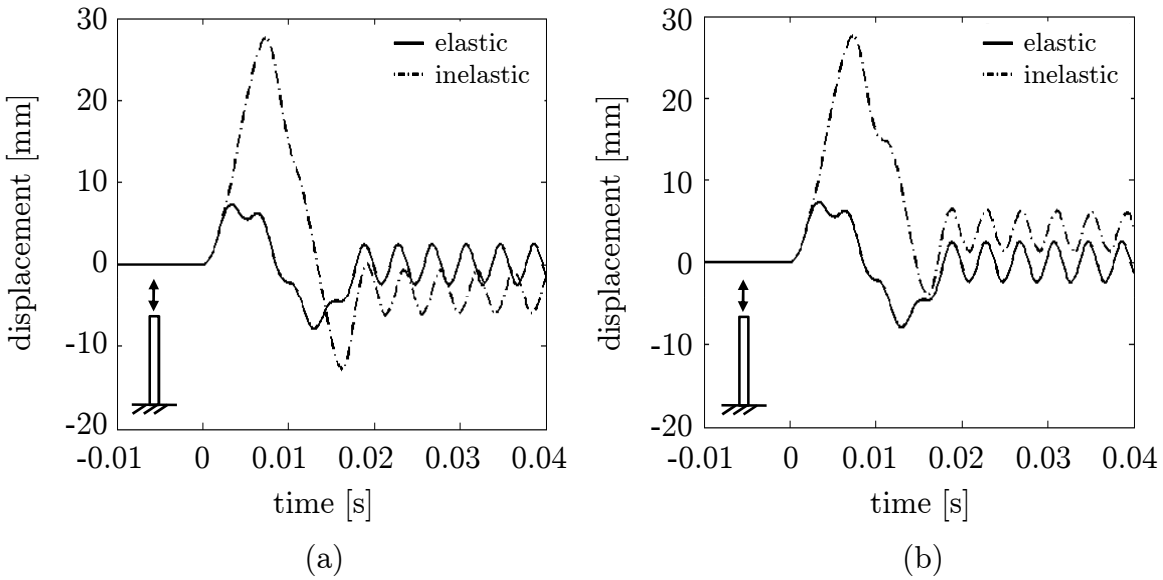

Figure 7.10: Inelastic response for different material behavior considering:
(a) damage evolution and reduction of stiffness under tension and compression,
(b) damage evolution and reduction of stiffness only under tension

The influence of damage on further loading situations

After earthquakes, structures are subjected to their service loads. If an earthquake has caused damage to a structure, the structural behavior deviates from the behavior of the undamaged structure. In order to evaluate the influence of damage caused by earthquakes on structural performance, the cantilever described in figure 7.8 is investigated under constant loading in z-direction. The loading represents a total wind force of $P = 325$ N, which is assumed to act on the top of the cantilever. The top displacement of the undamaged cantilever due to the static load is $w = 0.301$ mm. Table 7.3 presents the percentaged deviations of top displacements of predamaged cantilevers from the top displacement of the undamaged cantilever. As predamage two different values of damage with different volume percent are considered in which damage is assumed to be evenly spread across the cross-section.

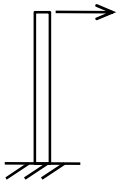	D=0.1	D=0.5
1 vol-% at the base	0.7 %	9.0 %
10 vol-% at the base	6.3 %	81.4 %
10 vol-% in the middle	1.7 %	18.6 %
100 vol-%	23.6%	300.3%

Table 7.3: Increase of top displacement in % due to damage

It can be seen that the top displacement is affected by the amount of damage and the volume percent of damaged material. Increasing amount or volume of damage leads to bigger top displacements. Service loads, which after an earthquake only activate elastic material behavior, thus result in bigger deformations, which influence the structure's serviceability but are not critical in view of structural collapse. However, service loads, which incipiently led to elastic material behavior, may cause inelastic material behavior after an earthquake, since damage reduces the yield surface. If the material behaves inelastically, damage increases further, which is again connected with bigger deformations and a reduction of the yield surface, and can finally lead to the structure's exclusion from further use.

The influence of the time-step width

The accuracy of time integration methods is strongly connected with the selection of an appropriate time-step width. While different recommendations can be found in literature concerning structures subjected to pulse-shaped, harmonic, rectangular, or triangular loading conditions, no consistency is given for the choice of the time-step width for structures subjected to earthquakes. In this section different time-step widths are investigated in order to find a suitable criterion for the selection of the time-step width at seismic loading for further investigations.
In literature, different proposals for the ratio $\frac{T}{\Delta t}$ for the analysis of structures subjected to earthquakes can be found. While Lee and Fenves [79] use a ratio of $\frac{T}{\Delta t} = 70$ in order to investigate the behavior of concrete dams subjected to earthquakes, Cervera et al. [21] base their calculation on a ratio of approximately $\frac{T}{\Delta t} = 160$. For the investigation of reinforced concrete frames under seismic loading Faleiro et al. [46] employ a ratio of $\frac{T}{\Delta t} = 18$. An error estimation for different ratios $\frac{T}{\Delta t}$ was not performed in either of the three cases.
In order to evaluate the influence of the time-step width for seismic excitation, the cantilever described in figure 7.8 is subjected to the north-south component of the Kobe

earthquake from 1995 (see figure 7.12). Linear elastic material behavior and a neglection of damping is assumed. The original acceleration record has a time-step width of $\Delta t = 0.02$ seconds. The cantilever is loaded in x-direction so that the time-step width has to be related to the first eigenfrequency in x-direction $f_{I,x} = 9.78$ Hz. Considering the first vibration period $T = 1/f_{I,x} \approx 0.1$ seconds, six calculations are performed using different ratios $\frac{T}{\Delta t}$. Figure 7.11 represents the results by comparing the maximum top displacement of the solution under investigation with the maximum top displacement of the reference solution with the ratio $\frac{T}{\Delta t} = 200$. It can be seen that calculations performed with ratios $\frac{T}{\Delta t} = 50$ and $\frac{T}{\Delta t} = 100$ both obtain results close to the reference solution. Ratios of $\frac{T}{\Delta t} = 5$, $\frac{T}{\Delta t} = 10$, and $\frac{T}{\Delta t} = 20$ are not recommended for elastic analysis of the structure subjected to the Kobe earthquake.

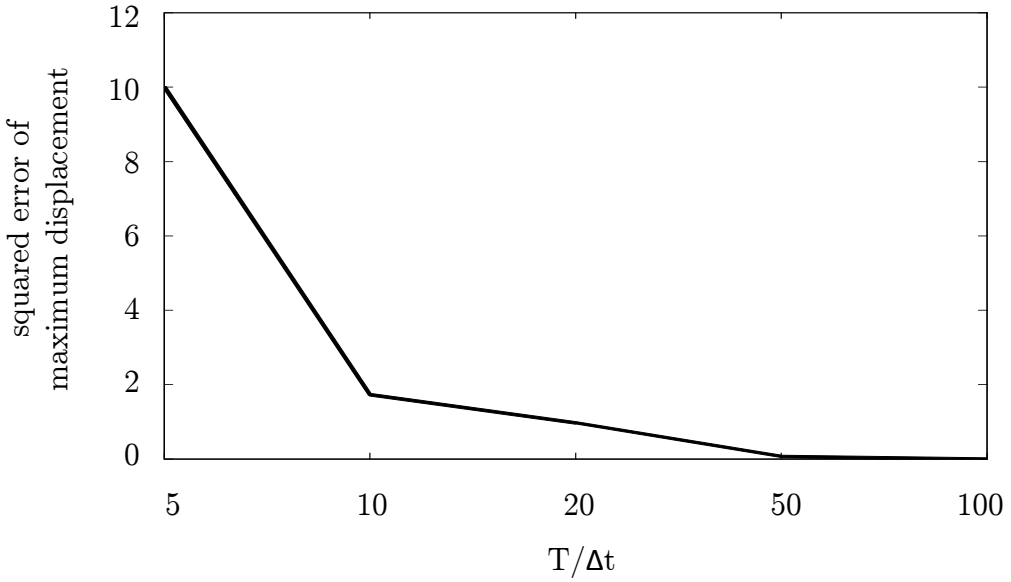

Figure 7.11: Squared error of maximum displacement for different ratios $\frac{T}{\Delta t}$

Another factor which should be considered if the time-step width is not small enough in order to produce a negligible error, is the relation between the eigenfrequency of the structure and the frequency content of the earthquake. Due to the elongation of vibration period using the Newmark method, the eigenfrequency of the structure may be shifted towards frequencies with high energy in the frequency content of the earthquake. Thus, resonance may occur.

Due to the analysis of figure 7.11, a ratio of period and time-step width of $\frac{T}{\Delta t} \geq 50$ is proposed for elastic calculation steps. An adaptive time-step reduction is suggested for inelastic material behavior which is based on a check of convergence of the Newton-Raphson approach. For a realistic description of structures, damping is considered which additionally reduces the effects of resonance in case the eigenfrequency of the structure falls into the range of the frequency content of the earthquake.

7.6 3D-columns under seismic excitation

In the following, structures subjected to seismic loading of the Kobe earthquake from 1995 are evaluated in terms of damage and stability. The selected acceleration record of the north-south component of the Kobe earthquake is shown in figure 7.12. The acceleration record has a length of 40 seconds but the strong motion duration, which can be determined via the Arias intensity [135], is only about 8.4 seconds and is indicated by dotted lines. The sampling frequency of the acceleration record is 50 Hz. The magnitude on the Richter-scale of the Kobe earthquake is 6.9 and the peak ground acceleration is about 0.8 g.

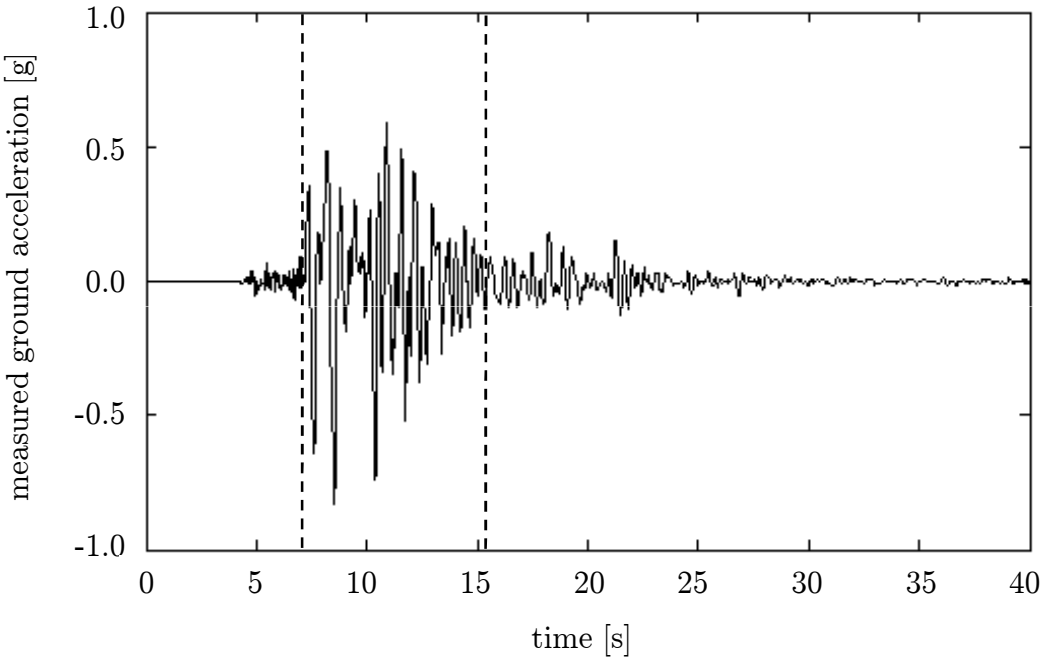

Figure 7.12: Acceleration record of the north-south component of the Kobe earthquake (1995)

The selection of the examples, which are used within this work in order to assess structures under seismic action, is based on some important limiting factors. The limiting factors aim at a small computation time and comprise the choice of structure, dimensioning, and discretization. Therefore, cantilevers are investigated. In order to assess different vibration behaviors, two cantilevers are considered. The first cantilever has a symmetric cross-section (IPE 80 profile, see figure 7.13a). Since the investigations assume that the north-south component of the Kobe earthquakes acts parallel to the web of the profile, the cantilever with symmetric cross-section is only subjected to bending. The second cantilever has an unsymmetric cross-section (U 80 profile, see figure 7.13b) in order to induce both bending and torsion.
Following the investigations in the last preceding section, a ratio $\frac{T}{\Delta t} \geq 50$ is used for calculating the elastic structural response under seismic loading. An additional mass

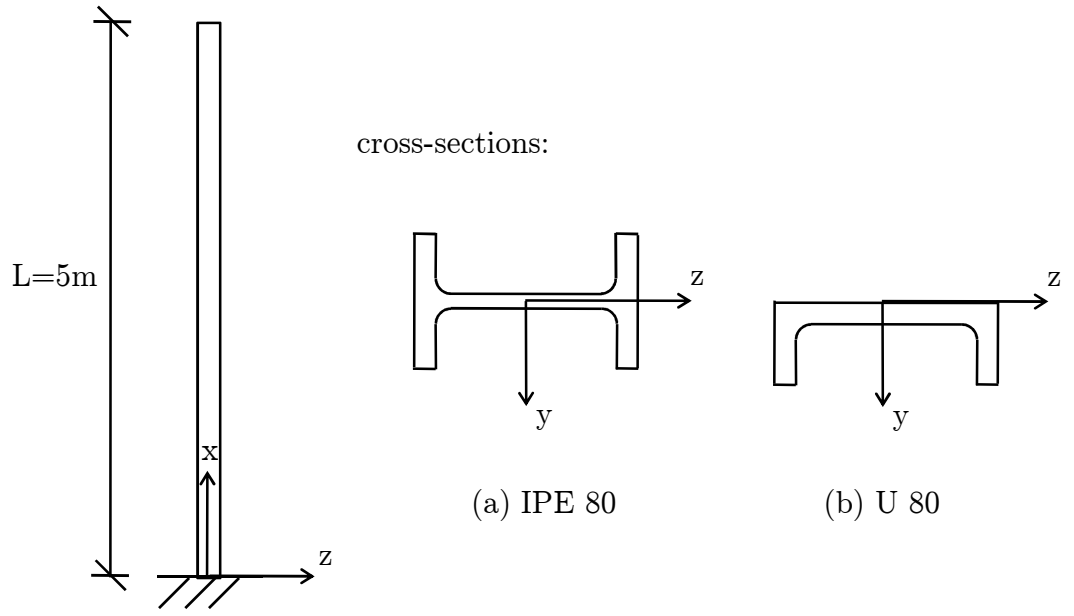

Figure 7.13: Geometries of the cantilevers: (a) IPE 80, (b) U 80

representing connected structural members is assigned to the top of the cantilever. The mass leads to a reduced eigenfrequency and larger top displacements causing inelastic deformations at the base of the cantilever. The eigenfrequency of the fundamental mode in x-direction is adjusted by means of the masses in order to obtain equal fundamental frequencies for both profiles. The time-step width, here set to $\Delta t = 0.01$ seconds, is decreased for time-steps with inelastic material behavior controlled by a check of convergence.
The following examples show columns with a length of 5 meters and either symmetric (IPE-profile) or unsymmetric cross-section (U-profile), which are subjected to seismic loading. The internal length is set to $l_c = 3.5$ mm in order to exceed the maximum element size of 3.2 mm at the base of the structure where damage will occur. The crack closure parameter is assumed to be $h = 0.5$ in order to bisect the influence of damage under compression. The parameters for Newmark integration are set to $\gamma = \frac{1}{2}$ and $\beta = \frac{1}{4}$, which guarantees amplitude conservation. The Rayleigh damping parameters, which can be approximated using the eigenfrequencies of the structure and the damping ratios of the material, are determined as $c_\alpha = 0.01$ and $c_\beta = 0.001$ (see equation 5.34 and 5.35).

7.6.1 3D-column with symmetric cross-section

First, the structure with symmetric cross-section (IPE profile) is subjected to seismic loading. The column is excited by the north-south component of the acceleration record of the Kobe earthquake from 1995 which acts parallel to the web. The accelerations create inertial forces that cause the cantilever to vibrate.

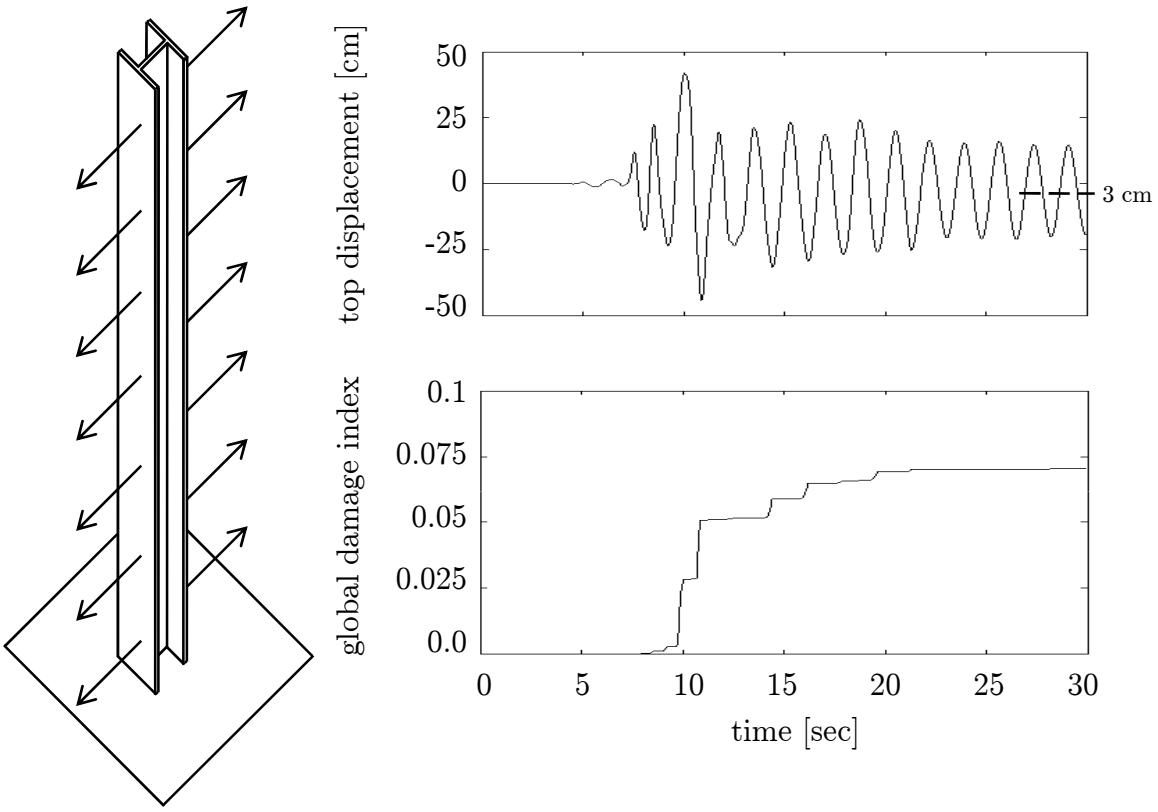

Figure 7.14: Displacement at the top of the column (IPE profile) and evolution of the global damage index GDI_{III} due to the 1995 Kobe earthquake

Figure 7.14 shows the evolution of the displacement at the top of the column and of the global damage index GDI_{III} following equation (4.115). The displacement record can be divided into a forced vibration and a free vibration. During the forced vibration, which takes place roughly between $7-15$ seconds, a maximum top displacement of about 44 cm is reached. The free vibration following the earthquake reveals the first eigenfrequency $f = 0.6$ Hz of the structure. The amplitude of the free vibration is decreasing due to damping. The structure shows a slight permanent deformation of 3 cm, since the free vibration does not occur around its zero position.
The evolution of the global damage index shows that the index increases rapidly for big top displacements. During the free vibration, the index only increases slightly, since the excitation decreases and damping leads to reduced displacement amplitudes. Figure 7.14 also reveals that damage increases only under tension. While the displacement amplitudes increase continuously, the index evolutes for both positive and negative displacements as soon as the absolute value of displacement exceeds the previous absolute maximum value. After the absolute maximum displacement of about 44 cm has been reached, a further increase of the index only takes place for displacements which occur in the same direction as the absolute maximum displacement. This is due to the fact that the index GDI_{III} reflects the maximum obtained amount of damage whose location of

occurrence is fixed with the tension side during the absolute maximum deformation. At the end of the earthquake the index yields a value of 0.071. Following the interpretation proposal for the globale damage index GDI_{III} made in chapter 4.5, this indicates that the column is only slightly damaged and is still in a serviceable condition.

Reliability analysis of structures requires the assessments of structural responses caused by a multitude of different loading histories. In order to investigate the vibration behavior due to varying loading conditions within this work, the cantilever is subjected to a synthetic acceleration record. According to Chiostrini & Facchini [28], the acceleration record is modeled as a stationary process using stationary noise multiplied by a specific function of time, called envelope, which includes information about the original acceleration record. The synthetic acceleration record represents an earthquake with the same intensity as the Kobe earthquake and is depicted in figure 7.15. While the peak ground acceleration is considerably smaller ($PGA = 0.5$ g), the strong motion duration, which is indicated by dotted lines, is longer (12.4 seconds).

The top displacement of the column clearly represents the different character of the synthetic earthquake. The excitation increases slower than for the Kobe earthquake and does not coincide with the first eigenfrequency of the structure at the beginning. During the second half of the strong motion period the excitation amplifies the vibration in the first eigenmode which leads to high values of top displacement. The maximum top displacement is reached after 12.7 seconds and is about 30 cm. After the strong motion period the vibration is only slightly influenced by the acceleration values and the free vibration, which is decreasing due to damping, starts. The column shows a permanent deformation of approximately 1.5 cm.
The evolution of the global damage index corresponds to the development of top displacement and increases for high amplitudes. Again it can be seen that the index only evolutes under tension. At the end of the earthquake the index yields a value of about 0.035. This corresponds to a slightly damaged but still serviceable condition. In comparison with the damage state of the structure after the Kobe earthquake, the synthetic earthquake causes a smaller amount of damage.

7.6.2 3D-column with unsymmetric cross-section

Finally, a three-dimensional column with unsymmetric cross-section (U-profile) is subjected to seismic loading. The excitation by the measured acceleration record of the north-south component of the Kobe earthquake from 1995 acts again parallel to the web. Structures with unsymmetric cross-section, where the loading is not acting on the shear center as it is the case for seismic excitation, exhibit bending as well as torsion.
Figure 7.16 shows the results obtained for the column. Besides the displacement in z-direction, the displacement in y-direction of the top of the flange is depicted. The vibration in z-direction shows a similar displacement development as the IPE profile

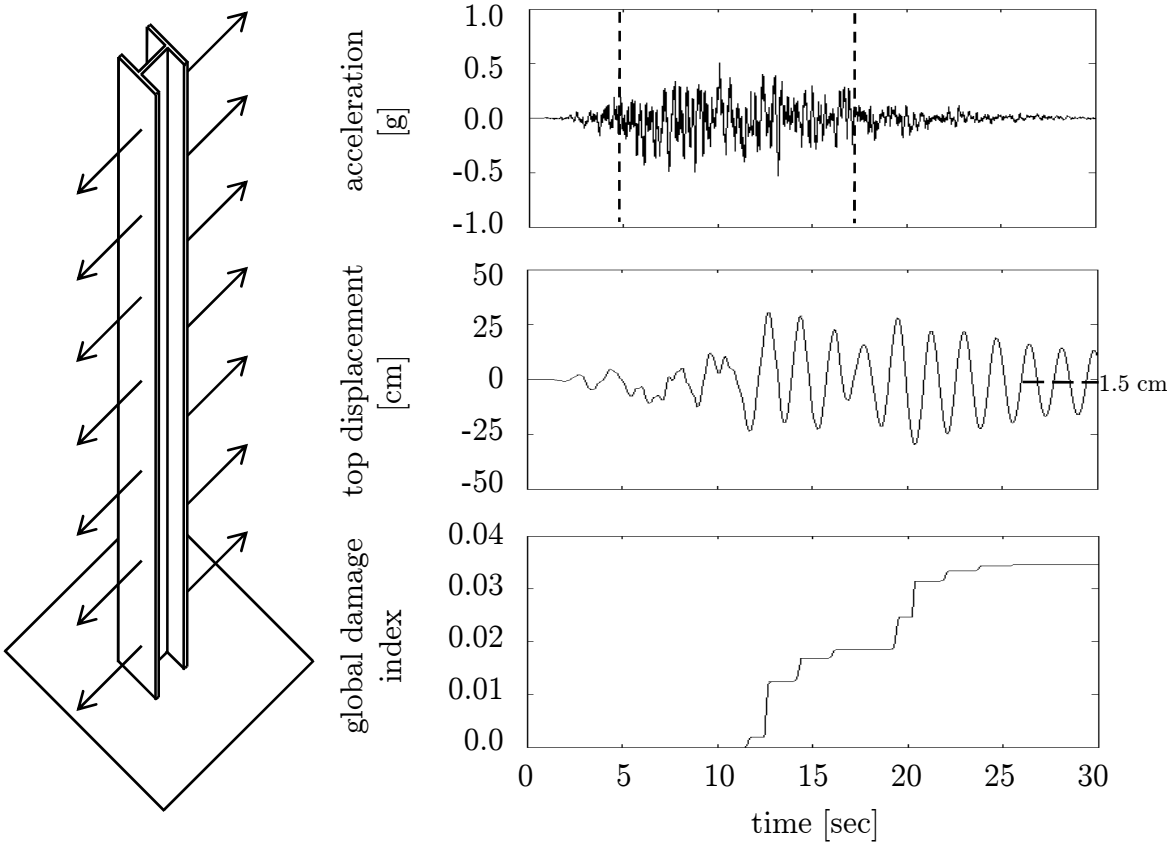

Figure 7.15: Displacement at the top of the column (IPE profile) and evolution of the global damage index GDI_{III} due to a synthetic acceleration record with the same intensity as the 1995 Kobe earthquake

with an eigenfrequency of $f_{B,z} = 0.6$ Hz and a maximum displacement of 44 cm. The vibration in y-direction indicates a superposition of three modes. The mid frequency mode corresponds to a twist in accordance with the bending mode in z-direction while the high frequency mode ($f_T = 2.4$ Hz) is induced by torsion. The low frequency mode corresponds to a bending vibration in y-direction ($f_{B,y} = 0.13$ Hz) which is induced by the seismic excitation due to the unsymmetric cross-section. The superposition of the three modes yields a maximum displacement in y-direction of 3.9 cm. After the earthquake, the higher frequency torsional mode is damped more quickly than the bending modes, so that the twist during the free vibration is related to the bending vibration in z-direction. It can also be seen that the column is permanently deformed. The permanent deformation in z-direction is about 3 cm and in y-direction about 2.5 cm.
The evolution of the global damage index corresponds to the development of displacement and shows that the index only increases under tension. The index reaches a value of 0.068, which indicates that the column is slightly damaged and still serviceable.

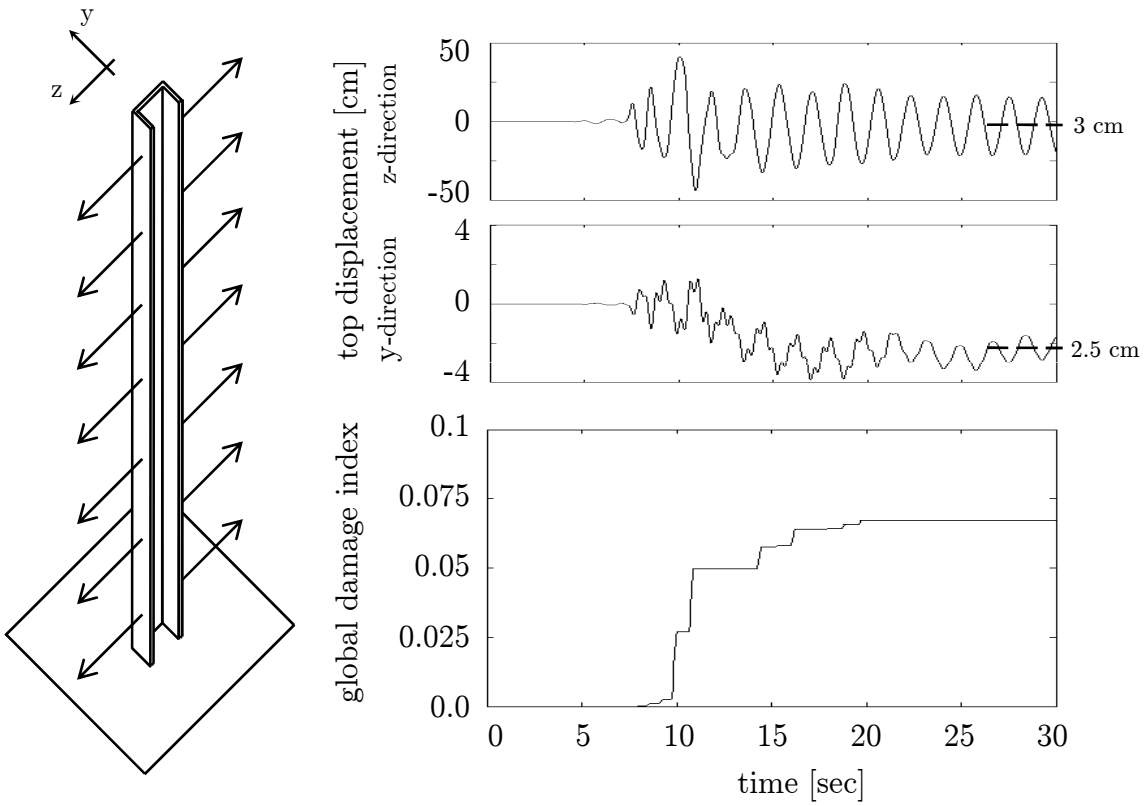

Figure 7.16: Displacements at the top of the column (U profile) and evolution of the global damage index GDI_{III} due to the 1995 Kobe earthquake

The results for the column with unsymmetric cross-section subjected to the synthetic acceleration record are shown in figure 7.17. The development of the top displacement in z-direction confirms the observations already made for the IPE profile, namely the amplification of the vibration in the first eigenmode during the second half of the strong motion period. The maximum top displacement is about 30 cm. The development of the top displacement in y-direction again shows the superposition of the bending modes and the torsional mode. A maximum displacement in y-direction of about 1.4 cm is obtained. Without excitation, it can be seen that the higher frequency torsional mode is damped more quickly than the bending modes, so that the free vibration is mainly characterized by a twist in accordance with the first bending vibration in z-direction. After the synthetic earthquake, the column is permanently deformed in z-direction by 1.5 cm and in y-direction by 0.3 cm.
The evolution of the global damage index is again connected with the development of displacement and reveals that the index only increases under tension. The index reaches a value of about 0.031, which indicates slight damage and a still serviceable condition. The comparison to the IPE shows that both structures suffer similar damages.

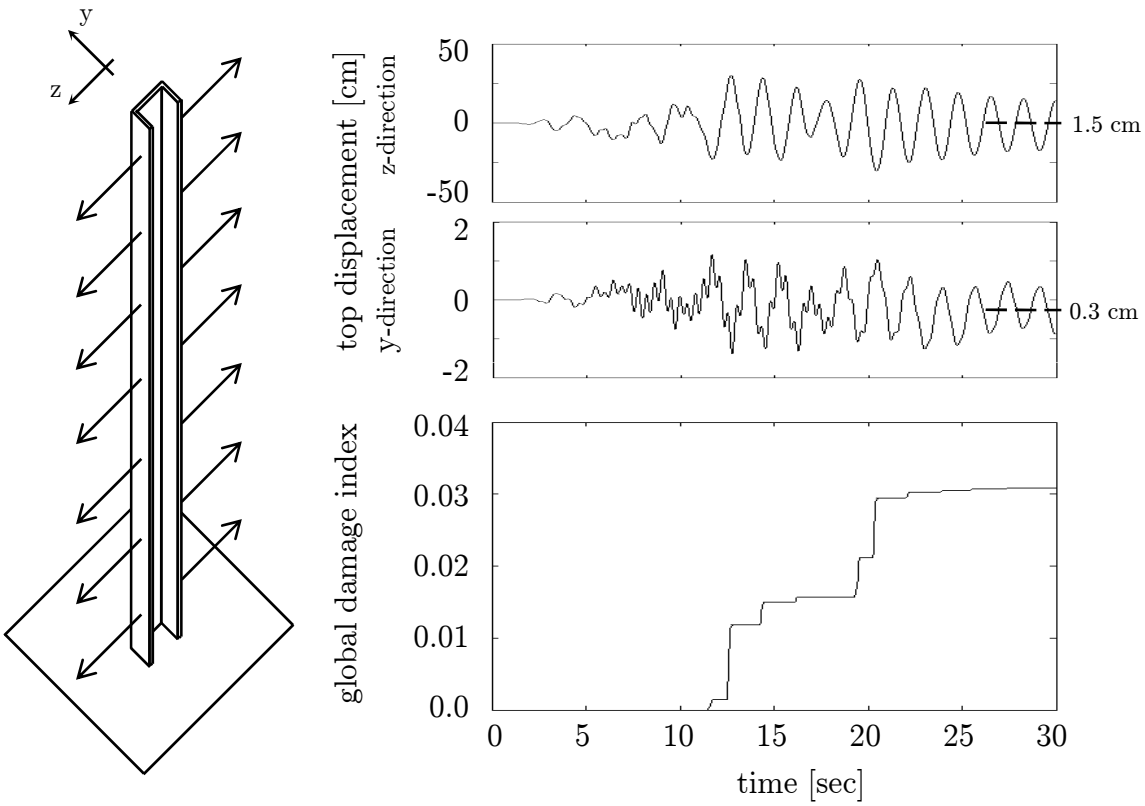

Figure 7.17: Displacements at the top of the column (U profile) and evolution of the global damage index GDI_{III} due to a synthetic acceleration record with the same intensity as the 1995 Kobe earthquake

Comments

The preceding investigations have shown that the proposed model is a powerful tool for the prediction of seismically induced damage. The model provides information about the vibration behavior and the evolution of the material condition. It permits to identify the positions of damage and to quantify the amount of damage locally and globally.
The analyzed structures made of mild structural steel were subjected to two different acceleration records, one representing the north-south component of the Kobe earthquake from 1995 and one being a synthetic acceleration record. The synthetic record which is based on the original Kobe record has the same intensity but shows a variation in the time response. The peak ground acceleration of the synthetic record ($PGA = 0.5$ g) is considerably smaller than the peak ground acceleration of the Kobe record ($PGA = 0.8$ g). In return, the strong motion duration of the synthetic record (12.4 seconds) is longer than the one of the Kobe record (8.4 seconds). Regardless of these facts the structures do not show the same amount of global damage after the earthquakes. This may be due to the explosive excitations at the beginning of the Kobe earthquake which are not present in the synthetic record. The Kobe earthquakes causes a strong increase in global

damage within the first seconds of vibration since the explosive excitations lead to a quick activation and amplification of the vibration in its first eigenmode combined with inelastic deformations. The synthetic earthquake activates this vibration more slowly and leads to smaller top displacements. Thus, less inelastic deformations occur and the global damage index yields a smaller value than for the original acceleration record. Investigations of the frequency content of both records confirm that frequencies close to the eigenfrequency of the first vibration mode are contained three times stronger in the Kobe record than in the synthetic record and underline that the amount of damage in a structure subjected to an earthquake strongly depends on the relation between the eigenfrequencies of the structure and the frequency content of the earthquake.
For both excitations the structures show only minor damage. On the one hand, this is due to the simple structure of a cantilever, which was chosen in order to reduce the computation time. More complex structures like frame structures have bigger masses and exhibit higher stresses and damage in the area of connections under seismic action. On the other hand, the damage parameters determine the amount of damage. A wider basis of experimental investigations will allow a more accurate adjustment of the model parameters including the size of the internal length.
Increasing computing power and high performance computations will additionally enable investigations of complex and therewith even more realistic examples including a high fineness of discretization in space and time.

8 Summary and outlook

In the past, earthquakes have caused immense damages to the human built environment which created the need for tools being able to cope with the unpredictable nature of this hazard. One fundamental tool helping to calculate the expected number of losses due to seismic catastrophes and helping to make decisions to reduce the losses is risk management. The vulnerability assessment as part of seismic risk management comprises mathematical tools for the prediction of seismic damage. The variety of methods in order to assess structural vulnerability is wide and offers results with different accuracy varying from simple practical approaches to complex numerical time domain analyses under consideration of the required material behavior. Due to the increase of computing power, methods based on numerical time integration become more and more practicable. Into those models the material behaviour can be embedded with different approaches up to an arbitrary level of precision.

Within this work, a new approach is developed in order to evaluate seismic damage of steel structures using continuum damage mechanics and numerical time integration of the equation of motion. The model uses the finite-element method for spatial discretization while discretization in time is performed using the Newmark method. The material model considers viscoplasticity, isotropic and kinematic hardening and ductile damage. The approach is modeled within the framework of thermodynamics and is based on evolution equations of internal variables which characterize the state of the material. The time-dependent constitutive equations are solved with the implicit Euler approach.

The main focus of this work is on the description of damage evolution under seismic loading. Since earthquakes cause large cyclic inelastic strains in the material, a ductile damage evolution law is considered and extended in order to correctly represent damage evolution due to alternating stress states.

Softening and damage are always accompanied by localization of the deformation field. Within this work, the phenomenon of strain localization and its mesh-independent modeling is taken into account by a nonlocal implicit gradient enhanced extension including an additional partial differential equation for the nonlocal damage variable.

In order to assess not only the material behavior at the material points but also the consequences for the whole structure, different global damage indices are investigated. The global damage index proposed within this work is based on the eigenvalue decomposition of the initial and the current stiffness matrix where the latter considers a reduction of the modulus of elasticity due to damage.

Since models based on continuum damage mechanics have mainly been applied to mechanical engineering steel, the model is adapted in order to adequately represent the special behavior of mild structural steel which is used for civil engineering steel structures. The model parameters are obtained from monotonic and cyclic tests on specimens made of the structural steel S 355. In order to obtain a sufficient basis of experimental

data new experiments have been conducted. The applied parameter identification procedure is based on genetic algorithms.
After a suitable set of model parameters has been identified, the ability of the model is shown by means of different tests under static and dynamic loading conditions. The accuracy of the damage model is proven by tests on CT-specimens and comparison with experimental data. Cyclic tests on simple specimens are used in order to estimate the material behavior under alternating tension and compression. The combination of damage and structural dynamics is evaluated using cantilevers. Finally, three-dimensional structures under seismic loading are analyzed and assessed with respect to damage and stability using the newly defined global damage index.
The results indicate that the proposed model is a valuable tool for predicting damage in steel structures and can be of great help in order to evaluate the vulnerability, safety, and residual life time of steel structures after seismic excitation.
Future trends towards increasing computing power and high performance computations using e.g. parallel computing will allow the investigation of complex three-dimensional structures and improve the practicability of the proposed model. Especially for irregular structure where simplified approaches cannot be applied, the model is of great benefit. Further requirements and extensions can easily be embedded into the model.

References

[1] Abdul-Latif, A., and Chadli, M. Modeling of the heterogeneous damage evolution at the granular scale in polycrystals under complex cyclic loadings. *International Journal of Damage Mechanics 16* (2007), 133–158.

[2] Ahrens, H., and Dinkler, D. *Finite-Element-Methoden Teil II.* Institut für Statik, TU Braunschweig, 1996.

[3] Ahrens, H., and Dinkler, D. *Finite-Element-Methoden Teil I.* Institut für Statik, TU Braunschweig, 2006.

[4] Allemang, R., and Brown, D. A correlation coefficient for modal vector analysis. *Proceedings of the 1st International Modal Analysis Conference* (1982).

[5] Alves, M. Measurement of ductile material damage. *Mechanics Based Design of Structures and Machines 29* (2001), 451–476.

[6] Ambroziak, A., and Klosowski, P. The elasto-viscoplastic Chaboche model. *TASK Quarterly 10* (2006), 49–61.

[7] Bachmann, H. *Erdbebensicherung von Bauwerken.* 2002.

[8] Bathe, K.-J. *Finite-Elemente-Methoden.* Springer-Verlag, Berlin, 1990.

[9] Bazant, Z. Instability, ductility, and size effect in strain-softening concrete. *Journal of Engineering Mechanics Division 102* (1976), 331–334.

[10] Bazant, Z., and Belytschko, T. Wave propagation in a strain-softening bar: Exact solution. *Journal of Engineering Mechanics 111* (1985), 381–389.

[11] Bazant, Z., and Jirasek, M. Nonlocal Integral Formulations of Plasticity and Damage: Survey of Progress. *Journal of Engineering Mechanics 128* (2002), 1119–1149.

[12] Bazant, Z., and Pijaudier-Cabot, G. Nonlocal continuum damage, localization instability and convergence. *Journal of Applied Mechanics 55* (1988), 287–293.

[13] Belytschko, T., Liu, W., and Moran, B. *Nonlinear Finite Elements for Continua and Structures.* John Wiley & Sons, 2000.

[14] Benavent-Climent, A. An energy-based damage model for seismic response of steel structures. *Earthquake Engineering and Structural Dynamics 36* (2007), 1049–1064.

[15] Bleck, W., Dahl, W., Nonn, A., Amlung, L., Feldmann, M., Schäfer, D., and Eichler, B. Numerical and experimental analyses of damage behaviour of steel moment connection. *Engineering Fracture Mechanics 76* (2009), 1531–1547.

[16] Bonora, N., Gentile, D., Pirondi, A., and Newaz, G. Ductile damage evolution under triaxial state of stress - theory and experiments. *International Journal of Plasticity 21* (2005), 981–1007.

[17] Bracci, J., Reinhorn, A., Mander, J., and Kunnath, S. Deterministic model for seismic damage evaluation of RC structures. Tech. Rep. NCEER-89-0033, National Center for Earthquake Engineering Research, State University of New York, Buffalo NY, 1989.

[18] Böttcher, C. *Geschwindigkeitssensitivität des mechanischen Verhaltens unlegierter Baustähle bei wiederholter Beanspruchung bis in den inelastischen Bereich - experimentelle Untersuchung und Modellierung.* Fortschritt-Berichte VDI Reihe 5, Nr. 654, 2002.

[19] Calayir, Y., and Karaton, M. A continuum damage concrete model for earthquake analysis of concrete gravity dam-reservoir systems. *Soil Dynamics and Earthquake Engineering 25* (2005), 857–869.

[20] Carmeliet, J. Optimal estimation of gradient damage parameters from localization phenomena in quasi-brittle materials. *Mechanics of Cohesive-Frictional Materials 4* (1999), 1–16.

[21] Cervera, M., Oliver, J., and Manzoli, O. A rate-dependent isotropic damage model for the seismic analysis of concrete dams. *Earthquake Engineering & Structural Dynamics 25* (1996), 987–1010.

[22] Chaboche, J. Le Concept de Constrainte Effective Appliqué à l'Elasticité et à la Viscoplasticité en Présence d'un Endommagement Anisotrope. *Proceedings of the Euromech Colloquium 115* (1982), 737–760.

[23] Chaboche, J. Continuum damage mechanics: Present state and future trends. *Nuclear Engineering and Design 105* (1987), 19–33.

[24] Chaboche, J., Dang Van, K., and Cordier, G. Modelization of the strain memory effect on the cyclic hardening of 316 stainless steel. *Transaction of the 5th International Conference on Structural Mechanics in Reactor Technology L* (1979), Paper No. L11/3, Berlin, Germany.

[25] Chaboche, J., and Rousselier, G. On the Plastic and Viscoplastic Constitutive Equations - Part I: Rules Developed with Internal Variable Concept. *Journal of Pressure Vessel Technology 105* (1983), 153–158.

[26] Chaboche, J., and Rousselier, G. On the Plastic and Viscoplastic Constitutive Equations - Part II: Application of Internal Variable Concept to the 316 Stainless Steel. *Journal of Pressure Vessel Technology 105* (1983), 159–164.

[27] Chen, W., and Scawthorn, C. *Earthquake Engineering Handbook*. 2003.

[28] Chiostrini, S., and Facchini, L. Response analysis under stochastic loading in presence of structural uncertainties. *International Journal for Numerical Methods in Engineering 46* (1999), 853–870.

[29] Chow, C., and Wang, J. A continuum damage mechanics model for crack initiation in mixed mode ductile fracture. *International Journal of Fracture 47* (1991), 145–160.

[30] Chu, C., and Needleman, A. Void nucleation effects in biaxially stretched sheets. *Journal of Engineering Materials and Technology 102* (1980), 249–256.

[31] Chung, Y., Meyer, C., and Shinozuka, M. Automatic seismic design of reinforced concrete building frames. *Structural Journal, American Concrete Institute 87* (1990), 326–340.

[32] Colliat, J.-B., Hautefeuille, M., Ibrahimbegovic, A., and Matthies, H. Stochastic approach to size effect in quasi-brittle materials. *Comptes Rendus Mecanique 335* (2007), 430–435.

[33] Colombo, A., and Negro, P. A damage index of generalised applicability. *Engineering Structures 27* (2005), 1164–1174.

[34] Cordebois, J., and Sidoroff, F. Damage Induced Elastic Anisotropy. *Proceedings of the Euromech Colloquium 115* (1982), 761–774.

[35] Cosenza, E., and Manfredi, G. Damage indices and damage measures. *Progress in Structural Engineering and Materials 2* (2000), 50–59.

[36] Cosserat, E., and Cosserat, F. *Theorie des corps deformable*. Herman et files, 1909.

[37] Cotterell, M., Schambergerova, J., Ziegelheim, J., and Janovec, J. Dependence of micro-hardness on deformation of deep-drawing steel sheets. *Journal of Materials Processing Technology 124* (2002), 293–296.

[38] Cottrell, A. The relation between structure and mechanical properties of metals. *Proceedings of the 15. NPL-Symposium, Teddington, 456-473* (1963).

[39] Dannemeyer, S. *Zur Änderung der Fließfläche von Baustahl bei mehrachsiger plastischer Wechselbeanspruchung*. PhD thesis, Institut für Stahlbau, TU Braunschweig, 1999.

[40] Dazio, A. Antwortspektren. *Tagungsband "Erdbebenbemessung mit den neuen SIA-Tragwerksnormen". Zürich (10 pp)* (2004).

[41] De Borst, R., and Mühlhaus, H.-B. Gradient-dependent plasticity: Formulation and algorithmic aspects. *International Journal for Numerical Methods in Engineering 35* (1992), 521–539.

[42] DIN EN 10025. Warmgewalzte Erzeugnisse aus Baustählen. Tech. rep., Deutsches Institut für Normung (DIN), 02:2005.

[43] DiPasquale, E., Ju, J.-W., Askar, A., and Cakmak, A. Relation betwenn global damage indices and local stiffness degradation. *Journal of Structural Engineering 116* (1990), 1440–1456.

[44] Engelen, R., Geers, M., and Baaijens, F. Nonlocal implicit gradient-enhanced elasto-plasticity for the modelling of softening behaviour. *International Journal of Plasticity 19* (2003), 403–433.

[45] Fahr, A., Chapman, C., Laliberte, J., Forsyth, D., and Poon, C. Nondestructive evaluation methods for damage assessment in fibre-metal laminates. *Polymer Composites 21* (2000), 568–575.

[46] Faleiro, J., Oller, S., and Barbat, A. Plastic-damage seismic model for reinforced concrete frames. *Computers and Structures 86* (2008), 581–597.

[47] Fleck, N., and Hutchinson, J. *Strain Gradient Plasticity.* In: Hutchinson, J.W. and Wu, T.Y., Advances in Applied Mechanics 33, Academic Press, New York, 1997, pp. 287–293.

[48] Geers, M., de Borst, R., Brekelmans, W., and Peerlings, R. Validation and internal length scale determination for a gradient damage model: application to short glass-fibre-reinforced polypropylene. *International Journal of Solids and Structures 36* (1999), 2557–2583.

[49] Ghobarah, A., Abou-Elfath, H., and Biddah, A. Response-based damage assessment of structures. *Earthquake Engineering and Structural Dynamics 28* (1999), 79–104.

[50] Giovinazzi, S. *The vulnerability assessment and the damage scenario in seismic risk analysis.* PhD thesis, Università degli Studenti di Firenze, 2005.

[51] Giurgiutiu, V., and Cuc, A. Embedded non-destructive evaluation for structural health monitoring, damage detection, and failure prevention. *The Shock and Vibration Digest 37* (2005), 83–105.

[52] Goods, S., and Brown, L. The nucleation of cavities by plastic deformation. *Acta Metallica 27* (1979), 1–15.

[53] Gorman, M. Plate wave acoustic emission. *Journal of the Acoustical Society of America 90* (1991), 358–364.

[54] Guelorget, B., Francois, M., and Lu, J. Microindentation as a local damage measurement technique. *Materials letters 61* (2007), 34–36.

[55] Gurson, A. Continuum Theory of Ductile Rupture by Void Nucleation and Growth: Part I - Yield Criteria and Flow Rules for Porous Media. *Journal of Engineering Materials and Technology 99* (1977), 2–15.

[56] Hayhurst, D. Creep Rupture under multi-axial states of stress. *Journal of the Mechanics and Physics of Solids 20* (1972), 381–390.

[57] Hoefnagels, J., Tasan, C., Louws, L., and Geers, M. Comparison of quantitative damage characterization methodologies. *Proceedings of the 12th International Conference on Fracture* (2009).

[58] Hornbogen, E., and Warlimont, H. *Metalle: Struktur und Eigenschaften der Metalle und Legierungen.* Springer, 2006.

[59] Hughes, T. *The Finite Element Method - Linear Static and Dynamic Finite Element Analysis.* Prentice-Hall, New Jersey, 1987.

[60] Hunsche, A., and Neumann, P. Quantitative measurement of persistent slip band profiles and crack initiation. *Acta Metallurgica 34* (1986), 207–217.

[61] Hwang, B., Lee, S., Kim, Y., Kim, N., and Shin, D. Microstructural development of adiabatic shear bands in ultra-fine-grained low-carbon steels fabricated by equal channel angular pressing. *Material Science and Engineering A 441* (2006), 308–320.

[62] Jeong, G., and Iwan, W. Effect of earthquake duration on the damage of structures. *Earthquake Engineering and Structural Dynamics 16* (1988), 1201–1211.

[63] Jirasek, M., and Rolshoven, S. *Regularized Formulations of Strain-Softening Plasticity.* In: Kolymbas, D., Advanced Mathematical and Computational Geomechanics, Springer, 2003, pp. 269–299.

[64] Kachanov, L. On Creep Rupture Time. *Izvestija Akademii Nauk SSSR 8* (1985), 25–31.

[65] Kachanov, L. *Introduction to continuum damage mechanics.* Martinus Nijhoff, 1986.

[66] Kang, G., Gao, Q., and Yang, X. A visco-plastic constitutive model incorporated with cyclic hardening for uniaxial/multiaxial ratcheting of SS 304 stainless steel at room temperature. *Mechanics of Materials 34* (2002), 521–531.

[67] Kanvinde, A., and Deierlein, G. Cyclic void growth model to assess ductile fracture initiation in structural steels due to ultra low cycle fatigue. *Journal of Engineering Mechanics 133* (2007), 701–712.

[68] Khashaee, P. Damage-based Seismic Design of Structures. *Earthquake Spectra 21* (2005), 371–387.

[69] Kowalsky, U., Zümendorf, T., and Dinkler, D. Random fluctuations of material behaviour in FE-damage-analysis. *Computational Materials Science 39* (2007), 8–16.

[70] Kreiser, D., Jia, S., Han, J., and Dhanasekar, M. A nonlinear damage accumulation model for shakedown failure. *International Journal of Fatigue 29* (2007), 1523–1530.

[71] Krätzig, W., Meyer, I., and Meskouris, K. Damage evolution in reinforced concrete members under cyclic loading. *Proceedings of the 5th International Conference on Structural Safety and Realiability (ICOSSAR 89), San Francisco CA 2* (1989), 795–802.

[72] Krätzig, W., and Petryna, Y. Structural damage and life-time estimates by nonlinear FE simulation. *Engineering Structures 27* (2005), 1726–1740.

[73] Krümmling, S. *Schallemissionsanalyse zum Nachweis der Materialermüdung von Baustahl*. PhD thesis, Institut für Stahlbau, TU Braunschweig, 1999.

[74] Kuck, D. *Experimentelle Untersuchungen zum Ratchetting-Verhalten bei Baustahl St52-3*. PhD thesis, Institut für Stahlbau, TU Braunschweig, 1996.

[75] Kunnath, S., Reinhorn, A., and Park, Y. "analytical modeling of inelastic seismic response of r/c structures". *Journal of Structural Engineering 116* (1990), 996–1017.

[76] Lange, G. *Systematische Beurteilung technischer Schadensfälle*. 5. Auflage, Wiley, Weinheim, 2001.

[77] Lasry, D., and Belytschko, T. Localisation limiters in transient problems. *International Journal of Solids and Structures 24* (1988), 581–597.

[78] Leblond, J., Perrin, G., and Devaux, J. An improved Gurson-type model for hardenable ductile metals. *European Journal of Mechanics and Solids 14* (1995), 499–527.

[79] Lee, J., and Fenves, G. A plastic-damage concrete model for earthquake analysis of dams. *Earthquake Engineering & Structural Dynamics 27* (1998), 937–956.

[80] Lemaitre, J. *A Course on Damage Mechanics*. Springer, 1992.

[81] Lemaitre, J., and Chaboche, J.-L. *Mechanics of solid materials.* Cambridge, 1990.

[82] Lemaitre, J., and Dufailly, J. Damage measurements. *Engineering Fracture Mechanics 28*, 5-6 (1987), 643 – 661.

[83] Leppin, C. *Ein diskontinuierliches Finite-Elemente-Modell für Lokalisierungsversagen in metallischen und granularen Materialien.* PhD thesis, Institut für Baustatik und Numerische Methoden, Universität Hannover, 2000.

[84] Liebe, T., and Steinmann, P. Theory and numerics of a thermodynamically consistent framework for geometrically linear gradient plasticity. *International Journal for Numerical Methods in Engineering 51* (2001), 1437–1467.

[85] Lieven, N., and Ewins, D. Spatial correlation of mode shapes the coordinate modal assurance criterion (COMAC). *Proceedings of the 6th International Modal Analysis Conference* (1988).

[86] Maire, E., Bouaziz, O., Di Michiel, M., and Verdu, C. Initiation and growth of damage in a dual-phase steel observed by X-ray microtomography. *Acta Materialia 56* (2008), 4954–4964.

[87] Mata, P., Barbat, A., Oller, S., and Boroschek, R. Non-linear seismic analysis of RC structures with energy-dissipating devices. *International Journal for Numerical Methods in Engineering 78* (2009), 1037–1075.

[88] Medgenberg, J. *Investigation of localized fatigue properties in unalloyed steels by infrared thermography.* PhD thesis, Institut für Bauwerkserhaltung und Tragwerk, TU Braunschweig, 2008.

[89] Mediavilla, J., Peerlings, R., and Geers, M. A nonlocal triaxiality-dependent ductile damage model for finite strain plasticity. *Computer Methods in Applied Mechanics and Engineering 195* (2006), 4617–4634.

[90] Mkaddem, A., Gassara, F., and Hambli, R. A new procedure using the microhardness technique for sheet material damage characterisation. *Journal of Materials Processing Technology 178* (2006), 111–118.

[91] Mohrmann, R., and Sester, M. *A Multiaxial Model for the Evolution of the Microstructure and for the Mechanical Behaviour of a 12% Chromium Steel under Creep Conditions.* In: Mughrabi, H., Microstructure and Mechanical Properties of Metallic High-Temperature Materials, 1999, pp. 206–221.

[92] Murakami, S. *Anisotropic damage in metals.* In: Boehler, Failure criteria of structured media, Balkema, 1993, pp. 99–119.

[93] Murakami, S., and Ohno, N. *A Continuum Theory of Creep and Creep Damage.* In: Hayhurst, Ponter, Creep in Structures, Springer Verlag, 1981, pp. 422–443.

[94] Mühlhaus, H.-B., and Aifantis, E. A variational principle for gradient plasticity. *International Journal of Solids and Structures 28* (1991), 845–857.

[95] Neilson, M., and Schreyer, H. Bifurcations in elastic-damaging materials. *Damage Mechanics and Localization 142* (1992), 53–67.

[96] Newmark, N. A method of computation for structural dynamics. *ASCE Journal of the Engineering Mechanics Division 85* (1959).

[97] Niessner, M., Seeger, T., Hohe, J., and Siegele, D. Festigkeitsberechnung scharf gekerbter Bauteile. *Materialwissenschaft und Werkstofftechnologie 34* (2003), 797–811.

[98] Ohata, M., and Toyoda, M. Damage concept for evaluating ductile cracking of steel structure subjected to large-scale cyclic straining. *Science and Technology of Advanced Materials 5* (2004), 241–249.

[99] Oliver, W., and Pharr, G. A new improved technique for determining hardness and elastic modulus using load and sensing indentation experiments. *Journal of Materials Research 7* (1992), 1564–1582.

[100] Pamin, J., and de Borst, R. Simulation of crack spacing using a reinforced concrete model with an internal length parameter. *Archive of Applied Mechanics 68* (1998), 613–625.

[101] Pandey, A., and Biswas, M. Experimental verification of flexibility difference method for locating damage in structures. *Journal of Sound and Vibration 184* (1995), 311–328.

[102] Pandey, A., Biswas, M., and Samman, M. Damage detection from changes in curvature mode shapes. *Journal of Sound and Vibration 145* (1991), 321–332.

[103] Park, Y., and Ang, A.-S. Mechanistic seismic damage model for reinforced concrete. *Journal of Structural Engineering 111* (1985), 722–739.

[104] Park, Y., Ang, A.-S., and Wen, Y. Seismic damage analysis of reinforced concrete buildings. *Journal of Structural Engineering 111* (1985), 740–757.

[105] Peerlings, R., de Borst, R., Brekelmans, W., and de Vree, J. Gradient enhanced damage for quasi-brittle materials. *International Journal for Numerical Methods in Engineering 39* (1996), 3391–3403.

[106] Peerlings, R., de Borst, R., Brekelmans, W., and Geers, M. Gradient-enhanced damage modelling of concrete fracture. *Mechanics of Cohesive-Frictional Material 3* (1998), 323–342.

[107] Peil, U., and Loppe, S. Detection of structural changes by means of piezo discs. *Proceedings of the Third European Workshop on Structural Health Monitoring* (2006).

[108] Peil, U., Scheer, J., Scheibe, H.-J., Reininghaus, M., Kuck, D., and Dannemeyer, S. *On the Behaviour of Mild Steel Fe 510 under Complex Cyclic Loading.* In: Steck, E., Ritter, R., Peil, U. and Ziegenbein, A., Plasticity of Metals: Experiments, Models, Computation, Wiley-VCH, 2001, pp. 218–252.

[109] Pensky, H. *Beschreibung von Materialverhalten und von Schädigung bei inelastischen Werkstoffen.* PhD thesis, Institut für Statik, TU Braunschweig, 2000.

[110] Petersen, C. *Dynamik der Baukonstruktionen.* Vieweg, Braunschweig; Wiesbaden, 1996.

[111] Petryna, Y., and Krätzig, W. On sensitivity of structural damage measures to stochastic uncertainties. *WCCM V, Vienna* (2002).

[112] Pirondi, A., and Bonora, N. Modeling ductile damage under fully reversed cycling. *Computational Material Science 26* (2003), 129–141.

[113] Pliefke, T., Sperbeck, S., Urban, M., Peil, U., and Budelmann, H. A Standardized Methodology for Managing Disaster Risk - An Attempt to Remove Ambiguity. *5th International Probabilistic Workshop, Ghent* (2007).

[114] Pohlheim, H. Geatbx introduction - evolutionary algorithms: overview, methods, operators. *http://www.geatbx.com* (2005).

[115] Rabotnov, Y. *Creep Problems in Structural Members.* Amsterdam, 1969.

[116] Reusch, F., Svendsen, B., and Klingbeil, D. Local and non-local Gurson-based ductile damage and failure modelling at large deformation. *European Journal of Mechanics and Solids 22* (2003), 779–792.

[117] Roufaiel, M., and Meyer, C. Analysis of damaged concrete frame buildings. Tech. Rep. NSF-CEE-81-21359-1, Columbia University, New York, 1981.

[118] Rösler, J., Bäker, M., and Harders, H. *Mechanisches Verhalten der Werkstoffe.* Vieweg+Teubner Verlag, 2008.

[119] Samal, M., Seidenfuss, M., Roos, E., Dutta, B., and Kushwaha, H. Finite element formulation of a new nonlocal damage model. *Finite Elements in Analysis and Design 44* (2008), 358–371.

[120] Scheibe, H.-J. *Zum zyklischen Materialverhalten von Baustahl und dessen Berücksichtigung in Konstruktionsberechnungen.* PhD thesis, Institut für Stahlbau, TU Braunschweig, 1990.

[121] Schott, G. *Werkstoffermüdung - Ermüdungsfestigkeit.* Deutscher Verlag für Grundstoffindustrie, Stuttgart, 1997.

[122] Scotta, R., Tesser, L., Vitaliani, R., and Saetta, A. Global damage indexes for the seismic performance assessment of RC structures. *Earthquake Engineering & Structural Dynamics 38* (2009), 1027–1049.

[123] Seal, C., Hodgson, M., Clifton, G., and Ferguson, W. A novel method for predicting damage accumulation in seismically deformed steel. *Journal of Constructional Steel Research 65* (2009), 2157–2166.

[124] Shen, Z., and Wu, A. Seismic analysis of steel structures considering damage cumulation. *Frontiers of Architecture and Civil Engineering in China 1* (2007), 1–11.

[125] Simo, J., and Ju, J. Strain- and stress-based continuum damage models - I. Formulation. *International Journal of Solids and Structures 23* (1987), 821–840.

[126] Simo, J., and Ju, J. Strain- and stress-based continuum damage models - II. Computational aspects. *International Journal of Solids and Structures 23* (1987), 841–869.

[127] Skrzypek, J., and Ganczarski, A. *Modelling of Material Damage and Failure of Structures*. Springer, 1999.

[128] Sozen, M. *Review of earthquake response of reinforced concrete buildings with a view to drift control*. In: State-of-the-Art in Earthquake Engineering, Turkish National Committee on Earthquake Engineering, 1981, pp. 383–418.

[129] Springmann, M., and Kuna, M. Determination of ductile damage parameters by local deformation fields: measurement and simulation. *Archive of Applied Mechanics 75* (2006), 775–797.

[130] Stephens, J., and Yao, J. Damage assessment using response measurements. *Journal of Structural Engineering 113* (1987), 787–801.

[131] Streilein, T. *Erfassung formativer Verfestigung in viskoplastischen Stoffmodellen*. PhD thesis, Institut für Statik, TU Braunschweig, 1997.

[132] Tasan, C., Hoefnagels, J., and Geers, M. A brittle-fracture methodology for three-dimensional visualization of ductile deformation micromechanisms. *Scripta Materialia 61* (2009), 20–23.

[133] Tasan, C., Hoefnagels, J., and Geers, M. A critical assessment of indentation-based ductile damage quantification. *Acta Materialia 57* (2009), 4957–4966.

[134] Thakkar, B., and Pandey, P. A high-order isotropic continuum damage evolution model. *International Journal of Damage Mechanics 16* (2007), 403–426.

[135] Trifunac, M., and Brady, A. A study on the duration of strong earthquake ground motion. *Bulletin of the Seismological Society of America 65* (1975), 581–626.

[136] Tvergaard, V. Material failure by void growth to coalescence. *Advances in Applied Mechanics 27* (1989), 83–151.

[137] Tvergaard, V., and Needleman, A. Analysis of the cup-cone fracture in a round tensile bar. *Archives of Mechanics 32* (1984), 157–169.

[138] Velay, V., Bernhart, G., and Penazzi, L. Cyclic behavior modeling of a tempered martensitic hot work tool steel. *International Journal of Plasticity 22* (2006), 459–496.

[139] Velde, J., Kowalsky, U., Zümendorf, T., and Dinkler, D. 3D-FE-Analysis of CT-specimens including viscoplastic material behavior and nonlocal damage. *Computational Material Science 46* (2009), 352–357.

[140] Voyiadjis, G., Alsaleh, M., and Alshibli, K. Evolving internal length scales in plastic strain localization for granular materials. *International Journal of Plasticity 21* (2005), 2000–2024.

[141] Wells, G., De Borst, R., and Sluys, L. *An Enhanced Finite Element Method For Analysing Failure in Elasto-Plastic Solids.* In: Wall, W.A., Bletzinger, K.-U. and Schweizerhof, K., Trends in Computational Structural Mechanics, 2001, pp. 397–406.

[142] Williams, M., and Sexsmith, R. Seismic damage indices for concrete structures: A state-of-the-art review. *Earthquake Spectra 11* (1995), 319–349.

[143] Yang, X. Constitutive description of temperature-dependent nonproportional cyclic viscoplasticity. *Journal of Engineering Materials and Technology 119* (1997), 12–19.

[144] Yang, X. A viscoplastic model for 316L stainless steel under uniaxial cyclic straining and stressing at room temperature. *Mechanics of Materials 36* (2004), 1073–1086.

[145] Zienkiewicz, O., and Taylor, R. *The Finite Element Method, Volume 2.* McGraw-Hill, London, 1991.

[146] Zümendorf, T. *Ein gradientenabhängiges Modell für Schädigung bei viskoplastischem Materialverhalten.* PhD thesis, Institut für Statik, TU Braunschweig, 2006.

Berichte aus dem Institut für Statik ab 1994

Nr.	94-78	U. KOWALSKY: Mikrophysikalisch begründetes Werkstoffmodell zur Berechnung thermomechanisch beanspruchter Konstruktionen (1994).
Nr.	95-79	N. OBERBECK: Instationärer Wärme-Feuchte-Schadstoff - Transport in Beton, Theorie und Berechnung (1995).
Nr.	95-80	N. MELEKA: Nonlinear Analysis of Flat Slab Floors (1995).
Nr.	97-81	H. FLOREN: Strukturanalysen unterirdischer Hohlräume im Salzgebirge mit hybriden Randelement-/Finite-Element-Methoden (1997).
Nr.	96-82	T. GARTUNG: Berechnung von Asphaltstraßen mit einem einheitlichen rheologischen Konzept einschließlich Schädigung (1996).
Nr.	97-83	T. STREILEIN: Erfassung formativer Verfestigung in viskoplastischen Stoffmodellen (1997).
Nr.	97-84	B. GUERICKE: Geomechanische Untersuchungen zur Sicherheitsanalyse von Deponien im Salzgestein (1997).
Nr.	97-85	U. GLABISCH: Stoffmodell für Grenzzustände im Salzgestein zur Berechnung von Gebirgshohlräumen (1997).
Nr.	97-86	E. ELARABI: Numerical Analysis of the Swelling Soil Effects on Structures (1997).
Nr.	98-87	I. SPOHR: Störenergie-Konzept für den elasto-plastischen Beulsicherheitsnachweis beliebig belasteter Zylinderschalen (1998).
Nr.	99-88	C.-X. HUANG: Berechnung von Temperaturspannungen und Rißbildungen infolge Hydratation in 3D-Betonkonstruktionen (1999).
Nr.	2000-89	H. PENSKY: Beschreibung von streuendem Materialverhalten und von Schädigung bei inelastischen Werkstoffen (2000).
Nr.	2000-90	A. STEFFENS: Modellierung von Karbonatisierung und Chloridbindung zur numerischen Analyse der Korrosionsgefährdung der Betonbewehrung (2000).
Nr.	2001-91	J. EBERS-ERNST: Modellierung des inelastischen Verformungsverhaltens von Siedlungsabfalldeponien (2001).
Nr.	2001-92	J. HANEL: Modell zur Analyse von gekoppelten Transport- und Stoffabbauprozessen in Deponien (2001).
Nr.	2002-93	B. WIEDEMANN: Modelle für vorgespannte Membranen mit Faltenbildung (2002).
Nr.	2002-94	R. TACKE: Feuchte- und Festigkeitsentwicklung hydratisierenden Betons – Modellierung und numerische Analyse (2002).
Nr.	2002-95	E. WALHORN: Ein simultanes Berechnungsverfahren für Fluid-Struktur-Wechselwirkungen mit finiten Raum-Zeit-Elementen (2002).

Nr. 2003-96 B. HÜBNER: Simultane Analyse von Bauwerk-Wind-Wechselwirkungen (2003).

Nr. 2003-97 J. GEISTEFELDT: Stochastische Finite-Element-Methoden mit Anwendung auf aeroelastische Tragsysteme (2003).

Nr. 2003-98 O. KNOKE: Beulwiderstände zusammengesetzter Zylinder-Kegel-Schalen (2003).

Nr. 2005-99 A. KÖLKE: Modellierung und Diskretisierung bewegter Diskontinuitäten in randgekoppelten Mehrfeldsystemen (2005).

Nr. 2006-100 D. DINKLER (HERAUSGEBER): Institut für Statik – Lehre und Forschung, 1996 - 2006 (2006).

Nr. 2006-101 A. VEHRE: Ein Reduktionsverfahren für Fluid-Struktur-Wechselwirkungen mit finiten Raum-Zeit-Elementen (2006).

Nr. 2006-102 M. LÖHR: Analyse aeroelastischer Systeme mit Spektralen Stochastischen Finite-Element-Methoden (2006).

Nr. 2006-103 L. ASCHENBRENNER: Mehrkomponenten-Modell zur Beschreibung des Deformationsverhaltens von Asphalt (2006).

Nr. 2006-104 T. ZÜMENDORF: Ein gradientenabhängiges Modell für Schädigung bei viskoplastischem Materialverhalten (2006).

Nr. 2007-105 C. LEPPERT: Mehrphasenmodell für granulare Medien zur numerischen Untersuchung des Phasenübergangs bei der Entleerung von Silos (2007).

Nr. 2008-106 V. KRASE: Stability of Municipal Solid Waste Landfills (2008).

Nr. 2009-107 J. PONTOW: Imperfektionsempfindlichkeit und Grenzlasten von Schalentragwerken (2009).

Nr. 2009-108 M. BECKMANN: Ein gradientenabhängiges Modell für anisotrope Schädigung von Beton unter Berücksichtigung von Porendruck (2009).

Nr. 2010-109 P. SUN: Fluid-Struktur-Wechselwirkung mit aktiver Schwingungskontrolle durch piezoelektrische Materialien (2010).

Sonderdrucke

Phänomenologische Modelle für Werkstoffe des Bauwesens.
Hermann Ahrens zum 60. Geburtstag (1998).
Herausgeber: D. Dinkler, U. Kowalsky.

Baustatik-Baupraxis 8.
Berichte der Fachtagung am 21. und 22. März 2002 in Braunschweig.
Herausgeber: D. Dinkler.

Institut für Statik, Technische Universität Braunschweig
Beethovenstraße 51, 38106 Braunschweig, Deutschland
Telefon: +49 (0)531/391-3668, Telefax: +49 (0)531/391-8116
E-Mail: statik@tu-bs.de, Homepage: http://www.statik.tu-braunschweig.de